SLAC-R-642

Timing and Spectral Studies of the Peculiar X-ray Binary Circinus X-1*

P. M. Saz Parkinson

Stanford Linear Accelerator Center
Stanford University
Stanford, CA 94309

SLAC-Report-642
August 2003

Prepared for the Department of Energy
under contract number DE-AC03-76SF00515

Printed in the United States of America. Available from the National Technical Information Service, U.S. Department of Commerce, 5285 Port Royal Road, Springfield, VA 22161.

---

*Ph.D. thesis, Stanford University, Stanford, CA 94309.

TIMING AND SPECTRAL STUDIES OF THE PECULIAR X-RAY BINARY CIRCINUS X-1

A DISSERTATION
SUBMITTED TO THE DEPARTMENT OF PHYSICS
AND THE COMMITTEE ON GRADUATE STUDIES
OF STANFORD UNIVERSITY
IN PARTIAL FULFILLMENT OF THE REQUIREMENTS
FOR THE DEGREE OF
DOCTOR OF PHILOSOPHY

Pablo Miguel Saz Parkinson
August 2003

I certify that I have read this dissertation and that, in my opinion, it is fully adequate in scope and quality as a dissertation for the degree of Doctor of Philosophy.

Elliott Bloom
(Principal Adviser)

I certify that I have read this dissertation and that, in my opinion, it is fully adequate in scope and quality as a dissertation for the degree of Doctor of Philosophy.

Robert Wagoner

I certify that I have read this dissertation and that, in my opinion, it is fully adequate in scope and quality as a dissertation for the degree of Doctor of Philosophy.

Peter Michelson

Approved for the University Committee on Graduate Studies:

To the loving memory of my Spanish grandmother
Dolores Pérez Crespo
who passed away while I was in graduate school
and
to my English grandmother
Amelia Grace Parkinson

Abstract

Circinus X-1 (Cir X-1) is an X-ray binary displaying an array of phenomena which makes it unique in our Galaxy. Despite several decades of observation, controversy surrounds even the most basic facts about this system. It is generally classified as a Neutron Star (NS) Low Mass X-ray Binary (LMXB), though this classification is based primarily on the observation of Type I X-ray Bursts by EXOSAT in 1985. It is believed to be in a very eccentric ∼16.5 day orbit, displaying periodic outbursts in the radio and other frequency bands (including optical and IR) which reinforce the notion that this is in fact the orbital period. Cir X-1 lies in the plane of the Galaxy, where optical identification of the companion is made difficult due to dust obscuration. The companion is thought to be a low mass star, though a high mass companion has not currently been ruled out.

In this work, I analyze recent observations of Cir X-1 made with the *Unconventional Stellar Aspect* (USA) experiment, as well as archival observations of Cir X-1 made by a variety of instruments, from as early as 1969.

The fast (< 1 s) timing properties of Cir X-1 are studied by performing FFT analyses of the USA data. Quasi-Periodic Oscillations (QPOs) in the 1–50 Hz range are found and discussed in the context of recent correlations which question the leading models invoked for their generation. The energy dependence of the QPOs (rms increasing with energy) argues against them being generated in the disk and favors models in which the QPOs are related to a higher energy Comptonizing component.

The power spectrum of Cir X-1 in its soft state is compared to that of Cygnus X-1 (Cyg X-1), the prototypical black hole candidate. Using scaling arguments I argue that the mass of Cir X-1 could exceed significantly the canonical 1.4 $M_\odot$ mass of a neutron star, possibly partly explaining why this object appears so different to other neutron stars.

The spectral evolution of Cir X-1 is studied by constructing both instrument-independent and model-independent color-color diagrams. Spectral fits are performed on all USA observations and physical parameters are derived. Cir X-1 periodically evolves from a ‘high/soft’ state to a ‘low/hard’ state within each orbital cycle.

The spectral fits obtained indicate that a two-component model provides an appropriate description of the Cir X-1 spectrum with one component representing the emission from a multicolor blackbody accretion disk while the other component represents the higher energy Comptonized emission probably coming from a boundary layer on the surface of the neutron star.

To study the long-term X-ray variability of Cir X-1 I analyze archival data from instruments going back to 1969 (Vela 5 satellite), up to more recent RXTE ASM data (for the last 6.5 years). I use various period finding techniques such as Lomb-Scargle periodograms and Phase Dispersion Minimization. Cir X-1 shows large variations in overall flux over the course of the last 30 years, with the brightest epoch corresponding to the recent RXTE/USA era. I derive an X-ray ephemeris based on these long term observations showing that the period of Cir X-1 is rapidly decreasing ($P/\dot{P} < 3000$ yrs), possibly implying a very young age for the system.

I compute dynamic periodograms and find some new, unexplained periodicities. There is a 250 day span of RXTE ASM data where the orbital period is undetectable while a new $\sim$40 day period is observed. Furthermore, a 335 day super-orbital period is detected, with a hardness ratio perfectly anti-correlated, possibly implying that this is due to obscuration arising from a precessing accretion disk.

After more than 30 years of study there is still much that is not known with certainty about the nature of Cir X-1. In this dissertation I shed some light on the behavior of this unique source in several domains: in the short time scales, in the long time scales, and in the inter-relationship between the time domain and the energy domain. In so doing, I explore models of quasi-periodic oscillations as well as spectral models of accreting sources and try to illustrate how these different phenomena arise in general, and how they might apply specifically to Cir X-1.

Acknowledgements

Figure 1: "Piled Higher and Deeper" by Jorge Cham www.phdcomics.com

Joking aside, I would like to express my deep appreciation to my adviser, Elliott Bloom, for his guidance, support, and encouragement during my graduate career. Working in group K at SLAC has been been a wonderful experience and I hope that in my future career I will find an environment as friendly and conducive to doing research as this has been. The last couple of years have been an extremely exciting time to be doing astrophysics at SLAC. I am sure that I will look back on this time with great fondness, recalling how astrophysics went from being a minor interest at SLAC, to being at the core of the lab's mission. It is quite an honor to have been a part of group K at a time when, due in no small part to Elliott's leadership, the lab was expanding its horizons in this new direction.

I have enjoyed interacting with all members of group K. It was always fun going into Gary Godfrey's office. Whether it was to listen to his explanations of instrumental effects, USA circuitry, or simply to discuss the latest paper or talk that was catching his interest (often about MOND). It is truly inspiring to see someone still enjoy physics as much as Gary does after so many years (oops, sorry Gary). I also want to thank many other members of group K who helped me along the way, including Al

Odian, John Broeder, Eduardo do Couto e Silva, Larry Wai, Chris Chaput, Andrew Lee, Andy Reid, and Chris Hall. Jeff Scargle, our resident NASA expert, was always willing to spend time discussing all sorts of issues. It is quite an honor to have worked with him, even if it is only to show off about the fact that I know the 'Scargle' in 'Lomb-Scargle' periodogram. I am also proud to have known Paul Kunz. I am sure I will have many occasions to boast about knowing the person who put up the first web site in the U.S. I enjoyed taking his C++ course and getting the latest news about Linux, Python, Hippodraw, or other really neat programs.

Berrie Giebels has been an incredible help throughout my (or rather his) time at SLAC. Berrie's comments, advice, and guidance have been one of the driving forces of my graduate career. His varied astrophysical interests have also served to expand my own field of interest and I hope we will get a chance to work together again in the future. Being from 'old Europe' himself, I also really enjoyed our lunch time conversations and appreciated having an 'ally' in the political debates that would invariably take place between us and more conservative members of the group. I would also like to express my sincere appreciation to Warren Focke, who at the moment is lying in bed recovering from a serious rollerblading accident. I hope he will fully recover soon. Much of the work in this dissertation would probably not have been done (or certainly would have taken a **lot** longer) without Warren's help. His expertise in so many fields, from programming to physics and statistics, and his constant willingness to share his time with others meant there was always a place to go to get the answers.

It has also been a pleasure having so many fellow graduate students in the group, including students from other departments, such as Michael Hicks and Alicia Kavelaars (the other half-Spaniard of the group). It is always easier to struggle through graduate school when you have people who are in the same boat (or satellite).

Ganya Shabad was extremely helpful when I first joined the group and it was a pleasure to work with her. I also enjoyed our conversations about cultural and political differences, despite her somewhat anti-European views (I promise I'm not a communist, Ganya).

I'm grateful to Daniel Engovatov (a.k.a. 'the crazy Russian') for convincing Elliott that Linux is not ‘just a toy’. It was a tough fight, but thanks to Daniel most of us managed to avoid using Windows at work.

Kaice Reilly was a great office mate (taekwondo kicks in the face aside), not least because he was surfing half the time (just kidding). It was extremely helpful to be working on USA at the same time as Kaice. Despite everyone else around, it was often thanks to the discussions we had in our office or work we were both doing separately that most progress was made.

What to say about Derek Tournear, other than he’s from middle (sorry, *real*) America (Kansas). To say that we have had some disagreements would be an understatement. Let’s just say that most of our debates ended by (either he or I) quoting one of his idols: ‘I guess we’re just going to have to agree to disagree on that one’. It is always interesting to find out that even good, highly intelligent people can have views that are so ... well, different from my own. Despite our many disagreements, I can honestly say that it has been a pleasure working with Derek and being in the same group and I hope we stay in touch.

I would like to thank all the members of the NRL group who collaborated with us, especially Kent Wood, Paul Ray, Reba Bandyopadhyay, Mike Lovellette, and Mike Wolff with whom I worked most closely. I am grateful for their hospitality during my visit to NRL. It was also great fun getting together with them at conferences at such exotic places as Hawaii, New Mexico, or more recently in Montreal.

I would like to thank the members of my dissertation defense committee: Bob Wagoner, Peter Michelson, Greg Madejski, and especially Antony Fraser-Smith, for chairing the committee.

Greg deserves a special mention, among other things, for inviting so many great people to SLAC. The meetings and astrophysics seminars that Greg has organized since arriving at SLAC have made it possible to really keep up with all the exciting developments in the field without even leaving SLAC. His efforts to increase the interaction between the campus and SLAC groups have also had great results.

I am grateful to Mallory Roberts for helping me to get started with XSPEC and the energy calibration of USA. I also would like to thank Chris Done for her very helpful discussions and suggestions and for her hospitality during my visit to Durham.

I am extremely grateful to Vahé Petrosian for taking me into his group so many years ago when I decided to switch my interests from mechanical engineering to astrophysics. I am convinced that were it not for his early encouragement, I would not be where I am today.

I have met many people at Stanford in these past years, whether it be playing soccer, inner-tube water-polo, or simply having a cup of coffee at the Co-Ho (for those who don't know, it's right next to Tres-Ex, not too far from Mem-Chu). I have enjoyed sharing these and many more experiences with them and I am sure I will be in touch with many of them for years to come.

My family, and in particular my parents, deserve most of the credit for me reaching this milestone. I think it would be difficult to find parents who gave their children (four of them!) such a balanced and privileged upbringing. More than anyone I know, my parents always understood, not only the value a good education, but also the importance of raising well-rounded individuals. Not that they are perfect (to paraphrase Sinatra: *mistakes, they made a few; but then again, too few to mention.*), but given what's out there these days ... I think I'll keep them!

Finally, I would like to thank the lovely Cathryn Donohue. Her kindness, sense of humor, intelligence, compassion, generosity, wonderful cooking (*wadda ye call that then?*) have made sharing these past years with her the best thing about my whole graduate school experience. To say that I have never met anyone like her doesn't do justice to the type of person she is. The fact that we have yet to have a serious argument only shows that even someone as confrontational as I am is powerless in front of her kindness. I will be submitting my dissertation at the same time and on the same day as she is defending hers, and I am sure this must be one of those 'cosmic coincidences' that my brother keeps trying to sell me.

Stanford, 22 August 2003

Contents

List of Tables

List of Figures

Chapter 1

Introduction

> *Something is happening here, but you don't know what it is.*
> *Do you, Mister Jones?*
> Bob Dylan, "Ballad of a thin man" (1965)

In this dissertation I investigate the timing and spectral properties of the X-ray binary source Circinus X-1 (hereafter, Cir X-1). I also discuss my contributions to the USA collaboration, mainly in the energy calibration of the instrument and in the development of a background model, both of which are crucial in the analysis and interpretation of USA data. I also discuss some other instrumental issues which arose during the mission.

1.1 A Brief Introduction to X-ray Astronomy

The first Nobel Prize in Physics was awarded in 1901 to Wilhelm Conrad Röntgen for his discovery of X-rays in 1895. However, it was not until 2002 that the field of X-ray astronomy, represented by Ricardo Giacconi, was rewarded with a Nobel Prize in Physics. This apparent lag (the use of X-rays in medicine, for example, was almost immediate) was due mainly to the fact that X-rays are easily absorbed in the atmosphere, as seen in Figure 1.1 (Charles and Seward 1995). This figure shows how high (both in km and in fraction of atmosphere left above such height) one must be in order to detect half the incoming radiation at a given wavelength. It is, therefore, not surprising that the birth of X-ray astronomy had to wait for the birth of the space age.

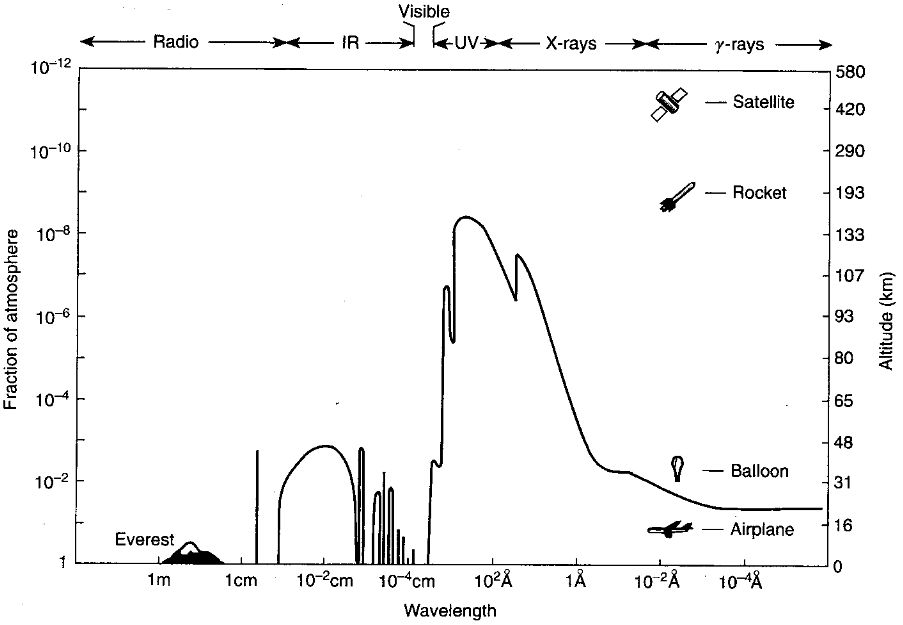

Figure 1.1: Absorption of radiation by the atmosphere (Charles and Seward 1995)

Early X-ray observations relied on rockets (many of them captured from the Germans after W.W.II). It is hardly surprising that the first astronomical source of X-rays observed was the Sun (by Herbert Friedman and collaborators at the U.S. Navy Research Laboratory (NRL) in 1949). More surprising was the discovery that sources other than the Sun could be observed in X-rays at all, given the (relatively) low X-ray luminosity of the Sun and the astronomical distances of other sources. It was not until 1962 that the first detection of a cosmic source of X-rays was made by Ricardo Giacconi of American Science and Engineering (AS&E) (Giacconi et al. 1962). The source became known as Scorpius X-1 (Sco X-1), on account of it being the first X-ray source detected in the constellation of Scorpius. Sco X-1 is the second brightest source in the X-ray sky (after the Sun), so it is no surprise that it should be the first cosmic source to be discovered (See Figure 1.2). In 1964, Herbert Friedman made the landmark observation of X-ray emission from the Crab Nebula as it was being occulted by the Moon (good pointing in those days was a big issue and this technique made it possible to conclude that the X-rays were indeed coming from the Crab). On 12 December 1970 the first X-ray satellite, Uhuru[1], was launched. Also known as the Small Astronomical Satellite 1 (SAS-1), this was the first Earth-orbiting mission dedicated entirely to celestial X-ray astronomy. The satellite operated until March 1973 and produced the first all sky survey of the X-ray sky. Since then, many more X-ray missions have flown and there are now hundreds of thousands of X-ray sources waiting to be studied and better understood. Figure 1.2 shows the X-ray map of the sky (in Galactic coordinates) obtained by the NRL Large Area Sky Survey Experiment (LASS) on the HEAO-1 satellite, which operated from 12 August 1977 until 9 January 1979 (Wood et al. 1984). The catalog contains 842 sources from a systematic sky survey, sensitive down to 0.001 Crab. For an excellent introduction to X-ray astronomy, see Charles and Seward (1995).

1.2 Circinus X-1

1.2.1 Discovery

The first recorded observation of Cir X-1 (though it was given a different name) was made during a survey conducted by NRL on 25 April 1965 (Friedman et al. 1967) in which the locations of 29 cosmic X-ray sources were determined. However, the source was observed in only one scan, leading to a large uncertainty in its position. The discovery of Cir X-1 was reported by Margon et al. (1971), based on an observation made from an Aerobee rocket launched on 14 June 1969.

1.2.2 Distance

Initial estimates of the distance to Cir X-1 (Goss and Mebold 1977), based on radio observations of the HI absorption profile, placed a lower limit of 8 kpc. to the source, though this is based on the assumption that the distance to the Galactic center is

---

[1] Swahili word for ‘freedom’. Uhuru was launched from Kenya on Kenyan Independence Day.

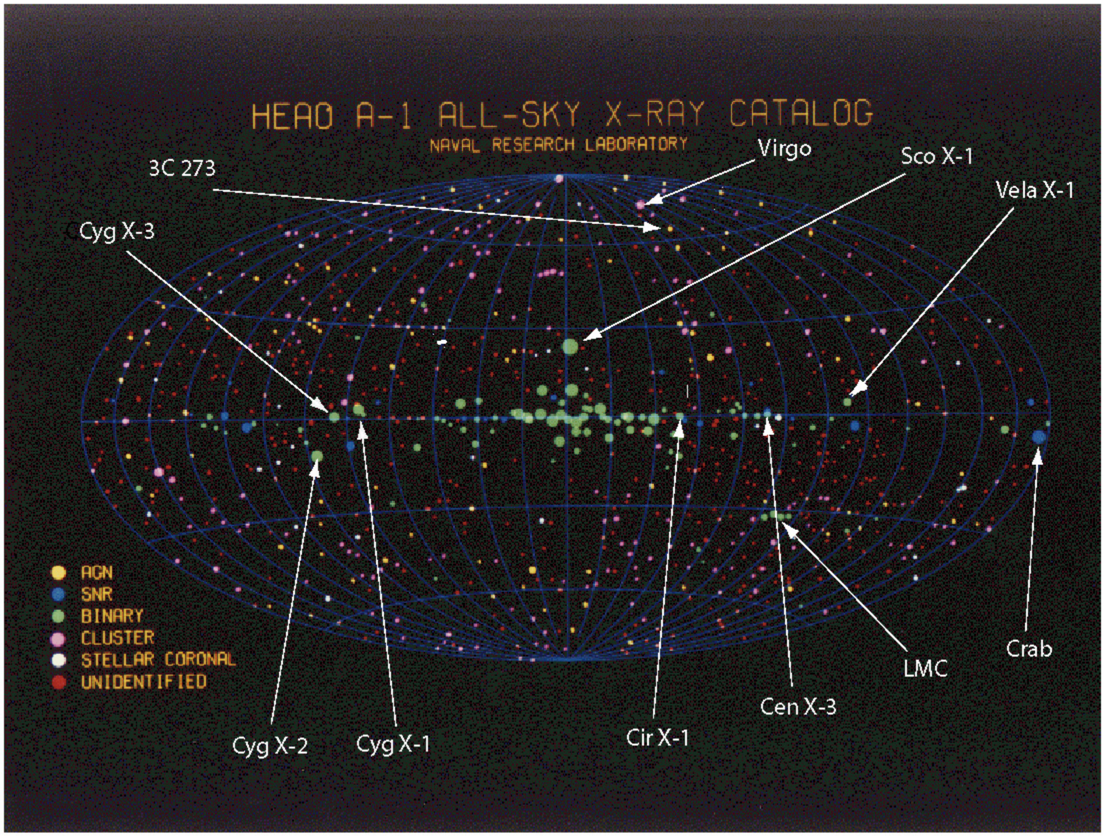

Figure 1.2: The HEAO-1 catalog (Wood et al. 1984)

10 kpc. A distance of 8 kpc to the Galactic center would give a minimum distance to Cir X-1 of 6.5 kpc (Stewart et al. 1991). An upper limit of ∼9 kpc was obtained by Clark et al. (1975) based on the attenuation of X-rays at energies < 2 keV. Later observations of Supernova remnant (SNR) G321.9-0.3 (Case and Bhattacharya 1998) and the assumption that Cir X-1 was associated with this SNR led to a downward revision of the distance to 5.5 kpc; however, this is no longer valid given that such an association has now been ruled out (Mignani et al. 2002).

1.2.3 Orbital Properties

Orbital Period

Observations made with Uhuru from 1971 to 1973 (Jones et al. 1974) suggested that Cir X-1 was a binary source with a period longer than 15 days. Later detections by Ariel V over 1975–1976 resulted in the determination of a 16.6 day period (Kaluzienski et al. 1976). The radio counterpart to Cir X-1 (Clark et al. 1975) was soon found to display periodic flares at the same 16.6 day period (Whelan et al. 1977). In addition, IR observations (Glass 1978) and optical observations (Moneti 1992) also show this periodicity, leading to the firm conclusion that this is the orbital period of the system. In Chapter 5 I discuss how the orbital period has changed over the course of the last 30 years.

Eccentricity

Clark et al. (1975) were the first to suggest that Cir X-1 may be associated with the then recently discovered SNR G321.9-0.3. The explosion resulting from such a supernova would give rise to the long orbital period as well as a high eccentricity and large space velocity of the resulting system. While recent observations have ruled out this association (Mignani et al. 2002), the hypothesis that Cir X-1 is a highly eccentric binary has proven to still be valid. Murdin et al. (1980) derived a value of the orbital eccentricity of 0.8 ± 0.1 based on the assumption that the changing shape of the X-ray light curve was due to absorption in the primary's stellar wind. Using radio observations, the authors derive a value of the eccentricity of $e = 0.72 \pm 0.02$, consistent with the previous value. More recently, Tauris et al. (1999) derived a value for the eccentricity of 0.94 ± 0.04 from Monte-Carlo simulations of a large number number of SN in binary systems. Shirey (1998) also found from Monte-Carlo population synthesis studies that the distribution of possible eccentricities is constrained to high values, with the peak of such distribution lying somewhere between 0.83 and 0.93. We should point out, however, that some of the parameters which went into these population studies were fixed at values that are not necessarily correct. For example, Shirey (1998) chose donor masses only in the range 0.8 to 3 $\mathrm{M}_\odot$ and fixed the mass of the compact object at 1.4 $\mathrm{M}_\odot$, both of which may turn out to be wrong.

1.2.4 The Compact Object (Secondary Star)

The nature of the compact object in Cir X-1 has been a matter of considerable debate. The determination of the compact object in an X-ray binary is crucial if we are to learn anything about these objects or about the extreme environments they live in. Compact objects represent the end states of stellar evolution and come in three main varieties: white dwarfs, neutron stars, and black holes.

White dwarfs are stars which are supported by the degeneracy pressure of their electrons, with a mass of less than 1.44 $\mathrm{M}_\odot$ (Chandrasekhar limit). Distinguishing white dwarfs from neutron stars and black holes is not difficult since their gravitational potential is so much weaker. Many isolated white dwarfs are observable in the optical and EUV, while some are found in interacting binary systems known as Cataclysmic Variables (CVs) which often undergo explosive outbursts and are observable in X-rays. Distinguishing between neutron stars and black holes, on the other hand, can be quite challenging. The best way to distinguish between them is by obtaining a mass function:

$$f_c(M) \equiv \frac{P_{orb} K_c^3}{2\pi G} = \frac{M_x \sin^3 i}{(1 + M_c/M_x)^2} \tag{1.1}$$

where $\mathrm{P}_{\mathrm{orb}}$ is the orbital period and K_{c} is the semi-amplitude of the optical radial-velocity curve. If we assume that M_{c} (the mass of the companion) is zero and the inclination angle (i) is maximum ($\pi/2$, i.e. we are looking parallel to the plane of the binary orbit), we obtain the smallest possible mass for the compact object. If this number is higher than $3M_{\odot}$ the object is classified as a *Black Hole Candidate* (BHC) (Rhoades and Ruffini 1971). Sometimes the mass function does not provide an interesting limit. The mass function for Cygnus X-1 (Cyg X-1), for example, is only 0.25 $M_{\odot}$, however, knowledge about the companion and the inclination angle places the best estimate for its mass safely above the 3 $M_{\odot}$ limit, making it one of the firmest BHCs currently known (see Figure 4.24).

Unfortunately, Cir X-1 has no observable mass function because it lies in the plane of the Galaxy, in a heavily obscured region, so we must use other methods to try to determine the nature of the compact object. Some characteristics once thought to be unique to BHs are: an ultrasoft spectrum, a high energy power-law tail (above 20 keV) and bi-modal spectral states (high/soft and low/hard). Cir X-1 shows all these characteristics. In fact, early observations of Cir X-1 also suggested a similarity to Cyg X-1, then one of the few black hole candidates (Jones et al. 1974), including the observation of millisecond bursts (Toor 1977), flickering in the hard state and a very soft energy spectrum in the high state, which taken together led to its classification as a BHC.

However, the detection in 1985 by EXOSAT of Type I X-ray bursts (Tennant et al. 1986a) led to Cir X-1 being classified as a neutron star. Type I bursts are thermonuclear explosions on the surface of a neutron star and are therefore not possible in black holes (assuming black holes have a horizon. See Tournear et al. (2003) for a discussion on the search for Type I bursts in black holes). No further bursts have been observed since the EXOSAT detections, although it is argued that this could be due to the high mass accretion rate of the source since then. At high accretion rates, the material is expected to burn continuously as opposed to burst. In Chapter 5 I discuss how the overall brightness of Cir X-1 has varied over the course of the last 30 years, showing that, indeed, when EXOSAT observed bursts, the luminosity of the source was significantly lower than it has been since. However, in recent times the source has dimmed considerably and could possibly return to a level where bursts would be expected to occur more frequently.

1.2.5 The Optical Companion (Primary Star)

X-ray binaries are not only classified according to the compact object they contain, but also by the type of companion from which matter is being accreted. The nature of this companion has important consequences for the observed system. Binary systems with companion masses $\gtrsim 10M_\odot$ are called High Mass X-ray Binaries (HMXBs) while those with a low mass companions ($\lesssim 1M_\odot$) are referred to as Low Mass X-ray Binaries (LMXBs).

HMXB systems normally have giants or supergiants as donor stars (Type O or B stars). These stars have strong winds, making spherical accretion the dominant form of mass transfer onto the compact object. The strong winds also cause photoelectric absorption in the X-ray spectrum. Their orbital periods tend to be in the order of days and are typically calculated from pulse arrival time analysis or from eclipses. They have relatively low luminosities (around $10^{33} - 10^{35}$ erg/s).

LMXBs have companion stars of spectral type A or later. These stars have very weak winds, making disk accretion (through Roche lobe overflow) the dominant form of mass transfer. They generally have shorter orbital periods than HMXBs (in the order of hours instead of days). They can be as short as 11.4 minutes (X1820-303), although some systems appear to have much longer periods. Cyg X-2 and Cir X-1, for example, have orbital periods of 9.8 and 16.6 days respectively.

The optical counterpart of Cir X-1 has been extremely difficult to classify. Moneti (1992) showed that Cir X-1 was associated with the southernmost of a group of three stars located within a 1.5 arcsecond diameter region (see Figure 1.3). The object is highly reddened and displays no prominent emission or absorption features, besides Hα emission (Johnston et al. 1999), making its spectral determination uncertain. Most authors classify Cir X-1 as an LMXB, based mainly on the presence of X-ray bursts, the high $\frac{L_X}{L_{opt}}$ (Oosterbroek et al. 1995), and the timing similarities to other LMXBs (Stewart et al. 1991; Shirey et al. 1999), though some propose an intermediate 3–5 $M_\odot$ companion (Johnston et al. 2001).

1.2.6 Mass Transfer in the System

Mass transfer is believed to occur by Roche lobe overflow as well as via stellar wind at or around periastron. The significance of wind accretion depends highly on the mass of the companion. The recent detection of P Cygni profiles from Cir X-1 (Brandt and Schulz 2000) implies that there is a high-velocity outflow in the system (up to $\sim 1900\,\mathrm{km\,s^{-1}}$), though the authors interpret this wind as coming from an accretion disk being viewed edge-on, rather than from a high-mass companion.

The Eddington Limit

As compact objects accrete matter, they become more luminous. Radiation, however, exerts pressure on infalling matter, pushing it away, so there is a limit to how luminous an accreting source can be. This is known as the Eddington limit. It is derived by assuming that the infalling matter is pure, fully ionized hydrogen, and that spherical accretion is taking place. The gravitational force exerted by a compact star of mass M_* on a hydrogen ion-electron pair can then be expressed approximately as:

$$F_g = -G\frac{M_* m_p}{r^2} \tag{1.2}$$

The force exerted by the radiation pressure (assuming spherical symmetry) will be equal to:

$$F_r = \frac{L}{4\pi r^2 c}\sigma_T \tag{1.3}$$

where $\sigma_T = 6.65 \times 10^{-25}\,\mathrm{cm}^2$ is the Thomson cross section. The Eddington luminosity is the luminosity at which these two forces exactly balance each other out.

$$L_{EDD} = \frac{4\pi G M_* c m_p}{\sigma_T} \approx 1.25 \times 10^{38} (M/M_\odot)\,\mathrm{erg\,s^{-1}} \tag{1.4}$$

For luminosities greater than the Eddington luminosity, radiation pressure would be so great that accretion would cease and the source would turn off. While the Eddington limit is not strictly an unreachable limit (given some of the unrealistic assumptions that go into its derivation), it nevertheless provides a useful scale, and it is common to find authors in the field quoting luminosities as a fraction of Eddington. In recent years, Cir X-1 has been very bright, at times greatly exceeding the Eddington limit for a distance of 5.5 kpc and a canonical mass of 1.4 $M_\odot$, though a mass twice as large would bring us down below the Eddington limit (see Chapter 4).

1.2.7 Radio Emission

As mentioned above, Cir X-1 shows periodic flares in its radio emission. The onset of radio flares has been used to derive an ephemeris for the source (Nicolson 1980; Stewart et al. 1991), though since the mid-1980's these flares have been too weak to derive an updated ephemeris (Fender et al. 1998). Besides showing periodic radio flares, Cir X-1 is embedded in a synchrotron nebula of arcminute scales and also displays an asymmetric jet on arcsecond scales (see Figure 1.3) with outflow velocity of at least 0.1c (Fender et al. 1998), making it part of a growing family of microquasars in our Galaxy (Mirabel 2001). Fender et al. (1998) stress that this is the first source to provide evidence that a black hole may not be necessary for the production of relativistic jets in X-ray binaries.

1.2.8 Timing Properties

In their paper which reported the discovery of Cir X-1, Margon et al. (1971) found a periodic pulse at 1.46 ± 0.06 Hz. A QPO close to this frequency was observed by Tennant (1988), as well as more recently by RXTE (Shirey et al. 1998). QPOs in the range 5–20 Hz were also observed by EXOSAT (Tennant 1987), as well as a broader one in a high (100-200 Hz) frequency (though this QPO does not meet the ususal standard of having a $Q > 2$). Shirey et al. (1999) used RXTE data to study the timing and spectral properties of Cir X-1 and found that they resembled those of other Z sources, displaying QPOs which they classify as Horizontal Branch Oscillations (HBOs) and Normal Branch Oscillations (NBOs). Unlike the six well-known Z sources, Cir X-1 does not show kHz QPOs. RXTE data show a high-frequency component in the range 20–100 Hz (Shirey 1998), but no QPOs above 100 Hz. The highest QPOs found with USA are $\sim$50 Hz, though our searches for high

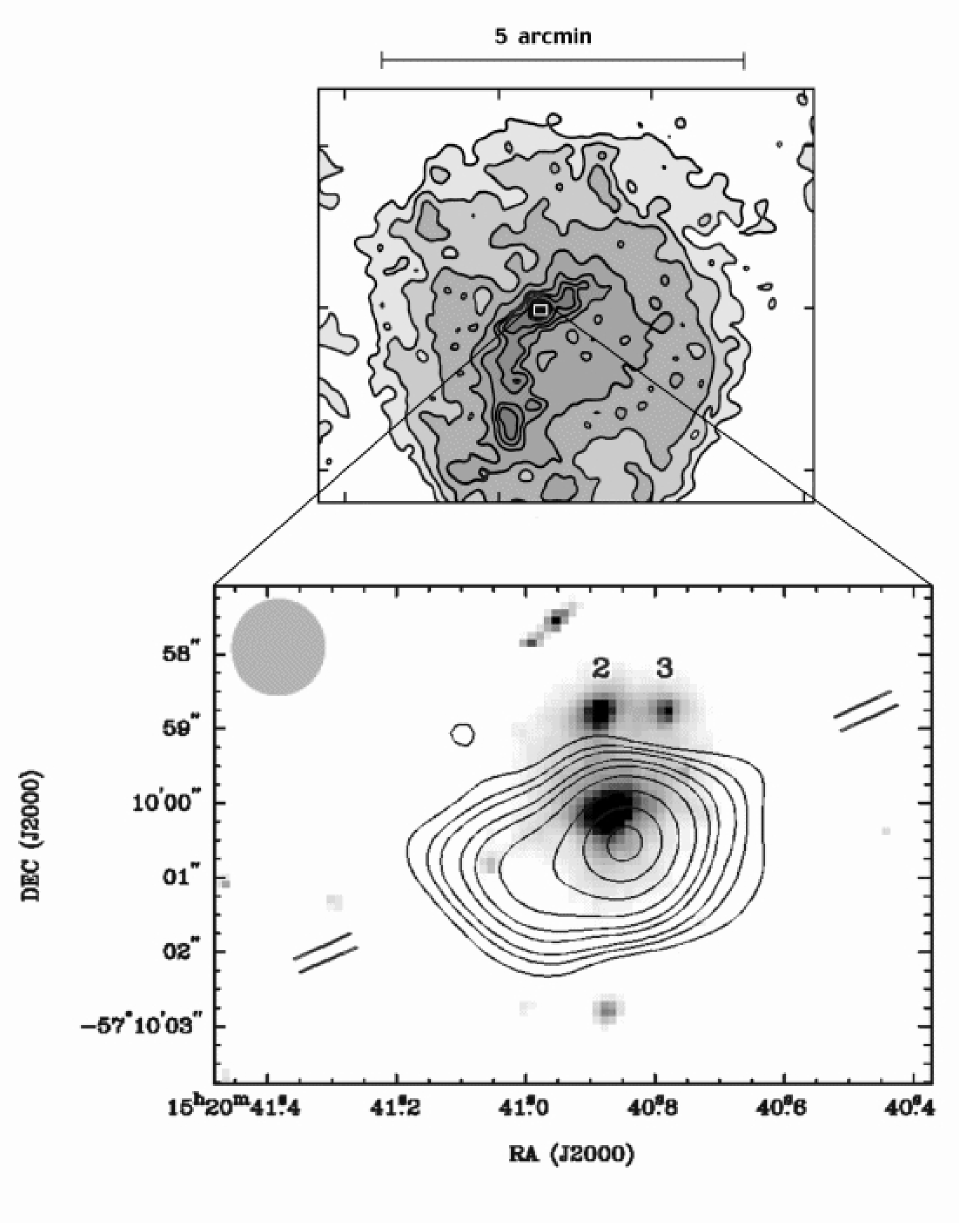

Figure 1.3: The asymmetric radio jet in Cir X-1. The top panel shows the extended radio emission on arcminute scales (Stewart et al. 1993). The bottom panel shows the high-resolution radio image at 3.5 cm overlayed on the HST optical image. The contours are at -5, 5, 7.5, 10, 15, 20, 30, 50, 75, and 100 times the rms noise of 40 μJy beam^{-1} (Fender et al. 1998).

frequency phenomena are hampered by the *Energy Dependent Instrumental Effect* (EDIE), a result of a pile-up problem in the electronics of USA which manifests itself as a distortion of the power spectrum in the high frequencies (for more details see Appendix C.2 and Reilly (2003)).

1.2.9 Spectral Properties

Z Source vs Atoll Source

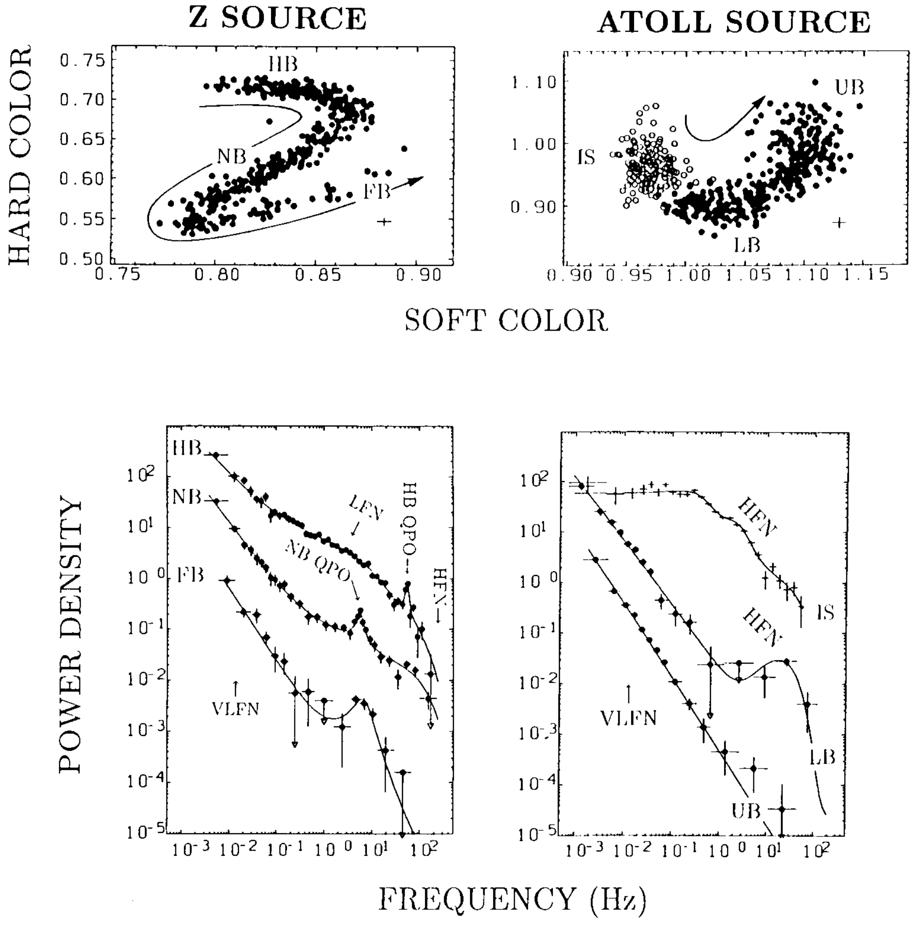

Figure 1.4: Color-Color diagrams and power spectra of a typical Z and Atoll source (Lewin et al. 1995)

LMXBs are normally classified following a convention introduced by Hasinger and van der Klis (1989) as Z sources or Atoll sources, based primarily on the pattern traced out by these different sources on a color-color diagram. A color-color diagram is formed by taking a photon count spectrum and dividing it into four *Pulse-Height Analyzer* (PHA) channel bands. The PHA channels contain the raw number of photon counts detected by the instrument. The ratio of the number of counts in the highest band to the number of counts in the second highest is designated as the "hard" color, whereas the ratio of the number of counts in the second lowest energy band to those in the lowest energy band is designated as "soft" color. Figure 1.4 shows a typical pattern traced out by a Z and an Atoll source. The different regions of each pattern are the Horizontal Branch (HB), Normal Branch (NB), and Flaring Branch (FB) for Z sources and Island State (IS) and Banana State (which is further subdivided into Upper Banana (UB) and Lower Banana (LB)) for Atolls. Hasinger and van der Klis found that in addition to tracing out different patterns on these color-color diagrams, the movement of a source along these tracks of the diagram was smooth and was correlated with the energy spectrum of the source and its timing behavior. Z sources tend to be very bright, reaching rates comparable to Eddington and are thought to have relatively strong magnetic fields ($B \geq 10^9 G$), whereas Atolls have much lower luminosities (less than $0.1 L_{Edd}$), and are believed to have much weaker magnetic fields. Recently, however, Muno et al. (2002) and Gierliński and Done (2002) have found that atoll sources and Z sources in fact can trace out similar patterns on color-color diagrams (see Figure 1.5) and that some of the previously observed differences could be explained by incomplete sampling over the dynamic range in intensity of the sources. While physical differences between Atoll and Z sources remain, they appear to be less clearly defined than once thought.

1.2.10 Summary

Cir X-1 is classified as a Neutron Star (NS) Low Mass X-ray Binary (LMXB), based primarily on the observation of Type I X-ray Bursts made by EXOSAT. The system is believed to be in a ∼16.5 day eccentric orbit and displays relativistic jets, making it a microquasar. It is a relatively distant source ($\sim$ 6.5kpc) which lies in the plane

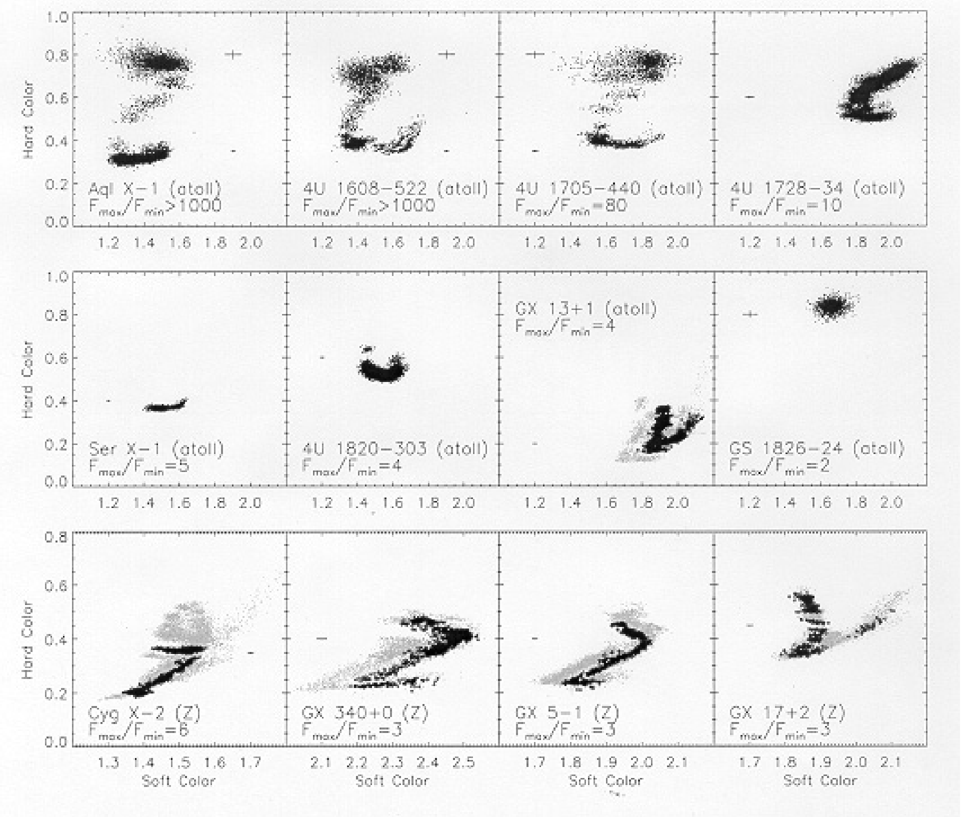

Figure 1.5: Color-Color diagrams of Atoll and Z sources showing similar patterns. The top 8 sources are Atoll sources while the bottom 4 are Z (Muno et al. 2002)

of the Galaxy, making the classification of its highly reddened companion uncertain.

1.3 Outline of this Work

In Chapter 1, I provide a brief history of X-ray binaries and a detailed introduction to Cir X-1. I describe the aspects which make this source unique, as well as those which I will expand on in more detail in my work.

In Chapter 2 I give a description of the USA detector, the main instrument used to carry out my 'short time scale' investigations. I provide a detailed account of the energy calibration of the instrument with extensive references where the reader can find more about specific aspects of the instrument.

Chapter 3 describes the data analysis techniques used to derive the main results in this thesis. First I discuss timing techniques such as the FFT, and period-searching techniques for unevenly sampled data, such as the Lomb-Scargle periodogram, the Phase Dispersion Minimization (PDM) method, and the χ^2 minimization technique. I then describe the energy spectral models used in XSPEC to fit the energy spectrum of Cir X-1, giving a physical interpretation for these models.

Chapter 4 discusses the fast (< 1 s) timing properties and energy evolution of Cir X-1. The spectral evolution of the source is presented using both an instrument-independent color-color diagram (constructed by making spectral fits to each individual observation and therefore taking ratios of actual fluxes) as well as by the more standard model-independent one (constructed by taking ratios of channel counts, therefore making it dependent on the instrument but not the spectral model). The evolution of the different individual spectral components is discussed. The correlated timing evolution is discussed including the many QPOs found in the system. I analyze the properties of these QPOs and discuss them in the context of recently published correlations which question the leading models for generation of such QPOs. I describe possible models for QPOs which could be consistent with these correlations, such as the Acoustic Oscillation Model (AOM) and the Dripping Hand Rail (DHR) model.

Chapter 5 is an investigation into the long-term X-ray variability of Cir X-1. I look at data from the last 30 years from several different instruments. I derive an X-ray ephemeris and discuss the rapid change in orbital period of the system. I discuss other periodicities previously unreported, such as a 40-day signal and a 335 super-orbital period and present an interpretation for such a periodicity.

In Chapter 6 I summarize the main conclusions of my investigations and suggest directions for future research.

In the appendices I provide the codes which were used to carry out the energy calibration of the instrument and an explanation of the background model for USA, as well as a description of several instrumental issues in which I have been involved.

Chapter 2

The USA Instrument Energy Calibration

Nowhere to run, ain't got nowhere to go.
I'm a long gone daddy in the U.S.A.
Bruce Springsteen, "Born in the U.S.A." (1984)

2.1 The ARGOS Mission

The *Advanced Research and Global Observation Satellite* (ARGOS) was launched on 23 February 1999 on a Boeing Delta II rocket from Vandenberg Air Force Base. The ARGOS mission was supported by the Department of Defense (DoD) Space Test Program (STP), a program set up in 1965 to provide spaceflight for DoD research and development experiments which are not authorized to fund their own flight. The satellite, weighing 5000 lbs, carried nine experiments (see Figure 2.1), covering such topics as ionospheric remote sensing, space dust, advanced electric propulsion, and high temperature superconductivity. ARGOS was launched into a circular near-polar (98.7° inclination) sun-synchronous orbit at $\sim$830 km altitude with a nominal duration of 3 years. The spacecraft operated in a 3-axis stabilized mode providing attitude control to 0.3°, and attitude knowledge to 0.05°. Spacecraft position knowledge was accurate to within 15m and velocity knowledge to within 0.08 ms^{-1}. The Z-axis of the spacecraft always points towards the center of the Earth, and the X-axis along the direction of the spacecraft velocity vector. The polar orbit unfortunately placed USA in a high radiation environment several times per orbit, greatly reducing the amount of time (duty cycle) during which observations can be made. The USA detector was forced to turn off when going through the Van Allen radiation belts and the South Atlantic Anomaly (See Appendix B for more details) and, as a result, the longest USA observations are approximately 20 minutes long.

Figure 2.1: Advanced Research and Global Observation Satellite (ARGOS)

2.2 The USA Instrument: Overview

The *Unconventional Stellar Aspect* (USA) experiment is a reflight of two proportional counter X-ray detectors that were used successfully in the NASA Spartan-1 mission (Kowalski et al. 1993). A few months after USA was launched, one of the detectors is thought to have been hit by a micrometeorite or a piece of space debris, puncturing the thin mylar window and causing the gas to leak, thus rendering it inoperative. Fortunately, the other detector was unaffected and was able to perform observations for around 18 months (until November 2001). The detector consists of a multiwire constant flow proportional chamber of roughly 1000 cm^2 (see Figure 2.2), covered with a 5.0 μm Mylar window. On top of the proportional chamber sits the copper collimator which restricts the USA field of view to 1.3° FWHM with a 0.05° flat top. The detector is filled with P-10 gas held at a pressure of 16.1 psi at room temperature. Precise absolute timing information can be achieved using a GPS receiver on board ARGOS and timing resolution is 2μs or 32μs depending on the mode (see Section 2.2.1 for details on the USA observing modes).

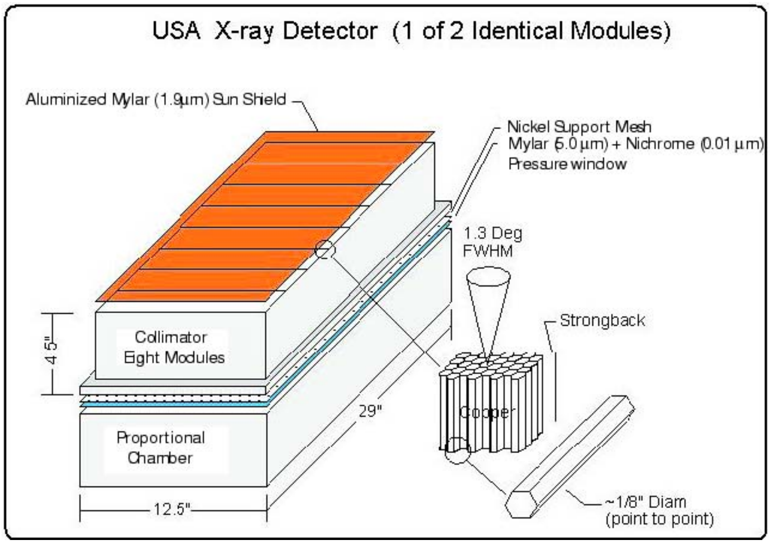

Figure 2.2: USA collimator and proportional chamber. The depth of the interior of the wire chamber is not shown and is 2.2 inches (5.6 cm).

Figure 2.3 shows a more detailed view of the USA proportional chamber, including the wire in the chamber and the periphery anode wire which serves as the charged particle veto system.

Figure 2.4 shows a front and side view of the whole USA detector, including the pilon on which it is mounted to ARGOS.

Table 2.1 summarizes the main technical characteristics of the USA instrument. References refer to sections of this dissertation, unless otherwise specified. For a more detailed description of ARGOS and USA see also Ray et al. (2000).

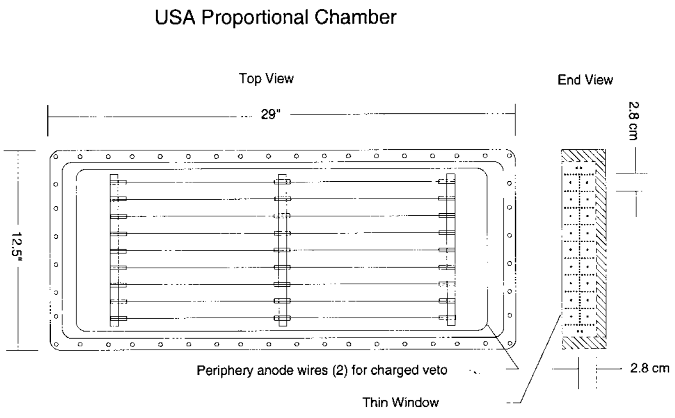

Figure 2.3: USA proportional chamber (top view). The active area of the proportional counter wire chamber is the area where the anode wires are directly illuminated by the cosmic sources through the thin window and collimator. The area around the sides of the detector chamber where the perimeter wire resides is not directly illuminated and thus not part of the effective detecting gas volume of USA. The active area is 9×2.8 cm $\times$ 60 cm = 1512 cm^2.

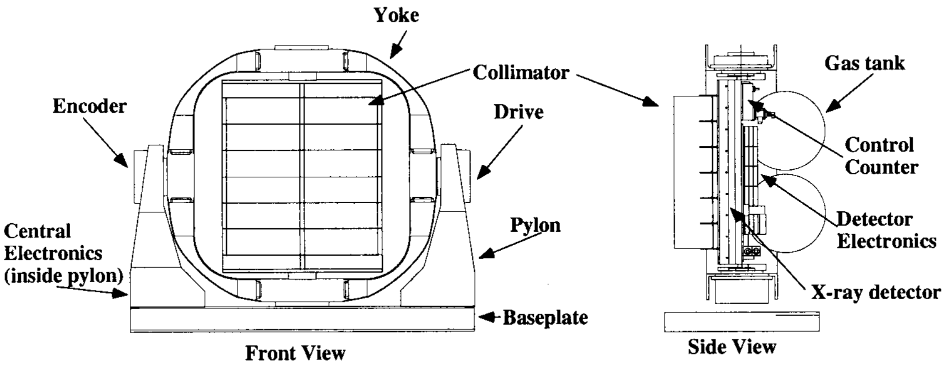

Figure 2.4: Front and side views of the USA experiment.

Feature		Reference
Gas:	P-10	Section 2.3
Energy Range:	1-15 keV	Figure 2.9
Energy Resolution:	17% (1 keV @ 5.9 keV)	Section 2.4.3
In-orbit calibration:	solenoid operated $^{55}_{26}$Fe source	Section 2.5.2
Effective Area:	1000 cm^2 @ 3keV	Figure 2.9, Section 2.4.2
1 Crab	$\sim$ 4000 cts/sec	
Background:	$\sim 20-50$ cts/sec	Appendix B, Wen (1997)
Field of view:	Collimation of 1.3° FWHM Cone 0.05° flat top	Wen (1997)
Heat Shield:	2.0 μ Mylar 30.0 $\mathring{A}$ Nickle-Chromium	
Window:	7.0 μ Mylar 800.0 $\mathring{A}$ Aluminum	
Timing Resolution:	$2\mu s$ or $32\mu s$	Ray et al. (2000)
Deadtime:	$\tau = 16.4\mu s$	Shabad (2000)

Table 2.1: Summary of USA instrument characteristics

2.2.1 USA Modes

The data gathered from USA observations is processed by the Detector Interface Board (DIB), which transmits it to the spacecraft interface. The DIB formats the data by determining how many bits will be used to store specific information about the events detected. Five different science modes were programmed into the DIB. These modes are summarized in Table 2.2.

Mode	Name	Time res.	# Channels	Telemetry rate (kbps)
1	Basic LR[a] Event Mode	32 μs	16	40
2	Basic HR[b] Event Mode	32 μs	16	128
3	Alternate LR Event Mode	2 μs	8	40
4	Alternate HR Event Mode	2 μs	8	128
5	Spectral	10 ms	47	40

[a] Low Telemetry Rate
[b] High Telemetry Rate

Table 2.2: USA observing modes

Modes 1 throgh 4 are known as ‘timing’ (or event) modes. In these modes, information is stored about individual photon events. The event modes allocate a fixed number of bits (12 or 15) to each event, as follows: Detector ID (1 bit), Layer ID (1 bit), PHA channel (4 bits in modes 1 and 2, 3 bits in modes 3 and 4), and Time (6 bits in modes 1 and 2, 10 bits in modes 3 and 4). Each event actually requires an additional number of bits to be added to the event time tag, to identify the block and vector of which that event is a member[1]. So, the full time tag of a photon (which comes from a 20 bit counter that counts microseconds into the second) looks like this:
BBBBBBVVVEEEEEEXXXXX (Modes 1,2 – LSB of E is 32 μs)[2]
BBBBBBVVVEEEEEEEEEEX (Modes 3,4 – LSB of E is 2 μs)
where BBBBBB is the block time tag, VVV is the vector time tag, EEEEEE is the event time tag and X’s are time bits which get thrown away.

The four different modes thus reflect a trade-off between how much ‘timing’ information and how much ‘spectral’ information USA stores. Modes 1 and 2 have 16 channels (binned linearly) of energy resolution and 32μs of timing resolution, whereas modes 3 and 4 have only 8 channels of energy resolution (also binned linearly) but 2μs of timing resolution.

The four different modes also reflect the different telemetry rates used. USA can only store a certain amount of data every second (in what is called a ‘frame’). When that frame is filled, no more events can be recorded until the beginning of the next second. Depending on the rate (i.e. brightness) of the source observed, it is possible to fill a frame of data in less than a second, thus causing gaps. The low telemetry rate (LR) modes were found to start filling up the frames at rates of just over 1000 cts s^{-1}, whereas the high telemetry rate (HR) modes could handle rates up to ~8000 cts s^{-1} (see Shabad (2000) for details). On the other hand, because USA shared the solid state recorder on ARGOS with the other instruments on board, there was a limit to how much data USA could store before ARGOS downloaded the data to a ground

---

[1] A vector is a collection of five photon events all of which occur within 2ms. Eight vectors form a block. The information was ‘packed’ in this way for greater efficiency by grouping together events which shared many common bits.

[2] There are actually 8 bits in the block timetag. The top two bits become the ‘frame tick’ when the events are unpacked and count 0, 1, 2, 3, 0, 1, 2, 3, 0, ... seconds. This allows the `dat2fits` program to determine which second an event is from when unpacking USA data(Reilly 2003).

station. The amount of space allocated to USA was not enough to allow us to observe continuously in a high telemetry mode. In short, the HR modes were reserved for ‘bright’ sources whereas the LR modes were used for ‘dim’ sources.

Mode 5 is known as a ‘spectral’ mode. Unlike modes 1 through 4, this is a binned mode: a 47[3] channel spectrum is taken every 10 ms, but no information is kept on individual events. The 47 channels are assigned to the raw PHA channels in a way so that there is finer resolution at lower energies where more counts are expected. Although it is a low telemetry mode, the fact that no information is stored about individual events means that this mode could actually accomodate rates as high as 20,000 cts s^{-1} (in fact, USA would shut down at 10,000 cts s^{-1}).

2.3 X-ray Proportional Counters

Proportional counters are a type of gas-filled detector that have been used in particle physics since the 1940s. Their origin dates back to 1908, when the first wire chamber, the Geiger-Müller counter, was invented. The modern multiwire proportional chamber (such as the one used in the USA experiment), however, was developed in the late sixties by Georges Charpak and his collaborators at CERN, something for which he was awarded the Nobel Prize in Physics in 1992. Multiwire proportional counters have been (and still are) used extensively in X-ray astronomy due to their many positive properties, such as good time resolution, reasonable spatial resolution, and relatively low cost. One of their less attractive features is their fairly poor energy resolution. Whereas some detectors, such as semiconductor diode detectors, can have energy resolutions $\leq$1%, multiwire proportional chambers have relatively poor energy resolution. The energy resolution of USA, for example, is around 17% at 6 keV (see Section 2.4.1).

In its most basic form, a wire chamber consists of a metallic cylinder containing an ionizing gas and a single anode wire strung along the axis kept at a high voltage. The electric field around the thin anode wire (see Figure 2.5) is given by formula 2.1:

---

[3] Mode 5 was originally meant to have 48 channels, but was accidentally coded up so as to give only 47. See Appendix A for details.

$$E(r) = \frac{V}{r \ln(b/a)} \tag{2.1}$$

where V is the voltage applied between the anode and cathode, a is the anode wire radius and b is the cathode inner radius. As can be seen from Figure 2.5, the electric field becomes very large as we get close to the anode wire.

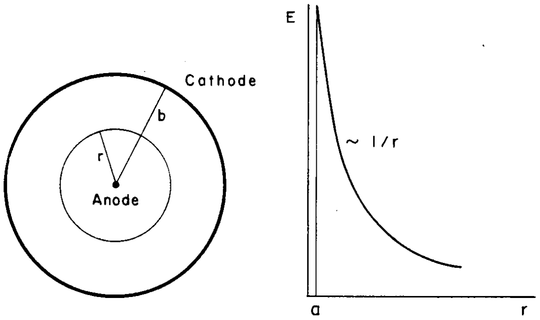

Figure 2.5: Electric field around a thin anode wire (Sauli 1977)

When a particle passes through the gas, it ionizes some of the gas molecules, producing ion-electron pairs. The electrons (−) are attracted towards the anode (+) while the ions (+) go in the opposite direction towards the cathode (−). As the electrons approach the anode wire, they are accelerated (Coulomb $F = eE$), and when an electron picks up enough energy, secondary electrons can be produced. These in turn can have enough energy to then ionize more gas molecules, and so on, creating an avalanche of electrons (see Figure 2.6). The electron avalanche becomes significant at about 50 μm from the wire. All the electrons are finally collected at the anode wire, giving rise to an electric pulse, while the positive ions are attracted to the cathode.

The proportional chamber gets its name from the fact that for a certain range of voltages, the final pulse recorded is proportional to the energy of the incoming particle. In general, the charge collected by the anode will depend on the intensity of the electric field (or voltage) applied to the chamber. Depending on this voltage, there will be four distinct regions of operation in the detector. At sufficiently low voltage, the gas can be ionized, but gas multiplication will not occur. The final signal

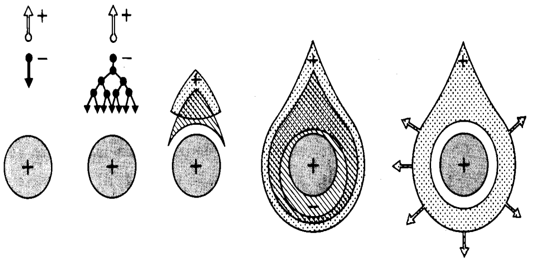

Figure 2.6: Development of an avalanche in a proportional counter (Sauli 1977)

is weak and insensitive to voltage (this is the ion saturation region in Figure 2.7). As the voltage is increased, the electrons produced in the first ionization of the gas are imparted with enough energy to ionize the gas again and produce secondary electrons, and so on, causing what is referred to as *gas multiplication* (this is the proportional region in Figure 2.7). Gas multiplication is needed to produce an electric signal of measurable amplitude. The multiplication factor can be as high as 10^5 to 10^6. As the voltage is increased even further, the positive ions begin to have an effect on the electric field and the signal is no longer strictly proportional to the energy of the particle (limited proportional region). If the voltage is increased further, photons from the recombination of ions propagate a discharge down the entire length of the anode wire (Geiger-Müller region). Figure 2.7 summarizes these four regions of operation in a gas-filled detector.

The choice of gas in a proportional chamber is crucial. Noble gases are normally used because multiplication in these gases takes place at lower fields than in more complex gases. The addition of other components raises the threshold voltage for multiplication to occur. Noble gases, however, have the drawback that the breakdown region also occurs at much lower voltages. As the atoms excited during the avalanche process return to the ground state, they emit photons at high enough energies to initiate a new avalanche in the gas or around the cathode. This can also be induced by the neutralization of ions that travel towards the cathode. The way around this problem is to add what is referred to as a “quenching gas”, which will absorb these energetic photons before they cause breakdown and then dissipate the excess energy either by inelastic collisions or by dissociation into simpler radicals.

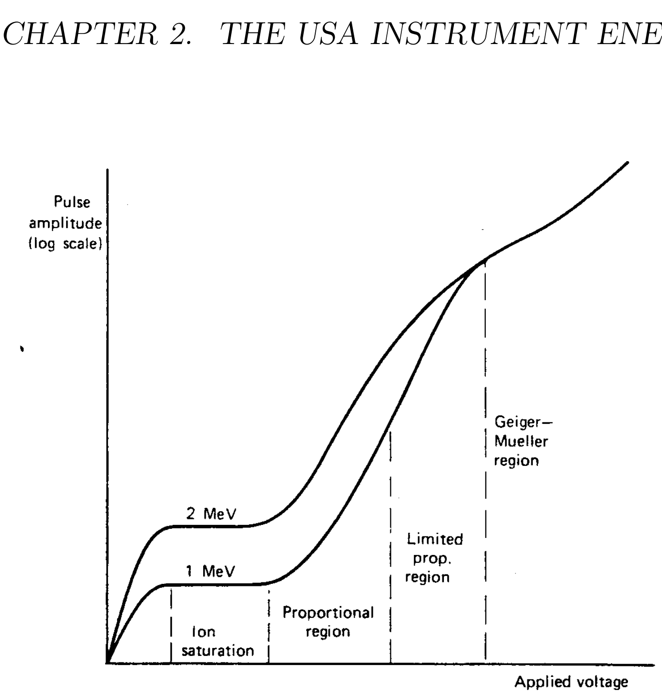

Figure 2.7: Different regions of operation of gas-filled detectors (Knoll 2000)

The most commonly used gases for this purpose are organic compounds such as hydrocarbons, which tend to be efficient at absorbing photons in these energy ranges. The addition of this quenching gas allows multiplication factors as high as 10^6.

A typical choice of gas for X-ray detectors (and the one used in USA) is P-10, a combination of 90% Argon (ionizing gas) and 10% Methane (quenching gas). For a detailed report on multiwire proportional chambers see Sauli (1977).

2.4 USA characteristics

2.4.1 Introduction

The USA instrument is a multi-wire gas-filled proportional counter which detects X-rays roughly in the 1–15 keV range. The absorption of photons by the detector gas in this energy range is recorded as a signal (voltage) proportional to the energy of the incoming photon. An analog-to-digital converter transforms the voltage signal into a *Pulse Height Analyzer* (PHA) channel, thus producing a *count* spectrum. In order to obtain an *energy* spectrum from this count spectrum, we must first understand the instrument response. In a sense, we must understand the path that a photon emitted at an astrophysical source must take to be recorded in our instrument in a specific channel and at the same time account for all the other photons which might have been emitted which *did not* make it into our instrument. This can be thought of as an inversion problem: from the spectrum of photons obtained at the instrument we would like to know the spectrum of photons emitted at the astrophysical source. In this section, I describe the physics underlying the response of proportional counters in general, and USA in particular. I explain how we used ground data and in-orbit calibration data of the characteristic K_α photons from a radioactive Fe_{55} source to determine the calibration parameters. Finally I describe the procedure for building the USA *response matrices* and test these out on observations of the well-known Crab nebula, to verify that the parameters we obtain are in agreement with what is known about the Crab from previous X-ray experiments.

2.4.2 USA Effective Area

One of the primary reasons that a *count* spectrum of a source observed by a particular instrument is different from the *energy* spectrum of that source is that the instrument is not equally as efficient at detecting photons of different energies. The efficiency of a gas proportional counter will depend on the properties of the gas used for the detection and will vary dramatically depending on the energy of the incoming photon. The gas used in USA is P-10, which consists of 90% Argon and 10% methane (CH_4). The interaction probabilities with the gas were computed by M. Wolff at NRL and independently by Gary Godfrey at SLAC and are shown in Figure 2.8. The nominal temperature and pressure at which these were computed were 22°C and 1.1 atmospheres (16.1 psia). The densities were taken from Vigele (1973). Mylar, Nichrome IV, and gas densities were calculated by M. Kowalski at NRL. Table 2.3 lists the different layers of material an incoming X-ray would have to traverse. Layer 1 interaction probabilities were computed by assuming a thickness of P-10 of only half the total 6.1925 cm.

The effective area of the instrument is obtained by multiplying the efficiency by the

Chemical formula of Material	Thickness	Density (g/cm^3)
Al	0.0800 microns	2.694 (Bulk)
$C_{10}H_8O_4$	1.8300 microns	1.397
$C_{10}H_8O_4$	7.0000 microns	1.397
Ni_8Cr_2	0.0028 microns	8.5
Ar_9CH_4	6.1925 cm	1.63E-3

Table 2.3: USA materials (both layers)

geometrical area of each detector and by the collimator response. The geometrical area of the detector is 1512 cm^2 and the collimator used on USA has a flat-top efficiency of 0.88 (Wen 1997).

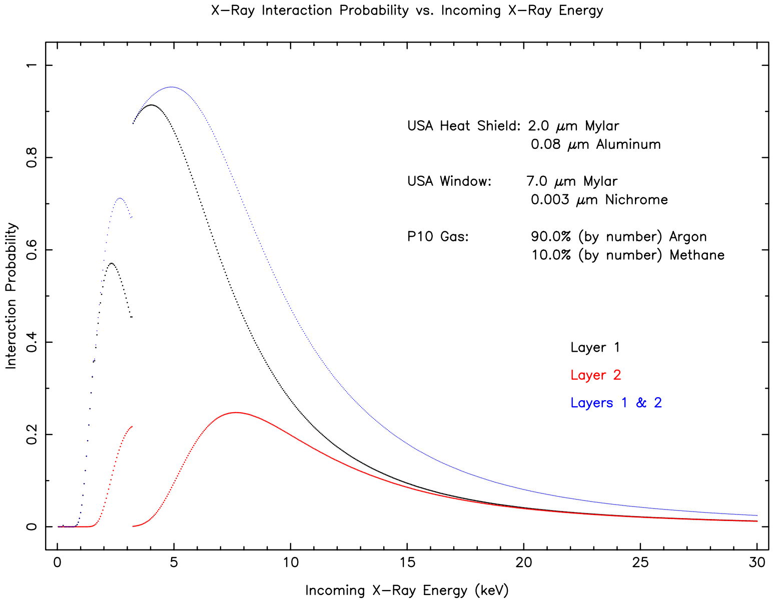

Figure 2.8: USA P-10 gas X-ray interaction probabilities as a function of energy: Layers 1, 2, and combined 1 & 2.

2.4.3 Energy Resolution

An ideal radiation detector would allow us to measure the energy of an incoming photon with exact precision; in other words, if we bombarded our detector with a source of mono-energetic photons, we would expect our *detector response* to be a

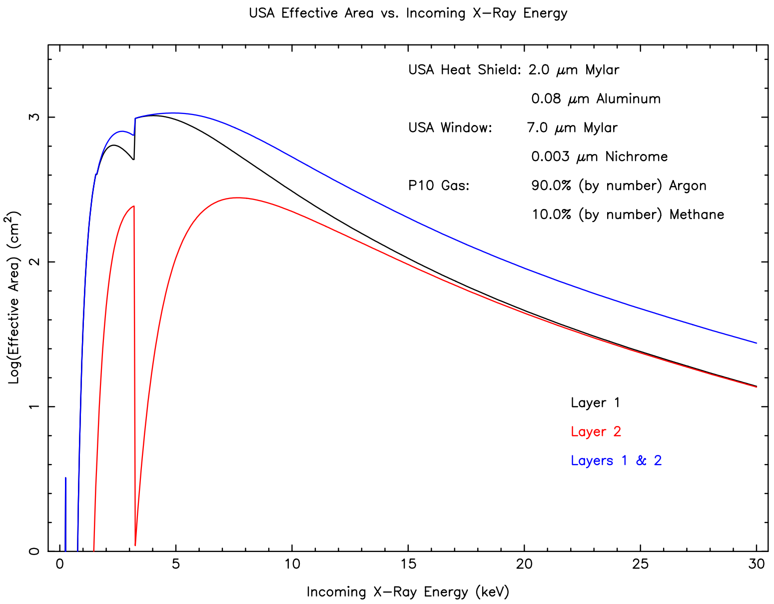

Figure 2.9: USA effective area as a function of incoming photon energy: Layers 1, 2, and combined 1 & 2.

delta function. Unfortunately, real detectors are far from perfect. In Section 2.3 we described the basic principles behind a multi-wire proportional counter, such as USA. We saw that these detectors rely on the ionization of a gas by an incoming photon. Due to the stochastic nature of this ionization process, the response of the detector to a mono-energetic source of photons is a pulse height distribution, rather than a pure delta function. The closer this distribution is to a delta function, the better its *resolution*. It is standard to define the (fractional) resolution of a detector at a given energy as the ratio of the full width at half maximum (FWHM) to the average pulse height $H_\circ$ at that energy, as seen in Figure 2.10. For a particular energy photon, the two main factors limiting the resolution of a proportional counter involve the variations in the number of ion pairs produced by the incoming photon, and the variations in the resulting single-electron avalanches (see Section 2.3 for a description of the avalanche creation process).

The relative variance in the number of ion pairs produced is normally expressed in terms of a *Fano factor*, defined as:

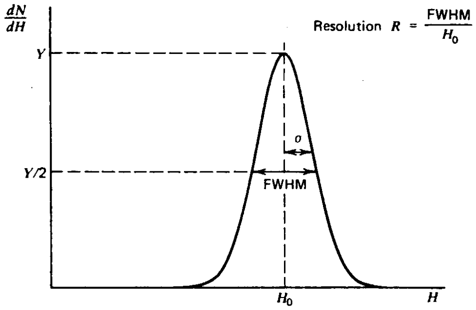

Figure 2.10: Definition of Energy Resolution (from Knoll (2000))

$$F \equiv \frac{\text{observed variance in N}}{\text{Poisson predicted variance in N}} \tag{2.2}$$

The second main factor limiting the resolution of proportional counters involves the fluctuations in single electron avalanche magnitude (see Knoll (2000) for details). This effect is normally parameterized by a factor b.

The overall statistical limit of a proportional counter can then be expressed as:

$$R = 2.35\sqrt{\frac{W(F+b)}{E}} \tag{2.3}$$

where E is the Energy of the incoming photon in keV, W represents the average energy required to form one ion pair, F is the Fano Factor, and b is sometimes referred to as the multiplication variance. For P-10, these constants have been measured to be: W=26 eV, F=0.17, and b=0.5 (Knoll 2000), giving a statistical limit for the resolution of:

$$R = \frac{0.31}{\sqrt{E}} \tag{2.4}$$

Other factors, such as imperfections in the anode wire and noisy electronics, will contribute to make the resolution in our detector worse than this statistical limit. We will, nevertheless, model the resolution of USA as the inverse square root of the photon energy, though the normalization constant will be greater than 0.31 and will be obtained from the calibration data.

2.4.4 Escape peak

Another feature of our detector response, causing it to deviate even more from an ideal delta function, is known as the *escape peak*. If the energy of an incoming X-ray is greater than the binding energy of the K-shell of the atoms in the interaction gas (which for USA is Argon), a characteristic X-ray (so-called K X-ray) is emitted. Argon has a K-shell binding energy of 3.203 keV. An incoming photon of 5.9 keV from our iron source would therefore produce a K-shell electron with an energy of roughly 2.69 keV, which is recorded by the chamber. When the L-shell electron in Argon drops down to fill the K-shell, a 2.956 keV photon is ejected ($K = 3.203$ keV, $L_{II} = 0.247$ keV, see Lederer et al. (1967)) which can 'escape' the chamber. If this happens, the resulting energy of our original 5.9 keV photon is recorded as having a deficit of 2.956 keV. For this reason, we expect the $^{55}_{26}$Fe calibration source to produce four peaks: two main peaks at roughly 5.89 keV and 6.5 keV (see Table 2.4) along with their respective (and much smaller) escape peaks at 2.94 keV and 3.53 keV. One of the parameters to be derived from our calibration will be the fraction of photons which end up in the escape peak, which is a number on the order of 5%.

2.5 The Energy Calibration of USA

The energy calibration of USA was carried out in several stages. Data were used from test runs done on the ground using the $^{55}_{26}$Fe source over the course of several years. Some calibration data were taken in 1996, before the Detector Interface Board (DIB) was in place. This produced the highest resolution (128 channels) possible. The observations were taken at different voltages, so we made sure the data we used were at the same nominal high voltage as in orbit, that is 2776.5 V. Later ground data were taken in August, September, and October of 1997 and in June of 1998, with the DIB in place. All the ground data were used to derive an initial calibration which was then verified with data taken in orbit. The calibration in orbit was done using observations of blank skies in which the $^{55}_{26}$Fe source was placed in the field of view. Calibration in orbit introduced the added complication of subtracting the background (diffuse X-ray and other). In addition, we had the issue of a reduced counting rate; by the time USA was in orbit, the iron calibration source only emitted about 50-60 cts/sec. Finally, we used observations of the Crab, which has a well understood energy spectrum, to measure how well our computed calibration performs.

2.5.1 The Auto Gain Control (AGC) System

An auto gain control (AGC) system was used to maintain a constant gain in USA by automatically controlling the High Voltage (HV) in the chamber. This was done via a feedback mechanism which monitors an iron source with a small proportional counter. The AGC circuit contains two discriminators. A low level discriminator which was set at a level close to the low end of the iron line, and a second discriminator set to approximately the mid-point of the iron line. The circuit counts events until it gets enough counts above the low level discriminator. The High Voltage (HV) is then judged to be set right if the number of counts in the upper discriminator is half the total number of counts (this makes the circuit work, independent of the level of activity of the source). It the number of counts is too low, then the voltage is raised, thus raising the gain in the chamber. The pressure in the chamber can be increased by letting more gas in, while it is decreased through a small fixed leak which continuosly releases gas at a small rate, allowing the pressure to slowly drop to within the desired range.

2.5.2 Calibration Source

A 200 μCi iron (${}^{55}_{26}\mathrm{Fe}$) source was placed on the narrow end of the detector, roughly equidistant from detectors 1 and 2. This iron source has a half-life of 2.73 years and through electron capture decays to ${}^{55}_{25}\mathrm{Mn}^{*}$ (equation 2.5). The excited Mn atom then relaxes to the ground state by filling the vacancy in the inner orbit with an outer electron and producing an X-ray photon. It is these X-ray photons that we use as our calibration signal. The source was placed on a small ($\sim$ 2 in) aluminum swing arm attached to a rotary solenoid which could then be used to turn the source into a position approximately 45° from the plane of the detector.

$$^{55}_{26}Fe + e^{-} \rightarrow^{55}_{25} Mn^{*} + \nu \rightarrow^{55}_{25} Mn + \gamma \qquad (2.5)$$

Table 2.4 summarizes the three main transitions with their relative intensities (Lederer et al. 1967):

Name	Transition	Energy (keV)	Relative Intensity
K_{α_1}	$2^2P_{3/2} \rightarrow 1^2S_{1/2}$ $(n = 2 \rightarrow n = 1)$	5.898	100
K_{α_2}	$2^2P_{1/2} \rightarrow 1^2S_{1/2}$ $(n = 2 \rightarrow n = 1)$	5.887	51
K_{β_1}	$3^2P \rightarrow 1^2S_{1/2}$ $(n = 3 \rightarrow n = 1)$	6.490	16

Table 2.4: Radioactive transitions of the $^{55}_{25}$Mn atom

2.5.3 Fitting Function

Given the effects described in Sections 2.4.3 and 2.4.4, it is reasonable to model our detector response to a mono-energetic source of photons as the sum of two gaussians, one corresponding to the main peak of the detector response, and the other (much smaller) corresponding to the escape peak. Each gaussian can be written as:

$$G(H) = \frac{A}{\sigma\sqrt{2\pi}} \exp(-\frac{(H - H_{\circ})^2}{2\sigma^2}) \qquad (2.6)$$

In this expression, A represents the area under the gaussian, $H_{\circ}$ is the centroid, and σ is the standard deviation. For a gaussian distribution, the standard deviation and the FWHM are related by FWHM$= 2.35\sigma$.

2.5.4 On-ground Calibration

In this section we use actual data obtained from bombarding USA with a source of mono-energetic photons, in an attempt to calibrate the energy response of the detector.

1996 Ground Data

Figure 2.11 shows a fit to some 1996 ground data. The two main gaussians, in red and blue, represent iron lines at 5.9 keV (which is actually a blend of two lines of very similar energies) and 6.5 keV (see table 2.4), as observed in layer 1 of the detector. The mean, 43.66 and 48.14 respectively, is expressed in channels out of 128. Figure 2.12 shows the best fit to the layer 2 spectrum. Once again, we see the main peak at 5.9 keV, and a smaller one at 6.5 keV, along with the corresponding escape peaks.

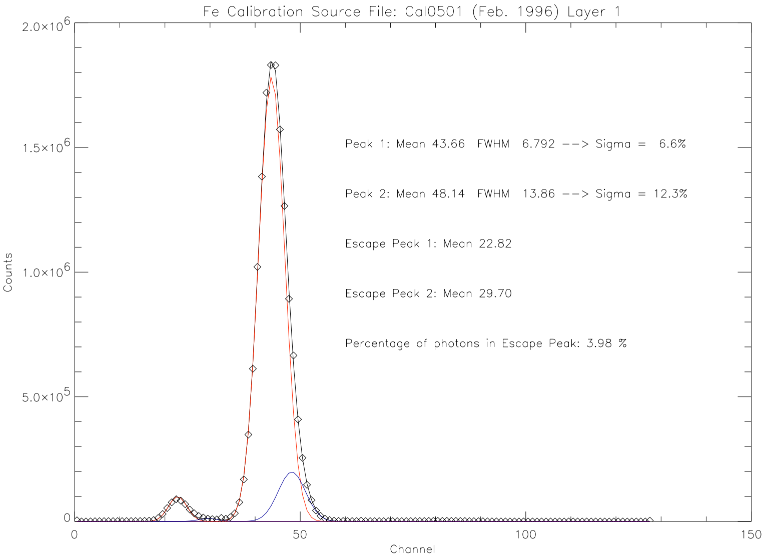

Figure 2.11: Fe calibration source (2 lines): Layer 1

Given the limited resolution of our in-orbit data, it becomes hard to fit the calibration data with four gaussians. We therefore decided to fit only one main peak and its escape peak. Figures 2.13 and 2.14 show such a fit to the same data as that shown in figures 2.11 and 2.12. Using the relative intensities of the lines (from table 2.4) we arrive at a mean energy of 5.95 keV for the blend of the three lines.

As can be seen from the figures, the result of considering the spectrum as one gaussian instead of two is to effectively shift the line up to a slightly higher energy (5.95 vs. 5.9) and increase the standard deviation of the gaussian by a small amount.

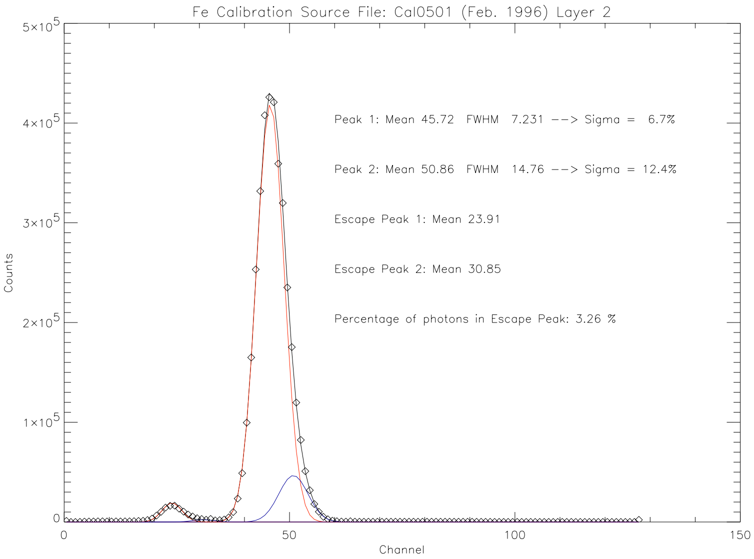

Figure 2.12: Fe calibration source (2 lines): Layer 2

1997 Ground Data

Figures 2.15 and 2.16 show a fit to some 1997 ground data (layers 1 and 2 respectively). These data were taken with the DIB already in place, and therefore the number of channels is now greatly reduced (16 vs 128). One key difference with the 1996 ground data is the location of the iron peak. In Figure 2.15 we find the mean in channel 6.40 (Figure 2.16 shows layer 2 peaking in channel 6.07). By comparison the 1996 observations show the layer 1 peak (see Figure 2.13) in channel 44.09 (or channel 5.51 in a 16 channel scale), and the layer 2 peak (see Figure 2.14) in channel 46.21 (5.78 in a 16 channel scale). Even more confusing is the fact that some 1997 data (see figure 2.17) shows the layer 1 peak in channel 5.47.

1998 Ground Data

We also examined some TVAC data taken in June, 1998. As with the 1997 data, given the poor resolution (16 channels), we decided to fit the energy spectrum of the calibration source with only two gaussians: one for the main peak at 5.95 keV and one for the escape peak.

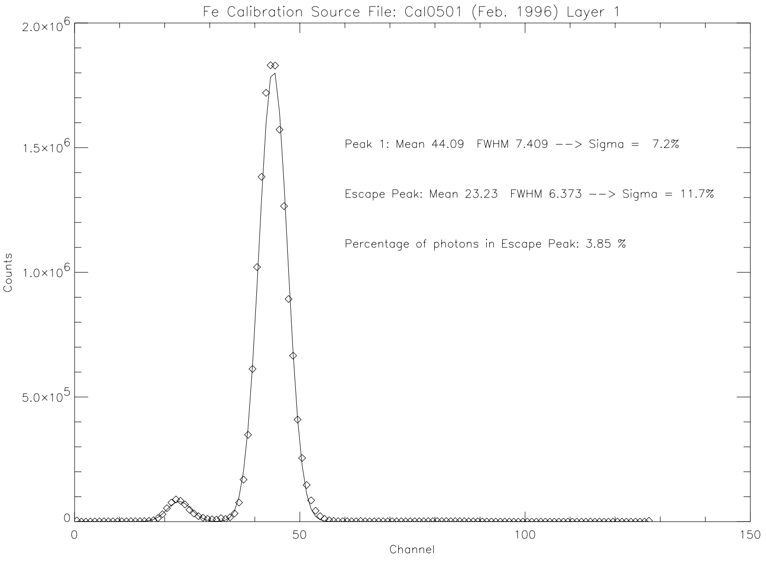

Figure 2.13: Fe calibration source: Layer 1

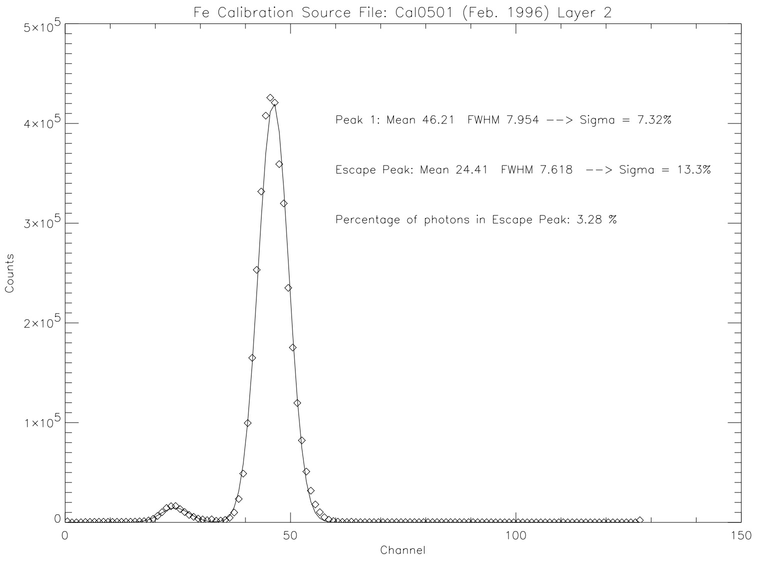

Figure 2.14: Fe calibration source: Layer 2

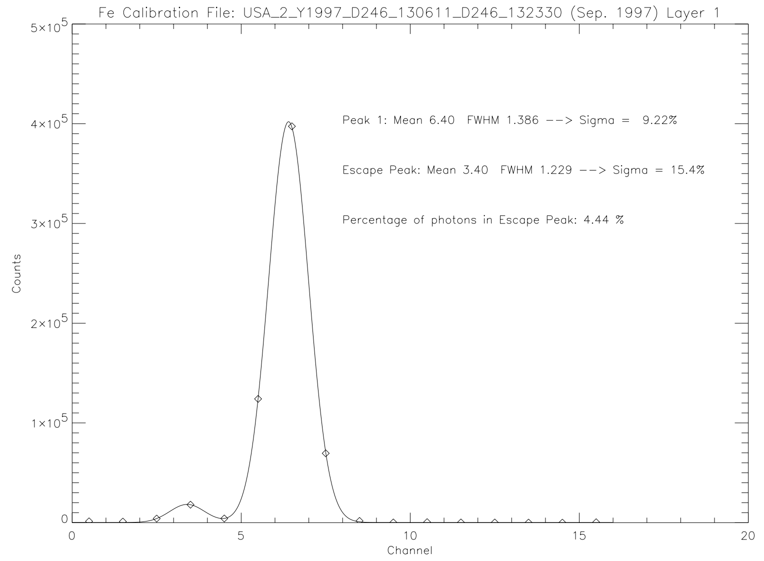

Figure 2.15: Fe Source 1997 TVAC : Layer 1

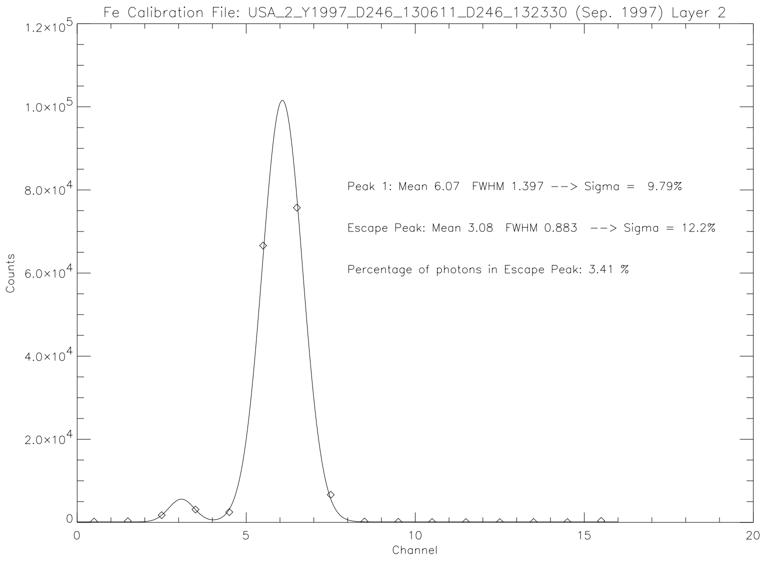

Figure 2.16: Fe Source 1997 TVAC : Layer 2

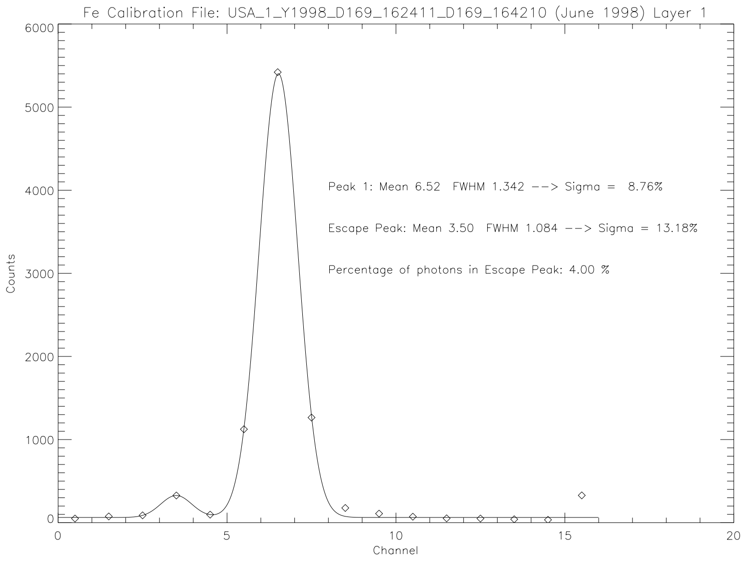

Figure 2.17: Fe Source 1998 TVAC : Layer 1

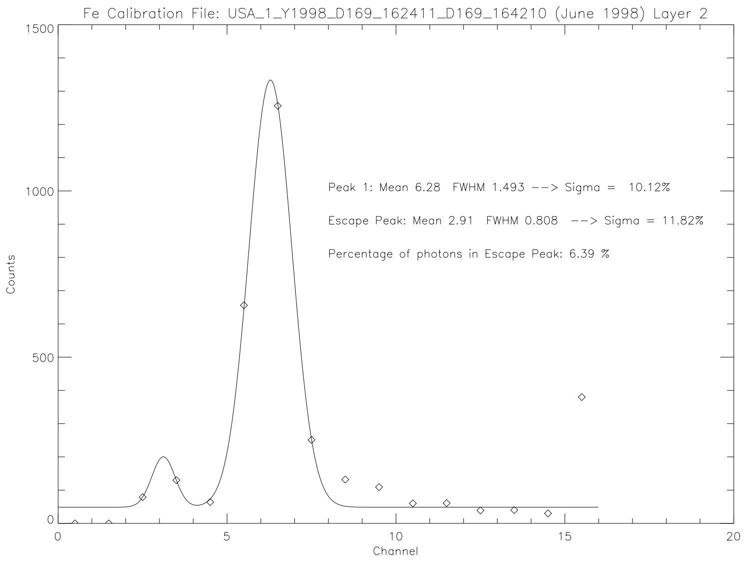

Figure 2.18: Fe Source 1998 TVAC : Layer 2

Layer 1	*Offset*	*Linear*	*Quadratic*
	-0.2888	0.1417	-
Layer 2	*Offset*	*Linear*	*Quadratic*
	-0.3009	0.1358	-

Table 2.5: Gain parameters: Energy (keV) to Channel (128) fit (ground)

Figures 2.17 and 2.18 show the fits to the layer 1 and layer 2 spectra respectively. Once again, the key parameter to notice is the channel where the energy spectrum peaks. Figures 2.17 and 2.18 show the layer 1 spectrum peaking in channel 6.52, and the layer 2 spectrum peaks in channel 6.28. This conflicts with the results obtained from the 1996 data and some of the 1997 data, but agrees with some of the 1997 ground data. It appears that the iron line in layer 1 of our detector varies its position from around channel 5.5 to 6.5.

By combining all available ground data from February 1996 (14 observations) and fitting a line to the main peak and escape peaks of the iron line, we obtain an energy to channel conversion equation with the parameters listed in Table 2.5.

2.5.5 In-orbit Calibration

Once USA was in orbit, the calibration of the instrument could be verified and, if necessary, improved. For this task, I analyzed observations of the iron calibration source as it was placed in front of the detector while pointing at a 'blank' part of the X-ray sky. The following figures show two typical calibration observations taken in orbit. The first one is taken on the ascending side of the orbit, while the second is taken on the descending part of the orbit. The observations normally consist of roughly 80 seconds of blank sky, followed by about 100 seconds of calibration ($^{55}_{26}$Fe) source. For each observation I obtained a rough estimate of the background in each layer, subtracted this background and then fit a gaussian to the resulting spectrum. As can be seen from these two observations, the peak in layer 1 falls about one channel higher in the ascending observation than in the descending one – a 20% difference in gain. Layer 2 does not show this dramatic difference.

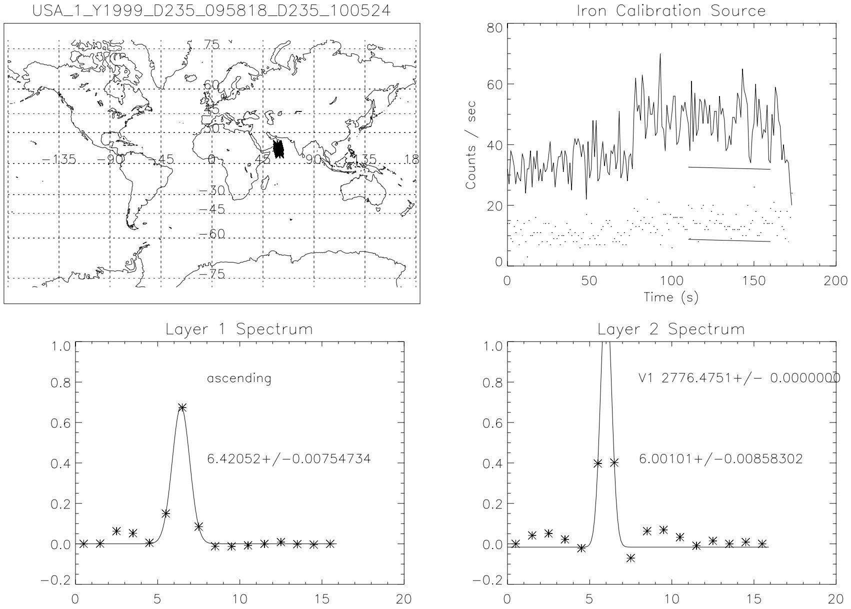

Figure 2.19: Typical Ascending Observation

In Figure 2.21 I plot the location of the gaussian peak obtained from fitting the layer 1 spectra as described in the previous section to about 75 individual calibration observations. Each point represents one of these calibration observations. While there are large gaps in the coverage, the observations span roughly 400 days. In red I show the ascending observations and in blue the descending ones. These form two distinct populations. Figure 2.22 shows the same information for layer 2 where the effect is not so pronounced.

To obtain better fits to the iron calibration data we can use the higher resolution mode 5 observations. Unfortunately, mode 5 does not provide a layer ID, so this calibration will only be valuable to obtain the mode 5 response matrices. Figure 2.23 shows all the combined observations of the iron calibration source taken in mode 5 in the descending mode. The data were fit with a third order polynomial and three gaussians. The main peak and the escape peak are clearly visible and the

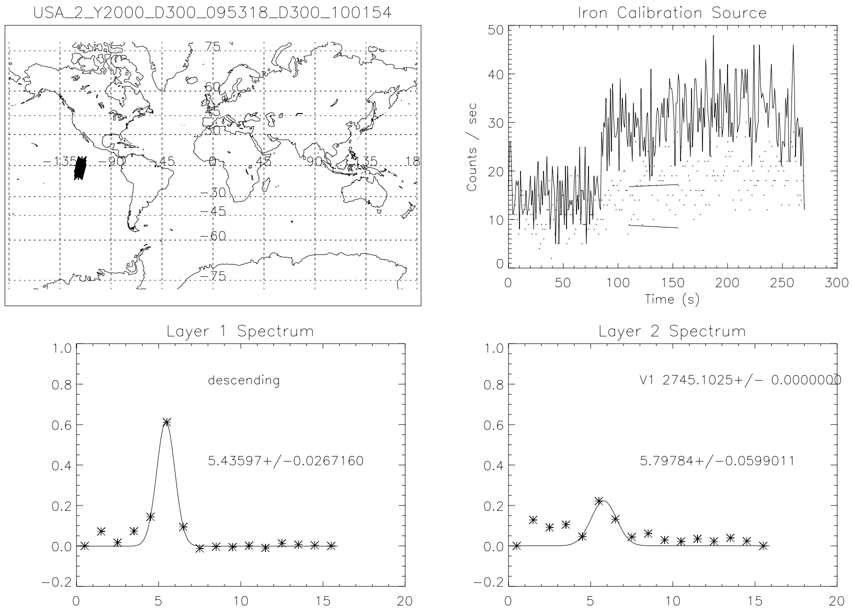

Figure 2.20: Typical Descending Observation

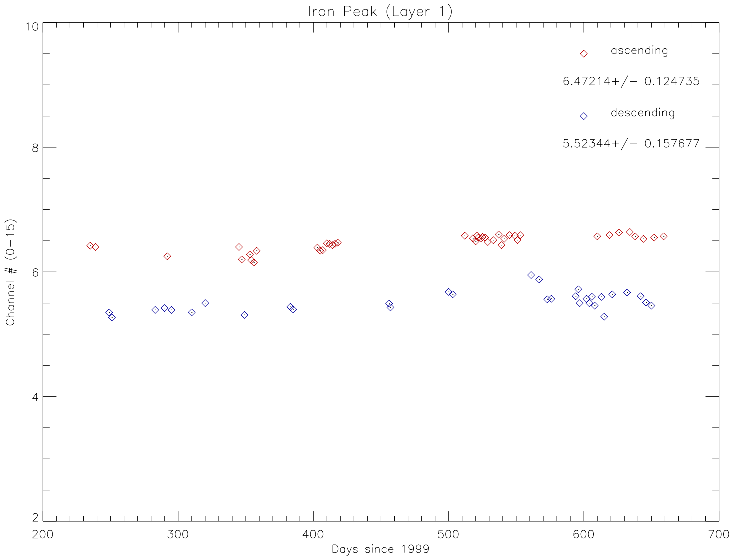

Figure 2.21: Fe Calibration Peak: Layer 1

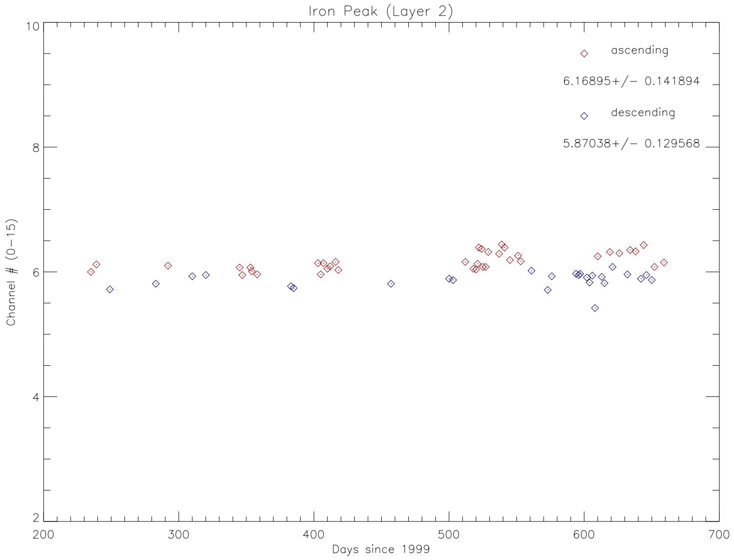

Figure 2.22: Fe Calibration Peak: Layer 2

parameters can be read off from the side of the plot, where P1 represents the area under the gaussian, P2 is the standard deviation, and P3 is the centroid. From these fit parameters we obtain a fractional energy resolution for USA of 0.1664±0.0009 at 5.95 keV and 0.3042±0.0124 at 3.0 keV.

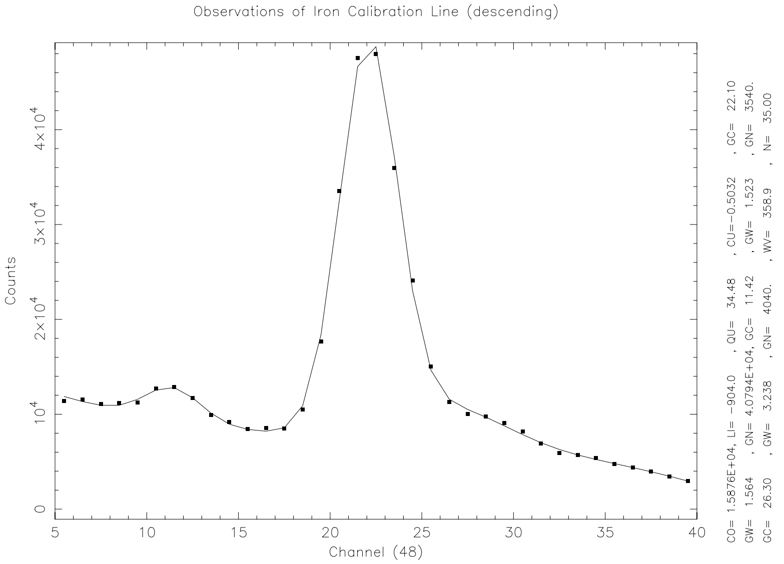

Figure 2.23: Fe Calibration Peak: Mode 5 Data (Descending)

Copper Fluorescence

The interaction of the charged particle environment with the USA collimator, which is made of copper (see Section 2.2) produces an 8.03 keV (Lederer et al. 1967) fluorescence line which is highly visible in the USA blank sky observations, something which was not anticipated. To verify that the copper fluorescence line was due to background particles colliding with the detector. Figure 2.28 shows the ratio of counts in channels 5–7 (which is where the copper peak roughly lies) to total counts versus the difference between counts in both layers of channel 15, which is a measure of the intensity of soft electrons. The plot shows that the intensity of this copper line is correlated (though weakly) with the rate of soft electrons hitting the detector. This copper peak was thus used as an extra calibration point, in addition to our iron source.

Using the mean values obtained for the locations of the iron peaks in the different orbital modes and different layers (as shown in Figures 2.21 and 2.22), as well as the location of the copper fluorescence peaks, I performed a new fit of the Energy (keV) to Channel (in a scale of 128) conversion. I use only a linear function (i.e. no quadratic term) to fit our data points. The resulting gain coefficients are shown in

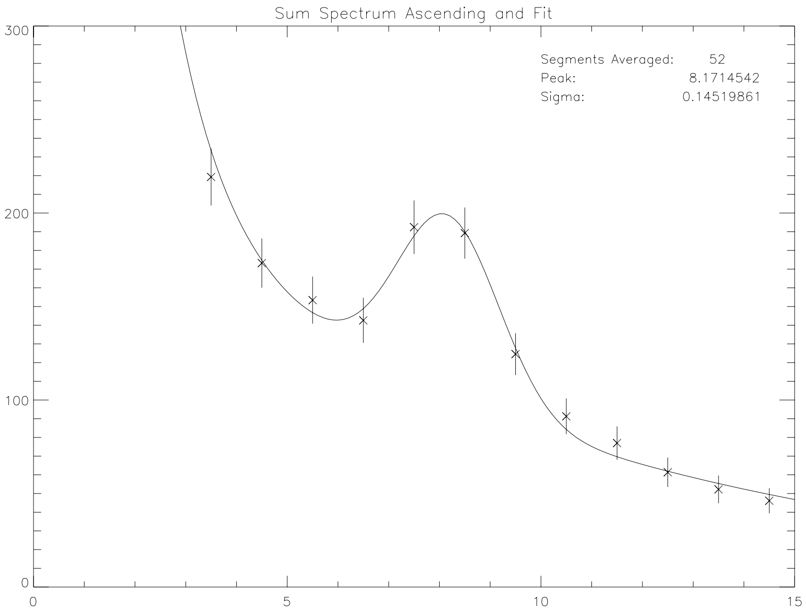

Figure 2.24: Cu Fluorescence Peak (ascending): Layer 1

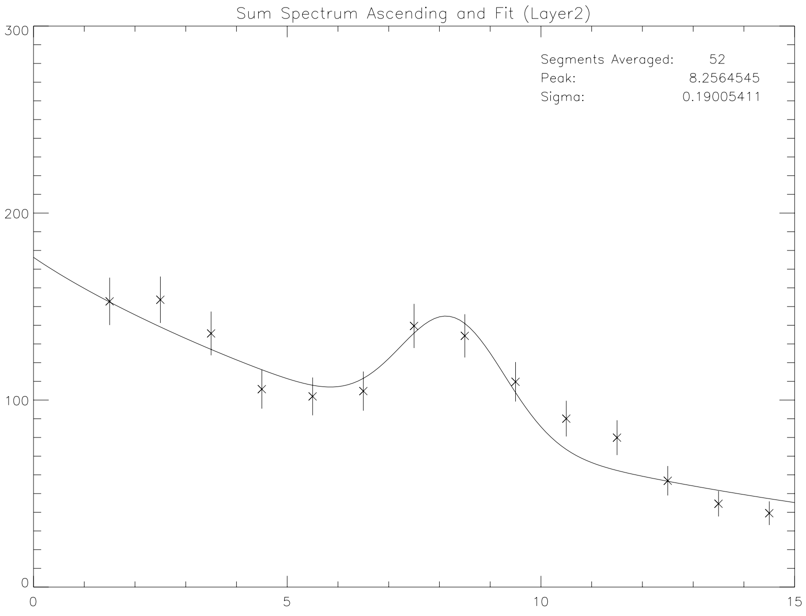

Figure 2.25: Cu Fluorescence Peak (ascending): Layer 2

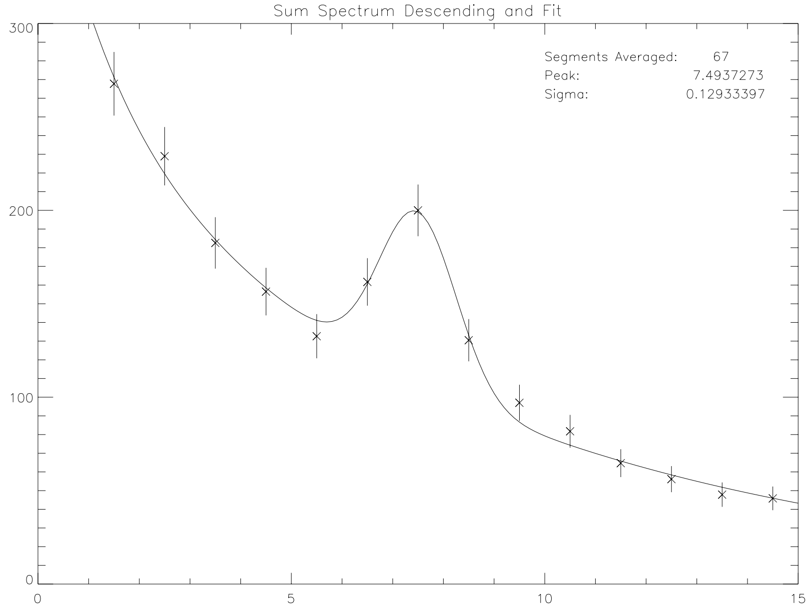

Figure 2.26: Cu Fluorescence Peak (descending): Layer 1

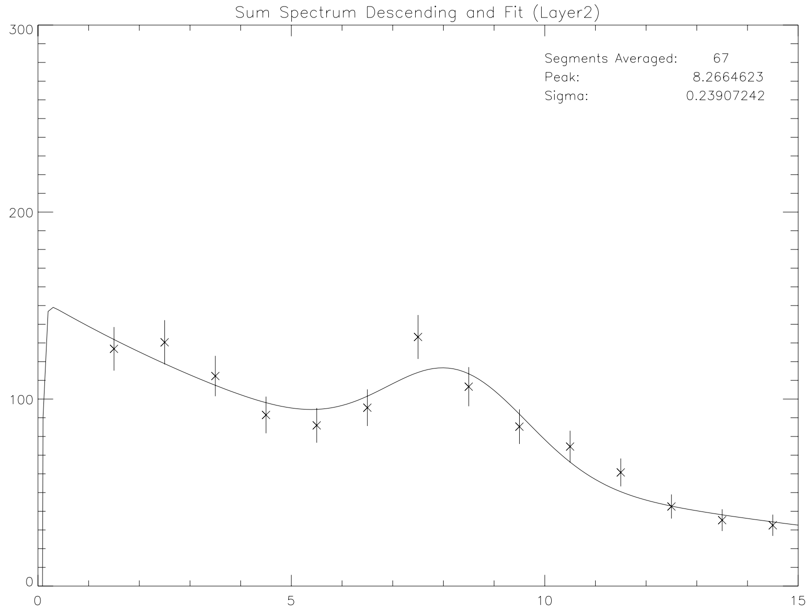

Figure 2.27: Cu Fluorescence Peak (descending): Layer 2

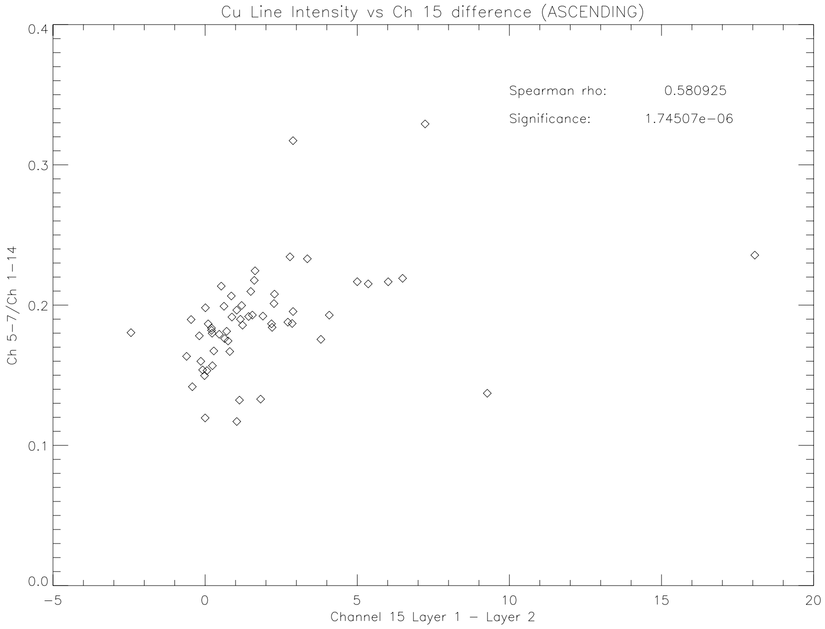

Figure 2.28: Cu Fluorescence correlation with soft electrons

Table 2.6. As of March 2003, these coefficients are the ones used in the USA response functions. Newer response functions can easily be created using the codes described in Appendix A.1. The most up-to-date version of the response matrices are available from the USA web site at `http://xweb.nrl.navy.mil/usa/index.html`.

Ascending	*Offset*	*Linear*	*Quadratic*
Layer 1	1.6430E-1	1.1359E-1	-
Layer 2	4.0176E-2	1.2089E-1	-
Descending			
Layer 1	1.6939E-1	1.2934E-1	-
Layer 2	3.9109E-2	1.2355E-1	-

Table 2.6: Gain parameters: Energy (keV) to Channel (128) fit (in orbit)

2.6 USA Response Matrices

The response matrix is a FITS[4] file which contains the arrays describing the characteristic response of USA to incoming X-rays. The response matrices are required by XSPEC[5], in combination with the observed source spectrum and a background spectrum, to perform spectral fits. As its name implies, it is a matrix and has the form R(I,E), giving the probability that an incoming photon of energy E will be detected in channel I (for more details on spectral fitting with XSPEC, see Section 3.2 or Arnaud and Dorman (2000)). In order to create these matrices, two main aspects of the instrument must be considered: the gain (which will determine the energy boundaries) and the detector efficiency as a function of energy. Using our calibration sources, we first created a raw (128 channels) energy to channel conversion. We then re-binned this into the different USA modes. Table 2.7 describes all the response matrices created for the different modes. Due to the temperature dependent gain variations, a different set of seven response matrices were created for ascending and descending node observations, bringing the total to 14.

Filename	Modes	Layers	Number of channels
usa_d1_l1_m1.rsp	1 and 2	1	16
usa_d1_l2_m1.rsp	1 and 2	2	16
usa_d1_l1_m3.rsp	3 and 4	1	8
usa_d1_l2_m3.rsp	3 and 4	2	8
usa_d1_m1.rsp	1 and 2	1 and 2	16
usa_d1_m3.rsp	3 and 4	1 and 2	8
usa_d1_m5.rsp	5	1 and 2	47

Table 2.7: USA response matrices

---

[4] Flexible Image Transport System data format, a standard in widely used in astronomy.

[5] The standard software package used to analyse X-ray spectra.

2.7 Crab Energy Spectrum

The Crab Nebula represents a standard X-ray source which has been used for calibrating most X-ray telescopes for the last 30 years. The X-ray emission from the diffuse region of the Crab appears to be constant, to within 10% (Noergaard-Nielsen et al. 1994). Toor and Seward (1974) used 28 different spectra obtained from rocket and balloon experiments to derive an absolute calibration for the Crab to within 10%. The spectrum they obtained between 2 and 60 keV is:

$$I(E) = 9.7 \pm 1.0 E^{-2.10 \pm 0.03} ph/cm^2/sec/keV \tag{2.7}$$

The value for the galactic absorption in units of the equivalent hydrogen column density is $n_H = 0.33 \times 10^{22}$ atoms/cm^2. Figure 2.29 shows a typical fit (in the 1.5–14 keV range) to a Crab spectrum (this particular observation is a descending node mode 2 observation). I use an absorbed power law (A(E)=K$e^{-p1\sigma(E)}$(E/1keV)$^{-p2}$, where K is in units of photons/keV/cm^2/s at 1 keV, $\sigma(E)$ is the photo-electric cross-section and p2 is the photon index of the power law) as the model. I obtain a power-law photon index of 2.112 ± 0.005 and a normalization of 6.763 ± 0.05 consistent with the accepted values (Willingale et al. 2001). Using a systematic uncertainty of 5% in our fits we obtain a reduced χ^2 of 0.76 for eight degrees of freedom. The flux we obtain for the Crab in the 2–10 keV region is $2.9 \times 10^{-8} \mathrm{erg\,cm^{-2}\,s^{-1}}$, which also agrees with previous observations.

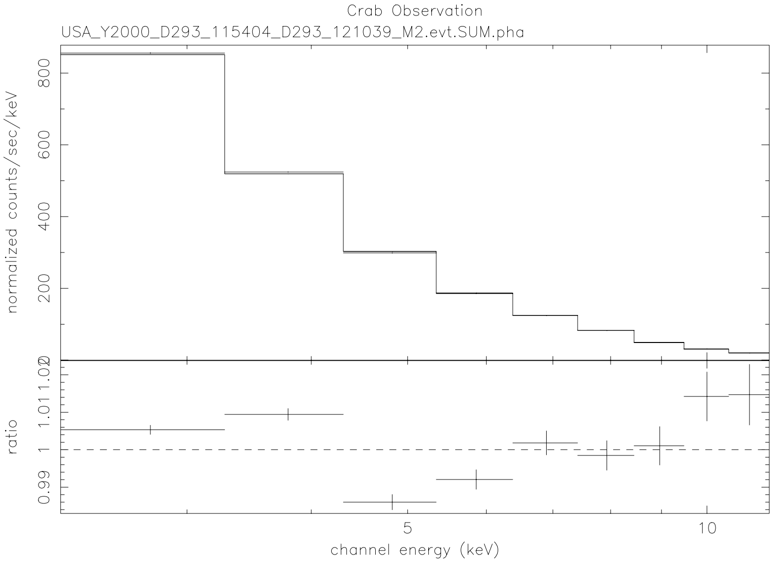

Figure 2.29: Crab Energy Spectrum USA_Y2000_D293_115404_D293_121039_M2. Observation was in the descending node. Resulting photon power-law index from the fit is 2.112 ± 0.006

2.8 Explanation for the Orbital Dependence of the Gain

Given the clear difference in gain detected between the ascending and descending observations, and given that we know that USA is always in the dark in descending orbits and in the sun when ascending, it would seem plausible that temperature is a factor in the observed differences in detector gain. Because of reduced gravity in space, convection currents are also greatly reduced and a temperature gradient could be maintained between the two different layers of the chamber (which are nevertheless connected, and therefore would quickly reach a thermal equilibrium on the ground where convection is present). The relevant question to ask, therefore, is how large a temperature gradient need there be to cause the observed 20% effect in gain?

In order to address this question, we begin by writing down a first order differential equation which describes the dependence of the gain on the voltage and the density.

A change in voltage implies a change in electric field strength (which is proportional to V, see Equation 2.1) and therefore an increase in gas amplification. Conversely, an increase in pressure (or decrease in density) increases the mean free path, and, once again, increases the amplification in the gas. In the proportional region of the gas (where USA operates), we can write:

$$\frac{dG}{dV^*} = \alpha G \tag{2.8}$$

where we have defined:

$$V^* = \frac{V}{\rho} \tag{2.9}$$

and therefore:

$$dV^* = -\frac{V}{\rho^2}\, d\rho \tag{2.10}$$

Separating variables in equation 2.8 and integrating, we obtain:

$$\frac{dG}{G} = \alpha\, dV^* \tag{2.11}$$

$$\int \frac{dG}{G} = \ln G = \alpha V^* + C = \int \alpha\, dV^* \tag{2.12}$$

We use the fact that for P-10 (90% Ar, 10% CH_4) in the proportional region, a change in voltage of 100 V has the effect of doubling the gain:

$$2Ce^{\frac{\alpha V_0}{\rho}} = Ce^{\frac{\alpha(V_0+100)}{\rho}} \tag{2.13}$$

from which we deduce that:

$$\alpha = \rho\frac{\ln 2}{100} \tag{2.14}$$

Using equations 2.14 and 2.10 into 2.11 we obtain the following:

$$\frac{dG}{G} = -V\frac{\ln 2}{100}\frac{d\rho}{\rho} \tag{2.15}$$

From the ideal gas law, we have:

$$PV = NkT \tag{2.16}$$

$$\rho = \frac{N}{V} \tag{2.17}$$

$$T = \frac{P}{\rho k} \tag{2.18}$$

$$\frac{dT}{T} = -\frac{d\rho}{\rho} \tag{2.19}$$

Finally, substituting this into equation 2.15, we get:

$$\frac{dG}{G} = V\frac{\ln 2}{100}\frac{dT}{T} \tag{2.20}$$

$$\Delta T \approx \frac{100T}{V\ln 2}\frac{\Delta G}{G} \tag{2.21}$$

where $\frac{\Delta G}{G}$ is the observed change in gain of around 20% between the ascending and descending node observations, V is the chamber voltage, which is roughly held constant at around $2775V$ and T is the temperature of the chamber, which is around $285K$. Using all these numbers, we get:

$$\Delta T \approx \frac{(100)(285K)}{\ln 2(2775V)}(0.20) \approx 3K \tag{2.22}$$

Observed Temperature Gradient

The following plots show the temperatures of the back plate (UD1TBP) and of the inside of the chamber (USAST4) plotted together. Tthe times span the calibration observations shown in Figures 2.19 and 2.20. The vertical line shows roughly where the calibration observation would fall. As can be seen in the first observation, there is a temperature gradient of around 2.5–3K, whereas in the second case there is essentially no temperature gradient. Furthermore, in the several orbits displayed in Figure 2.30 we can see that there is a temperature gradient whenever the satellite is in an ascending orbit, whereas there is virtually no temperature gradient when we it is on a descending one, especially in the middle of the orbit (i.e. between the belts) where USA would be observing. The phase lag between the two temperature curves is consistent with the fact that the "back" takes longer to heat up, and therefore to cool down than the 'front'.

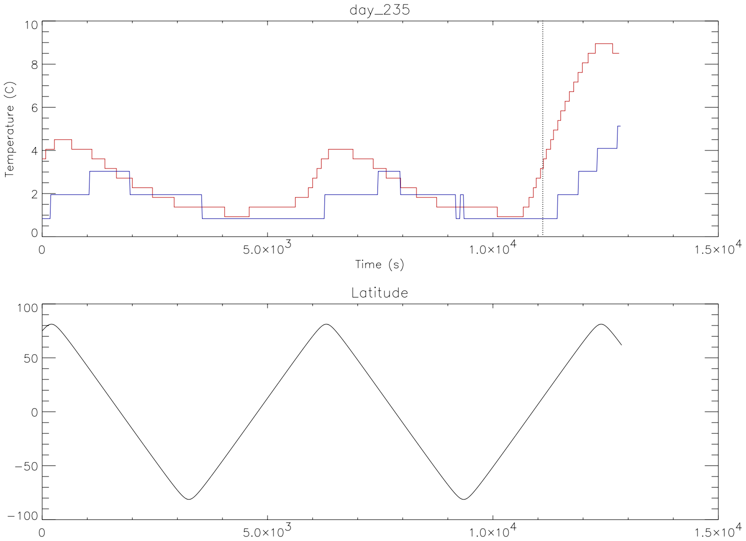

Figure 2.30: Day 235 (Ascending)

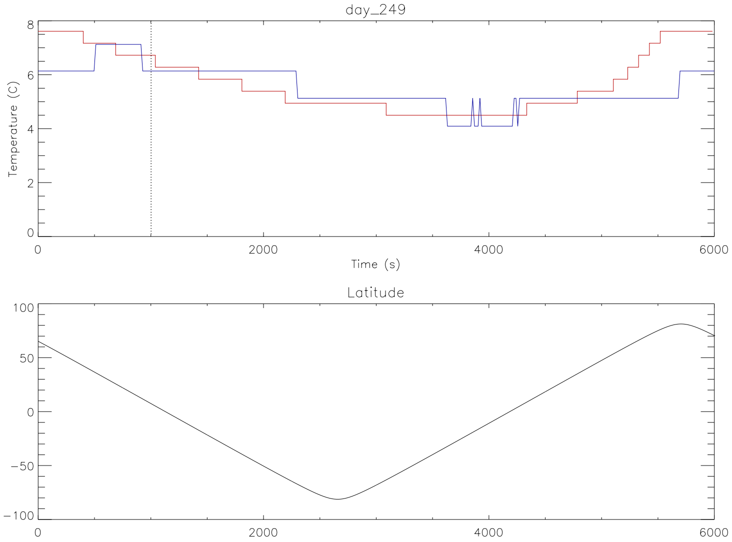

Figure 2.31: Day 249 (Descending)

2.9 Conclusions

An energy calibration of USA was carried out with 1996 ground data, which provided the highest resolution (128 channels). This calibration was then checked and improved with calibration data taken in orbit. A different energy calibration was required for ascending and descending node ('dark' side) observations. The 1996 ground calibration appears to be consistent with the descending node in-orbit calibration. I checked the energy calibration with 1997 and 1998 TVAC data and found that at times these data were consistent with the ascending node in-orbit calibration while at other times it was more consistent with the descending node calibration. The source of such discrepancies is not certain, but as a result, the 1997 and 1998 ground calibration data were not used to build the USA response matrices. The current USA response matrices were built using mainly in-orbit data. The peak of the iron calibration source as well as the observed copper fluorescence peak were used to produce a linear fit for the gain in both ascending and descending node observations. Using these fits and the USA efficiencies, two sets of response matrices were created, one for each of the ascending and descending sides of the orbit. Finally, these response matrices were tested in XSPEC to fit the Crab energy spectrum with an absorbed power law, yielding a power-law index and flux which agrees with past observations. Codes for the generation of USA response matrices were developed, greatly simplifying the task of generating new matrices, when the need arises.

Chapter 3

Data Analysis

Don't project. Don't connect. Protect. Don't expect. Suggest.
U2, "Numb" (1993)

In astrophysics, it is often useful to study objects or phenomena in different domains simultaneously. Just as we would often like to observe an object at different wavelengths at the same time, it is also often fruitful to study how an object is behaving simultaneously in the *timing* domain and in the *spectral* domain. In this dissertation, I will discuss features observed in the light curve and Fourier power spectrum of Cir X-1 as well as the overall energy spectrum evolution of the source in order to arrive at a more complete picture of the physical phenomena taking place in the system. In this chapter, I briefly review some techniques used in time series analysis, as well as the main tool used in spectral analysis. I also discuss some specific mechanisms/models used to interpret the observed X-ray energy spectra.

3.1 Timing

3.1.1 Fast Fourier Transform (FFT)

The main tool used in timing analysis owes its origins to the 18th century mathematician Daniel Bernoulli, who postulated that a function could be expressed as an infinite sum of sines. The French mathematician/physicist Fourier later expressed this more formally (Weaver 1983; Bracewell 1986):

$$f(t) = \sum_{k=1}^{n} A_k \cos 2\pi\omega_k t + B_k \sin 2\pi\omega_k t \tag{3.1}$$

If $f(t)$ is a periodic time signal described by equation 3.1 then we can think of the *frequency content* of that signal as the set of 3-tuples (A_k, B_k, ω_k). We can write equation 3.1 much more compactly if we express the sines and cosines as exponentials, using complex variables:

$$\cos\theta = \frac{e^{i\theta} + e^{-i\theta}}{2} \tag{3.2}$$

$$\sin\theta = \frac{e^{i\theta} - e^{-i\theta}}{2i} \tag{3.3}$$

Equation 3.1 then becomes:

$$f(t) = \sum_{k=-n}^{n} C_k e^{2\pi i\omega_k t} \tag{3.4}$$

where

$$C_k = \frac{A_k + iB_k}{2}, k < 0,$$
$$C_0 = 0,$$
$$C_k = \frac{A_k - iB_k}{2}, k > 0,$$
$$\omega_k = -\omega_k, k < 0.$$

In general, given a continuous function *f*, the *Fourier Transform pair* is defined by:

$$F(\omega) = \int_{-\infty}^{\infty} f(t) e^{i\omega t} dt \tag{3.5}$$

$$f(t) = \frac{1}{2\pi} \int_{-\infty}^{\infty} F(\omega) e^{-i\omega t} d\omega \tag{3.6}$$

Equation 3.5 is the *Fourier Transform* of 3.6, and 3.6 is the inverse Fourier transform of 3.5. We can think of these equations as the limiting case of equation 3.1 ($n \to \infty$), as the period T approaches infinity. C_k represents a measure of the *frequency content* (where the discrete frequencies are defined as $\omega_k = \frac{2\pi k}{T}$). Because digital computers work with *discrete* functions, rather than continuous functions, we will work with the *Discrete Fourier Transform.* Given a bounded Nth order sequence $\{f(k)\}$, the corresponding *Discrete Fourier Transform pair* is defined as:

$$F(j) = \sum_{k=0}^{N-1} f(k) e^{\frac{2\pi ijk}{N}}, j \in [-\frac{N}{2}, ..., \frac{N}{2} - 1], \tag{3.7}$$

$$f(k) = \frac{1}{N} \sum_{j=-N/2}^{N/2-1} F(j) e^{-\frac{2\pi ijk}{N}}, k \in [0, N-1]. \tag{3.8}$$

Equation 3.7 is the *Discrete Fourier Transform* of the time series represented by Equation 3.8. Alternatively, Equation 3.8 can be thought of as the *Inverse Discrete Fourier Transform* of Equation 3.5. According to Nyquist's theorem, the highest frequency that can appear in a sampled signal is half the sampling frequency, so given our sampling frequency of N/T, the maximum, or *Nyquist*, frequency will be $\nu_N = \frac{1}{2}N/T$. If the sampled signal contains frequencies higher than half the sampling frequency, these higher frequencies will appear folded down to below half the sampling frequency when the signal is reconstructed, causing what is known as *aliasing.*

To determine $F(j)$ for every value of j using Equation 3.7 would require $(N-1)^2$ operations. However, in 1965 J. W. Tukey and J. W. Cooley published an algorithm greatly reducing the number of operations needed. Assuming N is written as a power of 2 ($N = 2^k$), the number of multiplications now required is $\frac{N}{2} log_2 N$. For details on the FFT algorithm see Press et al. (1992).

In our timing analysis, $f(k)$ will represent the number of photons dectected in bin k of our light curve, corresponding to the time bin $t = k\Delta t$, where Δt is the width of the bin. We will use a bin width of 32, 96, or 960 μs, since these are the bin sizes for which we have good knowledge of the deadtime subtraction (see Shabad (2000) for a complete description of the USA deadtime model).

The *power* at the Fourier frequency $f_j = \frac{j}{T}$ is defined as the squared magnitude of the *jth* Fourier coefficient $\mid F(j) \mid^2$ and the collection of these *powers* is known as the *Power Density Spectrum* (PDS), which can be normalized in several ways, depending on different conventions. The Leahy-normalized PDS (Leahy et al. 1983) is defined as:

$$P_j = \frac{2\mid F(j) \mid^2}{N_{ph}} \tag{3.9}$$

where N_{ph} is the total number of photons within a time series of length T (i.e. the value of the zeroth Fourier coefficient). For a Poisson (counting noise) process, this gives a PDS with mean 2 and χ^2 distribution with two degrees of freedom, making it easier to visually determine the significance of high power in a given PDS.

We will often use another normalization, referred to as root-mean-squared (RMS) normalization (for a detailed account of Fourier techniques in X-ray timing see der Klis (1988)). To obtain the RMS normalized PDS we simply divide the Leahy normalized power spectrum by the total number of photons in the interval (N_{ph}). Using this normalization, we can determine the "strength" (or fractional rms variability) of a feature in the PDS spectrum (such as a QPO) simply by taking the square root of the area under the given PDS feature.

All power spectra computed in this thesis were done using the program `specan` written by Warren Focke (Reilly (2003) describes the full details of the program). Fits on the spectra were performed using the QDP program (Tennant 1991).

3.1.2 Lomb-Scargle Periodogram

When searching for long-term periodicities (i.e. very low frequencies) it is often the case that we have unevenly sampled data. Scargle (1982) modified the classical definition of the periodogram in order to retain the simple statistical behavior of the evenly spaced case. Under the new definition, Scargle (1982) showed that the periodogram analysis was exactly equivalent to least-squares fitting of sine waves to the data.

Given a time series: $X_i = X(t_i), i = 1, 2, ..., N_0$, the periodogram is then defined as:

$$P_X = \frac{1}{2}\{\frac{[\sum_j X_j \cos\omega(t_j - \tau)]^2}{\sum_j \cos^2\omega(t_j - \tau)} + \frac{[\sum_j X_j \sin\omega(t_j - \tau)]^2}{\sum_j \sin^2\omega(t_j - \tau)}\} \tag{3.10}$$

where τ is defined as:

$$\tan(2\omega\tau) = \frac{\sum_j \sin 2\omega t_j}{\sum_j \cos 2\omega t_j} \tag{3.11}$$

With this definition, if X is pure Gaussian noise, P_X then has an exponential distribution. Since one of the key questions which arises when looking for periodicities in a signal is whether a certain peak in the periodogram is spurious or not, it is useful to define the False Alarm Probability (FAP). The probability, p_0, that a random fluctuation would exceed a power level of z_0 is given by the following expression:

$$z_0 = -\ln[1 - (1 - p_0)^{1/N}], \tag{3.12}$$

where N is the number of independent frequencies searched. It is customary to set the FAP to some fixed value (such as $p_0 = 0.01$), and then claim a detection of a peak (which should exceed z_0) at greater than $1 - p_0$ confidence.

3.1.3 Phase Dispersion Minimization

In the Phase Dispersion Minimization (PDM) method (Stellingwerf 1978) we start with a time series $X_i = X(t_i), (i = 1, 2, ..., N)$ and define an overall variance:

$$\sigma^2 = \frac{\sum(X_i - \bar{X})^2}{N - 1}, \tag{3.13}$$

where $\bar{X} = \frac{\sum X_i}{N}$ is the mean. For any subset of our original time series, we can select a sample and define the sample variance in a similar fashion. By choosing M different samples, with sample variances s_j^2 (j=1,...,M), each containing n_j data points, we can compute the overall variance for all the samples as:

$$s^2 = \frac{\sum (n_j - 1) s_j^2}{\sum n_j - M} \tag{3.14}$$

If we now choose a trial period, Π, which we wish to search for in our time series, we can compute a so-called phase vector ϕ, defined as $\phi_i = t_i \bmod \Pi$. By taking M samples from our original series, choosing them in such a way as to make each member of sample j have a similar ϕ, we can then compute the variance of these samples and compare it to the overall variance of our original time series by computing the following statistic:

$$\Theta = \frac{\sigma^2}{s^2} \tag{3.15}$$

The behavior of this statistic will tell us whether the chosen period, Π, is present in the data or not. If this periodicity is *not* present in the original time series then we will have $s^2 \approx \sigma^2$ (i.e. $\Theta \approx 1$), whereas if Π is a true periodicity, we will get $\Theta < 1$. The more significant the periodicity, the smaller the value of the Θ statistic.

Stellingwerf (1978) shows that the Θ statistic has a probability density function given by an F distribution with $\sum n_j - M$ and $N - 1$ degrees of freedom. For convenience (so that $F > 1$) he defines:

$$F_{N_1,N_2} = \Theta^{-1}, N_1 = N - 1, N_2 = \sum n_j - M \tag{3.16}$$

This way, the probability that a periodicity with a value of Θ is due to random fluctuations can easily be computed, as twice the area of the F distribution above Θ^{-1}. For a large value of N ($N > 100$), the χ^2 distribution can be used as an approximation:

$$\chi^2 = N\Theta, \mathrm{where\,N} = \sum \mathrm{n_j} - \mathrm{M} \tag{3.17}$$

This method is ideally suited to search for non-sinusoidal periodicities.

3.1.4 χ^2 Minimization

In the χ^2-Minimization method (Horne et al. 1986), the original time series is folded on a search period Π. The folded light curve is then fit to a sine curve and a value of χ^2 is obtained. This is done for a series of trial periods and the one with the minimum χ^2 is taken to be the true periodicity being searched for. One drawback of this method is that it is not especially well suited for non-sinusoidal signals.

3.2 Spectroscopy (XSPEC)

Most of the spectral analyses and all the spectral fits in this thesis were carried out using XSPEC (Arnaud 1996). XSPEC is a spectral-fitting program which has become the standard in X-ray astronomy. It is used to analyze data from most X-ray detectors and is the default for all modern X-ray missions, such as RXTE, Chandra, or XMM-Newton. XSPEC takes as inputs the instrument response and the data (or count spectrum), and attempts to produce a detector-independent result for the intrinsic spectrum of a source. The number of photon counts obtained in a particular channel n is related to the intrinsic spectrum of the source by the following equation:

$$C(\text{channel n}) = \int_0^\infty f(E)R(n,E)dE \tag{3.18}$$

where R(n,E) is the response matrix, which is proportional to the probability that an incoming photon of energy E will be detected in channel n (Chapter 2 gives a detailed description of the response matrices and how they were created for USA). Ideally we would like to use Equation 3.18 and our knowledge of the response of the instrument to solve the inversion problem and obtain the intrinsic spectrum of the source $f(E)$. Unfortunately, the solution is non-unique and the matrices involved are very close to being singular, making the problem highly unstable. Instead, XSPEC uses a different technique to arrive at a solution of the problem. It allows the user to pick a model spectrum with certain parameters. The model is then fed through the response of the instrument and the results are compared with the actual data. The parameters of the model are varied in order to find the optimal, or best-fit, values.

This is done by minimizing the χ^2 parameter, defined as:

$$\chi^2 = \Sigma(C(n) - C_p(n))^2/(\sigma(n))^2 \tag{3.19}$$

where C_p represents the predicted count spectrum for the model with the chosen parameters, and $\sigma(n)$ represents the error for channel n, normally estimated by $\sqrt{C(n)}$. The models are normally chosen based on reasonable assumptions of the physical mechanisms which might be taking place, but a good χ^2 fit to a model is, of course, no guarantee that the model used is an accurate description of what is physically happening at the source. For a complete description of XSPEC see Arnaud and Dorman (2000).

3.2.1 Diskbb

The XSPEC model `diskbb` describes the spectrum from an optically thick, geometrically thin accretion disk consisting of multiple blackbody components (Pringle and Rees 1972; Shakura and Sunyaev 1973). If $T(r)$ denotes the local blackbody temperature of the disk at a distance r from the central compact object of mass M_X, then we can express the (non-relativistic) effective temperature of an annular disk element of thickness dr as:

$$T(r) = (\frac{3G\dot{M}M_X}{8\pi\sigma r^3})^{\frac{1}{4}} \tag{3.20}$$

where σ is Stefan-Boltzmann's constant, G is Newton's constant, and $\dot{M}$ is the mass accretion rate.

The composite photon spectrum of such a disk, at an inclination angle θ, can then be expressed as a superposition of blackbodies at different temperatures. The expression for the diskbb spectrum can be obtained by integrating from an inner radius r_{in} to an outer radius r_{out} (Makishima et al. 1986):

$$f(E) = \int_{r_{in}}^{r_{out}} 2\pi r \cos\theta B[E, T(r)]dr = \frac{8\pi}{3} r_{in}^2 \cos\theta \int_{T_{out}}^{T_{in}} (T/T_{in})^{-11/3} B(E,T) dT/T_{in} \tag{3.21}$$

where $T_{in} = T(r_{in})$ and $T_{out} = T(r_{out})$ are the inner and outermost disk temperatures. E is the emitted photon energy and B(E,T) is a blackbody photon flux per unit photon energy per unit surface area at temperature T. Diskbb therefore depends on only two parameters:

par 1 = T_{in} (temperature at the inner disk radius, in keV).

par 2 = $r_{in}(\cos\theta)^{1/2}$.

The total luminosity of the disk is given by $4\pi r_{in}^2 \sigma T_{in}^4$. For photon energies $E \gtrapprox 2kT_{in}$, diskbb can be approximated as a blackbody spectrum of temperature $T = 0.7T_{in}$ and for energies $kT_{out} \ll E \lesssim 0.3kT_{in}$ the spectrum can be approximated as a power-law with photon index of $-2/3$.

3.2.2 Comptt

Compton scattering is one of the most important radiative processes in high energy astrophysics. In this process, photons and electrons exchange energy by scattering off each other and the average energy exchanged in each scattering is dependent on the relative photon and electron energies. In the case of a thermal distribution of non-relativistic electrons, the change in frequency of the average photon can be expressed by:

$$\frac{< \Delta\nu >}{\nu} = \frac{4kT_e - h\nu}{m_e c^2} \tag{3.22}$$

From this equation we see that if the energy of the photon is much lower than the mean electron energy, then the photon will gain energy, whereas if the photon energy is much greater than the electron energy, the photon will lose energy. The resulting spectrum due to Comptonization is a balance between these two effects.

The XSPEC model `compTT` (Titarchuk 1994) is a model which describes the Comptonization of soft photons by hot electrons in a plasma, taking into account the relevant relativistic corrections. The model is valid for both the optically thin and thick regimes. The Comptonized spectrum is determined by the plasma temperature, the optical depth of the plasma and the injected soft photon spectrum, as well as the geometry of the system. The parameters of this model in XSPEC are as follows:

par 1 = Source redshift
par 2 = Input soft photon (Wien) temperature (keV)
par 3 = Plasma temperature (keV)
par 4 = Plasma optical depth
par 5 = Geometry switch
K = Normalization

3.2.3 The 'Eastern' Model

A popular model for fitting spectra of X-ray binaries is the so-called 'Eastern' Model (Mitsuda et al. 1989), a two-component model in which an optically thick accretion disk dominates at low energies, while a Comptonized component, possibly coming from the neutron star surface (boundary layer) dominates at higher energies. This model has also been used successfully for black hole binaries, where the Comptonized component is thought to be due to the presence of a corona. We find that the combination of `diskbb` and `comptt`, with the addition of an iron line, provides reasonable fits to our data, as will be shown in the next chapter. Due to the low energy resolution of our observations and the limited number of degrees of freedom we have, the input soft photon temperature in `comptt` (par 2) will be set equal to the inner disk radius temperature (par 1 in `diskbb`). Parameter 5 is set to 1 (corresponding to a disk geometry) and the redshift equal to zero, since Cir X-1 is a Galactic source.

Chapter 4

Correlated spectral and timing studies of Circinus X-1 with USA

The ocean is the river's goal,
a need to leave the water knows
We're closer now than light years to go.
REM, "Find the river" (1992)

4.1 Introduction

Cir X-1 was initially classified as a black hole candidate (BHC) due to its temporal and spectral similarities to Cyg X-1: ms variability (Toor 1977), flickering in the hard state and very soft energy spectrum in the high state. It also displays a high energy (>20 keV) power law tail (Iaria et al. 2001) which is considered a signature of BHCs. The discovery by EXOSAT of Type I X-ray bursts in 1985 (Tennant et al. 1986a; Tennant et al. 1986b) led to the classification of Cir X-1 as a neutron star (LMXB). This source forced people to conclude that neither rapid variability nor bimodal spectral behavior could be used as a reliable signature of a BH. It is also one of the few sources which relies on Type I X-ray bursts as the sole basis for the classification of its compact object (Tournear et al. 2003).

In this chapter, I analyze the extensive observations of Cir X-1 made by USA starting in May 2000. I first look at the light curve and explain it in the context of a 'disk-diffusion propagation' model (Wood et al. 2001). Next I study the Energy Spectrum of Cir X-1 and how it evolves. The spectrum of Cir X-1 can be well fit by a model in which the lower energy photons come mainly from an optically thick accretion disk, while the higher energies are dominated by Comptonized emission. This emission could be coming from a boundary layer on the surface of a neutron star, but it could also be coming from a hot corona surrounding the system, with the seed photons arising in the inner part of the disk. I then study the timing properties of Cir X-1. I perform power spectra of the USA data and find numerous quasi-periodic oscillations (QPOs). The QPOs appear to be distributed into two populations, with the lower frequency QPOs increasing in frequency with orbital phase. I show how the USA Cir X-1 observations fit in with recent correlations dicovered in other sources and mention possible mechanisms for the production of these QPOs, including the disk-diffusion propagation model (Wood et al. 2001) and the dripping handrail (DHR) model (Scargle et al. 1993; Young and Scargle 1996). I compare Cir X-1 to other other sources, including a BHC (Cyg X-1) and three neutron stars (Cyg X-2, GX 349+2, and GX 340+0). In addition to showing that these neutron stars explore different parts of the color-color diagram, I compare the power spectrum from Cir X-1's softest region to that of Cyg X-1 and draw some conclusions regarding the possible mass of Cir X-1. Finally, I present evidence for possible sub-ms variability in Cir X-1, in the form of 6 rapid bursts detected in USA data.

4.2 USA Observations and Data Analysis

USA began an observing campaign on Cir X-1 on 2000 May 2 (MJD 51666) lasting approximately 100 days. During this period, USA accumulated approximately 200 ksec of data and achieved significant coverage over the 16.6 day orbital period of the source. For a complete list of the USA observations of Cir X-1 analyzed in this dissertation, see Appendix D. For reasons of consistency, I do not include a small number of observations of Cir X-1 which were taken early in the mission (1999). These observations were not part of the targeted campaign on Cir X-1 and were taken in Mode 1, which present the problem of over-filling the buffer (see Section 2.2.1 for a description of the different modes and the limitations of the low telemetry rate modes). Figure 4.1 shows the 2-10 keV Cir X-1 light curve obtained with USA (top), as well as the corresponding RXTE ASM light curve (bottom). For purposes of comparison, 1 Crab is ~75 ASM cts s^{-1}.

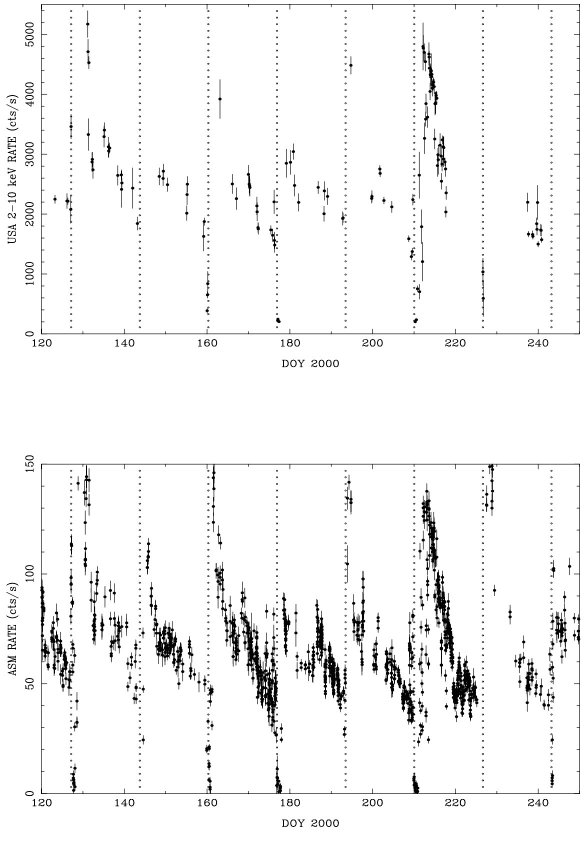

Figure 4.1: **Top** – USA light curve of Cir X-1. The dotted lines represent phase 0, or the onset of radio flares, as defined by the radio ephemeris (Stewart et al. 1991). **Bottom** – RXTE ASM light curve of Cir X-1 for the same period as above.

The USA light curve has been background-subtracted and corrected for the collimator response. The dotted lines represent phase 0 as defined by the radio ephemeris (i.e. the onset of radio flares) (Nicolson 1980). The light curve shows clearly the transition which occurs first around day 127 and subsequently every ~16.5 days. Note that phase 0 slightly precedes the X-ray outburst.

4.2.1 Light Curve: Disk Diffusion Model

The first thing which stands out about the character of the Cir X-1 light curve is its Fast Rise and Exponential Decay (FRED) profile. Wood et al. (2001) show that this type of curve is typical of diffusion processes. It can be obtained by postulating that matter is being deposited at the outer radius of the accretion disk and then diffusing in through the disk. In the case of Cir X-1, the mass deposition could be happening periodically at each periastron passage; blobs of matter are accreted from the companion star to the disk and then diffuse in.

Before fitting any light curves, I will give a brief description of the model. For full details, see Wood et al. (2001).

The first assumption is that we have a thin disk, characterized by its surface density $\Sigma(R,t)$ (mass per unit surface area of the disk). Using cylindrical coordinates (R,ϕ,z), where the matter in the disk lies very close to the plane z=0, and writing down the conservation equations for the mass and angular momentum transport in the disk in the radial direction, and assuming a Keplerian angular velocity (i.e. $\Omega(R) = \sqrt{GM/R^3}$), we obtain a diffusion equation for the system (see Frank et al. (2002) or Wood et al. (2001) for a full derivation):

$$\frac{\partial\Sigma}{\partial t} = \mathbf{\Lambda}_R\Sigma = \frac{3}{R}\frac{\partial}{\partial R}\left(R^{1/2}\frac{\partial}{\partial R}[\nu\Sigma R^{1/2}]\right) + Q(R,t) \tag{4.1}$$

In this equation, ν represents the kinematic viscosity in the disk and Q(R,t) is the source term, which Wood et al. (2001) take as an injection at the outer boundary of the disk, R_0:

$$Q(R,t) = \frac{A(t)\delta(R-R_0)}{2\pi R}. \tag{4.2}$$

where $A(t)$ is the mass input rate as a function of time at the outer edge of the disk.

Wood et al. (2001) derive an analytical solution to this diffusion equation by making use of several asymptotic approximations to obtain a Green's function, $K(t)$,

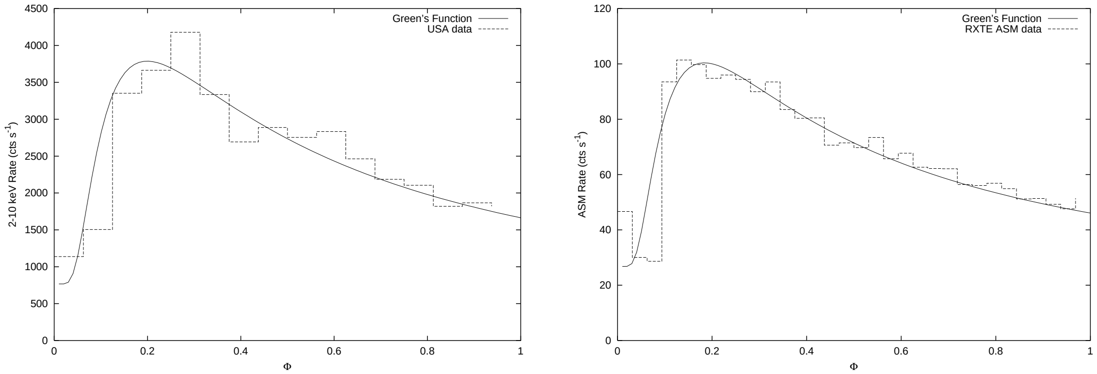

Figure 4.2: **Left** – Fit of Green's function (plus a constant) to the USA folded light curve of Cir X-1. I have used $\psi = 1.0$ for the fit and obtain a constant (DC) level of 767±177 and a $t_0 = 1.06 \pm 0.05$. **Right** – Fit of Green's function for RXTE ASM data. The fit parameters obtained are $t_0 = 0.97 \pm 0.04$ and a DC level of 26.80±2.9.

which represents the flux through the inner edge of the disk at time t from the delta-function injection at the outer edge at time t=0.

$$K(t) = \frac{1}{C}\{\frac{2.5}{\sqrt{\pi}}(\frac{t_0}{2t})^{\gamma+1/2}\sin(\frac{\pi(2\nu+1)}{4}) + (z_1^2)^{\gamma/2}\cos[\frac{2(1-\gamma)}{\pi(\gamma-3)}]\}e^{-(\frac{t_0}{4t}+\frac{z_1^2 t}{t_0})} \tag{4.3}$$

In this equation, C is a normalization constant chosen to make the integral of $K(t)$ equal to unity, $t_0 = 4x_0^2/3\nu_0 = 4R_0^2/3\nu(R_0)$ is the viscous timescale, which determines both the rise and fall time of the response function, ψ is a parameter related to the kinematic viscosity (assumed to be a power-law function of the radial coordinate, i.e. $\nu(x) = \nu_0 x^{\psi}$, where $x = R^{1/2}$), $\gamma = \frac{6-\psi}{2(4-\psi)}$, the factor 2.5 in the first term was empirically determined, and $z_1 \simeq \left[\frac{\pi(6-\psi)}{4(4-\psi)} - \frac{2(2-\psi)}{\pi(6-\psi)}\right]$; see Wood et al. (2001) for a full derivation of this equation. This analytical form of the solution is only valid for values of $\psi < 3$.

Although this is a very long expression, it is essentially a function of two parameters: t_0, the viscous timescale, and ψ which determines the viscosity parameter. It is assumed that time starts at the moment when the injection of matter at the outer edge takes place.

Figure 4.2 shows a fit of the folded light curve of Cir X-1 to equation 4.3. I have chosen ψ to be 1.0 and have added a constant (DC) term to account for the quiescent level of the flux. The left figure shows the fit made to the USA folded light curve, while the right figure shows the fit to the folded RXTE ASM data for the same time period. The viscous timescales obtained for both are of the order of the orbital period (1.0 in units of phase). Having no *a priori* preference for values of ψ, I chose $\psi = 1.0$ because it gave the best fits. However, it is important to note that different values of ψ would yield different values of the viscous timescale t_0, so one should not take the numerical values of t_0 too literally. However, it is interesting, nevertheless, to study the *relative* values of these timescales. I attempted to fit the folded light curves of the RXTE ASM epoch (which will be discussed in the next chapter and are shown in Figure 5.8). I was not able to fit the 3rd and 4th light curves in that figure with a FRED, so Figure 4.3 only shows the eight which provided reasonable fits.

Table 4.1 shows the parameters of each fit and in Figure 4.4 I plot the viscous timescale parameter t_0 vs. the DC rate. As can be seen from the table, the viscous timescale in the system varies by up to a factor of 3, though there is no clear correlation between such a timescale and the 'quiescent' luminosity of the system.

Dates (MJD)	t_0	DC Rate
50088–50337	0.5879 ± 0.04	72.35 ± 3.3
50338–50587	0.5939 ± 0.04	74.21 ± 2.9
50589–50838	0.6755 ± 0.07	76.22 ± 4.9
51339–51588	1.7793 ± 0.13	46.47 ± 5.9
51588–51837	0.9663 ± 0.05	33.12 ± 3.5
51838–52087	0.6662 ± 0.03	23.73 ± 1.3
52089–52338	0.6905 ± 0.04	17.30 ± 2.6
52338–52536	0.6327 ± 0.04	14.08 ± 2.2

Table 4.1: Disk Diffusion fits to RXTE ASM folded light curves ($\psi = 1.0$)

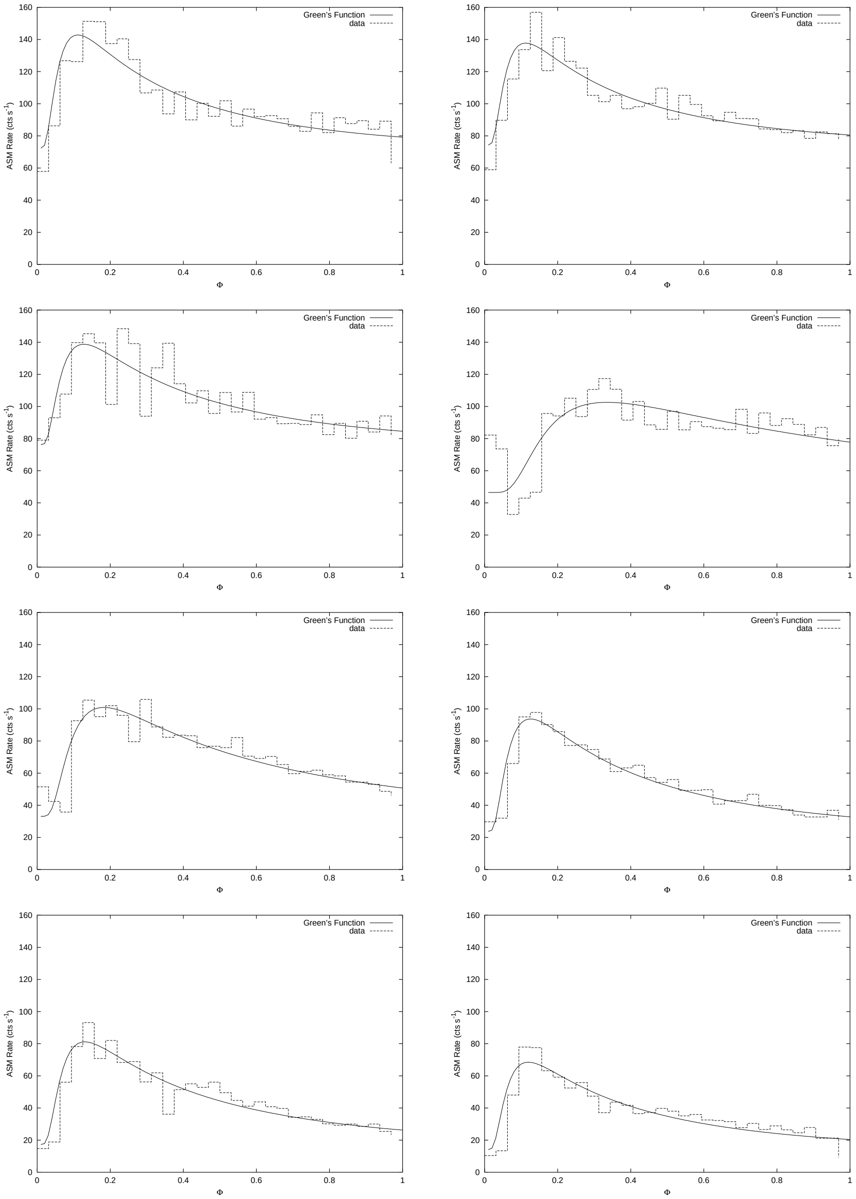

Figure 4.3: Disk Diffusion Model applied to folded light curves of RXTE ASM data (MJD 50088–52536). From top left to bottom right.

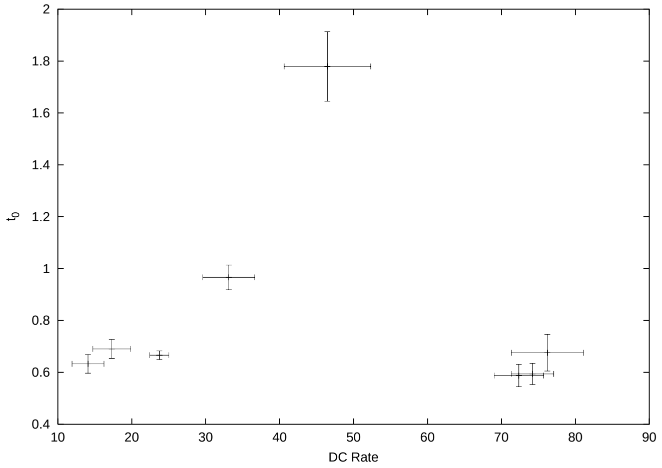

Figure 4.4: Disk Diffusion model: viscous timescale parameter t_0 vs. DC rate. Parameters are those from the fits shown in Figure 4.3.

4.2.2 Energy Spectrum Evolution

Color-Color Diagrams

In order to study the spectral evolution of the source, I first attempted to construct an instrument-independent color-color diagram by fitting each observation to a model spectrum and taking the ratio of fluxes for the model fit. The spectra were fit to the so-called 'Eastern' model (Mitsuda et al. 1989). In section 3.2 I discuss some details of this model. I analyzed a total of 117 Ascending Node (AN) observations and 55 South Polar (SP) observations (see Appendix D for a list of the observations). Due to the different energy calibrations required for each type, we performed the analyses separately. Our observations were first filtered to remove the data of poor quality (e.g. data taken in high background regions, contaminated with soft electrons, etc.). I subtracted the background estimate for each one and then fit the observations to a multicolor blackbody (`diskbb` in XSPEC) representing the emission from the optically thick accretion disk, a Comptonization model representing the upscattering of soft photons from the disk to higher energies by hot electrons (`comptt` in XSPEC) and an iron line (`gaussian`). I fixed the interstellar column density to Cir X-1 at $n_H = 1.38 \times 10^{22}\,\mathrm{cm}^{-2}$, a value obtained from the observed visual extinction to the secondary star (Iaria et al. 2001). After fitting the data, I obtained fluxes for the model in four different energy bands : 2–4, 4–6.4, 6.4–9.7, and 9.7–16 keV. I also computed the total flux in the 2–10 keV range. The 'soft' color was defined as the ratio of the flux in the range 4–6.4 keV, to that in the 2–4 keV, while the 'hard' color was defined as the ratio of the flux in the 9.7–16 keV range to that in the 6.4–9.7 keV range. Figure 4.5 shows the resulting color-color diagrams. In the top panel, the z-coordinate (color) represents the orbital phase, as defined by the radio ephemeris. In the bottom panel, z-coordinate represents the source intensity. This is the 2–10 keV luminosity of the source, assuming a distance of 5.5 kpc.

In order to make model-independent comparisons between different sources, it is often better to construct a color-color diagram by taking ratios of counts in particular PHA channels. While this has the disadvantage that it will be instrument-dependent (making comparisons between different missions more complicated), it has the advantage that for a given mission (such as USA), this is a quick, 'model-independent' (no spectral fitting is involved) way of comparing different sources. I constructed such a color-color diagram for Cir X-1 by defining 'soft' color as the ratio of counts in Channels 4–5 to those in Channels 2–3, and the 'hard' color as the ratio between counts in channels 9–11 and 6–8 (the approximate energy boundaries are quoted in Figure 4.6). The choice of channels was driven by two factors: channels 0 and 1 were not used because they can be heavily influenced by absorption and high backgrounds. Channels 12 and above, on the other hand, were not used because the rates in those channels were so low that the influence of the background (with its corresponding uncertainty) would be too significant. Figure 4.6 shows the model-independent color-color diagram I obtained in this way. I have divided the observations up into 5 different segments (parameterized by an S coordinate) to study in more detail the average evolution of the source along the color-color diagram. It should be noted at this point that although the value of S could correspond to some physical parameter (such as mass accretion rate) of the source at a given time, there is, most likely, not a smooth evolution between the values of S=4 and S=5. It is also important to note that only three observations are contained in the S=5 box, making it an area of the color-color diagram which is far less sampled than the other locations.

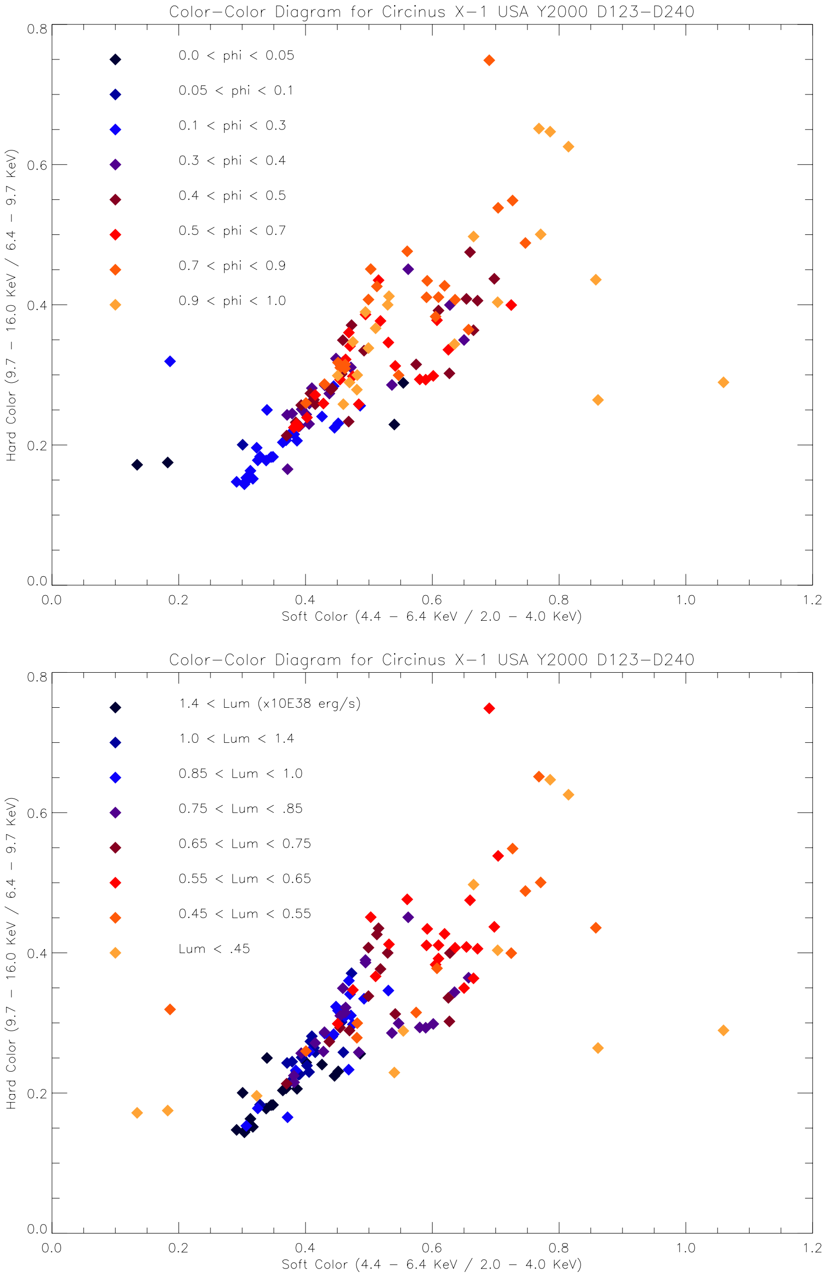

Figure 4.5: Instrument-independent color-color diagram of Cir X-1. **Top** – Z coordinate (color) represents orbital phase **Bottom** – Z coordinate (color) represents source intensity.

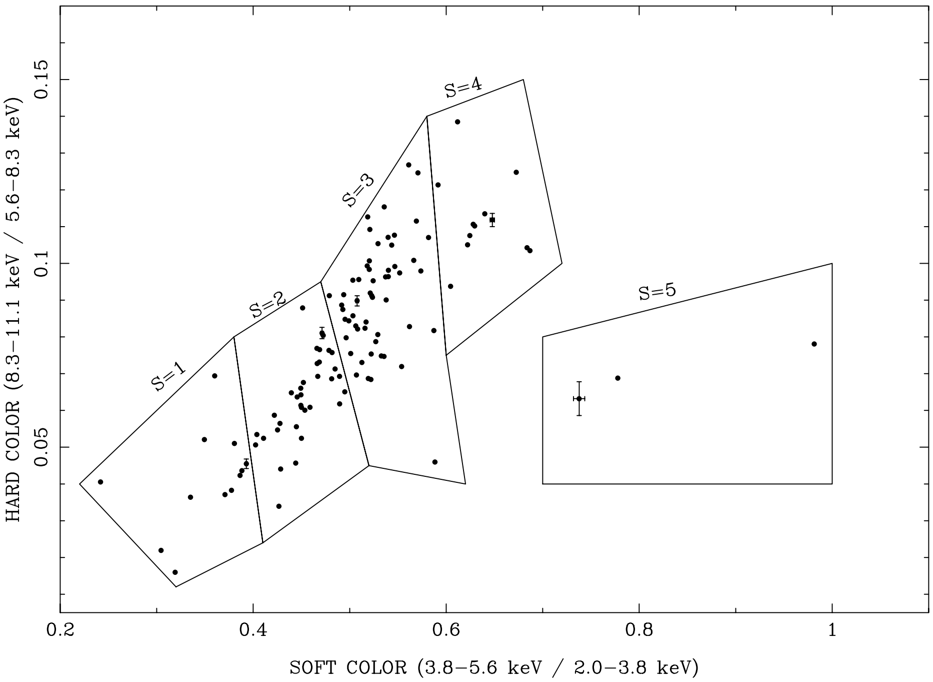

Figure 4.6: Model-independent color-color diagram of Cir X-1

Hardness Intensity Diagram

Another way of representing the spectral evolution of the source is by a so-called hardness-intensity diagram. Figure 4.7 shows the hardness-intensity diagram of Cir X-1. The hardness ratio in this plot (the X axis) is defined as the ratio of the number of counts in channels 6–11 divided by the number of counts in channels 2–5. The intensity (Y axis) is defined as the total number of counts (with the background subtracted out) in Channels 2–11. The different symbols shown in the figure are used to represent the five different regions of the color-color 'path' represented in Figure 4.6.

Evolution of Spectral Parameters

Figure 4.8 shows a sample of different energy spectra of Cir X-1. The left column shows the data with the spectral fits, and the right column shows the fit models (extrapolated to the 0.1–100 keV range). The plots show a representative observation

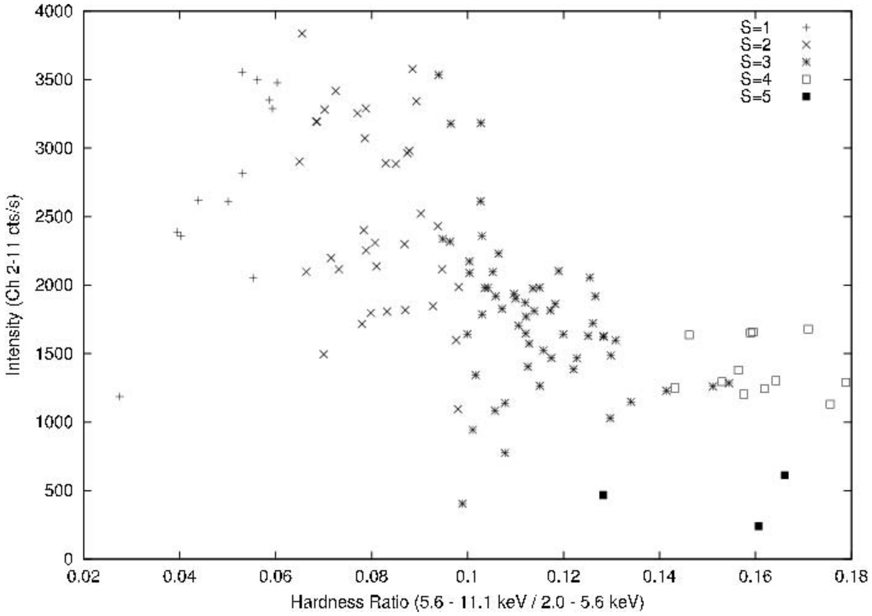

Figure 4.7: Hardness-Intensity diagram of Cir X-1. Different symbols represent different locations on the color-color diagram in Figure 4.6

from each of the five regions in the color-color diagram of Figure 4.6 (regions labeled S=1 through S=5).

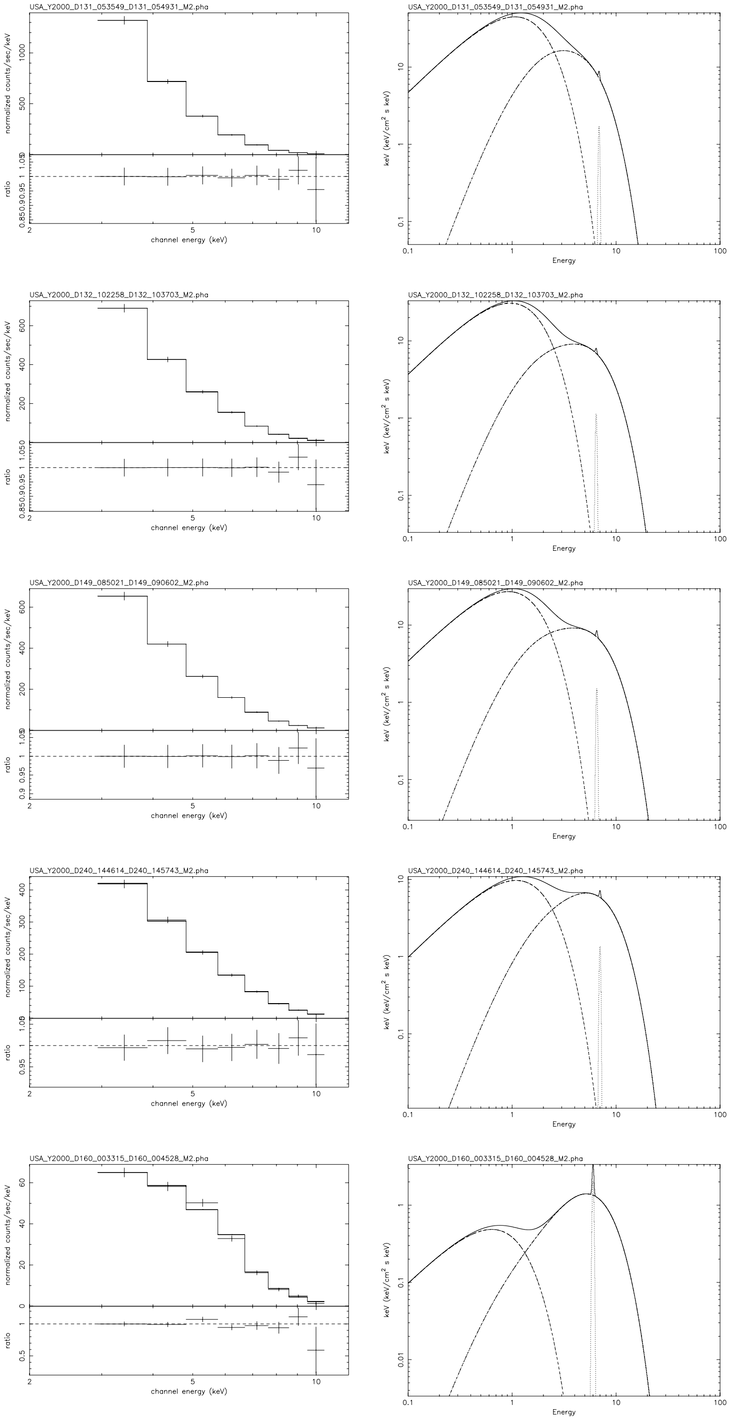

Figure 4.8: Spectral evolution of Cir X-1 along the color-color diagram. Plots show representative observations of each stage of the spectral evolution, starting at the top (S=1 in Figure 4.6) and ending at the bottom (S=5 in Figure 4.6). The left column shows the spectral fit to USA data and the right column shows the model in an expanded energy range (.1–100 keV).

S	$kT_{\rm diskbb}$ (keV)	$kT_{\rm e}$ (keV)	$f_{\rm diskbb}$ [a]	χ^2	*Flux* [b]	Norm [c]
1	0.48 ± 0.03	1.27 ± 0.30	0.79 ± 0.05	1.90 ± 0.49	3.63 ± 1.21	1.5 ± 1.5
2	0.45 ± 0.02	1.33 ± 0.09	0.74 ± 0.06	1.46 ± 0.68	3.14 ± 0.83	1.3 ± 0.30
3	0.45 ± 0.03	1.50 ± 0.12	0.71 ± 0.09	1.31 ± 0.73	2.30 ± 0.67	1.0 ± 0.41
4	0.45 ± 0.05	1.65 ± 0.09	0.64 ± 0.11	0.99 ± 0.98	1.82 ± 0.30	0.48 ± 0.17
5	0.60 ± 0.28	1.38 ± 0.07	0.24 ± 0.08	2.38 ± 0.06	0.42 ± 0.19	0.13 ± 0.12

[a] as a fraction of the total flux

[b] flux for the unabsorbed model integrated from 0.01–100 keV, in units of 10^{-8} ergs s^{-1} cm^{-2}

[c] $\times 10^5((R_{in}/km)/(D/10kpc))^2 \cos\theta$

Table 4.2: USA data fit to the 'Eastern' model (`diskbb + comptt + gaussian`)

Table 4.2 shows the average value of the fit parameters in the five different regions (S=1 through S=5).

Figure 4.9 shows the evolution of the fit parameters with location on the color-color diagram (S coordinate). The top panel shows the evolution of the two key temperatures in the model (the inner disk temperature $T_{\rm in}$ and the plasma temperature $T_{\rm e}$. The bottom line in this panel represents the mean inner disk temperature (0.45 keV), while the upper line of zero slope shows the mean plasma temperature, indicating that the data points are not well fit with a constant mean plasma temperature. The sloped line is the fit to the first four regions (S=1 through S=4), showing the increase in plasma temperature along the S-path on the color-color diagram. The middle panel in Figure 4.9 shows the relative contributions (as a fraction of the total flux) of each component in the spectral model. The bottom panel shows the ratio of the `diskbb` contribution to the `comptt` contribution.

To test how reasonable it is to conclude that the plasma temperature is increasing along the color-color diagram path, we fit the data from Table 4.2 with three different functions: a constant, a linear function, and a quadratic polynomial. In addition to fitting all five (S=1 through S=5) data points, we also tried fitting only to four points (S=1 through S=4), for the reasons expressed previously. S=5 is only represented with three observations and therefore the statistical errors are large. In addition, there is a clear jump in the color-color diagram path between the S=4 and S=5 locations. It is reasonable to suppose that, whereas S=1 through S=4 probably represents a

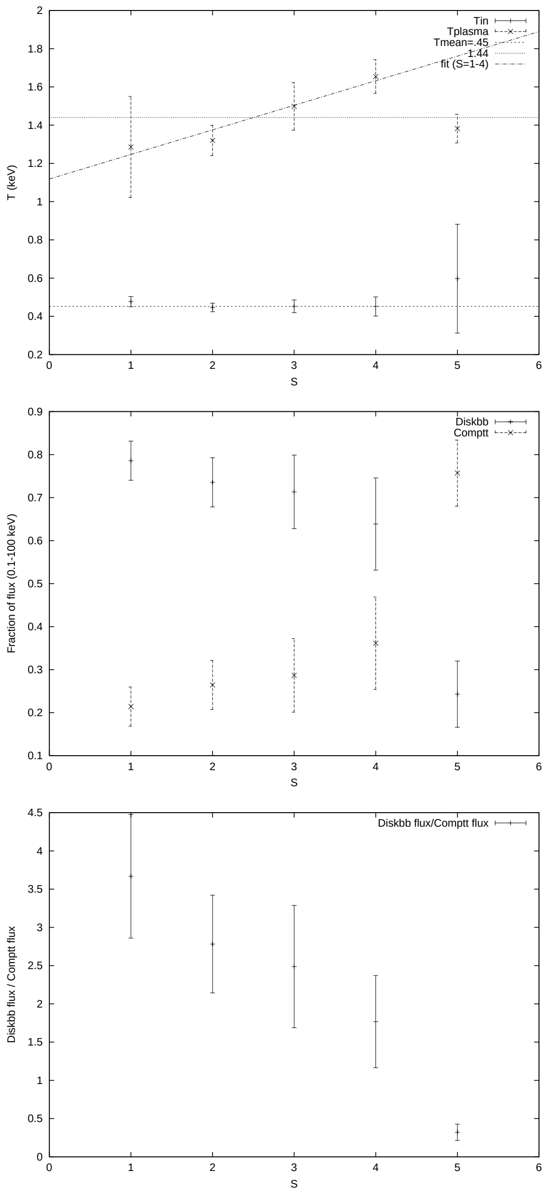

Figure 4.9: **Top Panel** – Evolution of inner disk temperature ($T_{\rm in}$) and comptonizing medium temperature. **Middle Panel** – Contribution of `diskbb` and `comptt` components to total flux. **Bottom Panel** – Ratio of `diskbb` contribution to `comptt` contribution.

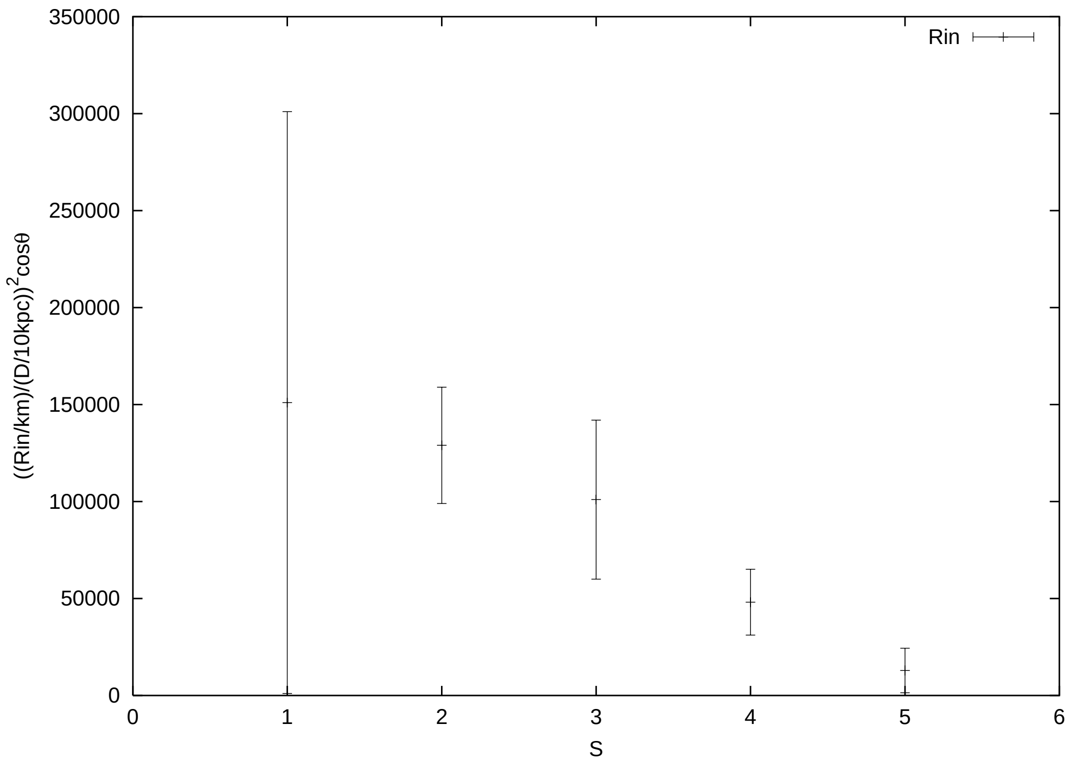

Figure 4.10: Evolution of the inner radius (from Table 4.2). For a distance D of 6.5 kpc, and θ =0 degrees, $R_{\rm in}$ ranges from ~250 km (S=1) to ~75 km (S=5)

continuum of physical parameters, S=5 represents a discrete jump in such parameter. The results of all our fits are shown in Table 4.2.2.

Figure 4.11 shows the evolution of the inner radius of the disk, as derived from the normalization parameter in the fits. While the error bars are sometimes very large, and the absolute value of this radius is very uncertain (in part also due to the uncertainty on the distance and inclination angle), nevertheless there is a clear trend that is present in the data, with the radius decreasing with increasing value of the 'S' parameter.

S	Model	d.o.f.	χ^2/d.o.f.	Q[a]
1–5	constant	4	2.3305	0.0535
1–5	linear	2	2.7593	0.0406
1–5	quadratic	2	1.3715	0.2537
1–4	constant	3	2.8203	0.0373
1–4	linear	2	0.1035	0.9017
1–4	quadratic	1	0.0993	0.7526

[a] probability that the χ^2 is consistent with the hypothesis that the given model fits the data.

Table 4.3: Comptonizing temperature, kT, as a function of color-color path S

4.2.3 Timing Evolution

I will discuss the timing evolution of Cir X-1 at long timescales (days and years) in Chapter 5. In this section I discuss the faster timescales (faster than 1s). To do this, Fourier power spectra (van der Klis 1989) were performed on each observation and the deadtime correction was subtracted (see Shabad (2000) for details on the deadtime model for USA). I used a 96 μs bin time resolution for the FFTs and fractional rms normalization. All power spectra were performed using the program `specan`, developed at SLAC by W. Focke (see Reilly (2003) for details). The spectra were then fit to multiple Lorentzians using the *Quick and Dandy Plotter* (QDP) program (Tennant 1991). Equation 4.4 gives the definition of a Lorentzian in terms of three parameters: the fractional RMS variability (which under our normalization is equal to the square root of the area), P_1, the Full Width at Half Maximum (FWHM), P_2, and the centroid frequency P_3.

$$F(x) = \frac{2{P_1}^2}{\pi[\frac{4}{P_2}(x-P_3)^2+P_2]} \tag{4.4}$$

We can also define a quality factor Q of the Lorentzian as the ratio of the centroid frequency to the FWHM. Lorentzians with Q >2 are generally referred to as QPOs (der Klis 2000). Figure 4.11 shows a typical observation containing a QPO, which has been fit using QDP. The values of the parameters are shown on the side. While some observations contained more than one QPO, others contained no QPOs. It was not always necessary to have three Lorentzians to fit the power spectra.

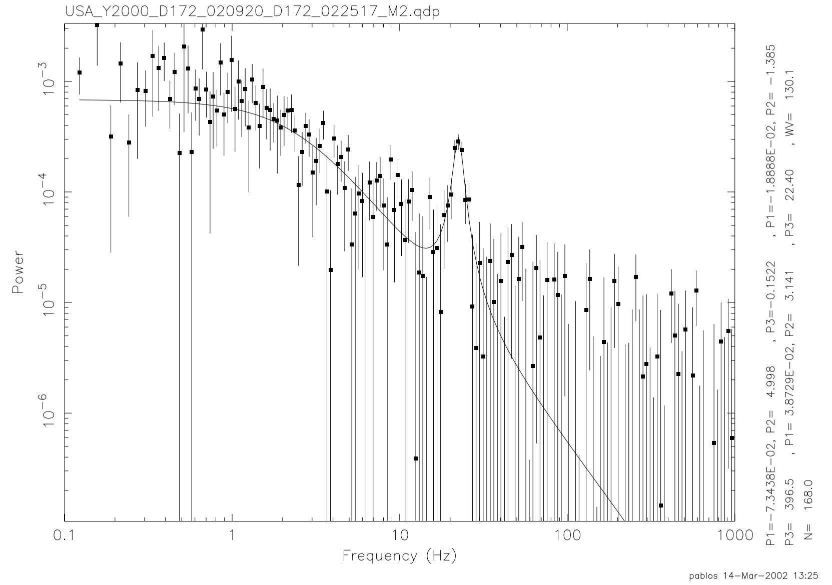

Figure 4.11: Typical QPO fit

Table 4.4 shows the value of the fit parameters for all QPOs found in the USA data analyzed.

QPO fit parameters

File	S	Freq. (Hz)	FWHM (Hz)	Rms (%)
USA_Y2000_D123_061540_D123_062331	3	$15.10^{+0.14}_{-0.13}$	$2.12^{+0.35}_{-0.49}$	$5.3^{+0.3}_{-0.7}$
USA_Y2000_D131_035510_D131_040445	2	$42.63^{+1.54}_{-1.26}$	$12.71^{+6.9}_{-4.7}$	$2.89^{+0.5}_{-0.5}$
USA_Y2000_D132_052019_D132_052907	2	$3.51^{+0.04}_{-0.04}$	$0.80^{0.14}_{-0.12}$	$6.66^{+0.7}_{-0.4}$
USA_Y2000_D132_052019_D132_052907	3	$6.95^{+0.39}_{-0.48}$	$1.60^{+2.58}_{-1.05}$	$2.20^{+1.7}_{-0.8}$
USA_Y2000_D132_070221_D132_071045	2	$4.77^{+0.06}_{-0.06}$	$1.21^{+0.19}_{-0.17}$	$7.37^{+0.4}_{-0.5}$
USA_Y2000_D132_102451_D132_103401	2	$4.79^{+0.04}_{-0.04}$	$1.08^{+0.12}_{-0.18}$	$7.54^{+0.2}_{-0.4}$
USA_Y2000_D135_024446_D135_025535	2	$27.10^{+0.58}_{-0.61}$	$11.51^{+2.09}_{-1.78}$	$5.39^{+0.3}_{-0.4}$
USA_Y2000_D139_082348_D139_083248	3	$1.34^{+0.05}_{-0.04}$	$0.64^{+0.05}_{-0.05}$	$11.8^{+0.5}_{-0.5}$
USA_Y2000_D139_082348_D139_083248	3	$4.70^{+0.08}_{-0.08}$	$0.85^{+0.12}_{-0.11}$	$4.71^{+0.3}_{-0.3}$
USA_Y2000_D139_082348_D139_083248	3	$7.78^{+0.13}_{-0.15}$	$0.87^{+0.36}_{-0.30}$	$2.51^{+0.3}_{-0.3}$
USA_Y2000_D142_004115_D142_005419	3	$1.56^{+0.04}_{-0.04}$	$0.33^{+0.09}_{-0.07}$	$3.56^{+0.3}_{-0.3}$

QPO fit parameters (Continued)

USA_Y2000_D142_004115_D142_005419	3	$4.48^{+0.23}_{-0.18}$	$1.76^{+0.74}_{-0.59}$	$2.68^{+0.3}_{-0.3}$
USA_Y2000_D148_105326_D148_110145	3	$3.12^{+0.03}_{-0.02}$	$0.34^{+0.09}_{-0.07}$	$5.40^{+0.4}_{-0.4}$
USA_Y2000_D148_105326_D148_110145	3	$39.65^{+1.56}_{-2.58}$	$7.63^{+15.5}_{-4.52}$	$2.68^{+0.8}_{-0.7}$
USA_Y2000_D149_085225_D149_090249	3	$6.01^{+0.04}_{-0.03}$	$0.96^{+0.11}_{-0.10}$	$7.35^{+0.3}_{-0.3}$
USA_Y2000_D149_103343_D149_104429	3	$7.50^{+0.04}_{-0.04}$	$1.15^{+0.12}_{-0.11}$	$7.13^{+0.3}_{-0.3}$
USA_Y2000_D150_101617_D150_102706	3	$7.04^{+0.04}_{-0.05}$	$1.14^{+0.11}_{-0.10}$	$6.97^{+0.3}_{-0.3}$
USA_Y2000_D155_020046_D155_021413	3	$21.57^{+0.17}_{-0.15}$	$2.77^{+0.60}_{-0.60}$	$4.29^{+0.3}_{-0.3}$
USA_Y2000_D155_034352_D155_035548	3	$27.43^{+0.64}_{-0.67}$	$7.55^{+2.49}_{-1.76}$	$4.03^{+0.4}_{-0.3}$
USA_Y2000_D155_034352_D155_035548	3	$7.70^{+0.13}_{-0.15}$	$0.70^{+0.69}_{-0.36}$	$1.67^{+0.3}_{-0.3}$
USA_Y2000_D159_041552_D159_042818	3	$4.55^{+0.06}_{-0.06}$	$0.63^{+0.12}_{-0.12}$	$4.34^{+0.3}_{-0.3}$
USA_Y2000_D159_041552_D159_042818	3	$7.71^{+0.16}_{-0.13}$	$1.61^{+0.72}_{-0.42}$	$3.86^{+0.4}_{-0.3}$
USA_Y2000_D163_030536_D163_031906	2	$19.02^{+0.18}_{-0.18}$	$6.58^{+0.37}_{-0.45}$	$7.64^{+0.3}_{-0.3}$
USA_Y2000_D166_021231_D166_022717	3	$17.71^{+1.49}_{-1.81}$	$5.04^{+5.3}_{-2.8}$	$1.99^{+0.7}_{-0.7}$
USA_Y2000_D166_021231_D166_022717	3	$7.61^{+0.04}_{-0.04}$	$1.18^{+0.11}_{-0.10}$	$6.81^{+0.2}_{-0.2}$
USA_Y2000_D167_015522_D167_020946	3	$7.86^{+0.04}_{-0.04}$	$1.19^{+0.10}_{-0.09}$	$6.70^{+0.2}_{-0.2}$
USA_Y2000_D172_020920_D172_022517	3	$22.4^{+0.22}_{-0.22}$	$3.14^{+0.45}_{-0.45}$	$3.87^{+0.2}_{-0.2}$
USA_Y2000_D172_071640_D172_073009	3	$12.66^{+0.07}_{-0.08}$	$1.51^{+0.26}_{-0.23}$	$4.78^{+0.3}_{-0.3}$
USA_Y2000_D172_085752_D172_091145	3	$1.34^{+0.09}_{-0.09}$	$0.26^{+0.31}_{-0.14}$	$1.22^{+0.4}_{-0.3}$
USA_Y2000_D172_085752_D172_091145	3	$11.97^{+0.06}_{-0.07}$	$1.30^{+0.18}_{-0.16}$	$4.71^{+0.3}_{-0.3}$
USA_Y2000_D179_033210_D179_034721	1	$4.29^{+0.04}_{-0.04}$	$1.24^{+0.16}_{-0.14}$	$8.42^{+0.5}_{-0.4}$
USA_Y2000_D180_031409_D180_033017	2	$8.53^{+0.05}_{-0.05}$	$2.59^{+0.17}_{-0.16}$	$9.33^{+0.2}_{-0.2}$
USA_Y2000_D181_025655_D181_031259	2	$4.68^{+0.03}_{-0.03}$	$1.02^{+0.09}_{-0.08}$	$8.30^{+0.2}_{-0.2}$
USA_Y2000_D182_024036_D182_025406	2	$51.73^{+2.98}_{-1.68}$	$4.74^{+0.05}_{-0.33}$	$1.77^{+0.6}_{-0.7}$
USA_Y2000_D182_024036_D182_025406	2	$4.54^{+0.02}_{-0.02}$	$0.70^{+0.07}_{-0.06}$	$7.53^{+0.2}_{-0.2}$
USA_Y2000_D188_060036_D188_061659	3	$22.75^{+0.24}_{-0.23}$	$5.61^{+0.59}_{-0.55}$	$6.01^{+0.2}_{-0.3}$
USA_Y2000_D188_074230_D188_075842	3	$35.04^{+0.81}_{-0.74}$	$8.24^{+2.60}_{-1.99}$	$3.55^{+0.3}_{-0.3}$
USA_Y2000_D194_175947_D194_180629	1	$17.54^{+0.27}_{-0.26}$	$4.64^{+0.57}_{-0.55}$	$7.75^{+0.5}_{-0.5}$
USA_Y2000_D199_181352_D199_182039	4	$7.67^{+0.07}_{-0.07}$	$0.68^{+0.21}_{-0.22}$	$5.38^{+0.8}_{-1.1}$
USA_Y2000_D213_053153_D213_055101	1	$52.94^{+2.06}_{-2.28}$	$8.48^{+7.24}_{-3.72}$	$1.70^{+0.4}_{-0.4}$

QPO fit parameters (Continued)

USA_Y2000_D213_141050_D213_141926	2	$2.16^{+0.16}_{-0.15}$	$0.72^{+0.35}_{-0.24}$	$2.48^{+0.4}_{-0.4}$
USA_Y2000_D214_015521_D214_020322	2	$36.76^{+1.16}_{-1.25}$	$15.14^{+4.09}_{-3.40}$	$4.75^{+0.6}_{-0.6}$
USA_Y2000_D214_235132_D215_000635	2	$23.53^{+0.18}_{-0.18}$	$7.81^{+1.00}_{-0.75}$	$7.28^{+0.5}_{-0.3}$
USA_Y2000_D215_013702_D215_014622	2	$33.92^{+1.72}_{-1.56}$	$10.33^{+2.99}_{-3.81}$	$4.40^{+0.8}_{-1.1}$
USA_Y2000_D216_062021_D216_064033	3	$13.51^{+0.36}_{-0.30}$	$1.92^{+1.19}_{-0.89}$	$1.55^{+0.3}_{-0.3}$
USA_Y2000_D216_062021_D216_064033	3	$28.46^{+0.41}_{-0.38}$	$12.09^{+1.44}_{-1.41}$	$5.52^{+0.3}_{-0.3}$
USA_Y2000_D216_131453_D216_132726	3	$28.14^{+0.58}_{-0.55}$	$12.82^{+2.00}_{-2.01}$	$6.31^{+0.3}_{-0.1}$
USA_Y2000_D216_150017_D216_150902	3	$20.76^{+0.17}_{-0.17}$	$3.39^{+0.57}_{-0.49}$	$5.78^{+0.4}_{-0.4}$
USA_Y2000_D216_182138_D216_182842	3	$29.54^{+0.68}_{-0.68}$	$8.25^{+2.51}_{-2.10}$	$5.14^{+0.5}_{-0.6}$
USA_Y2000_D217_023946_D217_025812	3	$15.51^{+1.94}_{-1.27}$	$6.67^{8.96}_{-3.68}$	$2.37^{+1.1}_{-0.7}$
USA_Y2000_D217_023946_D217_025812	3	$31.11^{+0.58}_{-0.56}$	$11.92^{+1.51}_{-1.59}$	$5.57^{+0.3}_{-0.4}$

Table 4.4: QPO fit parameters

Figure 4.12 shows how the QPO centroid evolves during one particular orbital cycle, clearly showing the evolution of the QPO centroid towards a higher frequency within that cycle. This appears to happen during every orbital cycle, although the coverage was not always good enough to capture it so clearly as in Figure 4.12.

Next, we focus on how the ‘strength’ of these QPOs depends on frequency. Here again we note that there are two distinct populations of QPOs. Figure 4.13 shows the fractional RMS variability of the QPO plotted against the centroid frequency of the QPO. The right panel on that figure focuses on the higher frequency QPOs, showing there is an anti-correlation between the RMS and QPO centroid. The correlation coefficient between the RMS and the QPO frequency for the higher frequencies (>20 Hz) is -1.2×10^{-3}, whereas for the lower frequencies (<20 Hz) the correlation coefficient is 4.1×10^{-4}. Furthermore, we carried out an F-test to test the linearity of regression (Kanji 1999). For frequencies less than 20 Hz, the F-value obtained ($F_{1,27} = 0.17$) is less than the critical value ($F_{1,27;\alpha=.05} = 4.21$). We must therefore accept the null hypothesis that there is no correlation between the frequency and the RMS of the

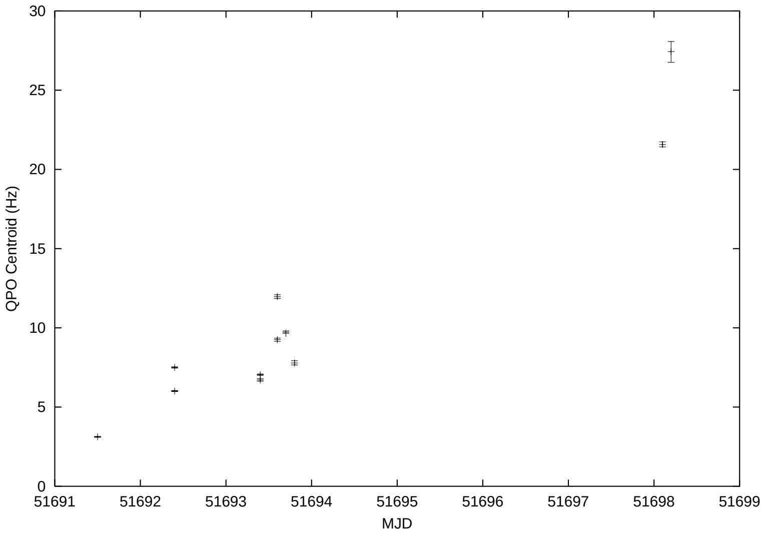

Figure 4.12: QPO centroid frequency (Hz) vs. day (MJD).

QPO, whereas for QPOs above 20 Hz, the F-value obtained ($F_{1,16} = 14.96$) is significantly higher than the critical value ($F_{1,16;\alpha=.05} = 4.49$) showing that there is indeed a negative correlation between frequency and RMS variability.

Some observations show more than one QPO. In Figure 4.14 I show those observations which contain two QPOs and plot the high frequency vs the low frequency. No clear correlation is found between the high and low frequency QPOs although the number of observations with more than one QPO is small and the individual observations often do not have enough counts in them to provide adequate fits to the multiple QPOs present in them.

Figure 4.15, on the other hand, shows the combined power spectrum of 7 observations taken between day 131 18:49 and day 132 13:27. These observations were chosen because they contained multiple QPOs and by combining all of them, their statistical significance was increased greatly. The combined power spectrum is well fit by three Lorentzians, two of which represent QPOs, while the third can be thought of as low frequency noise.

We also examined the energy dependence of a QPO. Due to insufficient statistics, we are not able to do this with individual observations and therefore need to combine

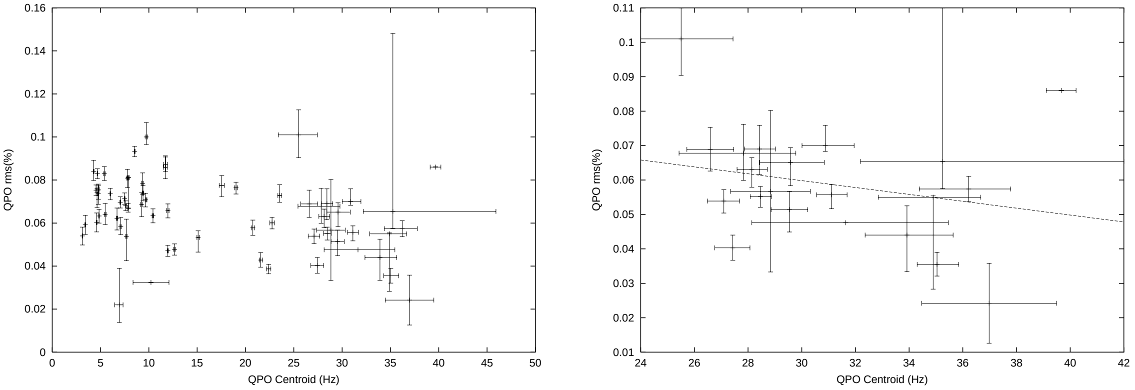

Figure 4.13: **Left** – QPO RMS% vs. QPO Centroid. **Right** – Same as left panel, zoomed in to show the higher frequencies.

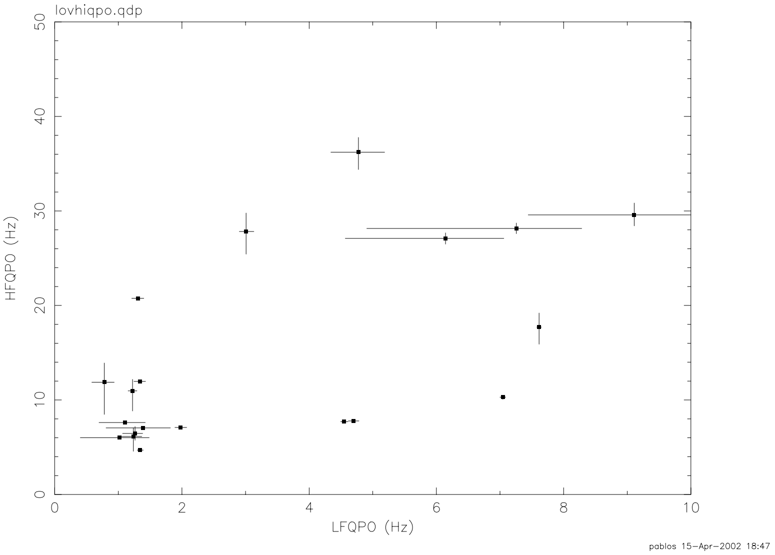

Figure 4.14: High frequency QPO vs. low frequency QPO

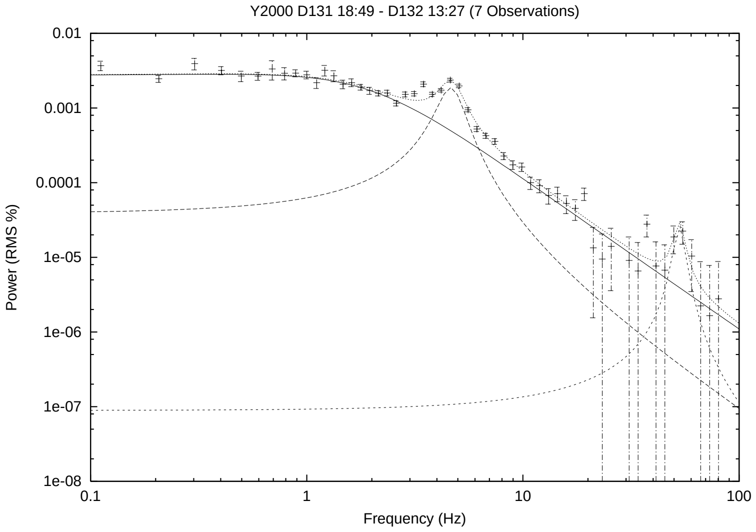

Figure 4.15: Combined power spectrum of 7 USA observations taken between Y2000 D131 18:49 and D132 13:27. The centroid frequencies of the three Lorentzians are: $0.38^{+0.12}_{-0.13}$, $4.64^{+0.04}_{-0.04}$, and $52.94^{+2.84}_{-1.16}$ Hz.

several observations to see this. Figure 4.16 shows the energy dependence of the low frequency (∼5Hz) QPO shown in Figure 4.15. It is now clear that the strength of the QPO increases with energy.

Finally, I looked at how the power spectra of Cir X-1 changes along the different parts of the color-color diagram (S locations in Figure 4.6), by combining all the observations contained in the different S locations and computing their power spectra (Figure 4.17). The shape of the power spectrum clearly changes. The QPO found at ∼5 Hz becomes weaker as S increases, to the point where it is no longer present after S=3.

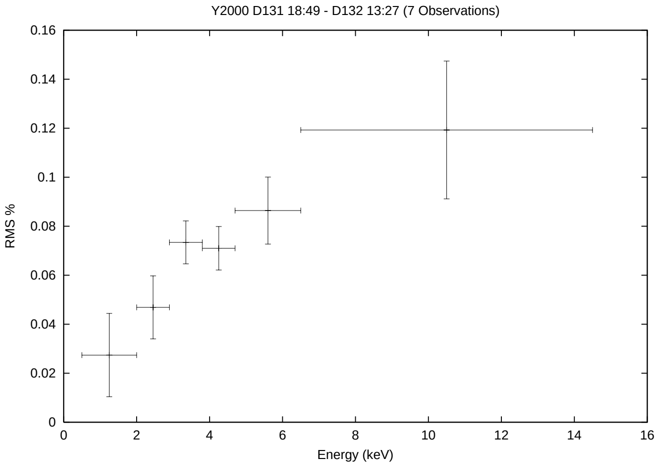

Figure 4.16: Energy dependence of the QPO rms variability

4.2.4 A Comparison of Circinus X-1 with other Sources

In order to shed some light on the nature of Cir X-1, I have compared both its spectral and timing properties to those of other, better understood sources. The sources I have chosen for comparison are the BHC Cyg X-1 and the bright Z sources Cyg X-2, GX 340+0, and GX 349+2. I analyzed ∼10.5 ks of Cyg X-1 data, ∼18.5 ks of Cyg X-2 data, ∼22 ks of GX 340+0, and ∼50 ks of GX 349+2 data, all of it from USA. All the data I analyzed were taken in mode 2, at the same resolution as the Cir X-1 data, and in the ascending node of the orbit to ensure the instrumental differences were kept to a minimum (see Chapter 2 for a description of the different energy calibrations needed in USA).

I compared the spectral evolution of these sources by looking at the 'model-independent' color-color diagrams, that is, by computing ratios of counts in different detector channels (after subtracting for the background). This allows a direct comparison (without spectral fitting) of the behavior of these different sources. I chose the same bands as for the Cir X-1 color-color diagram: 2.0–3.8 keV, 3.8–5.6 keV, 5.6–8.3 keV, and 8.3–11.0 keV.

Cyg X-1 is probably the best understood persistent BHC (most BHCs are X-ray transients). Although its mass function is only 0.25 $M_\odot$, the most probable mass

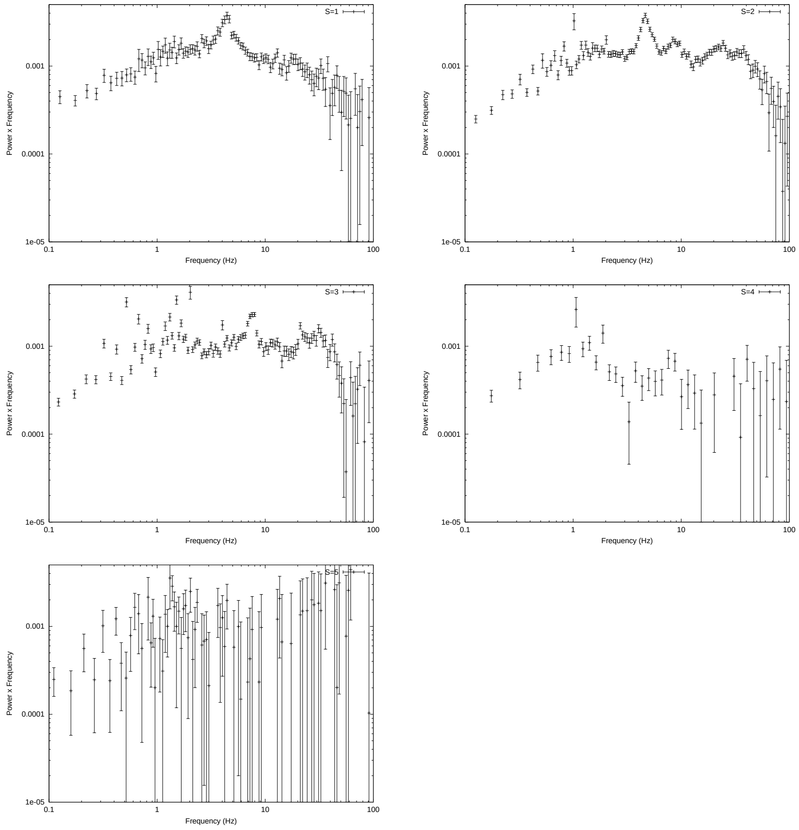

Figure 4.17: Timing evolution along of Cir X-1 along the color-color diagram. Plots show the power spectra (plotted in units of Power × Frequency vs Frequency) for the combined observations in the different locations of the color-color diagram in Figure 4.6, with S=1 at top left and S=5 at bottom left.

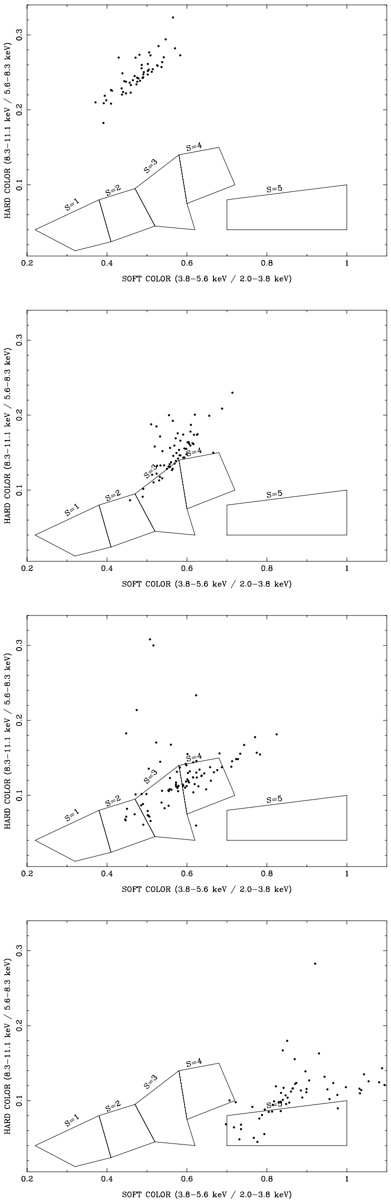

Figure 4.18: Model independent color-color diagrams of (from top to bottom) Cyg X-1, Cyg X-2, GX 349+2, and GX340+0

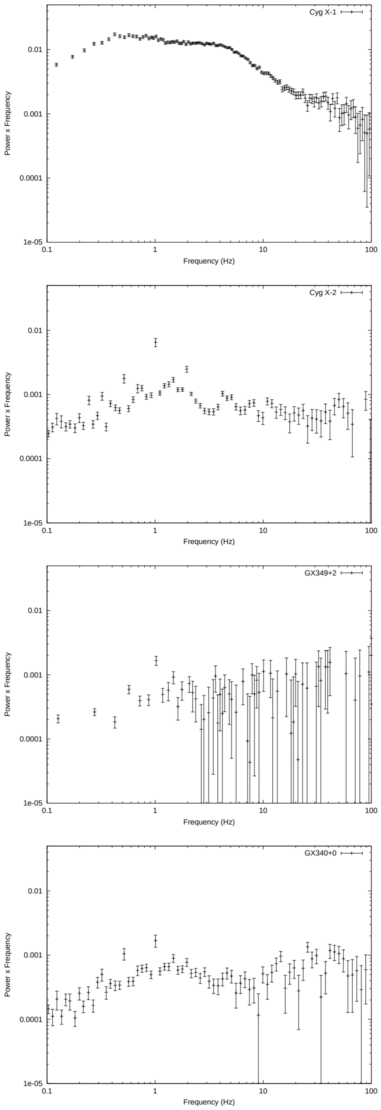

Figure 4.19: Power spectra of (from top to bottom) Cyg X-1, Cyg X-2, GX 349+2, and GX340+0

estimates range from 16 $M_\odot$ (Gies and Bolton 1986) to a more recent 10.1 $M_\odot$ (Herrero et al. 1995). The 6 Z-sources (der Klis 2000) are bright neutron star LMXBs which are sometimes subdivided into 'Cyg-like' (Cyg X-2, GX 340+0, GX 5-1) and 'Sco-like' (Sco X-1, GX 349+2, GX 17+2), and it is believed that the observational differences between them can be attributed, at least in part, to the higher inclination of the Cyg-like sources (Kuulkers et al. 1994). I chose to look at sources from each of these categories.

Figure 4.18 shows the color-color diagrams of the four sources I am comparing. Plotted over their color-color diagrams are the S segments from the Cir X-1 color-color diagram. The most obvious difference between all these sources and Cir X-1 is that none of them reach the softest region of the color-color diagram (S=1). Figure 4.19 shows their respective power spectra, displayed in units of power times frequency, giving a better sense of how the power is distributed over the Fourier spectrum. None of the power spectra of these three neutron stars show the break that can be seen in the Cir X-1 power spectrum in the softest state (S=1), a break which is very similar to that observed in the power spectrum of Cyg X-1.

Characteristic Frequencies of Cyg X-1 and Cir X-1

In Figure 4.20, I compare the PDS of Cir X-1 in its 'high/soft' state (S=1) with that of Cyg X-1. For GX 349+2 and GX 340+0 I also chose those observations which had the 'softest' color (A soft color of less than 0.85 for GX 340+0 and less than 0.55 for GX 349+2). For Cyg X-1 and Cyg X-2 I used all the data shown in the color-color diagrams.

The power spectra are in units of Power × Frequency. In Figure 4.20 I plot the PDS of Cyg X-1 scaled by 3.8 in Frequency and by 0.1 in Power.

The PDS of Cyg X-1 is a doubly broken power-law. The power spectrum is flat below $\nu \sim 0.37$ where it shows its first characteristic break frequency. Between the frequencies of 0.37–3.4 Hz it is a power-law approximately $\alpha f^{-1.1}$. At frequencies higher than $\sim$3.4 the power-law steepens to approximately $\alpha f^{-2.0}$. The power spectrum of Cyg X-1 has been scaled by a factor of 3.8 to make both break frequencies coincide with those in Cir X-1.

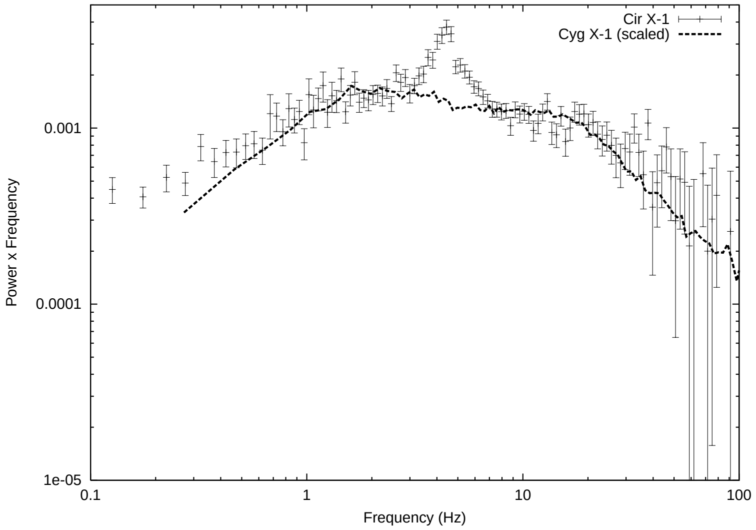

Figure 4.20: Power Density Spectrum of Cir X-1 (in units of Power × Frequency). Plotted over it is the PDS of Cyg X-1 scaled by a factor of 3.8 in frequency and 0.1 in Power

4.2.5 Possible Detection of Sub-ms Bursts in Cir X-1

Finally, I report the possible discovery of sub-ms bursts in Cir X-1. A search through all Cir X-1 observations yielded six of these burst-like events. These bursts could represent sub-ms variability coming from the source, but could also be due to some other factors, either environmental or electronic. My preliminary studies show that the bursts are very soft, with the majority of the photons coming from the lowest two channels in USA. Five of the six bursts occur within the same orbital cycle of Cir X-1, with two occuring in the same observation.

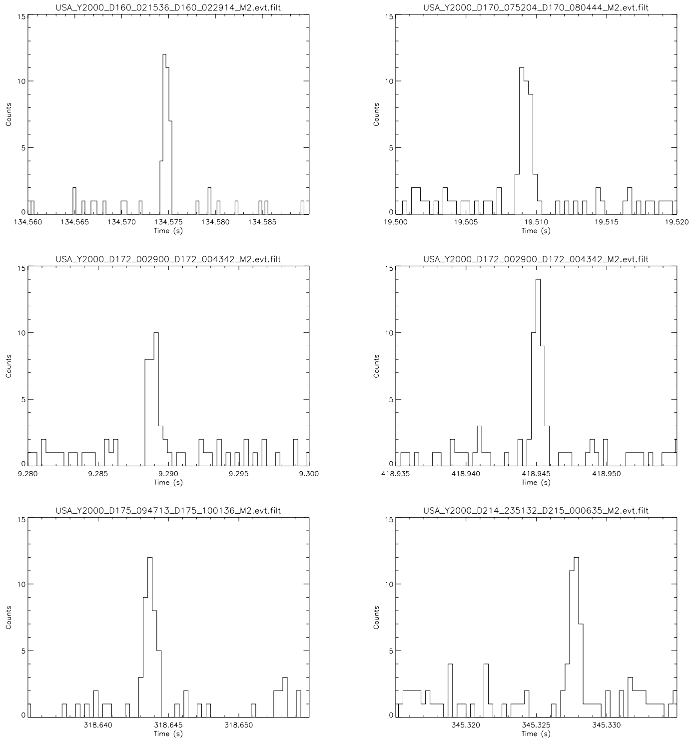

Figure 4.21: Possible detection of sub-ms variability in Cir X-1. The five observations (Day 172 contains two bursts) are ∼500–650 s long and have mean rates and standard deviations of (chronologically): $660 \pm 69\,\mathrm{cts\,s^{-1}}$, $2458 \pm 229\,\mathrm{cts\,s^{-1}}$, $2129 \pm 293\,\mathrm{cts\,s^{-1}}$, $1751 \pm 136\,\mathrm{cts\,s^{-1}}$, and $3257 \pm 360\,\mathrm{cts\,s^{-1}}$. The light curves are binned in $320\,\mu$s bins.

4.3 Discussion

4.3.1 Light Curve and Energy Spectrum

I have shown that the Cir X-1 light curve can be modeled as a disk-diffusion process, following the model of Wood et al. (2001). In this model, blobs of matter are believed to be periodically injected into the outer disk at each periastron passage and then diffuse in with a timescale which is comparable to the orbital period of the system. The fact that this diffusion process might be slower than the orbital period could be the reason why the source always maintains a relatively bright level, even at quiescence. By fitting the folded light curves of Cir X-1 during the entire 6.5 year RXTE era, I find that the viscous timescale is not constant, and in fact can vary by a factor of ∼3. The viscous timescale and the quiescent level are probably related, but a simple linear correlation was found not to accurately describe the data. As the viscous timescale increases, more material should, in theory, be left in the disk so that as the next periastron passage comes along the source should be brighter.

The color-color diagrams show clearly that the spectral evolution of the source is directly related to its orbital evolution. Cir X-1 follows a path on the color-color diagram which takes it from a high/soft state to a low/hard state. This can also be observed in the hardness-intensity diagram (Figure 4.7).

By performing spectral fits on the Cir X-1 data, I found that its spectra can be adequately described by a two-component model in which a soft component is caused by the accretion disk, while a harder component is due to Comptonization, probably taking place in the boundary layer of the neutron star, though a hot corona is also a possibility. There is a clear evolution along the path on the color-color diagram and the physical parameters along this path are explored. Figure 4.8 shows how the disk slowly decreases in its importance as the source progresses along the path S (which correlates with orbital phase). The temperature of the disk, as can be seen from Figure 4.9 is consistent with a constant. The temperature of the Comptonizing medium, however, when taken only for points S=1 through S=4 can be ruled out to be consistent with a constant at the 95% level, and is better fit by a linear model in which the temperature increases as the source moves along the S. As the source evolves along the color-color path (or the orbit), the contribution from the disk is found to decrease in importance. This could be an indication that, although the temperature of the disk is not changing, the disk is being depleted, thereby reducing its surface area. As the neutron star swings by again at periastron, the disk could be replenished, making it once again the dominant component. Figure 4.11 shows how the inner radius evolves along the 'S' path and reinforces the idea that the disk is being depleted. The inner radius moves in as the disk is consumed, getting closer to the neutron star surface. For a Newtonian case, one would expect roughly half the flux to be coming from the disk. However, for the case of Cir X-1, it appears that for most of the orbit, the disk flux is several times that of the boundary layer flux. If this emission is coming from a boundary layer on a neutron star, this would indicate that the neutron star could be spinning very fast (faster than 1 kHz) (Sibgatullin and Sunyaev 2000a; Sibgatullin and Sunyaev 2000b).

The color-color diagrams in Figure 4.6 and 4.18 show that Cir X-1 reaches a region (S=1) that none of the other three neutron stars we looked at reach. In addition, while Cir X-1 and Cyg X-1 reach 'soft color' values of less than 0.3, the other three neutron stars we observed always have values higher than 0.4. This 'softest' region corresponds to the region where Cir X-1 is most luminous and it is in this region that the power spectrum of Cir X-1 most resembles that of Cyg X-1. It is possible that in the early phases of the orbit, as the source goes through its periastron, Cir X-1 is accreting so much matter onto it (making it very luminous), that Compton cooling becomes significant. As the source evolves around its orbit, as mentioned above, the disk is being consumed, diminishing in surface area (hence luminosity) and the boundary layer is becoming more significant.

4.3.2 Power Spectra and QPOs

The power spectra of Cir X-1 analyzed in this dissertation show *Quasi Periodic Oscillations* (QPOs) from ~1 Hz to ~50 Hz. It is interesting to note that while the six well known Z sources all display kHz QPOs, Cir X-1 has shown no kHz QPO at present (though this might be explained by heavy absorption around the source). The highest frequency QPOs detected by USA were around 50 Hz, though USA is limited by the Energy Dependent Instrumental Effect (EDIE) in the high-frequency (> 100 Hz) regime (see Section C.2 in the Appendix), which could explain why none were detected. The origin of QPOs is still hotly debated. Figure 4.22 shows a $\sim$5 Hz QPO found in Cir X-1, shown in the time domain. The top curve is constructed by taking the elapsed time between 100 contiguous photons to compute an instantaneous rate, and then sliding through each of the individual photons. The bottom curve is a 10 ms binned light curve. As shown in these two figures, QPOs can be thought of as finite trains of oscillations of slightly varying period.

One simple interpretation for these QPOs would have them arising from temperature or density inhomogeneities at some particular radius in the disk. The observed increase in the frequency of the QPO could then be interpreted as the disk moving in (maybe as it is being consumed), leading to the increase in frequency. The different frequencies observed could simply correspond to different radii in the disk which are being excited by some mechanism. The energy dependence of the QPO RMS variability, however, as seen in Figure 4.16 seems to contradict this naive interpretation. As the energy increases, the 'strength' of the QPO increases too, making it much more relevant in the energy range corresponding to the Comptonizing component than in the energies corresponding to the disk.

This interpretation is also called into question by recent correlations found between the different frequency QPOs, which I will describe in the following paragraphs.

There are many models for producing QPO, most of which aim to tell us something fundamental about the system (such as mass or spin). Diskoseismology, for example (Perez et al. 1997; Silbergleit et al. 2001; Ortega-Rodríguez et al. 2002), describes the QPOs as trapped GR modes of oscillation in an accretion disk. There are different modes which can be produced in the disk depending on the restoring force one invokes, but all of these frequencies share the property that they lie close to the innermost stable circular orbit (ISCO) and are therefore are at higher frequencies than the ones observed in Cir X-1. These QPOs are also expected to exist at a fixed frequency, such as in certain objects like GRS 1915.

Other models for QPO generation include the so-called Beat-Frequency models,

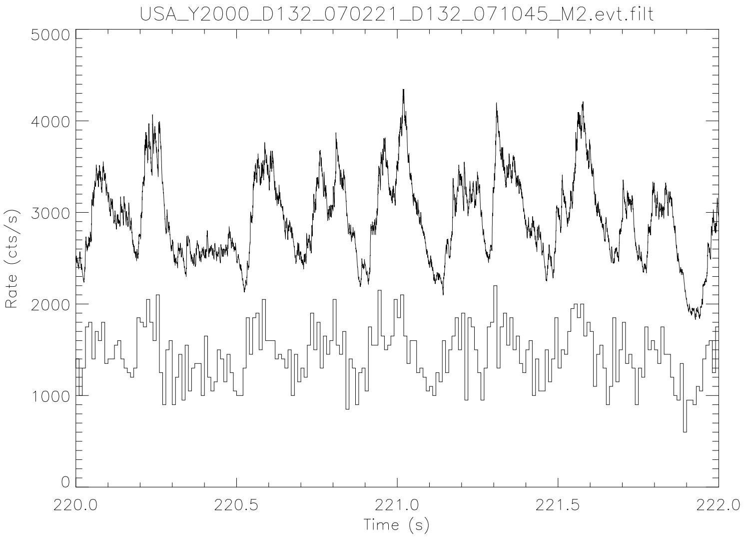

Figure 4.22: A QPO in the time domain. Top curve represents an instantaneous rate for each photon, computed by taking the 100 nearest photons and dividing by the time elapsed between the first and last. Bottom curve is binned in 10 ms and scaled by 50, for ease of viewing. Both figures show the QPO present in the observation as a modulation in the light curve at ∼5 Hz.

as described, for example, by Argue et al. (1984, Lamb et al. (1985), or Miller et al. (1998) and the Relativistic Precession models (e.g. Stella and Vietri (1998), Stella and Vietri (1999)).

In the last several years, an interesting correlation has been found between frequencies occurring in neutron stars and black holes (Wijnands and van der Klis 1999; Belloni et al. 2002). The choice of which frequencies to use for this correlation are not always clear; nevertheless, recently white dwarfs were also added to this correlation (Mauche 2002), expanding it by several decades in frequency and raising the possibility that all these frequencies are generated by a common mechanism. Figure 4.23 (taken from Mauche (2002)) shows that these two frequencies (ν_{low} and ν_{high} are related by a simple proportionality: $\nu_{low} = 0.08\nu_{high}$.

Indeed, Cir X-1 also sometimes follows this correlation. In Figure 4.15, for example, I fit the power spectra with three Lorentzians, with centroid frequencies equal to $0.38^{+0.12}_{-0.13}$, $4.64^{+0.04}_{-0.04}$, and $52.94^{+2.84}_{-1.16}$ Hz, with the ratio of the two lowest equal to 0.08 (the ratio of the two higher frequencies is also close to 0.08). Nevertheless, when looking at all the observations containing more than one QPO (Figure 4.14) the correlation is not present, although as mentioned previously, this could be due to insufficient statistics in individual observations of multiple QPOs. Figure 4.15 was obtained by adding 7 observations together, thereby significantly increasing the statistics.

There are many implications of this correlation. Firstly, it appears to imply that both the high frequency QPOs and the low frequency QPOs are related, and therefore one should not simply think of the low frequency QPOs as happening somewhere further out in the disk and the high frequency happening somewhere further in (this was also indicated by the energy dependence of the QPO RMS). In addition, if both QPOs are created by the same mechanism, both must reflect the properties of the system as a whole. This means that we can hope to learn something about the properties of the compact object by studying not only the high frequency (up to KHz) QPOs, but also by studying these lower frequency QPOs.

A further consequence of this correlation, as stated by Mauche (2002), is that it would seem to exclude both the relativistic precession model and the magnetospheric

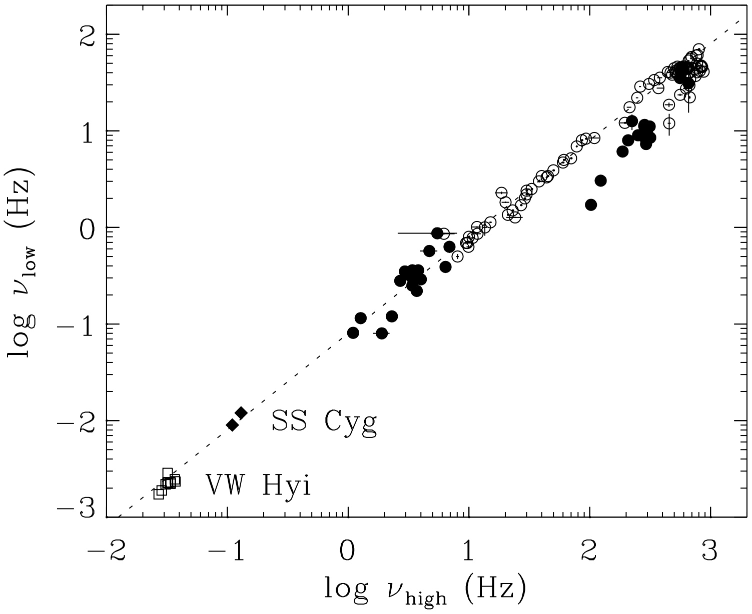

Figure 4.23: QPO relationship (Mauche 2002)

and sonic-point beat-frequency models of QPOs, along with any other model which would require the presence or absence of a stellar surface or magnetic field.

This still leaves several models of QPOs which would not be excluded by this new result. One of them is the Acoustic Oscillation Model (AOM) in which QPOs are generated by acoustic oscillations of a Transition Layer (TL) at the inner boundary of the accretion disk (see Reilly (2003) for a detailed description of this model, as well as its application to the BHC XTEJ 1550).

Another model which has received a lot less attention and which is also not excluded by this correlation is the so-called 'Dripping handrail' (DHR) model (Scargle et al. 1993; Steiman-Cameron et al. 1994; Young and Scargle 1996). This model was used to explain both the Very Low Frequency Noise (VLFN) and the QPOs observed in Sco X-1 (Scargle et al. 1993), as well as the QPOs observed in the so-called AM Her objects, a subclass of the white dwarf binary systems known as Cataclysmic Variables (CVs).

In the DHR model, both QPOs and the VLFN are different aspects of the same physical process, which is the random accretion of 'blobs' of matter of a wide range of sizes. The 'rail', in this picture, could be the inner edge of the disk. This inner edge is supported in such a way that matter (blobs) diffuses on the rail tangentially. A density threshold determines when the blob of matter falls off the rail and onto the star (like drops of water condensation dripping off a rail). Three parameters are therefore important in this model: the threshold density, the accretion rate, and the diffusion coefficient. In fact, the last two parameters can be thought of as one by looking simply at the ratio of accretion to diffusion (Young and Scargle 1996).

In this model, QPOs would thus not be a function of the compact object, nor a property of strong gravity, but merely a manifestation of *transient chaos*. Accretion and diffusion are in competition in this model, and for a given ratio of these two, QPOs will arise naturally. The frequency of the QPOs can be thought of as a rate at which blobs are 'filling up' and falling off the rail. In the case of Cir X-1, the increase in frequency could be interpreted to mean that the matter which had been deposited on the outer disk had diffused in and was causing an increased rate of accretion at the inner disk, where the blobs are forming. One drawback of this model, however, is that in its current incarnation it says nothing about the energy dependence of the QPOs.

4.3.3 Comparison with other Sources

The major difference between neutron stars and black holes is the absence of both a solid surface and a co-rotating magnetosphere in the case of black holes. Far away from the compact object, the observable differences between a black hole and a neutron star are not easily discernible. Both have similar accretion disks around them given their relatively similar gravitational potentials. Closer to the compact object, however, there should be detectable differences arising from the fact that neutron stars have a surface as well as from the absence of magnetospheres in the black hole. The neutron star surface, for example, allows a boundary layer to be formed, whereas none could be formed in the black hole.

Most black holes show a rapid decline in power at frequencies higher than several tens of hertz. Of the sources I looked at, the only ones that show this decline are Cyg X-1 and Cir X-1. The other three neutron star sources show a flat spectrum (in units of power times frequency) up to 100 Hz. It is believed that the high frequency variability associated with neutron stars is related to the boundary layer which forms on the surface of the neutron star (Sunyaev and Revnivtsev 2000). Since the black hole has no surface, and therefore no boundary layer, the highest possible frequencies will be those associated with the last stable orbit. This frequency is known to scale like M^{-1} (Sunyaev and Revnivtsev 2000).

The break frequencies in Cyg X-1 are not well understood, just like the correlation between low and high frequency QPOs is not well understood either. However, assuming that these break frequencies are related to the mass of the compact object, it is reasonable to assume that it should scale inversely proportionately with the mass. By simple scaling of the break frequencies of Cir X-1 (around 1 Hz and 20 Hz) to match those of Cyg X-1 (.5 and 5 Hz respectively), we would obtain a mass of Cir X-1 approximately four times smaller than Cyg X-1, that is, a mass in the range 2.5-4 $M_\odot$. This is an interesting range, since no neutron stars are currently known to have a mass greater than 2 $M_\odot$ (Thorsett and Chakrabarty 1999). See Figure 4.24 (from Orosz (2002)). Figure 4.20 shows the spectrum of Cyg X-1 scaled in order to make the two break frequencies in Cyg X-1 coincide with those in Cir X-1.

4.3.4 Sub-ms Bursts from Cir X-1

In Figure 4.21 I show 6 bursts which were detected in the Cir X-1 data. The light curves in these figures are binned in 320 μs (i.e. the variability observed is faster than 1 ms). Most of the bursts show an excess of counts in 4–6 bins, making the duration of these bursts extremely short ($\lesssim$ 2ms), and containing only $\sim$30 photons, most falling in channels 0 and 1. Interestingly, the first 5 bursts fall within the same orbital cycle of Cir X-1, with two of the bursts falling in one observation. More work needs to be done to confirm that these bursts are really coming from Cir X-1, and not from somewhere else (such as the atmosphere or soft electrons), or are even caused by some unknown instrumental effect. However, if real, these bursts present evidence

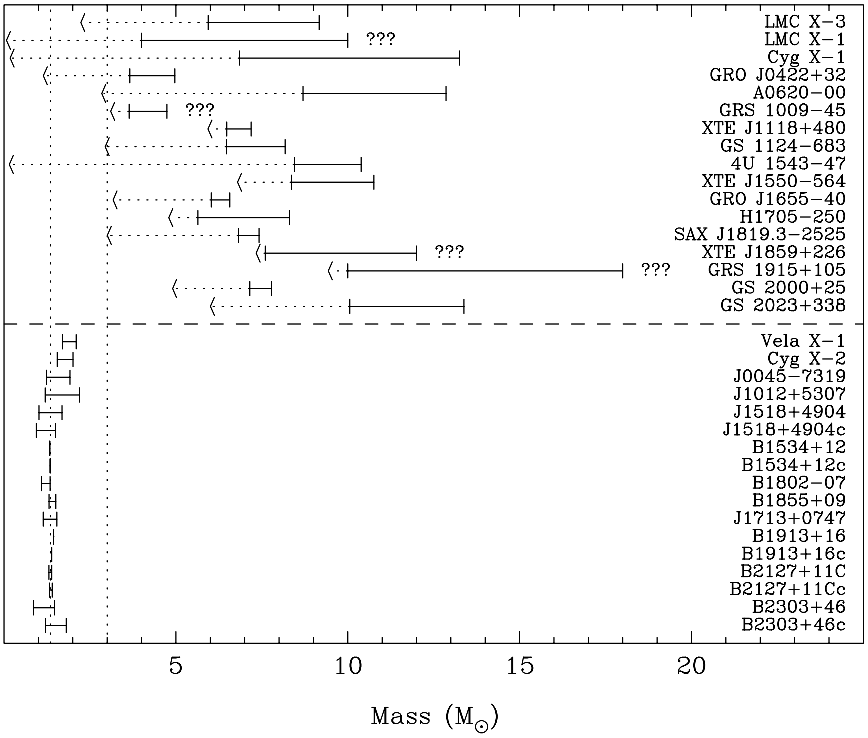

Figure 4.24: Summary of black hole masses (top, Orosz (2002)) and selected neutron star masses (bottom, Thorsett and Chakrabarty (1999)). The ranges are 1σ in most cases. The arrows in the top indicate the measured mass functions.

that Cir X-1 has variability at timescales much faster than previously reported.

4.4 Conclusions

I have analyzed the spectral and timing evolution of Cir X-1 along its 16.6 day orbit and shown that the spectral properties of the source correlate both with orbital phase and intensity. I have modeled the light curve as a diffusion process in which matter is deposited periodically at the outer disk and diffuses in, causing the FRED light curve.

The Energy Spectrum can be well modeled by two components: a multicolor disk which remains at roughly constant temperature, and a Comptonized component which could be coming from a boundary layer on the surface of the neutron star (or a hot corona). The Comptonized component appears to increase in temperature as the object moves around the orbit. The disk component dominates heavily but the Comptonized component gains in importance as the system progresses around its orbit. This could be the result of the accretion disk being consumed and then replenished at every periastron passage. The inner radius of the disk is also found to move in as the source evolves around its orbit, further reinforcing this hypothesis.

Numerous QPOs were detected ranging in frequency from a few Hz to approximately 50 Hz. These QPOs generally increase in frequency within an individual orbital cycle. The higher frequency QPOs (>20 Hz) show a decrease in 'strength' with increasing frequency. The evolution of the Comptonizing component (increasing temperature along the orbital cycle) as well as the energy dependence of the RMS variability of these low frequency QPOs (increasing with energy and peaking well outside the energy range of the accretion disk) appear to imply that the origin of these QPOs is not in the disk, but rather in the higher energy Comptonizing component. In the AOM model, QPOs are related to the hot Comptonizing medium. This model is also not ruled out by the recent correlations between high and low frequency QPOs discussed in the previous section. This makes the AOM a promising candidate for explaining QPOs. In the DHR model, QPOs would originate from blobs falling off the inner edge of the disk and the increase in frequency could imply an increase in the accretion rate at the inner radius as the inner radius shrinks and more matter diffuses in from the outer disk which is being consumed.

Cir X-1 is a highly variable source which at its most luminous (softest) appears to display properties more similar to black holes than to neutron stars. I have compared the color-color diagram and power density spectrum to those of better studied sources such as Cyg X-1, Cyg X-2, GX 340+0, and GX 349+2. Whereas the Cyg X-2, GX 340+0, and GX 349+2 all show a flat power spectrum up to 100 Hz, Cyg X-1 shows a significant drop-off at 5 Hz and Cir X-1 shows one at 20 Hz. None of the other neutron stars reach the 'S=1' region of the color-color diagram that Cir X-1 reaches. By scaling the break frequencies observed in Cyg X-1 to match those in Cir X-1 and assuming these frequencies scale inversely with mass Cir X-1 is postulated to be in the 2.5-4 $M_\odot$ range, based on the best current mass estimates for Cyg X-1.

Finally, I tentatively report the detection of six sub-ms bursts. The very short timescales of these bursts would make them extremely interesting but further analysis is required to verify their true origin.

Chapter 5

Long-term X-ray variability of Circinus X-1[1]

Not just a fad 'cause it's been going on so long.
Beach Boys, "Catch a wave" (1963)

5.1 Introduction

In this chapter I present an analysis of long-term X-ray monitoring observations of Cir X-1 made with four different instruments: Vela 5B, Ariel V ASM, Ginga ASM, and RXTE ASM, over the course of more than 30 years. I use Lomb-Scargle periodograms to search for the ~16.5 day orbital period of Cir X-1 in each of these data sets and from this derive a new orbital ephemeris based solely on X-ray measurements, which I compare to the previous ephemerides obtained from radio observations. I also use the Phase Dispersion Minimization (PDM) technique, as well as FFT analysis, to verify the periods obtained from periodograms. I obtain dynamic periodograms (both Lomb-Scargle and PDM) of Cir X-1 during the RXTE era, showing the period evolution of Cir X-1, and also displaying some unexplained discrete jumps in the

---

[1] The content of this chapter is a slightly modified version of an article to appear in the September 20, 2003 issue of The Astrophysical Journal.

location of the peak power. Finally, I find evidence for a possible ∼335 day period in the RXTE ASM data, which I tentatively conclude is due to the precession of an accretion disk. Cir X-1 thus joins the growing list of sources which now display so-called 'super-orbital' periods.

5.2 Observations

I used a series of observations taken by four different instruments over the course of the last ∼33 years. I chose those instruments which had an All Sky Monitor (ASM) which allowed us to study the long-term behavior of the source. Figure 5.1 shows the composite light curve obtained by incorporating all the observations by the different instruments into one single plot. All the data have been normalized to the Crab. Included in this plot are the EXOSAT observations which displayed the Type I X-ray bursts to illustrate what the flux level of the source was at the time, though in this chapter I do not analyze the EXOSAT data. Figure 5.2 shows the light curves obtained by the four ASM instruments, individually plotted for greater clarity. In the short paragraphs that follow I briefly describe the four instruments for which data was analyzed in this chapter.

5.2.1 Vela 5B

The Vela 5B satellite (Conner et al. 1969) was placed in orbit on 1969 May 23 and operated until 1979 June 19, although telemetry tracking was poor after mid-1976. The X-ray detector covered the celestial sphere twice per orbit and had an effective area of 26 cm^2, with an energy range of 3–12 keV. In this analysis I use 485 observations of Cir X-1 made between MJD 40368 and MJD 42692.

5.2.2 Ariel V

Ariel V was launched on 1974 October 15 and operated until 1980 March 14. The ASM experiment (Holt 1976) consisted of two small X-ray pinhole cameras with an effective area of ∼1 cm^2 and an energy range of 3–6 keV. In this chapter, I look at 1173 observations of Cir X-1 made between MJD 42345 and MJD 42692.

5.2.3 Ginga ASM

The Ginga observatory was launched on 1987 February 5 and reentered the Earth's atmosphere on 1991 November 1. The ASM instrument (Tsunemi et al. 1989) consisted of two proportional counters operating in the 1–20 keV energy range, covered by six different collimators, each with a field of view of roughly $1^\circ \times 45^\circ$ (FWHM) and an effective area of ∼70 cm^2 (for a total effective area of ∼420 cm^2). For more details of the Ginga ASM see Tsunemi et al. (1989). In this chapter, I analyze 300 observations of Cir X-1 taken between the dates of MJD 46855 and MJD 48532.

5.2.4 RXTE ASM

The Rossi X-ray Timing Explorer (RXTE) (Bradt et al. 1993), was launched on 1995 December 30. The ASM instrument (Levine et al. 1996) consists of 3 Scanning Shadow Cameras (SSCs) with a total effective area of 90 cm^2 and a sensitivity to 1.5–10 keV X-rays in three energy channels (roughly corresponding to 1.5–3, 3–5, and 5–12 keV). Both individual "dwell" by "dwell" (where a "dwell" refers to a 90 s observation) and one-day average measurements are made available by the ASM/RXTE team via their website. The data analyzed here spanned the dates MJD 50088 (6 January 1996) through MJD 52536 (19 September 2002) and consisted of 1972 daily-averaged measurements.

5.3 Data Analysis and Results

I computed the Lomb-Scargle periodograms (Scargle 1982) of the four different data sets. These are shown in Figure 5.3. A fiducial period of 16.6 days is shown on each plot with dashed lines, for comparison between the different epochs. I found peaks in the periodograms of the Vela 5B data (16.69 ± 0.015 days), Ariel V (16.66 ± 0.01 days), Ginga ASM (16.577 ± 0.001 days), and RXTE ASM (16.5427 ± 0.0001 days).

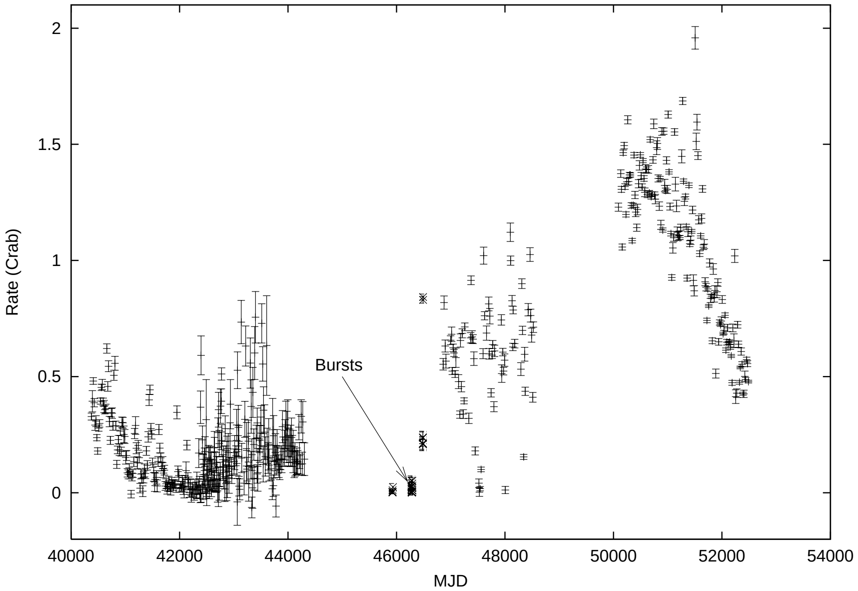

Figure 5.1: Long-term Light Curve of Cir X-1. Fluxes have been normalized to the Crab. The figure includes data (in chronological order) from Vela 5B, Ariel V ASM, EXOSAT, Ginga ASM, and RXTE ASM. The arrow points to the EXOSAT observations which displayed Type I X-ray bursts.

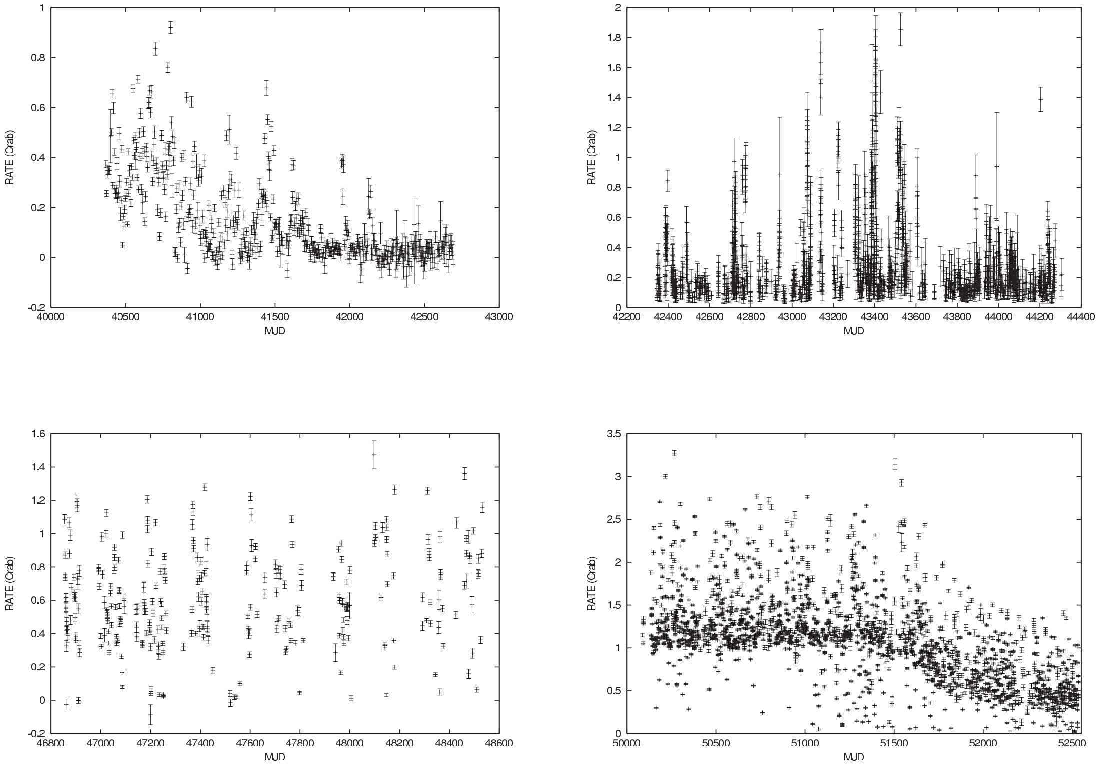

Figure 5.2: Individual light curves of Cir X-1 obtained by various instruments. Fluxes have been normalized to the Crab. **Top Left** – Vela 5B (26 May 1969 - 7 October 1975). **Top Right** – Ariel V ASM (25 October 1974 – 8 March 1980). **Bottom Left** – Ginga ASM (1 March 1987 – 2 October 1991). **Bottom Right** – RXTE ASM (6 January 1996 – 19 September 2002).

I computed the uncertainty on the period through Monte Carlo simulations of 1000 light curves, assuming the errors on the counting rate have a gaussian distribution. After computing the periodograms of the 1000 light curves generated, I took the mean and standard deviation of the peak frequency.

I also used the Phase Dispersion Minimization (PDM) technique (Stellingwerf 1978) and compared the values obtained from this method with the periods obtained from the Lomb-Scargle periodograms. The results are shown in Figure 5.4: Vela 5B data (16.67 ± 0.01 days), Ariel V (16.644 ± 0.001 days), Ginga ASM (16.565 ± 0.004 days), and RXTE ASM (16.5421 ± 0.0001 days).

Finally, Fourier analysis was performed on each of the archival data sets to search for orbital periodicities[2]. A detailed review of Fourier analysis techniques in X-ray timing is given by van der Klis (1989). A time bin of 7 days for the Fast Fourier Transform (FFT) was chosen. This gives a Nyquist frequency of 8.267×10^{-7}, or a minimum period of 14.0 days. The analysis was performed by oversampling the FFT.This process creates an FFT with finer detail than a non-oversampled FFT. However, not all of the bins are independent. This method allows one to estimate the frequency of the maximum power in a power density spectrum (PDS) with greater accuracy. Middleditch (1976) shows that if the peak power in the signal occurs in frequency bin k (where k need not be an integer), then the best estimate of the signal frequency is given by

$$\hat{\nu}_0 = \nu_k + \frac{3}{4\pi^2 \epsilon T}\left(\frac{\bar{P}_{k+\epsilon} - \bar{P}_{k-\epsilon}}{\bar{P}_k}\right) \tag{5.1}$$

where $\bar{P}$ is normalized power, T is the length of the time series, and $n = 1/\epsilon$ is the oversampling factor. For this analysis I used $n = 8$. The uncertainty on the frequency determination is given by Equation 5.2 (Middleditch 1976).

$$\sigma_{\hat{\nu}_0} \approx \frac{1}{2\pi T}\sqrt{\frac{6}{P_k}} \tag{5.2}$$

The Vela, Ariel and Ginga data sets were each FFT'd as a single data set. The

---

[2] The period by FFT values in this section were obtained by Derek Tournear.

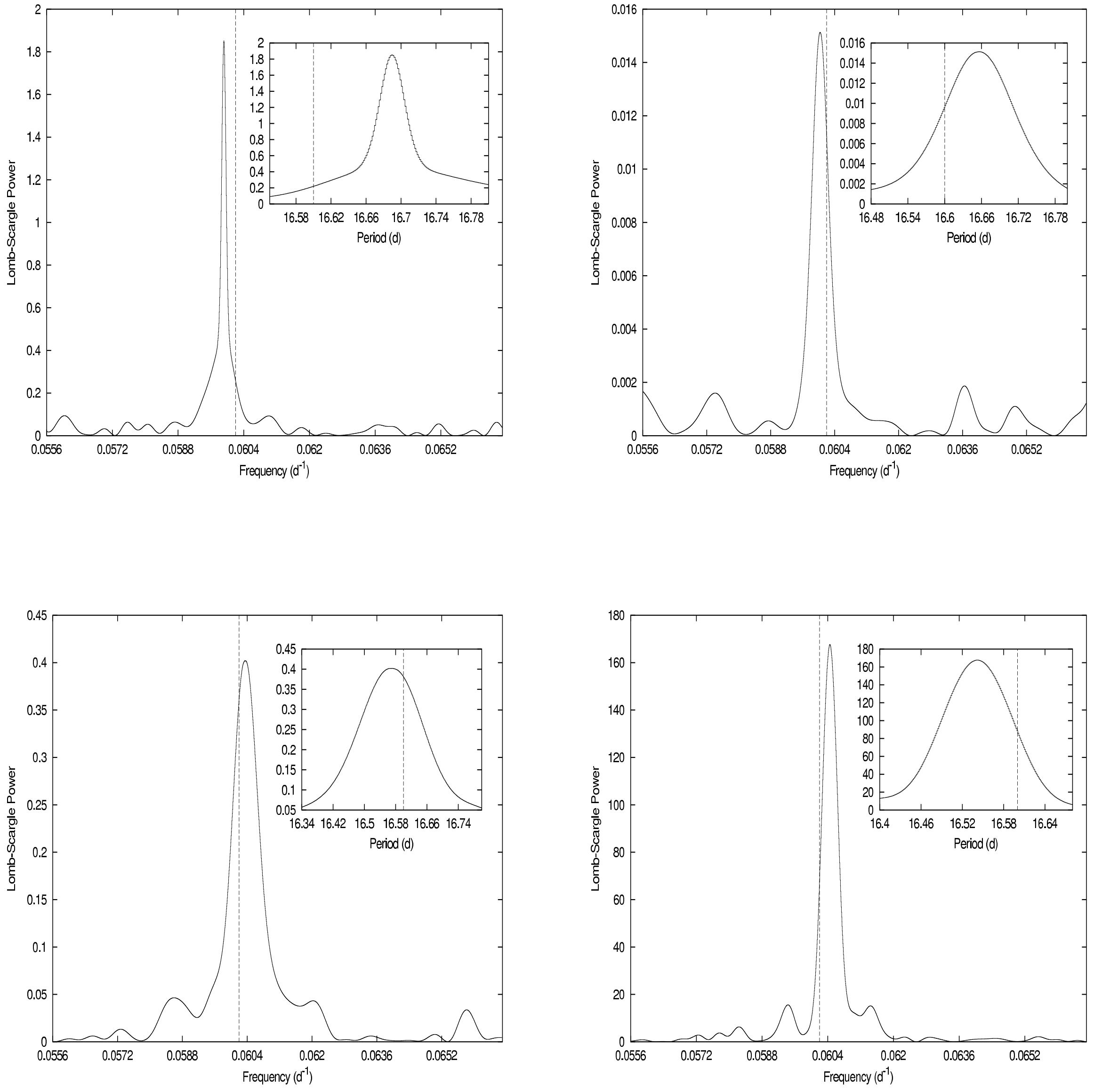

Figure 5.3: Lomb-Scargle periodograms of Cir X-1. The periodograms correspond to the data shown in the light curves in Figure 5.2. Inset plots show region around the orbital period in greater detail (with the x axis in units of time, for greater clarity). A fiducial period of 16.6 days is shown (with dashed lines) on each plot for comparison between epochs. **Top Left** – Vela 5B: Peak at 16.69 days. **Top Right** – Ariel V ASM: Peak at 16.66 days. **Bottom Left** – Ginga ASM: Peak at 16.57 days. **Bottom Right** – RXTE ASM: Peak at 16.54 days.

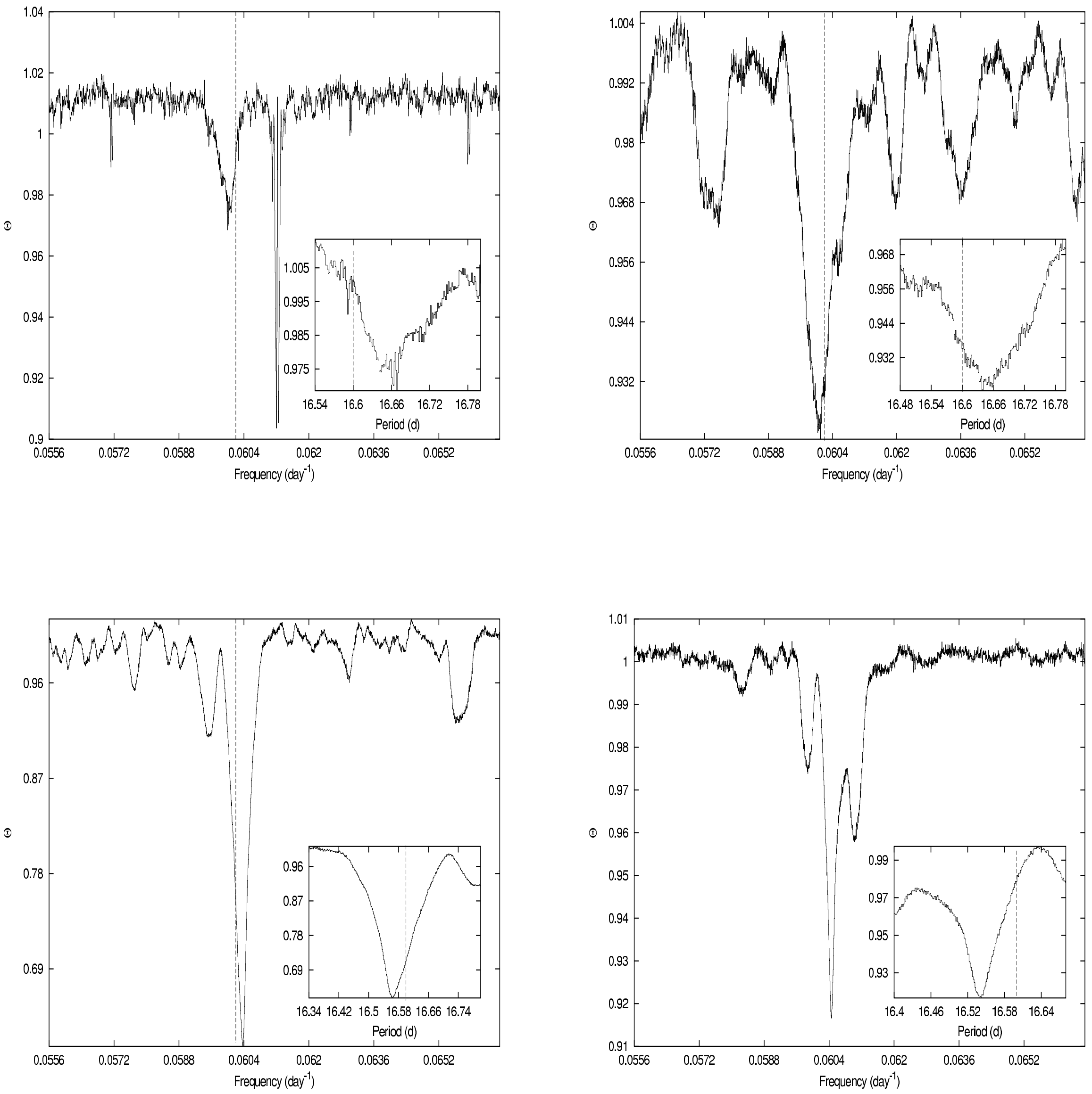

Figure 5.4: PDM periodograms of Cir X-1. The periodograms correspond to the data shown in the light curves in Figure 5.2. Inset plots show region around the orbital period in greater detail (with the x axis in units of time, for greater clarity). A fiducial period of 16.6 days is shown (with dashed lines) on each plot for comparison between epochs. **Top Left** – Vela 5B: Θ_{min} at 16.33 days, but a second prominent period is present at Θ=16.67 days. **Top Right** – Ariel V ASM: Θ_{min} at 16.64 days. **Bottom Left** – Ginga ASM: Θ_{min} at 16.56 days. **Bottom Right** – RXTE ASM: Θ_{min} at 16.54 days.

Experiment	Start MJD	Stop MJD	Period (days)	error
Vela	40367	42687	16.677	±0.028
Ariel	42345	44306	16.664	±0.029
Ginga	46855	48531	16.551	±0.028
RXTE ASM set 1	50088	50829	16.528	±0.063
RXTE ASM set 2	51575	52536	16.502	±0.019

Table 5.1: Period searching results from FFT analysis.

RXTE ASM data set, however, was split into two separate data sets. The first data set spans the dates MJD 50088 through 50829, while the second data set covers the dates from MJD 51575 to MJD 52536. The reason for splitting up the observations is that there is a span of almost two years during which the orbital modulation is not clearly detectable. Starting at around MJD 50830, the period (and power) of the peak intensity in the FFT starts to rapidly decrease until it becomes undetectable. While it reappears soon after MJD 52200, there are other unexplained phenomena in the spectra which prevent a good measurement of the period. I describe this in more detail in section 5.3.2. It is only after MJD 51575 that the orbital modulation once again becomes unambiguously detectable. Table 5.1 shows the details and results of the FFT analysis, which are also plotted in Figure 5.5).

I also used epoch folding techniques to determine the period, but the results were inconclusive. This was most likely due to the changing shape of the pulse profile (see for example Figure 5.8 for the change in pulse profile in the RXTE era).

5.3.1 X-ray Ephemeris

Several ephemerides have been published for Cir X-1 over the years. Figure 5.5 shows some of those most often cited in the literature. Nicolson (1980) published an ephemeris based on radio flares that took place between 1976–1980. This ephemeris gave the following equation for the onset of the Nth onset of flares (phase 0):

$\mathrm{MJD_N} = 43,076.26 + \mathrm{N}(16.588 - 1.66 \times 10^{-4}\mathrm{N})$, giving a $\dot{\mathrm{P}} = -2.00 \times 10^{-5}$ (labelled Nicolson 1980 in Figure 5.5). In the same IAUC, Nicolson reports that using the mean X-ray/radio period of 16.594 days derived for 1976–1977 he obtains the following ephemeris:

$\mathrm{MJD_N} = 43,076.26 + \mathrm{N}(16.594 - 2.5 \times 10^{-4}\mathrm{N})$, giving a $\dot{\mathrm{P}} = -3.01 \times 10^{-5}$ (labelled Nicolson 1980b in Figure 5.5)

A more recent ephemeris, also calculated by Nicolson, though reported by Stewart et al. (1991), was based on the onset times of radio flares observed between 1978 and 1988. This gives the following time for phase 0:

$\mathrm{MJD_N} = 43,076.37 + \mathrm{N}(16.5768 - 3.53 \times 10^{-5}\mathrm{N})$, which yields a $\dot{\mathrm{P}} = -4.26 \times 10^{-6}$ (labeled Stewart 1991 in Figure 5.5).

Figure 5.5 shows the different data points obtained by applying three different techniques to the four separate data sets. The individual Lomb-Scargle periodograms for each instrument are shown Figure 5.3. The PDM periodograms for each data set are shown in Figure 5.4. I also include in Figure 5.5 the points obtained by using an over sampled FFT (labelled 'Period by FFT').

I use all the measurements obtained from the various data sets and period-finding techniques to determine a best fit. I fit the period to the function:

$\mathrm{P} = \mathrm{P_0} + \dot{\mathrm{P}}(\mathrm{T} - \mathrm{T_0})$ where I use $\mathrm{T_0} = 43,076.37$. The best fit parameters are: $\mathrm{P_0} = 16.6534 \pm 5.6 \times 10^{-3}$ and $\dot{\mathrm{P}} = -1.6261 \times 10^{-5} \pm 1.109 \times 10^{-6}$. The function of best fit is also plotted in Figure 5.5 ($\mathrm{P} = 17.35 - 1.6352 \times 10^{-5}\mathrm{T}$, where T is time, in MJD). This $\dot{\mathrm{P}}$ results in a characteristic time scale of $\mathrm{P}/2\dot{\mathrm{P}}$ ∼1400 years, which is around a factor of ∼4 shorter than that obtained from the previous ephemeris (Stewart 1991).

I assume that the ephemeris is quadratic (i.e. constant $\dot{\mathrm{P}}$) and follows the equation (for small $\dot{\mathrm{P}}$):

$\mathrm{MJD_N} = \mathrm{MJD_0} + \mathrm{P_0}\mathrm{N} + \frac{1}{2}\mathrm{P_0}\dot{\mathrm{P}}\mathrm{N}^2$ where N is the cycle number and $\mathrm{MJD_N}$ is the Nth occurrence of phase 0. I use the same $\mathrm{MJD_0}$ as the previous ephemeris, which combined with the values of $\mathrm{P_0}$ and $\dot{\mathrm{P}}$ obtained from my fit yields the following ephemeris:

$\mathrm{MJD_0} = 43,076.37 + \mathrm{N}(16.6534 - 1.354 \times 10^{-4}\mathrm{N})$

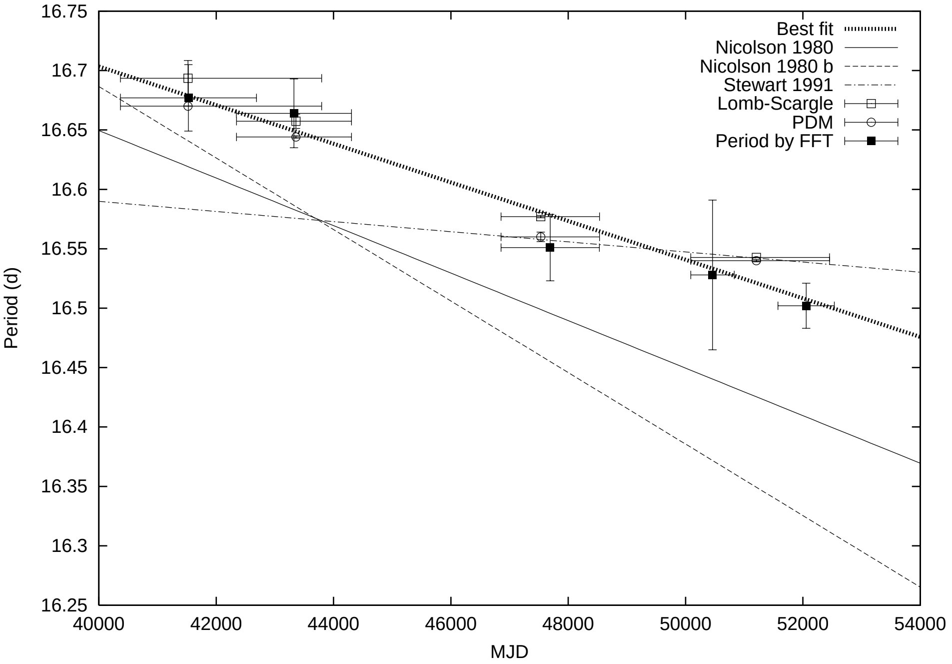

Figure 5.5: Evolution of the orbital period of Cir X-1. The data points represent the best estimate for the orbital period based on Lomb-Scargle periodograms of the Vela 5B, Ariel V ASM, Ginga ASM, and RXTE ASM data, as well as the PDM periodograms, and the FFT technique (period by FFT).

5.3.2 Dynamic Periodograms

Using the RXTE ASM daily averaged data, I performed 'dynamic' periodograms by selecting segments of data of length ~200 days and then stepping through the entire data set in increments of 20 days. Each periodogram was taken in the frequency range between 0.02 and 0.2 d^{-1} (5 to 50 day period). Although this involves an oversampling of the data, and therefore does not produce statistically independent periodograms, this technique nevertheless allows us to observe long-term trends in the time-frequency space which would otherwise not be so clearly visible. I tried several different values for the length of our periodogram, as well as for the step. While these parameters changed the resolution of the figure, the overall features and their time scales remained the same.

The left side of Figure 5.6 shows a dynamic Lomb-Scargle periodogram, while the plot on the right in the same figure shows a dynamic PDM periodogram. Both plots share many of the same features: the ~16.5 day orbital period is clearly visible in both, along with some harmonics (at 1/2 and 1/3 the orbital period). The PDM dynamic periodogram also shows several sub-harmonics (at 2 and 3 times the orbital period) which are picked out naturally by this period searching technique (Stellingwerf 1978) but do not represent real variability of the source. A key feature of both plots is the suppression of the 16.5 day peak starting at ~MJD 50830 and lasting for around 270 days, until ~MJD 51100. During this time, the most significant peak in both periodograms is centered at ~40 days.

To make sure that this feature is not an artifact of our periodogram technique, I look at its manifestation in the time domain by splitting up the RXTE ASM data into ten separate segments, each roughly of ~250 days in length. Figure 5.8 shows the different segments of data folded at the "orbital" period of 16.54 days. The profiles show that in the first several segments of data, the light curve is clearly modulated at the orbital period. However, the fourth segment (MJD 50839–51081) shows no sign of this modulation. Furthermore, when the fourth segment of data is folded at 40 days, instead of the 16.54, one can see the clear modulation of the light curve. Figure 5.9 shows this segment of data folded at 40 days. The inset plot shows the Lomb-Scargle periodogram for the same data, with a clear peak at 40 days (and no detectable peak at ∼16.5 days). To confirm these results, I took the 10 individual light curves shown in Figure 5.8 and folded them at a period of 40 days. As expected, only the fourth segment shows a significant modulation at this period, and none of the other nine show this modulation. There is an indication that the cessation of the X-ray periodicity could be related to the absorption dips seen in Cir X-1 before each flare. In the first three segments of Figure 5.8 (those immediately preceding the disappearance of the 16.5 day period), the absorption dips are very narrow and centered around phase 0. In the segments immediately following segment 4, however, the absorption dips become wider and appear to shift closer to 0.1 in phase.

The dynamic periodogram also shows an important peak at around 22 days. This peak is present for ∼200 days before the 16.5 day peak is suppressed and right before the 40 day peak appears. When the 16.5 day orbital signal finally returns, it starts off at a period slightly shorter than 16.5 days and takes almost 100 days to ramp back up to its previous 16.5 day peak. Finally, there is another feature common to both dynamic periodograms. At around MJD 51410, the 16.5 signal splits into two separate signals, one slightly longer period (∼18.4 days) and one slightly shorter (∼15.9 days). This split lasts for ∼165 days, until both signals finally converge back into one at around MJD 51575. This last feature roughly coincides with the point in the light curve where the overall flux of the source begins its steady decline (see Figure 5.2). After several years in a high flux state, where its baseline flux was greater than 1 Crab, Cir X-1 has begun a steep decline in flux, towards a lower intensity state; a decline which currently (January 2003) appears to have stabilized.

To test that a change in window length and step in the dynamic periodograms did not significantly change the time scales of the phenomena observed I tried many different values. Figure 5.7 shows two such examples. The plot on the left was carried out with a window of 150 days in length and a 15 day time step, while the one on the right used a 180 day window and a 30 day time step. All the main features are still visible at the same times and on the same time scales, though the resolution of the plot has varied. The white lines are a result of the lower time resolution due to the longer window length used.

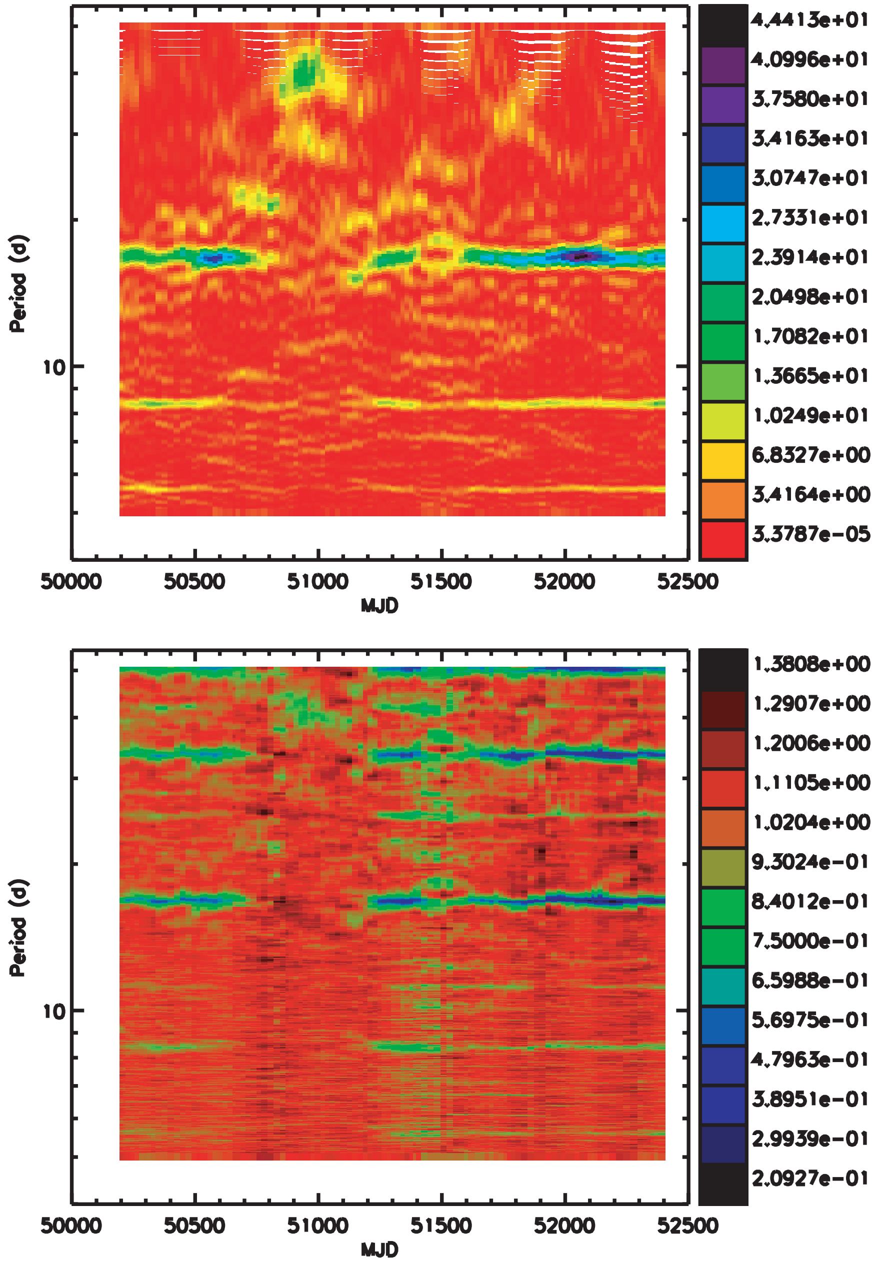

Figure 5.6: Dynamic Periodogram of RXTE ASM data. A sliding window of length ~200 days was stepped through the entire data set in ~20 day increments. **Top** – Lomb-Scargle dynamic periodogram. The color scale represents Lomb-Scargle power. **Bottom** – PDM dynamic periodogram. The color scale represents the value for the theta statistic.

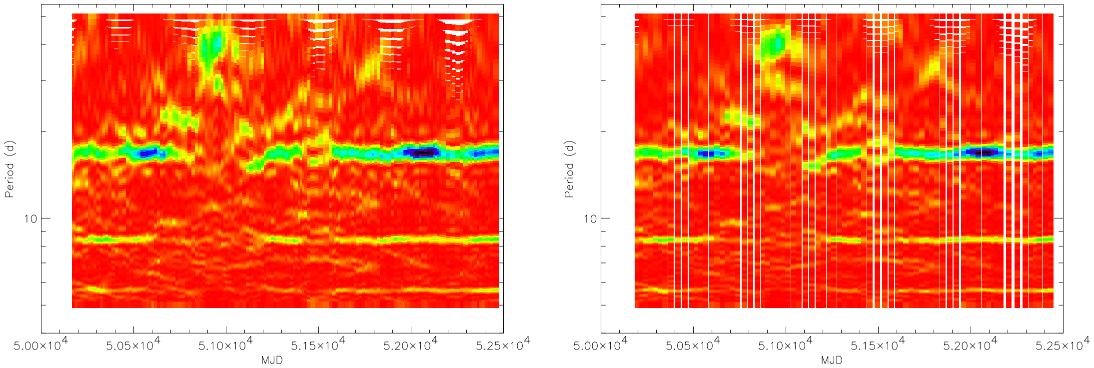

Figure 5.7: Dynamic Periodogram of RXTE ASM data. **Left** – A sliding window of length ∼150 days was stepped through the entire data set in ∼15 day increments. **Right** – Window length is now 180 and step is 30 days.

5.3.3 Super-orbital Period

Using the Lomb-Scargle periodogram on the RXTE ASM data, I searched for periodic signals longer than the orbital period. I limited the search to signals of periods shorter than ∼400 days, so that I would obtain at least five cycles from the RXTE ASM data currently available. I worked with the daily-averaged data, though I also checked that the results could be reproduced with the dwell by dwell data. I find a significant peak at 335.3 days. This result was verified by applying two other independent methods to the same data. First, I used the Phase Dispersion Minimization (PDM) technique and found that the θ statistic is minimized at 332.2 days. I also used a χ^2 minimization technique. In this technique, the data are folded on a series of trial periods and at each trial period the results are fit with a sine curve. The resulting reduced-χ^2 values are plotted as a function of the trial period used and the minimum in the plot indicates a possible period. Using this method I found a minimum at 331.7 days. Figure 5.10 shows the three separate results obtained by the different methods. Also in Figure 5.10 (bottom left) I show the RXTE ASM light curve folded (in 32 phase bins) at the 335 day period (with zero phase starting arbitrarily at time of the first ASM observation). I fit the folded light curve with a sine curve and find that there is a significant (∼13% amplitude) modulation at this period.

Given the proximity of this period to one year (the ASM could be subject to an

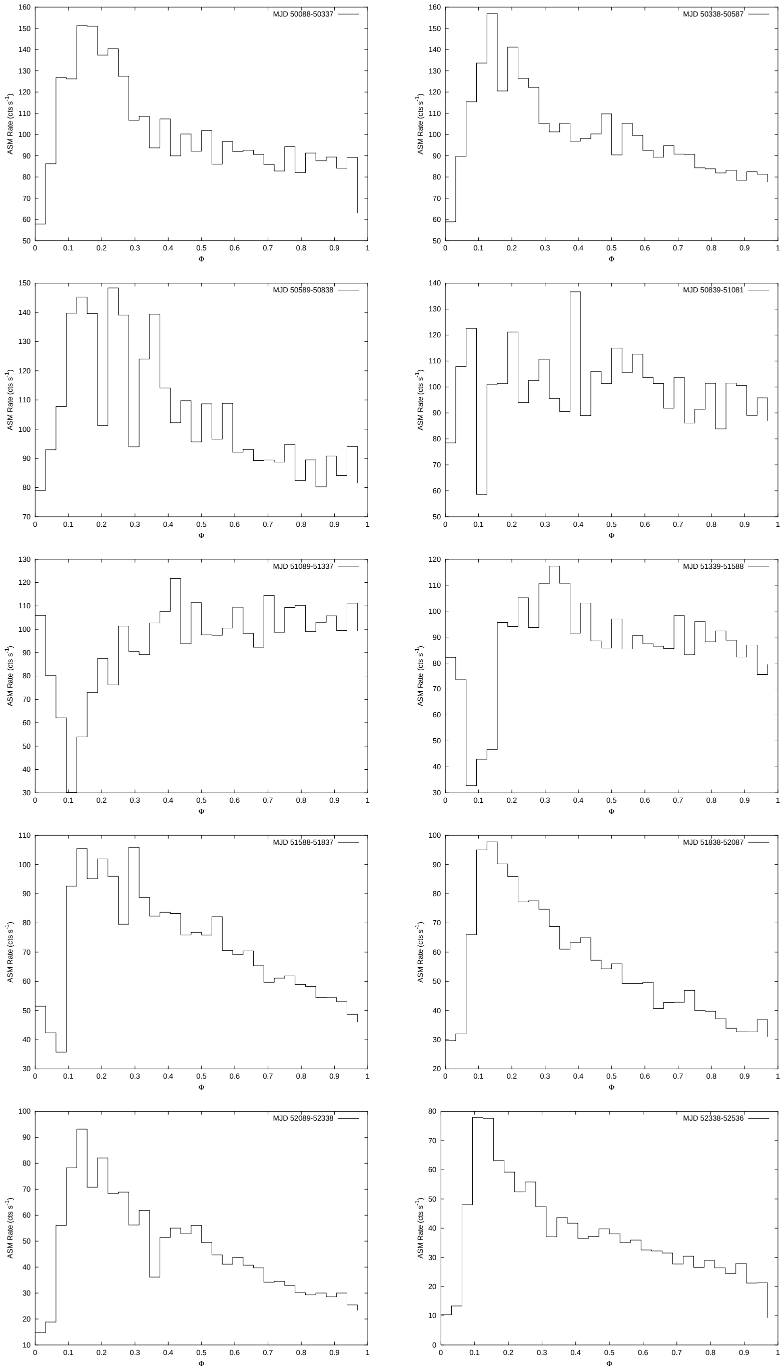

Figure 5.8: RXTE ASM data split into 10 segments (∼250 days long each) and folded at the 16.54 orbital period. Segments are ordered from top left (MJD 50088–50337) to bottom right (MJD 52338–52536). Segment 4 (MJD 50839–51081) shows no significant modulation at the 16.54 orbital period.

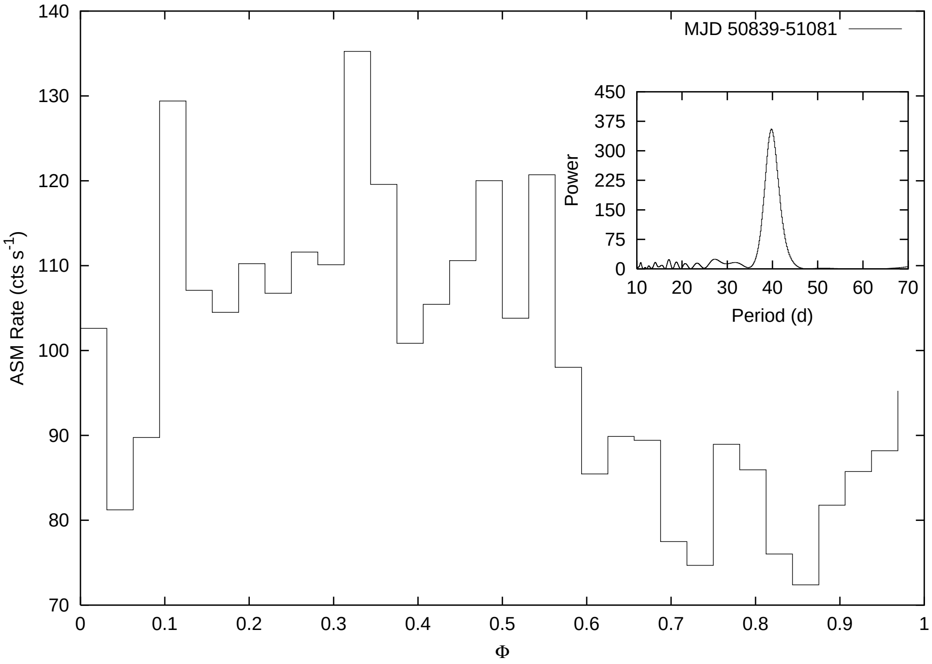

Figure 5.9: **Main Figure:** Segment 4 from Figure 5.8 (MJD 50839–51081) showing a ∼40 day modulation. **Inset:** Periodogram showing a peak at 40.0 days (and no significant peak at the orbital period 16.5 d).

annual modulation due the constraint of observing a source too close to the Sun), I performed several checks to increase the confidence in my result. In Figure 5.10 I point out where a one year modulation would lie. In order to test whether our 335 day modulation could be produced by the window function (i.e. the observation 'gaps' in the ASM data set), I created two data sets representing two pure sine waves of amplitude 10 $\mathrm{cts\,s^{-1}}$ (roughly the size of our observed signal) and period 335 days and 365.25 days respectively. I sampled these sine curves at the same times as the ASM observations and then performed the Lomb-Scargle periodograms on the data. Figure 5.12 (left) shows the results. Plotted over each periodogram is the best fit gaussian. The periods of best fit are 335.26 ± 0.36 and 365.66 ± 0.26 days respectively. I therefore conclude that the window function is unlikely to cause a shift in the period from 365.25 days (which could be caused by a yearly modulation) to the observed peak of 335 days. As a further check, I took the RXTE ASM data set and randomly permuted the rates to create 1000 'new' data sets with the same sampling times and average as the original ASM light curve. I then performed the periodograms on each of these light curves to see if any peak was detected at 335 days. Figure 5.12 (right) shows the results, including three lines indicating where the false alarm probabilities (FAP) of 1%, 5%, and 10% would lie. None of the peaks are significant (i.e. FAP level below 1%), with only one peak falling below a FAP of 5%. In other words, I can rule out that the 335 day peak I find is a result of the data sampling imposed on RXTE by yearly sun-constraints due to the location of Cir X-1.

In Figure 5.11 (top left panel) I show the evolution of the hardness ratio (5–12 keV/3–5 keV) during the entire RXTE era. There is a clear anti-correlation between the flux and hardness; as the source begins its decline in flux after MJD 51500, the hardness ratio (5–12 keV/3–5 keV) increases. I calculate the three different possible hardness ratios for the RXTE ASM (i.e. 3–5 keV/1.5–3 keV, 5–12 keV/3–5 keV, and 5–12 keV/1.5–3 keV) and fold them at the 335 day period (once again with 32 phase bins and phase 0 at the time of the first observation). I then fit the three folded hardness-ratio curves with a constant plus a sine curve of same phase and period as used for Figure 5.10 (i.e., the amplitude and overall constant term are the only parameters allowed to float). All three ratios are well fit by such a curve, showing an

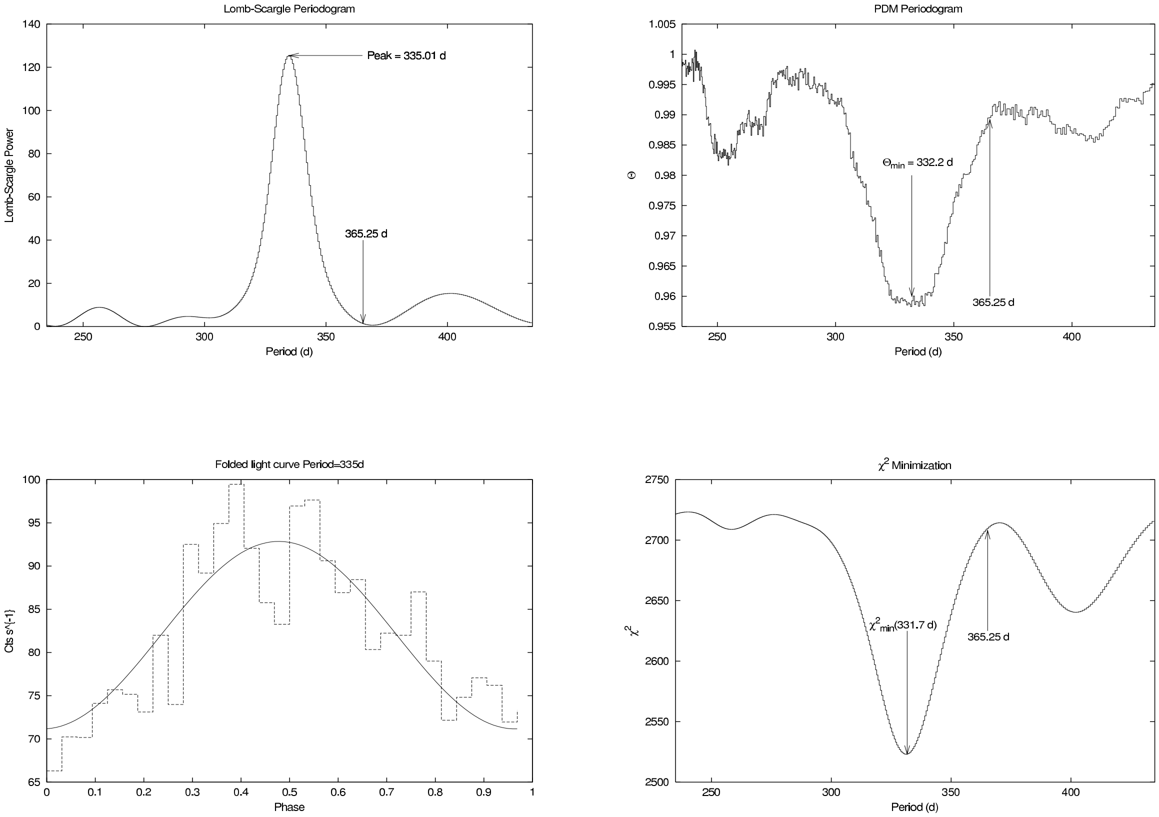

Figure 5.10: Possible period at ∼335 days. I indicate in the plots where the one year modulation would lie. **Top Left** – Lomb-Scargle periodogram showing a peak at 335.0 days. **Top Right** – PDM periodogram showing Θ_{min} at 332.2. **Bottom Right** – χ^2 Minimization technique showing a minimum χ^2 at 331.7. **Bottom Left** – RXTE ASM light curve folded at 335 days, binned into 32 phase bins and taking phase 0 arbitrarily as the start time of the observations. The solid line represents the best fit to a sine curve, showing a modulation of amplitude ∼13%.

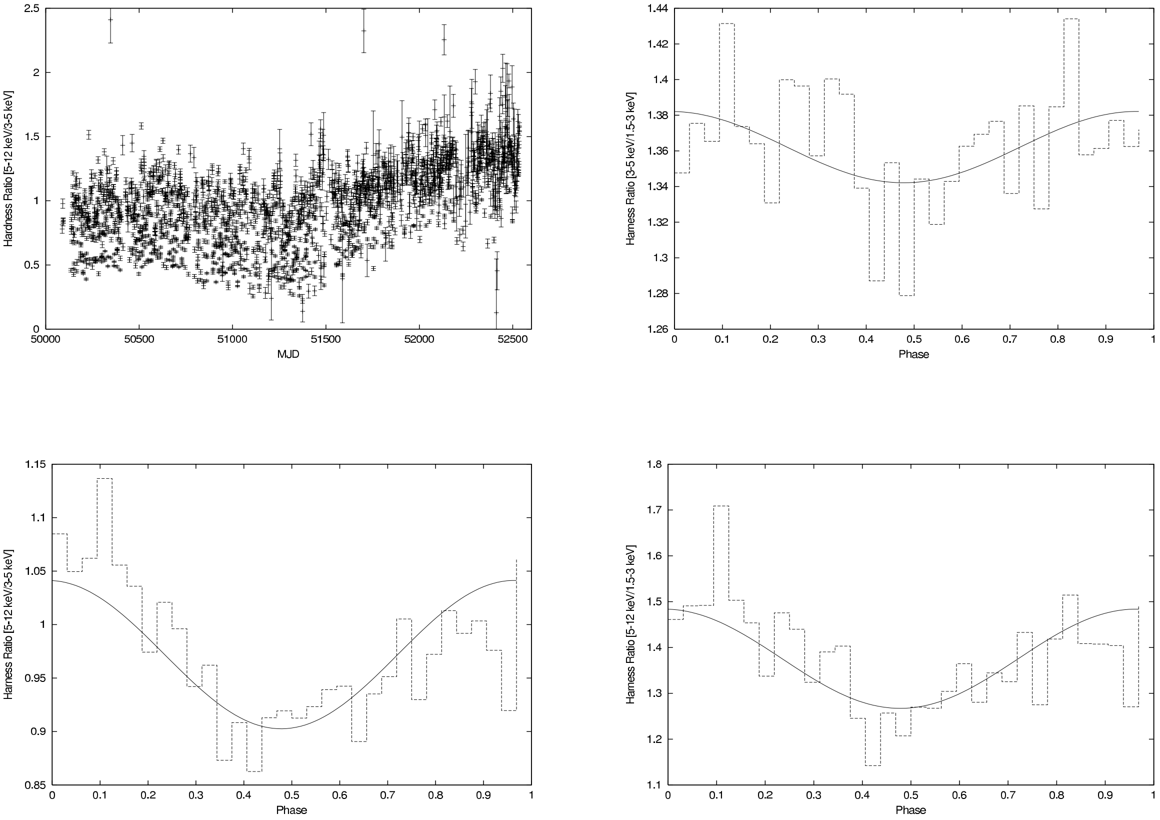

Figure 5.11: Hardness Ratios of RXTE ASM data. Top Right, Bottom Left, and Bottom Right are folded (in 32 phase bins) at 335 days. Phase 0 is taken as the time of the first observation. The solid lines in the figures represent the best fit sine curve, where the phase and period are fixed at the values obtained from the fit in the Bottom Left plot of Figure 5.10. **Top Left** – Channel C/Channel B (5–12 keV/3–5 keV) Hardness Ratio for the entire RXTE ASM epoch. **Top Right** – Channel B/Channel A (3–5 keV/1.5–3 keV) folded Hardness. **Bottom Left** – Channel C/Channel B (5–12 keV/3–5 keV) folded Hardness Ratio. **Bottom Right** – Channel C/Channel A (5–12 keV/1.5–3 keV) folded Hardness Ratio.

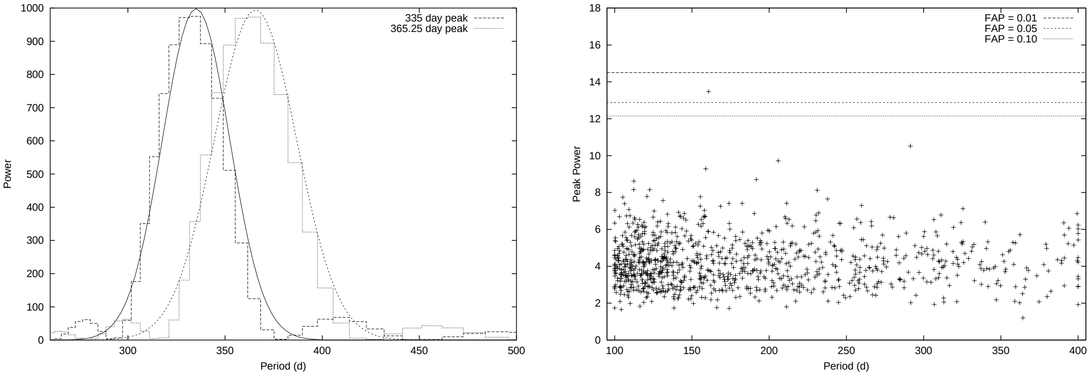

Figure 5.12: **Left** – This figure shows the periodograms of two sine curves, one of period 335 days and the other of period 365.25 days. The sine curves have been sampled at the same times as the RXTE ASM observations to determine the possible effects of the window function. The amplitude I chose for the sine curve was 10 counts per second (roughly the size of the 335 day modulation which was detected), as shown in Figure 5.10. Plotted over the periodograms are the best fit gaussians, which have a period of 335.26 ± 0.36 and 365.66 ± 0.26 days respectively. **Right** – Figure shows the peak power in the periodograms of 1000 random permutations of the RXTE ASM data set. Lines indicate the false alarm probability (FAP) values of 1%, 5%, and 10%.

anti-correlation between flux and hardness. The modulation in the hardness ratio is especially pronounced in the ratio computed from the two highest channels B and C (5–12 keV/3–5 keV). This, once again, is consistent with the modulation being due to obscuration caused by a precessing disk.

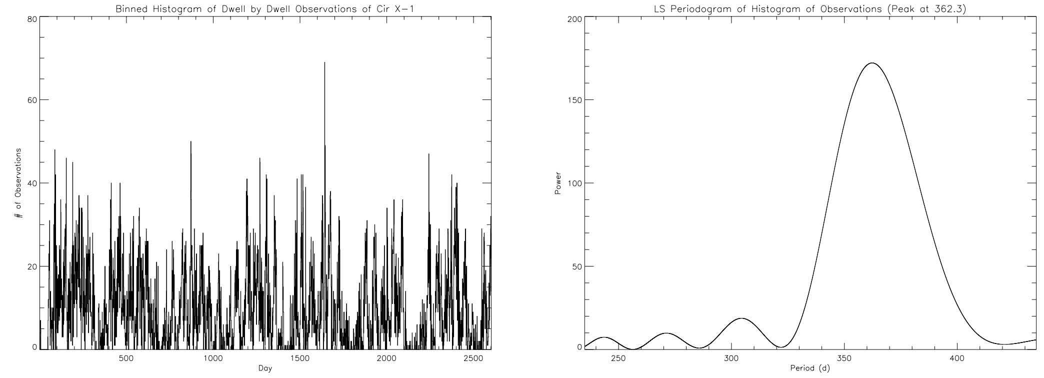

Figure 5.13: Influence of ASM window function. **Left** – Number of dwell observations taken on a particular day (from them beginning of RXTE mission) **Right** – Periodogram of the histogram on the left, showing yearly modulation (peak at 362.3 days).

Some additional checks

Given the Sun-angle observing constraints of RXTE, it is reasonable to ask whether the 335 day period could be related to the yearly modulation due to these constraints. In Figure 5.13 (left) I show a histogram of the number of observations of Cir X-1 taken by the ASM on every day of the mission to date. The yearly variation in the number of observations is clearly visible. In fact, the periodogram of this histogram shows a highly significant peak. However, this peak is very close to a year (362.3 days) and not 335 days.

To further test whether the 335 day peak could be due to observational effects, I look at the periodogram of the window function (obtained by taking the ASM data and replacing the values of the rates by ones). The result (shown in Figure 5.14), once again, is a peak at close to one year (372.2), but not 335 days.

Another possibility is that the 335 day peak could be caused by the yearly modulation in conjunction with a sudden drop in the overall rate of Cir X-1 (which is observed starting at around MJD 51500), possibly causing a 365 day peak to shift down to 335 days. In Figure 5.15 (top panel) I plot a binned (at the orbital period of 16.54 days) light curve of Cir X-1, showing the clear sloping tendency of the overall

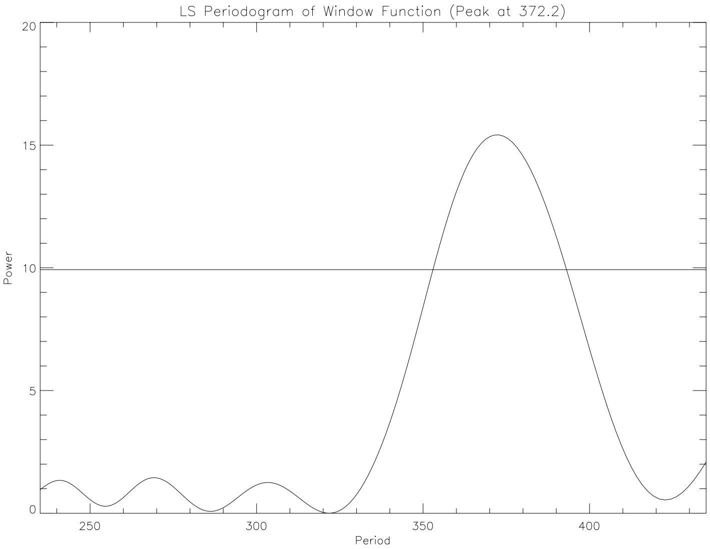

Figure 5.14: Lomb-Scargle periodogram of the RXTE ASM window function, showing a peak at close to the yearly modulation (372.2). The line shows the 99% significance level.

rate starting around 1000 days into the mission. Using a simple two-line function to model the overall trend in the data, I subtract this trend from the ASM data. The resulting light curve is shown in the middle pannel. The bottom panel of Figure 5.15 shows the periodogram of the 'de-trended' data set, showing that a peak is still present, roughly at the same location of 335 days, although its significance is reduced.

To test whether the 335 day peak could be produced by a combination of the window function (i.e. the yearly modulation) and a sloping rate. I again used a two-line function to represent the overall trend of the data. This time, however, instead of taking the periodogram of the 'de-trended' data set, I compute the periodogram of the two-line function, sampled at the ASM times. Roughly speaking, this is equivalent to taking the periodogram of a window function which starts out flat and then slopes down. Figure 5.16 shows an example of one of the two-line functions used, with its corresponding periodogram. I sampled 45 different functions to ensure that the results were not sensitive to the particular function used. Each of these functions was

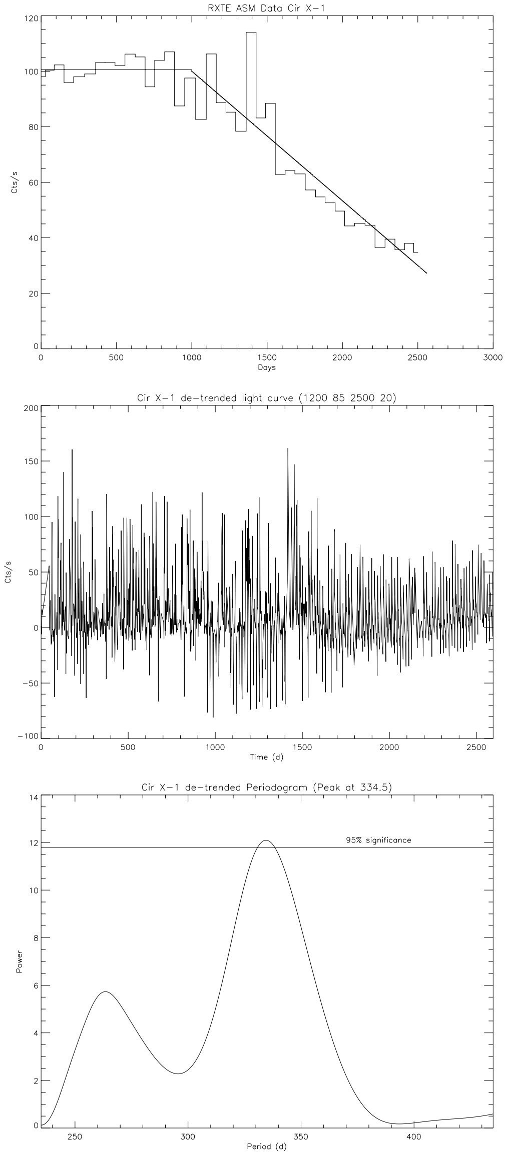

Figure 5.15: Influence of a sloping ASM window function. **Top** – Binned ASM light curve with two-line fit. **Middle** – De-trended (data minus two-line fit) ASM light curve. **Bottom** – Periodogram of de-trended light curve showing a peak at ∼335 days at the 95% significance level.

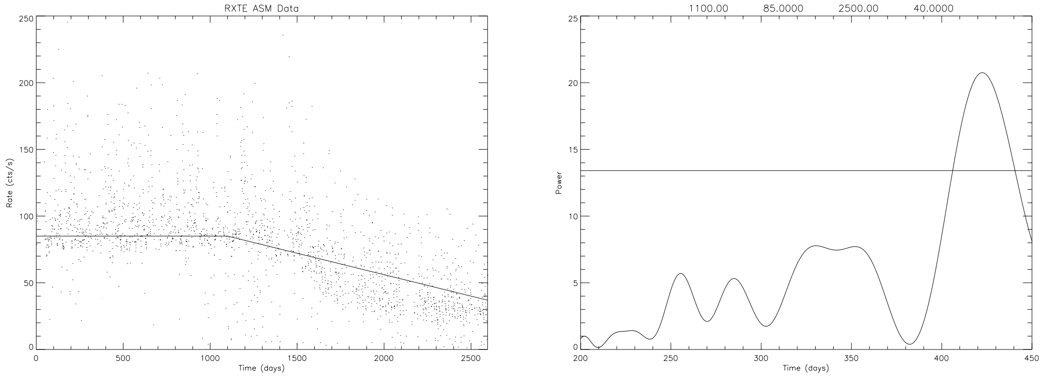

Figure 5.16: Influence of a sloping ASM window function. **Left** – RXTE ASM data (dots) and a two-line function representing the change in the trend (from flat to sloping). **Right** – Periodogram of the two-line function shown on the left, showing no significant peak at 335 days (the line on the plot represents the 99% significance level) and a significant peak above 400 days. The four numbers on the top represent the x and y coordinates of the two points defining the two-line function.

defined by two points, the inflection point (where the flat segment meets the sloping segment) and the end point of the sloping segment. Figure 5.16 shows a representative example of the results that were obtained. No significant peak was found at 335 days. Furthermore, the only significant peak found is at greater than 400 days. A second peak is sometimes present at a period slightly smaller than 365 days but never closer to 335 days than to one year. In conclusion, I was not able to demonstrate that the 335 day peak could be produced by a combination of the ASM window function and the sloping trend in the Cir X-1 light curve. I therefore conclude that it is likely that the 335 day period truly originates in Cir X-1.

5.4 Discussion

Cir X-1 has been extensively monitored now for over 30 years, though there have been long gaps in the observations, as can be seen from Figure 5.1. The first thing to note about the long-term light curve shown in Figure 5.1 is the large variation in the source intensity. Ignoring the large variability within the 16.6 day orbit (itself very significant), the overall average flux level of the source has gone from about 0.4 crab at the beginning of the Vela 5B era, down to almost zero a few years later, then increasing at every epoch since then, until reaching a peak of more than 1 Crab in the RXTE era, only to begin its decline once again at ∼MJD 51600, a decline which levelled off at about 0.4 Crab and now (May 2003) seems to be declining further. Included in Figure 5.1, besides the data from the four observatories which had an ASM, are the individual pointed observations from EXOSAT. It is interesting to note that the Type I X-ray bursts which led to the classification of Cir X-1 as a neutron star (Tennant et al. 1986a) were all detected during one EXOSAT observation taken on 1985 August 12 (∼MJD 46290) at a time when Cir X-1 was much dimmer than it has been ever since. The mean rate at the time of the first Type I burst was ∼15 $\mathrm{cts\,s^{-1}}$ and at the time of the other two it was ∼90 $\mathrm{cts\,s^{-1}}$ (see Tennant et al. (1986a) for more details); this corresponds to ∼1–5% of the Crab. This has been offered as an explanation as to why no more bursts have ever been observed. However, it appears that Cir X-1 could soon have a flux similar to its 1984–85 level, making it an interesting potential target for the detection of new Type I X-ray bursts.

In this chapter, I have derived a long-term ephemeris for Cir X-1 based solely on X-ray observations. Using the results obtained from Lomb-Scargle periodograms, PDM periodograms, and FFT analyses, I derived a line of best fit which provides, as far as I know, the first ephemeris solely derived from X-ray observations. Although the X-ray emission of Cir X-1 is correlated with the radio observations (Stewart et al. 1991), the peak in X-ray emission sometimes precedes and sometimes follows the onset of the radio flares (Shirey 1998). It would be interesting to compare our newly derived X-ray ephemeris with a more recent one obtained from radio observations. Unfortunately since the late 1980's the radio flares from Cir X-1 have been too weak to update the ephemeris (Shirey 1998).

I obtain a characteristic time scale of $P/\dot{P}$ ~3000 years, raising the possibility that this is a much younger system than was previously believed. I should note, however, that although I detect a fairly large decrease in the orbital period over the course of the more than 30 years of monitoring, I am not able to confirm this relatively rapid decrease in period in the RXTE observations alone, which span more than 6.5 years. As I have noted (and is clearly visible in the dynamic periodograms in Figure 5.6), the orbital period of Cir X-1 was not always detectable during the RXTE observations. In our FFT analysis we split the data into two distinct epochs in which the orbital period was clearly detectable. While the two values obtained show a decrease in the orbital period (as would be indicated by the ephemeris), our result, given the errors, is consistent with a constant period over the entire RXTE era.

Many X-ray binaries display a 'super-orbital' period (sometimes referred to as a third period, P_3, to distinguish it from the orbital period and the rotation period). Although many different types of sources display this sort of long-term periodicity, a few patterns have begun to emerge. Both LMXBs (e.g. Cyg X-2, 4U1820-30, X1916-053) and HMXBs (e.g. Cyg X-1, LMC X-4, SMC X-1, SS 433) show these periods, but they appear to be much less common in LMXBs than in HMXBs (Smale and Lochner 1992). Another difference between LMXBs and HMXBs in this respect concerns the ratio of these long periods to their respective orbital periods. In LMXBs this ratio has been found to be very large (e.g. ~22000 for 4U1820-30 or ~6000 for X1916-053), whereas for HMXBs this ratio tends to be much smaller (e.g. ~21 for LMC X-4, ~13 for SS433, or ~5 for X 1907+097). However, there are cases like Cyg X-2, an LMXB, with an orbital period of 9.8 days and a super-orbital period of 77.8 days (i.e. a ratio of ~8) or LMC X-3, an HMXB with an orbital period of 1.7 days and a super-orbital period of 197.8 days (though it is argued that this might be a harmonic of 98.9 (Paul et al. 2000), giving a ratio of ~116 (or ~58 if I take P_3 to be 98.9 instead of 197.8). Recently, a 600 day super-orbital period (the longest to date) in the Galactic black-hole candidate 1E 1740.7-2942 was reported by Smith et al. (2002). In this case, the authors combined BATSE and RXTE data to detect this period.

The interpretations for the origin of these periodicities are as varied as the sources that display them, and include: changes in mass accretion rate (e.g. in LMC X-3 (Brocksopp et al. 2001)), presence of a third body in the system (e.g. 4U1820-30, see Grindlay, J. E. 1986 in Truemper et al. (1986)), and precession of a tilted accretion disk (e.g. in Her X-1 or Cyg X-2 (Wijnands et al. 1996). For a summary of super-orbital periods see Lewin et al. (1995) and references therein.

In this chapter, I have presented the detection of a ∼335 day modulation with amplitude of ∼13%. The ratio of this long period (P_3) to the orbital period (P_o) is ∼20, which is in the same range as that observed in most HMXBs. I suggest that the precession of an accretion disk could be a possible cause of such a modulation. Oosterbroek et al. (1995) describe such a model to explain what they describe as a long-term change in the behavior of Cir X-1 (a gradual increase in the brightness around phase zero, from 1984 to 1986). In the precessing accretion disk model we expect the inner part of the disk and the central source to become obscured. The increased absorption in the low-intensity phase would cause a hardening in the spectrum, something which is observed in both Her X-1 and LMC X-4 (Paul et al. 2000). In Figure 5.11 I show that the hardness of Cir X-1 is indeed anti-correlated with the intensity of the modulation, a fact which is consistent with this precessing disk model.

Chapter 6

Conclusions and Future Work

Then we sat on our own star and dreamed of the way that we were
and the way that we were meant to be.
Van Morrison, "The way young lovers do" (1968)

6.1 Results

Circinus X-1 is probably unique in the Galaxy in the variety of behavior that it exhibits. Controversy surrounds even the most basic facts about this system, though I believe that its study provides a great laboratory to test many models and to improve our understanding of the differences between black holes and neutron stars. The fact that Cir X-1 is so bright and periodically displays a wide range of luminosities, QPOs, and associated phenomena makes it an ideal source for challenging models of all such phenomena.

In this work, I started out by modeling the light curve of Cir X-1 as a disk-diffusion process in which the viscous timescale is found to vary by a factor of 3 over the 6.5 year RXTE epoch. This reinforces the idea that the cyclical outbursts of Cir X-1 are caused by a periodic mass deposition on the outer disk and subsequent diffusion into the inner disk. The viscous timescale is not found to follow a simple correlation with quiescent flux; however, the two must be related since a longer viscous timescale is expected to allow for the accumulation of material in the disk, with its corresponding effect on the luminosity of the disk.

To study the spectral evolution of Cir X-1 I constructed color-color diagrams in both an instrument-independent and a model-independent way. Spectral fits were performed and physical parameters were derived from these fits. The spectral parameters obtained from the fits indicate that a two-component model is appropriate for the description of the Cir X-1 spectrum. Furthermore, they show that the temperature of the multicolor disk remains roughly constant, while the Comptonizing component increases with temperature along the orbital phase. Cir X-1 is found to periodically evolve from a 'high/soft' state to a 'low/hard' state.

The relative contribution of the disk component decreases as the source moves along the orbit and the relative contributions of the two components could imply that the neutron star is rotating very fast ($>$ 1kHz).

In terms of timing, I find multiple QPOs in the 1–50 Hz range which appear to be split into a lower frequency population ($\sim$3–20 Hz) and a higher frequency one ($\sim 20-50$ Hz). The high frequency QPOs decrease in strength (% RMS) as the frequency increases, while the lower frequency QPOs stay roughly constant. Furthermore, the lower frequency QPOs appear to increase in frequency within each individual orbital cycle.

Some observations contain simultaneously a high and a low frequency QPO. When these QPO frequencies are plotted against each other, no simple correlation is found, although this could be due to poor statistics of individual observations. When combining many consecutive observations, the frequencies of the multiple QPOs present agree with the recently reported correlation ($\nu_{low} = 0.08\nu_{high}$).

The low frequency QPO RMS variability is found to increase with energy, which argues against a simple interpretation of these QPOs as arising in different locations of the disk and seems to imply that the QPOs are generated in the higher energy Comptonizing medium.

The power spectrum of Cir X-1 in its soft state closely resembles that of Cyg X-1, with both showing two breaks which can be made to coincide by scaling the spectrum by 3.8. If one assumes that the frequency of these breaks is inversely related to the mass, this would imply a mass for Cir X-1 in excess of the canonical mass for a neutron star.

I present the detection of 6 sub-ms bursts found in the USA data of Cir X-1. Most of these bursts were detected in a few observation and they are found to be very soft (mostly in the lower two USA channels).

Regarding the long-term behavior of Cir X-1, I showed that over the last 33 years Cir X-1 has undergone large variations in its flux, with the brightest epoch corresponding to the recent RXTE/USA era. Recent observations show that Cir X-1 may once again be entering into a 'quiet' period.

I have derived an X-ray ephemeris based on these long term observations showing that the period of Cir X-1 is rapidly decreasing ($P/\dot{P} < 3000$ yrs), possibly implying that it is a very young system.

I computed dynamic periodograms showing some unusual periodicities previously unreported. A 250 day span of data shows no sign of the orbital, while a new ~40 day period is observed.

Finally, a new 335 day super-orbital period is observed, with the hardness ratio perfectly anti-correlated, possibly implying that this is due to an obscuration effect arising from the precession of a tilted accretion disk.

6.2 Further Work

As previously noted, during the early RXTE epoch, Cir X-1 was very bright. It then decreased in flux considerably but appeared to settled on an overall rate of roughly 0.4 Crab. Cir X-1 now appears to be dimming further, maybe approaching levels not seen since the early 1980's. It would be desirable to schedule observations with RXTE in the next year, first to hopefully detect some Type I X-ray bursts (which would settle once and for all the nature of the compact object in the system). If the source has shown bursts once, it should show them again, and much can be learned from such bursts (such as the spin rate of the neutron star).

More multi-wavelength observations should also be carried out. The relationship between the relativistic jet of Cir X-1 and the energy spectrum needs to be explored.

Is the relationship similar to that in Black Hole Binaries? Cir X-1 could teach us a lot about the production of jets.

It would also be interesting to look at archival data in other wavelengths to see if any of the periodicities found here are also present in different wavelengths.

The dynamic periodograms of Cir X-1 can be constructed in different energy bands. The spectral behavior of the different periodograms could tell us something about where (or how) these periodicities are being produced.

In general, an overall model of the system should be developed which is consistent with the observations found in the different regimes mentioned in this work. This model should explain how the evolution of the energy spectrum (and in particular, that of the individual components) ties in with the evolution observed in the QPOs and how the two are related. What part does the viscous timescale of the disk play?

The relativistic precession and beat-frequency models for QPOs are probably not correct, so it would be interesting to explore other models for QPOs which might have better explain QPOs in Cir X-1 and other systems, and attempt to use such models to learn more about the physical parameters of the system: e.g. its mass or its spin.

The Acoustic Oscillation Model (AOM) is one possible model which is not ruled out at present. The radii for the transition layer predicted by this model should be computed and compared with the radii obtained from spectral fits.

The Dripping Hand-Rail (DHR) model is also an interesting alternative, though it would have to be further developed. It would be interesting to introduce some radiation mechanism into the model to attempt to provide an explanation for the energy dependence of the QPOs as well as the frequencies. Attempting to explaining the observations of Cir X-1 presented in this dissertation would present a challenge and would constitute an important first step in that direction.

Appendix A

Energy Calibration Codes

> *Well I'm beginning to see the light.*
> *Now I'm beginning to see the light.*
> Velvet Underground, "Beginning to see the light" (1969)

A.1 Codes[1]

Two programs serve to create all the response matrices for USA: `matrices.C` and `make_response.sh`. The first of these, `matrices.C`, does most of the work. It reads as input the efficiency of the USA detector (for layer 1, layer 2, and layers 1 and 2 combined). These efficiencies are provided as three separate files (eff_file_1, eff_file_2, and eff_file_12). They were computed first by Mike Kowalski and more recently by Mike Wolff, and are plotted in Figure 2.8). The second input required by `matrices` is the energy to channel gain parameters (e.g. Table 2.6). These gain parameters should be entered by the user in the form of a file (e.g. `gain_file.dat`) containing three lines, one for each of the two layers and one for both layers combined. Each line contains five columns. The first is the layer ID (1 for layer 1, 2 for layer 2, and 12 for the combined layers). The next four columns represent the offset, linear,

---

[1] These codes were current as of August 2003. This work has been done in collaboration with Michael T. Wolff at NRL.

quadratic, and cubic terms of the gain function (Energy vs Channel) used to compute the response of USA (currently only the first two of these terms are non-zero since we assume a linear response). To run the program, simply type the command, `matrices`, at the prompt, as illustrated below :

```
pavo :  1>matrices
Usage:  matrices <gain_file.dat>
pavo :  2>
```

The output of `matrices` is a set of nine files (three for each individual layer and three for the combined layers): ebounds1, ebounds2, ebounds12, rmfval1, rmfval2, rmfval12, effarea1, effarea2, effarea12. These files provide all the necessary information to build a 128 channel 'raw' response matrix. The *ebounds* files contain the derived energy channel boundaries. The *effarea* files contain the effective area of USA at the prescribed energies sampled in the response matrix. Finally, the *rmfval* files contain the redistribution matrices. These are currently matrices of 300 rows (representing the energy of a hypothetical incoming photon from 0.1 keV to 30 keV, in increments of 0.1 keV) and 128 columns (representing the 128 'raw' channels). Each element of the matrix represent the probability that a photon of energy equal to $0.1\times$row# keV would be detected in the channel corresponding to each column. Each column will have energy boundaries which are determined by the given gain parameters. The second program (`make_response.sh`) is a script which invokes a set of `FTOOLS` needed to perform all the required re-binning to create the final set of response matrices. These matrices are created as `FITS` files and can be used with `XSPEC` to perform spectral fits of USA data.

A.1.1 matrices.C

```
// Pablo Saz Parkinson
// 18 February 2000
// Last Updated: 5 August 2003
// program matrices.C

#define GW_1 0.2244 // (9.2% sigma)   (1997 TVAC data)
#define GW_2 0.2598 // (15.4% sigma)  (1997 TVAC data)
#define E_FRACTION_L1 0.0444 // Layer 1 (1997 TVAC data D246_1306)
#define E_FRACTION_L2 0.0341 // Layer 2
#define E_FRACTION_L12 0.0444 // Both layers
#define EPHALOW 0.31 // PHA lower energy bound for valid events
#define DE 2.956 // difference in energy between main and escape peak
#define Argon_Edge 3.203
#define AREA 1500 // Area of the detector in cm^2
#define MESH 0.85
#define COLL 0.88
#define g1 0.49 // fractional resolution constant: g = g1 * E^(-1/2)

#include <iostream.h>
#include <fstream.h>
#include <stdlib.h>
#include <math.h>

extern "C" {
   #include <nr.h>
   #include <nrutil.h>
}

float lo,hi; // channel boundaries (to be passed to R(E,h))
float ej;    // main peak
```

```
float ep;    // escape peak
float en[300],layer1_eff[300],layer2_eff[300],layer12_eff[300];
float ILOW;

/***********************************************************************
**
** Function: prob
** Purpose: This function gives the probability of a value lying
** between a and b in a normal distribution of average
** (mean) and standard deviation (sig).
**
***********************************************************************/
float prob(float mean,float sig, float a, float b)
{
   float  y1,y2;
   if ( mean==0.0 ) return 0 ;
   y1=(a-mean)/(sig*sqrt(2.0)) ;
   y2=(b-mean)/(sig*sqrt(2.0)) ;
   return ((erf(y2)-erf(y1))/2.0) ;
}

/***********************************************************************
**
** Function: width
** Purpose: This function gives the width (in channels) of the
** gaussian expected at a particular energy. It is based
** on the fractional resolution of the instrument.
**
**
***********************************************************************/
float width(float e, float off, float lin, float quad, float cube)
```

```
{
return ((g1/2.35)*e/sqrt(off+lin*e+quad*e*e+cube*e*e*e));
}

/*****************************************************************
**
** Function: reh
** Purpose: Formulate the USA response probablility to an incoming
** photon. This response will model the channel distribution
** as a double gaussian if the photon energy is above the
** Argon K-shell ionization energy of 3.2029 keV. Below this
** threshold the response is a single gaussian peak at the
** incoming photon energy. reh(energy,h1,h2) is the
** probability that a photon of incident energy "energy",
** falls between h1 and h2 (which are the boundaries of one
** of the 128 USA PHA channels.
**
*****************************************************************/
float reh(float main_peak, float s_main_peak, float escape_peak,
  float s_escape_peak, float h1, float h2, int layer)
{
   float  peak1 , peak2 ;
float s_peak1, s_peak2 ;
   float  ef , ef1 , ef2 ;
float hj1 , hj2 ;

/*
** ILOW is the index (a REAL number) of the low energy threshold for USA
** valid events. If the energy of the photon puts it in a channel below
** ILOW then USA's response should be zero!
*/
```

```
hj1 = h1 ;
hj2 = h2 ;
if ( hj2<=ILOW ) return ( 0.0 ) ;
if ( (hj1<ILOW) && (hj2>=ILOW) ) hj1 = ILOW ;
/*
** Set the flourescence yield values for each layer.
*/
   if ( layer==1 )  ef=E_FRACTION_L1;
   if ( layer==2 )  ef=E_FRACTION_L2;
   if ( layer==12 ) ef=E_FRACTION_L12;
   ef1=1.0-ef;
   ef2=ef;
/*
** If there needs to be an escape peak then set the
** two peak amplitudes. If not, then only set the amplitude
** of the main peak at energy "energy".
*/
   if ( escape_peak==0.0 ) {
ef2=0.0;
   ef1=1.0;
}
   peak1=main_peak;
   peak2=escape_peak;
s_peak1=s_main_peak;
s_peak2=s_escape_peak;

/*
** Ready to return the correct propability:
*/
   return (ef1*prob(peak1,s_peak1,hj1,hj2)
     + ef2*prob(peak2,s_peak2,hj1,hj2)) ;
```

```
}

int main(int argc, char *argv[]) {
  if (argc != 2) {
    cerr << "Usage: matrices <gain_file.dat>" << endl;
    return 1;
  }

  double lay;
  double off_1,lin_1,quad_1,cube_1;
  double off_2,lin_2,quad_2,cube_2;
  double off_12,lin_12,quad_12,cube_12;

  // Read gain parameters from gain file

  ifstream gain_file(argv[1]);
  cout << "The name of your file is: " << argv[1] << endl;

  gain_file >> lay >> off_1 >> lin_1 >> quad_1 >> cube_1 ;
  gain_file >> lay >> off_2 >> lin_2 >> quad_2 >> cube_2 ;
  gain_file >> lay >> off_12 >> lin_12 >> quad_12 >> cube_12 ;

  cout << "Your gain parameters are: " << endl;
  cout << "   Layer 1: " << "offset: " << off_1 << " Lin: " << lin_1
       << " Quad: " << quad_1 << " Cube: " << cube_1 << endl;
  cout << "   Layer 2: " << "offset: " << off_2 << " Lin: " << lin_2
       << " Quad: " << quad_2 << " Cube: " << cube_2 << endl;
  cout << "Layers 1+2: " << "offset: " << off_12 << " Lin: " << lin_12
       << " Quad: " << quad_12 << " Cube: " << cube_12 << endl;

int accept,i,j,n;
```

```
float energy,eff,avg,tot;
float ebounds_1[130];
float ebounds_2[130];
float ebounds_12[130];
float avg_eff_l1[128];
float avg_eff_l2[128];
float avg_eff_l12[128];
float rmfval1;
float rmfval2;
float rmfval12;

float lo,hi; /* channel boundaries (to be passed to R(E,h)) */
float ej;    /* main peak  */
float sj;    /* sigma of main peak */
float ep;    /* escape peak  */
float sp;    /* sigma of escape peak */
float ILOW ;   /* Index for lower PHA energy bound. */
float en[300],layer1_eff[300],layer2_eff[300],layer12_eff[300];

  ifstream in1("eff_file_1");
  ifstream in2("eff_file_2");
  ifstream in3("eff_file_12");

  ofstream out1("ebounds1");
  ofstream out2("ebounds2");
  ofstream out3("effarea1");
  ofstream out4("effarea2");
  ofstream out5("rmfval1");
  ofstream out6("rmfval2");
  ofstream out7("ebounds12");
  ofstream out8("effarea12");
```

```
  ofstream out9("rmfval12");

// Read in efficiencies

  i=0;
  while (in1 >> energy >> eff) {
    en[i]=energy;
    layer1_eff[i]=eff;
    i=i+1;
  }
  i=0;
  while (in2 >> energy >> eff) {
    layer2_eff[i]=eff;
    i=i+1;
  }
  i=0;
  while (in3 >> energy >> eff) {
    layer12_eff[i]=eff;
    i=i+1;
  }

// Calculate channel boundaries depending on the gain

    for ( i=0; i<=127; i+=1 ) {
           ebounds_1[i]=off_1+((float)i)*lin_1+((float)i*i)*quad_1+
                 ((float)i*i*i)*cube_1;
           ebounds_2[i]=off_2+((float)i)*lin_2+((float)i*i)*quad_2+
                 ((float)i*i*i)*cube_2;
           ebounds_12[i]=off_12+((float)i)*lin_12+((float)i*i)*quad_12+
                 ((float)i*i*i)*cube_12;
    }
```

```
// Introduce fake channel 129 which will be ignored in modes 1 through 4
// and used as the 48th channel in mode 5, containing only zeros.

   ebounds_1[128]=30.0;
   ebounds_2[128]=30.0;
ebounds_12[128]=30.0;
   ebounds_1[129]=30.0;
   ebounds_2[129]=30.0;
ebounds_12[129]=30.0;

 for (i=0;i<=126;i+=1) {
   out1 << i << " " << ebounds_1[i] << " " << ebounds_1[i+1] << "\n";
   out2 << i << " " << ebounds_2[i] << " " << ebounds_2[i+1] << "\n";
   out7 << i << " " << ebounds_12[i] << " " << ebounds_12[i+1] << "\n";
  }

 out1 << i << " " << ebounds_1[127] << " " << "30.0" << "\n";
 out2 << i << " " << ebounds_2[127] << " " << "30.0" << "\n";
 out7 << i << " " << ebounds_12[127] << " " << "30.0" << "\n";
 out1 << "128" << " " << "30.0" << " " << "30.0" << " " << "\n";
 out2 << "128" << " " << "30.0" << " " << "30.0" << " " << "\n";
 out7 << "128" << " " << "30.0" << " " << "30.0" << " " << "\n";

// Calculate response matrix at each of MPK's energy points

ILOW = (EPHALOW-off_1)/lin_1 ;

  for (i=0;i<=299;i+=1) {

// First print energy bounds and effective area (ARF files)
```

```
out3 << en[i]-.05 << " " << en[i]+.05 << " "
                     << layer1_eff[i]*AREA*MESH*COLL << endl;
out4 << en[i]-.05 << " " << en[i]+.05 << " "
                     << layer2_eff[i]*AREA*MESH*COLL << endl;
out8 << en[i]-.05 << " " << en[i]+.05 << " "
                     << layer12_eff[i]*AREA*MESH*COLL << endl;

// Next compute probabilities (RMF files)

    tot=0.0;
    out5 << en[i]-.05 << " " << en[i]+.05 << " " << " 1  0  129  ";
    out6 << en[i]-.05 << " " << en[i]+.05 << " " << " 1  0  129  ";
out9 << en[i]-.05 << " " << en[i]+.05 << " " << " 1  0  129  ";

for (j=0;j<=127;j+=1) {


  // Layer 1 Probability response:

      lo=j ;
      hi=j+1 ;
      ej=(float)((int)((en[i]-off_1)/lin_1));
      if (en[i] > Argon_Edge) {    /* There is an escape peak! */
       ep=abs((int)((en[i]-DE-off_1)/lin_1));
} else {      /* No escape peak! */
        ep=0.0 ;
}
sj=width(ej,off_1,lin_1,quad_1,cube_1);
sp=width(ep,off_1,lin_1,quad_1,cube_1);
if (en[i] > EPHALOW) {
```

```
  rmfval1=reh(ej,sj,ep,sp,lo,hi,1) ;
} else {
  rmfval1=0.0 ;
}

// Layer 2 Probability response:

      lo=j ;
      hi=j+1 ;
      ej=(float)((int)((en[i]-off_2)/lin_2)) ;
      if (en[i] > Argon_Edge) {    /* There is an escape peak! */
         ep=abs((int)((en[i]-DE-off_2)/lin_2)) ;
} else {     /* No escape peak! */
         ep=0.0 ;
}
sj=width(ej,off_2,lin_2,quad_2,cube_2);
sp=width(ep,off_2,lin_2,quad_2,cube_2);
if (en[i] > EPHALOW) {
  rmfval2=reh(ej,sj,ep,sp,lo,hi,2) ;
} else {
  rmfval2=0.0 ;
}
// Layers 1 and 2 Probability response together for mode 5 data:

      lo=j ;
      hi=j+1 ;
      ej=(float)((int)((en[i]-off_12)/lin_12)) ;
      if (en[i] > Argon_Edge) {    /* There is an escape peak! */
         ep=abs((int)((en[i]-DE-off_12)/lin_12)) ;
} else {     /* No escape peak! */
         ep=0.0 ;
```

```
}
sj=width(ej,off_12,lin_12,quad_12,cube_12);
sp=width(ep,off_12,lin_12,quad_12,cube_12);
if (en[i] > EPHALOW) {
      rmfval12=reh(ej,sj,ep,sp,lo,hi,12) ;
} else {
  rmfval12=0.0 ;
}

       out5 << rmfval1 << " ";
       out6 << rmfval2 << " ";
out9 << rmfval12 << " ";
   }

//    cout << i << " " << tot << endl;
    out5 << "0" << endl;
    out6 << "0" << endl;
out9 << "0" << endl;
   //   cout << "Total=" << tot << endl;
  }
}
```

A.1.2 make_response.sh

```
#!/bin/csh
# Pablo Saz Parkinson
# 18 May 2000
# Updated: Paul Ray / 24 May 2000
# This program will create the response matrices for USA
./matrices dn_gaincurve.dat

# Create EBOUNDS FITS file (and set LAYER keyword)
fcreate eb.col ebounds1 ebounds1.eb headfile="eb.head"
        extname="EBOUNDS"
fparkey L1 ebounds1.eb+1 LAYER add+
fcreate eb.col ebounds2 ebounds2.eb headfile="eb.head"
        extname="EBOUNDS"
fparkey L2 ebounds2.eb+1 LAYER add+
fcreate eb.col ebounds12 ebounds12.eb headfile="eb.head"
        extname="EBOUNDS"
fparkey L12 ebounds12.eb+1 LAYER add+

# Create ARF FITS file (and set LAYER keyword)
fcreate arf.col effarea1 effarea1.arf headfile="arf.head"
        extname="SPECRESP"
fparkey L1 effarea1.arf+1 LAYER add+
fcreate arf.col effarea2 effarea2.arf headfile="arf.head"
        extname="SPECRESP"
fparkey L2 effarea2.arf+1 LAYER add+
fcreate arf.col effarea12 effarea12.arf headfile="arf.head"
        extname="SPECRESP"
fparkey L12 effarea12.arf+1 LAYER add+

# Create RMF FITS file (and set LAYER keyword)
```

```
fcreate rmf.col rmfval1 rmfval1.rmf headfile="rmf.head"
        extname="MATRIX"
fparkey L1 rmfval1.rmf+1 LAYER add+
fcreate rmf.col rmfval2 rmfval2.rmf headfile="rmf.head"
        extname="MATRIX"
fparkey L2 rmfval2.rmf+1 LAYER add+
fcreate rmf.col rmfval12 rmfval12.rmf headfile="rmf.head"
        extname="MATRIX"
fparkey L12 rmfval12.rmf+1 LAYER add+

# Append EBOUNDS extension onto RMF FITS file
fappend ebounds1.eb rmfval1.rmf
fappend ebounds2.eb rmfval2.rmf
fappend ebounds12.eb rmfval12.rmf

######### Mode 1 and 2 ##########
# Rebin for MODE 1 or 2 data
rbnrmf binfile="mode12.bin" infile=rmfval1.rmf outfile=usa_d1_l1_m1.rmf
fparkey 1 usa_d1_l1_m1.rmf+1 MODE
fparkey 1 usa_d1_l1_m1.rmf+2 MODE
marfrmf usa_d1_l1_m1.rmf effarea1.arf usa_d1_l1_m1.rsp rmfversn=1.3.0

rbnrmf binfile="mode12.bin" infile=rmfval2.rmf outfile=usa_d1_l2_m1.rmf
fparkey 1 usa_d1_l2_m1.rmf+1 MODE
fparkey 1 usa_d1_l2_m1.rmf+2 MODE
marfrmf usa_d1_l2_m1.rmf effarea2.arf usa_d1_l2_m1.rsp rmfversn=1.3.0

# Add layers together
addrmf usa_d1_l1_m1.rsp,usa_d1_l2_m1.rsp 1.0,1.0 usa_d1_m1.rsp
fparkey L12 usa_d1_m1.rsp+1 LAYER add+
fparkey L12 usa_d1_m1.rsp+2 LAYER add+
```

```
######### Mode 3 and 4 ##########
rbnrmf binfile="mode34.bin" infile=rmfval1.rmf outfile=usa_d1_l1_m3.rmf
fparkey 3 usa_d1_l1_m3.rmf+1 MODE
fparkey 3 usa_d1_l1_m3.rmf+2 MODE
marfrmf usa_d1_l1_m3.rmf effarea1.arf usa_d1_l1_m3.rsp rmfversn=1.3.0

rbnrmf binfile="mode34.bin" infile=rmfval2.rmf outfile=usa_d1_l2_m3.rmf
fparkey 3 usa_d1_l2_m3.rmf+1 MODE
fparkey 3 usa_d1_l2_m3.rmf+2 MODE
marfrmf usa_d1_l2_m3.rmf effarea2.arf usa_d1_l2_m3.rsp rmfversn=1.3.0

addrmf usa_d1_l1_m3.rsp,usa_d1_l2_m3.rsp 1.0,1.0 usa_d1_m3.rsp
fparkey L12 usa_d1_m3.rsp+1 LAYER add+
fparkey L12 usa_d1_m3.rsp+2 LAYER add+

######## Mode 5 #################
marfrmf rmfval12.rmf effarea12.arf usa_d1_raw.rsp rmfversn=1.3.0
rbnrmf binfile="mode5.bin" infile=usa_d1_raw.rsp outfile=usa_d1_m5.rsp
fparkey L12 usa_d1_m5.rsp+1 LAYER add+
fparkey L12 usa_d1_m5.rsp+2 LAYER add+
fparkey 5 usa_d1_m5.rsp+1 MODE add+
fparkey 5 usa_d1_m5.rsp+2 MODE add+
```

This script invokes a series of `FTOOLS` which use the 128 channel ‘raw’ output from the program `matrices.C` along with some additional information (described in the files below), it creates the actual response matrices, which are `FITS` files that can be used with the X-ray spectral fitting package `XSPEC`. The different modes are created by the appropriate re-binning of the raw 128 channel matrix created by `matrices.C`.

The script requires the following files which contain the names of the columns and headers which will form part of the `FITS` files created:

eb.col:
```
CHANNEL I channel
E_MIN E keV
E_MAX E keV
```

eb.head:
```
TELESCOP = 'ARGOS ' /
INSTRUME = 'USA ' /
FILTER = 'NONE ' /
DETNAM = 'D1 ' / USA D1 (numbered 1 or 2)
MODE = 'RAW ' / Data Mode
RMFVERSN = '1992a ' /
CHANTYPE = 'PHA ' /
```

`DETCHANS = 129`[2]

```
HDUCLASS = 'OGIP ' / format devised by the OGIP
HDUCLAS1 = 'RESPONSE' / dataset associated with instrument
HDUCLAS2 = 'EBOUNDS ' / dataset is the nominal energy/chan
HDUVERS1 = '1.0.0 ' / Obsolete (for backwards compat)
HDUVERS2 = '1.2.0 ' / Obsolete (for backwards compat)
HDUVERS = '1.2.0 '
TLMIN1 = 0 / Minimum PHA channel is 0
TLMAX1 = 128 / Maximum PHA channel is 1
```

arf.col:
```
ENERG_LO E keV
ENERG_HI E keV
SPECRESP E cm2
```

arf.head:
```
TELESCOP = 'ARGOS ' /
INSTRUME = 'USA ' /
FILTER = 'NONE ' /
```

---

[2] The real number of raw channels in USA is 128. Due to a mistake in the way mode 5 was coded up in the USA software, it became necessary to introduce a 'fake' 129th channel in order to make the USA mode 5 matrices compatible with XSPEC and the FTOOLS. In the re-binning of modes 1 through 4, the 129th column is ignored, whereas in the creation of mode 5 matrices, the 129th column becomes the 48th column of the mode 5 matrix, and contains only zeros.

DETNAM = ’D1 ’ / USA D1 (numbered 1 or 2)

ARFVERSN = ’1992a ’ /

HDUCLASS = ’OGIP ’ / Conforms to OGIP standards

HDUCLAS1 = ’RESPONSE’ /

HDUCLAS2 = ’SPECRESP’ /

HDUVERS1 = ’1.0.0 ’ / Now obsolete (only HDUVERS required)

HDUVERS2 = ’1.1.0 ’ / Now obsolete (only HDUVERS required)

HDUVERS = ’1.1.0 ’ /

EFFAREA = 1.0 / Area Scaling Factor

rmf.col: ENERG_LO E keV

ENERG_HI E keV

N_GRP I

F_CHAN I

N_CHAN I

MATRIX 129E

rmf.head: TELESCOP = ’ARGOS ’ /

INSTRUME = ’USA ’ /

FILTER = ’NONE ’ /

DETNAM = ’D1 ’ / USA D1 (numbered 1 or 2)

MODE = ’RAW ’ / Data Mode

RMFVERSN = ’1992a ’ /

DETCHANS = 129

CHANTYPE = ’PHA ’

HDUCLASS = ’OGIP ’ / format devised by the OGIP

HDUCLAS1 = ’RESPONSE’ / dataset associated with instrument response

HDUCLAS2 = ’RSP_MATRIX’ / dataset is a Response Matrix

HDUCLAS3 = ’REDIST ’ / dataset is a redistribution matrix

HDUVERS1 = ’1.0.0 ’ / Obsolete (for backwards compat)

HDUVERS2 = ’1.3.0 ’ / Obsolete (for backwards compat)

HDUVERS = ’1.3.0 ’

AREASCAL = 1.0

```
TLMIN4 = 0
TLMAX4 = 128
```

Finally, the following files are required inputs of the previous script. They specify how the original 128 “raw” channels are to be re-binned for the different modes:

mode12.bin:

```
0 127 8
128 128 -1
```

mode34.bin:

```
0 127 16
128 128 -1
```

mode5.bin:

```
0 59 2
60 127 4
128 128 1
```

Modes 1 and 2 are formed by re-binning the 128 ‘raw’ channels in groups of 8 (to yield 16 channels), while modes 3 and 4 are re-binned in groups of 16 (to yield 8 channels). In mode 5, the lower energies are more finely binned than the higher energies. Thus, the first 60 raw channels are binned into 30 channels, while the final 68 raw channels are binned in groups of 4 to yield a final 17 channels. A final 48th “fake” channel (containing only zeros) is introduced in order to make our matrices compatible with XSPEC and the rest of our analysis tools.

A.1.3 Makefile

```
# Makefile for USA response matrices
# Use "make rsp" to make a full set of matrices
# Use "make install" to install them in the $USAroot/cal directory
# Use "make cleanrsp" to delete the temporary files

CC = g++
RM = rm -f
CP = cp -f
USA_ROOT_DIR = $(USAroot)

all: clean compile rsp install

compile:
$(CC) matrices.C -o matrices

# Run the script to generate response matrices
rsp:
make_response.sh

# Clean up temporary files
clean:
$(RM) *.rmf *.eb *.rsp *.arf
$(RM) ebounds1 ebounds2 ebounds12
$(RM) rmfval1 rmfval2 rmfval12
$(RM) effarea1 effarea2 effarea12

install:
$(CP) usa_d1*m1.rsp usa_d1*m3.rsp usa_d1_m5.rsp $(USA_ROOT_DIR)/cal
```

Appendix B

The USA Background Model

Da da da, Da da da, Da da da
Ich liebe dich nicht, du liebst mich nicht.
Trio, “Da, da, da” (1982)

B.1 Introduction

The USA experiment is mounted on the back of the *Advanced Research and Global Observation Satellite* (ARGOS) (see Figure 2.1), launched into a 101.5 minute, sun-synchronous orbit with an inclination of 98.74° on 23 February 1999.

Due to its orbit, ARGOS regularly (4 times per orbit) traverses regions of intense particle radiation in its low earth orbit as it crosses either the auroral belts or the *South Atlantic Anomaly* (SAA).[1] Each individual USA target pointing consists of from 4 to up to 22 minutes of time tracking the source as ARGOS moves in its orbit. USA tracks the source using an equatorial-mounted tracking mechanism that offset points from the known position and attitude of the ARGOS space craft. While ARGOS moves USA compensates for that motion by tracking the sources in pitch at the same

---

[1] Region over the South Atlantic, off the coast of Brazil, where the Earth’s magnetosphere is weaker than normal, allowing a much higher flux of high energy particles to penetrate. Most detectors must be turned off when passing through this region. Figure B.2 shows the outer edge of this ‘eye-shaped’ region beginning at longitude ∼200° and latitude ∼0°.

rate as the satellite moves through its orbit.

B.2 The USA Background: General Properties

The USA background can be thought of as originating from two main components. The first is the Cosmic Diffuse X-ray background. These are X-rays coming isotropically from everywhere in the sky. The second component of the background is a result of the evironment of charged particles (protons and electrons) around the satellite, originating from both the solar wind and the Galaxy. The regions of highest density of trapped particles are the Van Allen radiation belts and the SAA, where USA is turned off, however, other regions still contribute a substantial particle background. Although the USA veto system eliminates most of these, a small percentage ($\lesssim 5\%$) make it through the veto system and are registered, incorrectly, as photons. Our assumption is that this component of the background scales proportionately with the coincidence veto rates, which can be obtained from the housekeeping files.

X-Ray Background Points

To derive and test our background model we used areas of the sky which are known to be free of sources (so-called 'blank-sky' observations). USA used some of the same blank-sky points as used by the PCA on RXTE. Table B.1 summarizes all the blank-sky pointings taken by USA.

Name	RA (deg)	Dec (deg)	# Observations
Bckgnd_1	5.00	-67.00	17
Bckgnd_2	60.00	2.00	41
Bckgnd_3	138.00	15.00	69
Bckgnd_4	235.00	10.00	46
Bckgnd_6	160.00	75.00	167

Table B.1: USA blank-sky observations

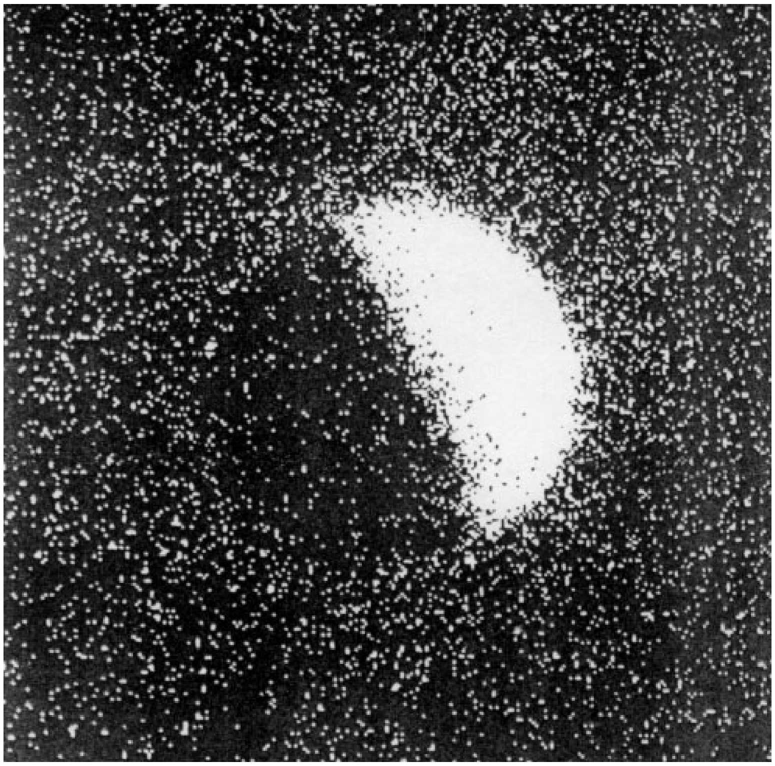

Figure B.1: ROSAT X-ray image of the moon in the 0.1-2 keV band (Schmitt et al. 1991).

B.3 Sources of the USA Background Counts

B.3.1 Cosmic Diffuse X-Ray Background

The diffuse X-ray background was discovered in 1962 (Giacconi et al. 1962) at the same time as the cosmic X-ray sources (and was listed by the Nobel committee as one of the achievements for which Giacconi was awarded the 2002 Nobel Prize in Physics). It has been found to be uniform to about 10% for the energy band of concern to USA (Charles and Seward 1995). For a full description of the diffuse X-ray background see Fabian and Barcons (1992). Figure B.1 from Schmitt et al. (1991) shows the diffuse X-ray emission surrounding an X-ray image of the moon. As can be seen from the picture, the diffuse X-ray background is brighter than the dark side of the moon.

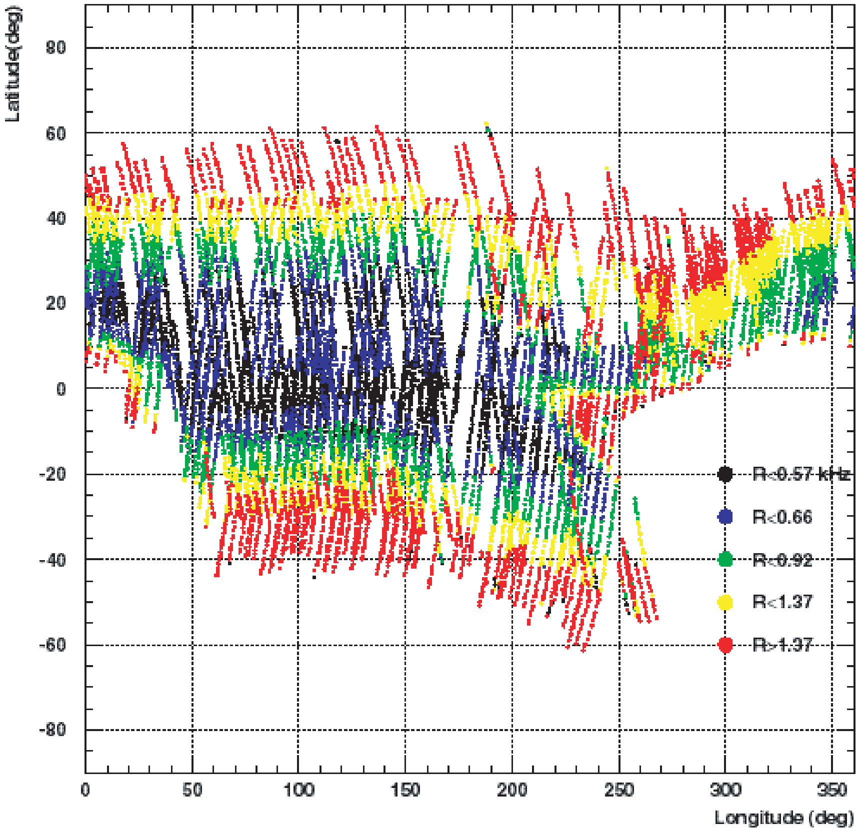

Figure B.2: USA particle veto rates

B.3.2 Trapped Charged Particles

The charged particle background interacting with USA originates primarily from the solar wind and the Galaxy. Electrons and protons coming from the Sun are trapped in the Earth's magnetic field. The South Atlantic Anomaly is a special region roughly above Brazil where the magnetic field of the Earth is unusually low, allowing particles to be present at much lower altitudes.

Cosmic Rays from the Galaxy are also a source of particles, mainly protons, which tend to be found more at the Earth's Poles, where the magnetic flux is the highest. For a description of the charged particle background encountered by USA see Wen (1997).

B.4 Modeling the USA Background

As described above, the background observed in USA is expected to come mainly from two separate components: the first one (the diffuse X-ray background) is an isotropic component coming from every direction and assumed to be constant, while the second component arises from the charged particle background and is expected to scale proportionately with the Coincidence Veto rates. This second component will therefore vary as the satellite moves along its orbit. The overall background in USA can therefore be modeled by the following equation:

$$R_{ij} = \alpha_{ij} C_i + D_{ij}$$

where R is the observed background rate in USA, the index i stands for the channel number, the index j for the layer (0 or 1), D stands for the Diffuse X-ray counts, and C stands for the coincidence veto rate. In mode 5 USA has no layer ID and it is not possible to distinguish between layer 1 and 2, so the model is simplified to:

$$R_j = \alpha_j C + D_j$$

In order to implement this model, we must obtain values for all the coefficients α_{ij}. This is done by first obtaining an estimate of the diffuse X-ray background as detected by USA. It is then possible to use blank sky observations to invert the above equation. To do this, of course, it is crucial to know the correct energy channel boundaries, something which has been described in Chapter 2 on the energy calibration.

Estimation of the Cosmic Diffuse X-Ray Background

The energy spectrum of the diffuse X-ray background in the USA energy range is well approximated by a power-law of index∼1.4 (Fabian and Barcons 1992). We can therefore use XSPEC (with the USA response matrices) to estimate the flux from the diffuse component of the background in the USA detector.

The total rate (in USA counts) estimated to be coming from the diffuse X-ray background is found to be ∼6–7 $\mathrm{cts\,s^{-1}}$. Estimates for the individual channels and layers are also obtained and used in the derivation of the background coefficients mentioned in the formulas above.

B.5 USA Background in Data Analysis

The main program used for the creation of a background model is `usabckgnd`. It takes as input an event fits file, and a desired name for the output file (usually the same). The output is a fits file (extension .bck.fits) containing an estimate for the number of background counts in each channel, layer, and second of the observation. The script `mkbckusa` allows the user to create a background (.bck.fits) file for each observation in a directory. It also has the option (only available at SLAC) of submitting all the jobs to the batch farm, thus making the process of creation of background files much more efficient. After creating a .bck.fits file for every observation, it is then possible to run the script `mktimeusa` (Reilly 2003)) on an entire directory of observations. This script filters the USA observations according to a set of parameters of the user's choosing. The output of `mktimeusa` includes (among many of its outputs) a series of `STAT` files which contain a variety of information for each second of data which passed the required cuts. Included in these `STAT` files is the background estimate for each channel and layer (see Reilly (2003) for full details of `mktimeusa`), making them very valuable tools for simple analyses of the data.

B.6 Testing of the USA Background Model

A crucial part in the development of the background model is testing whether it is indeed predicting the background with an acceptable precision. To test the model we can first run it on blank sky observations which were not used in deriving the

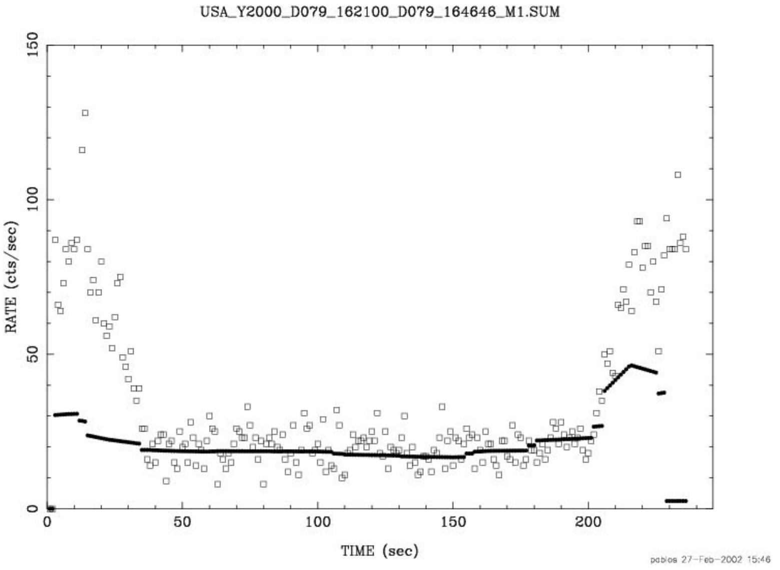

Figure B.3: Typical Background Observation. The solid line represents the background predicted by the model.

coefficients. A significant number of observations were required to produce coefficients for every possible mode (i.e. 1 through 5) and type (i.e. Ascending or Descending) of observation. The total amount of time spent on blank sky observations is ∼200 ksec. In addition, we can use all the drift observations (∼1200), to determine how good the overall background estimate is. Figure B.3 shows a typical observation for which our background model performed well. In the latest test of the background model, it was found that the model was acceptable in approximately 80% of the observations. The development and testing of the background model is ongoing as of March 2003.

Appendix C

Some USA Instrumental Issues

Ground Control to Major Tom
Your circuit's dead, there's something wrong.
David Bowie, "Space oddity" (1969)

C.1 The HKP/EVT Disparity[1]

C.1.1 Constraining the Problem

This section describes an inconsistency which was detected early on in the USA mission between the number of photons recorded in the housekeeping (HKP) files and those found in the corresponding science event (EVT) files. I first noticed this problem while working on developing a background model for USA. Due to the greater simplicity (and smaller size) of the HKP files (total count rates are recorded only once per second unlike EVT files which can contain millions of events) I had been working with these files to model the observed rates as a function of coincidence veto rates and other parameters. However, when implementing the model, it became clear that the rates in the HKP files were giving consistently higher values than those observed in the science event files. It became an important issue to determine what was causing

---

[1] This section has been adapted from two reports written for the USA SWG.

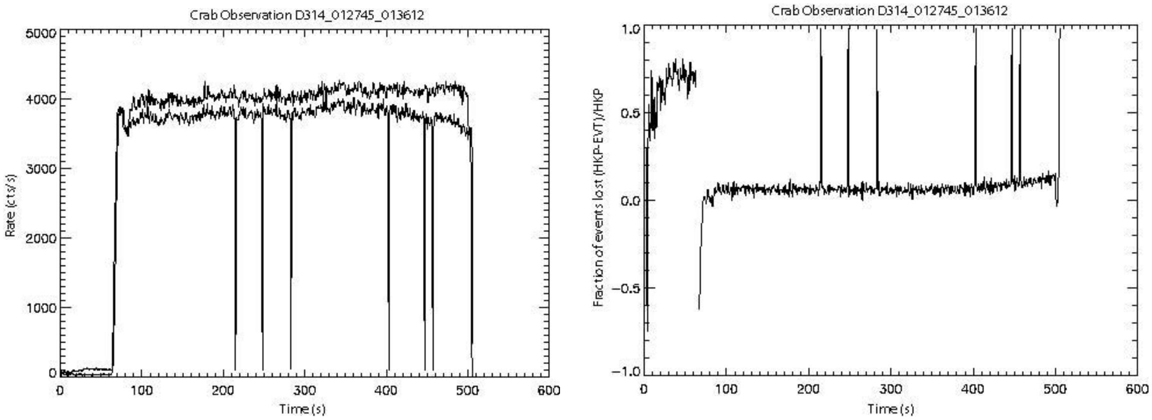

Figure C.1: Crab observation: 1999_D314_012745_013612. **Left** – HKP light curve (top) and EVT light curve (bottom) data. **Right** – Same as left Figure, expressed as a fractional loss of events.

this discrepancy, whether it might be a software bug (of which there were still many in the early days) or whether we were indeed somehow "losing" photons in the science data frames.

How large is the discrepancy?

The percentage difference between the HKP and EVT rates depends on the rate and, more importantly, whether USA is pointing on-source or off-source (i.e. at the background). Naturally, when looking at a source like the Crab, the difference is (not accounting for dead-time corrections) of the order of 10%-15%. For example, Figure C.1 shows an observation of the Crab[2] where we see an EVT rate (both layers) of ∼3700, whereas the measured rate in the HKP file is around 4100 (a difference of about 10%).

The difference is much more significant when looking at a background observation (blank sky). In this case the percentage difference is up to 80%. For example, if we look at the initial ∼60 s segment of the previous Crab observation (where USA is pointing off-source), we observe a disparity of up to 75% (see right panel of Figure C.1). In terms of absolute numbers, the disparity in the rates is of the order

---

[2] observation USA_2_Y1999_D314_012745_013612

of several hundred counts per second. In the above Crab observation, for example, the difference in the number of events was roughly 65 $\mathrm{cts\,s^{-1}}$ (with the HKP rate at $\sim$100 $\mathrm{cts\,s^{-1}}$), whereas when pointing on source, the difference is around 335 $\mathrm{cts\,s^{-1}}$ (with an HKP rate of $\sim$4100 $\mathrm{cts\,s^{-1}}$). While these numbers are for just one file, they are representative of the general trend observed in other files. When looking at the background, one hundred counts represents a much higher percentage than when looking at a bright source. In addition, it is safe to assume that the same background counts which are "lost" when pointing off-source are being lost when pointing on-source too, so the potential discrepancy between the actual source rates is likely to be significantly lower than the 10-15% estimated earlier.

Does it depend on rate?

Besides the dependence just noted (i.e. whether we are looking at a source or background), the percentage of events lost is correlated with the rate. If we plot the percentage of events lost versus the rate (see Figure C.2), we can generally distinguish two lines with very different slopes. The first line corresponds to when the rate is relatively low (less than 500 $\mathrm{cts\,s^{-1}}$) and has a very steep slope, reaching a maximum of events lost of around 80%. The second line corresponds to the higher rates (when USA is pointing on-source) and has a slope which is much more shallow, reaching a maximum of events lost of around 15%. Notice that this line goes negative for low rates. However, these are just a few points that could be due simply to the fact that the HKP second and EVT second do not begin exactly at the same time. If USA is moving onto the source, the rate could be changing rapidly. If the EVT second begins just slightly sooner than the HKP second, we would report a higher rate for those seconds in the EVT data. As soon as the rate is stable again, the HKP rate rises above the EVT rate.

Does it depend on what mode USA is observing in?

When looking at a bright source (over 1000 counts) in mode 1, we are sometimes faced with the problem of frame-overfill (Shabad 2000). Due to the packing inefficiency of

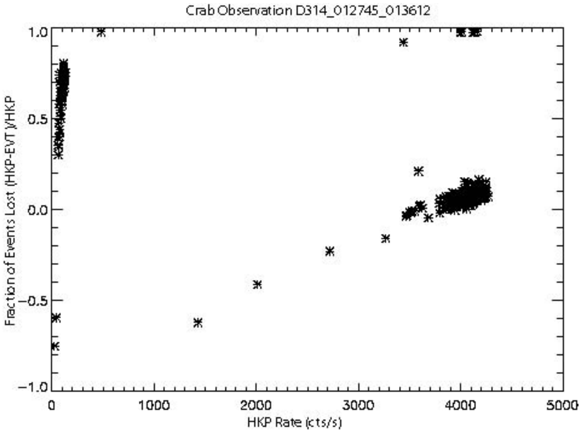

Figure C.2: Fractional loss of events as a function of Housekeeping rate

mode 1, the frame fills up in less than one second. When this happens, there will be an obvious discrepancy between the rates reported in the HKP and EVT files. This, however, is unrelated to the problem being discussed. To test for the dependence on the mode, I chose observations where the frame was not being filled in any of the modes. At a rate of less than 100 $\mathrm{cts\,s^{-1}}$ (i.e. background), frame filling is not an issue. After choosing the observations carefully, I determined that there was no observable difference between the different modes.

How are the different layers affected?

Both layers show a loss of events. The effect in layer 1, however, appears to be smaller than in layer 2. In the Crab observation mentioned earlier, the average loss in layer 1 is around 6%, whereas in layer 2 the loss is around 10% (see Figure C.3). The increase in number of lost events seen at the end of the observation is correlated with an increase in the coincidence veto rates, as ARGOS moves into the radiation belts. In looking at blank sky observations these percentages, as I have previously mentioned, increase considerably. As a rough estimate, for example, in five background observations taken on day 151 of 1999, layer 1 lost an average of 21% of the events, whereas layer 2 lost 41%.

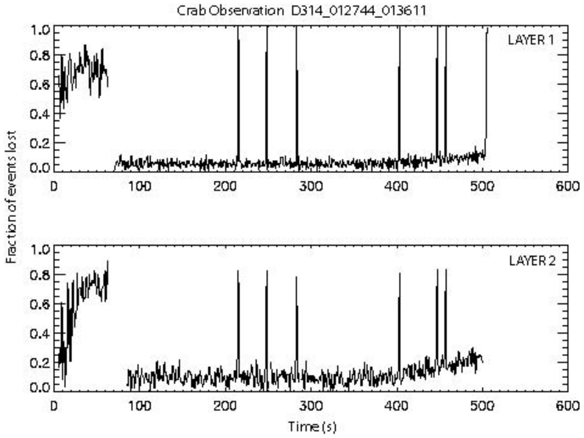

Figure C.3: Fractional loss of events in individual layers of the detector

Does it depend on the veto rates?

There does not appear to be a simple correlation between the coincidence veto rates and the fraction of events that are lost. At the poles, the veto rates are more than three times higher than in the equatorial regions, yet all else being equal (or as equal as can possibly be expected, i.e. same source, same approximate rate, same USA observing mode), the fractional loss is similar in both areas. The polar regions are known to have a fairly constant background. Both the coincidence and perimeter veto rates are essentially flat throughout most of the above mentioned Crab observation; this includes the time when USA is pointing off-source as well as when USA is looking straight at the source (see Figure C.4). I looked at Crab and Cyg X-1 observations made at the poles and they follow the same behavior described earlier. When pointing off-source, there is a high percentage of events lost (up to 70%), and when pointing on-source, this drops to around 15-20%. When USA enters a region of high background such as the particle belts, however, the coincidence veto rates jump and the fractional loss of events also increases, in a correlated fashion. (See Figure C.5). This leads to the conclusion that the events being 'lost' are mostly background (which is good).

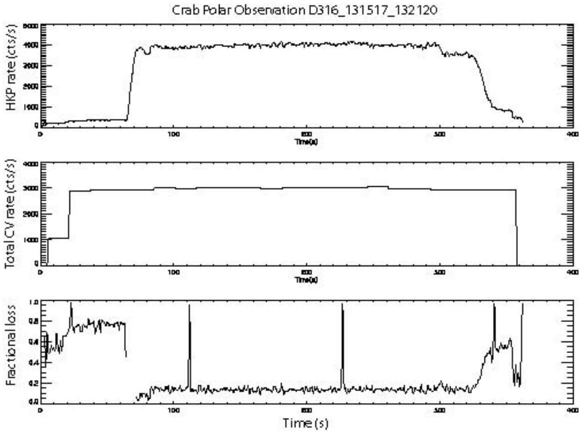

Figure C.4: Crab Polar Observation: Housekeeping light curve, Total Coincidence Veto rate and Fractional Loss of events.

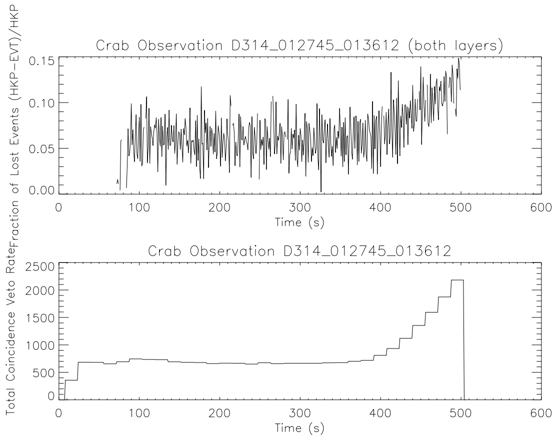

Figure C.5: Comparison of Fractional loss of events and Total Coincidence Veto rate when USA pointing is on-source.

What about Detector Dead-time Effects?

USA dead-time can account for a certain number of events being lost, but the numbers are not large enough to account for the entire disparity. However, the possibility of different dead-times for the HKP signal and the EVT signal should be explored. It was suggested that a difference in the discriminator thresholds going to the EVT and HKP signals could account for the difference in counts. The difference in such thresholds is 0.106 V vs. 0.140 V (Shabad 2000). The energy of an X-ray is linearly proportional to the amplitude of the pulse. Assuming that a 300mV (amplified x30 to 9V) corresponds to approximately 20 KeV (Shabad 2000), we estimate 0.106 V to correspond to a 0.24 keV photon, whereas 0.140 V would correspond to a 0.31 keV. This would mean that photons of energy greater than 0.24 KeV but less than 0.31 KeV would register in the HKP file, but not in the EVT data stream. Without even taking into account USA's almost negligible acceptance in that energy range, and assuming an exponential spectrum for the background, I arrive at a difference of less than one count per second. I performed a similar calculation for the crab spectrum and came up with difference of around 3 $\mathrm{cts\,s^{-1}}$. Again, this is far from the disparities we are searching for.

Does it depend on the hardness ratio of the source?

There is a hardness ratio dependence but it is not clear what it is. Figures C.6 and C.7 show four different sources (Aquila X-1, the Crab, Vela X-1, and Cas A) with very different energy spectra. Defining hardness ratio as the ratio of counts in channels 6 through 15 to the counts in channels 0 through 5, we see that whereas Aql X-1 has a greater hardness ratio, and a much larger loss of events than the Crab, Vela X-1 has a greater hardness ratio than Aql X-1, and yet the fractional loss of events is less.

In the Cas A observation (bottom right Figure C.6) there is another correlation between the fraction of events lost and the hardness ratio, which we explore in Figure C.8. Both the fractional loss of events and the hardness ratio seem to decrease in a correlated fashion. As the hardness ratio drops from about 0.13 at 100 s (average ratio from 80 to 120 s) to 0.09 at 400 s (average from 380 to 420 s), the fractional loss

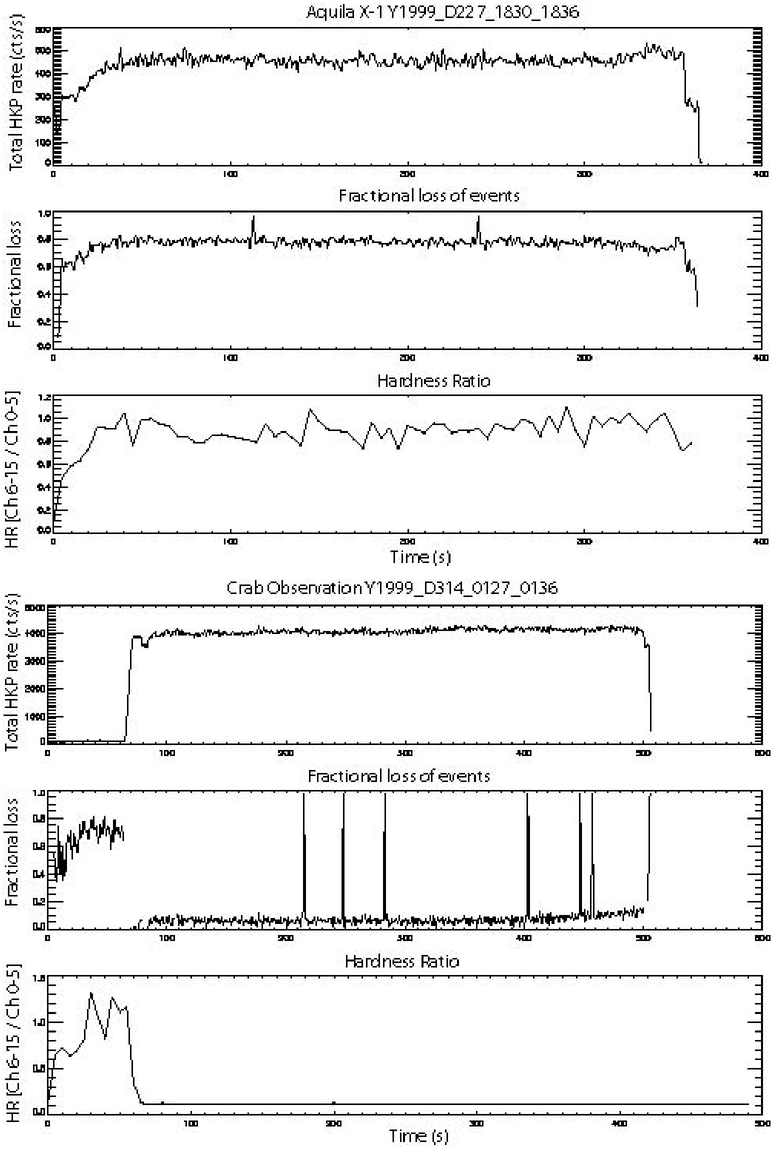

Figure C.6: Light curve, Fractional Loss, Hardness Ratio:
Top – Aquila X-1 **Bottom** – Crab

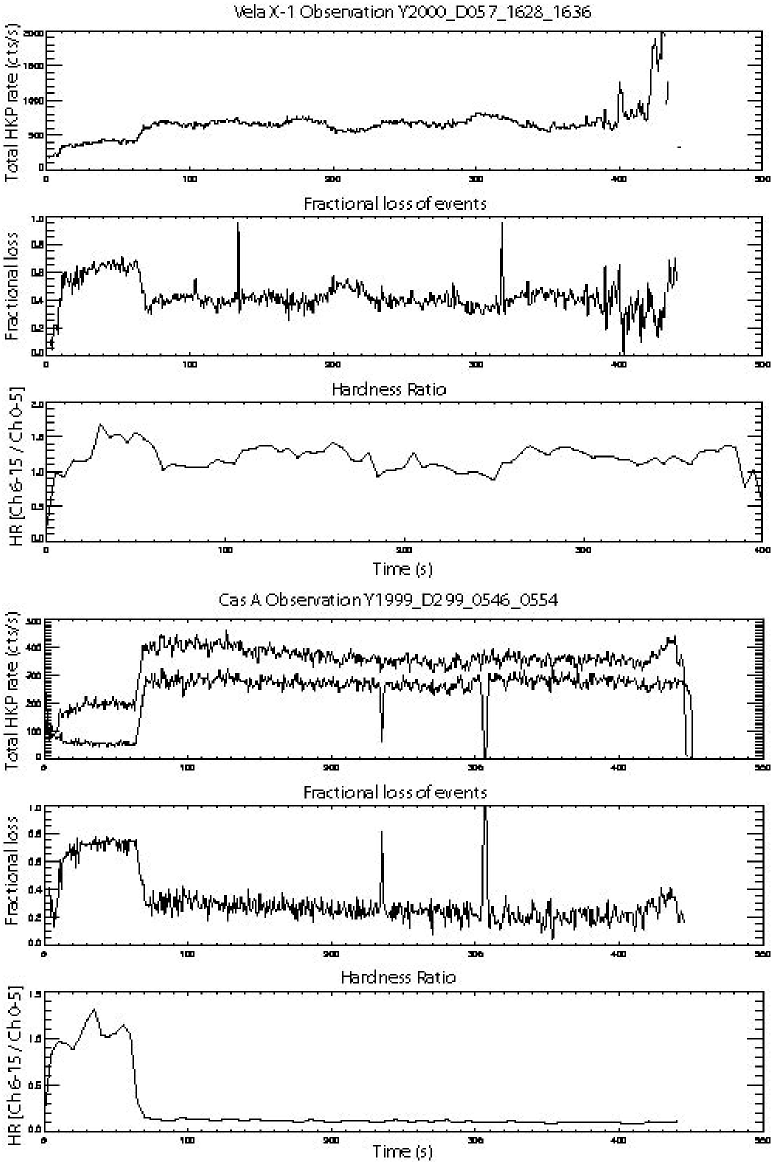

Figure C.7: Light curve, Fractional Loss, Hardness Ratio:
Top – Vela X-1 **Bottom** – Cas A

goes from 31.3% to 20.9%. Figure C.8 shows the ratio of the hardness ratio (HR) to fractional loss ((HKP-EVT)/HKP). Notice also that this ratio is significantly greater than 1 when observing the background, and significantly less than 1 when looking at the source.

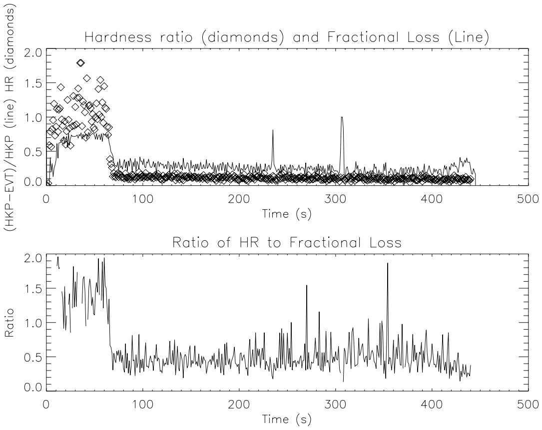

Figure C.8: Cas A Y1999_D299_054636_D299_055408: Hardness ratio and Fractional Loss relationship

Is the problem seen in the ground data?

To determine whether this was a problem that USA had developed since it was launched, I looked at data files from the 1997 TVAC tests taken with the iron calibration source. Figure C.9 shows one example of such a ground observation. None of the files examined displayed the problem seen in orbit. The average loss in all cases is less than 5%. As can be seen from the energy (count) spectrum of this source (See Figure C.10), most of the photons are found in channel 5, which corresponds to energies between 5.4 and 6.7 KeV. Furthermore, 99% of the photons fall between channels 0 through 6 (0 - 8.1 KeV). In other words, there are no high or soft energy photons in this data.

Is the problem found in the data before it is converted to fits files?

To find out whether the problem was being introduced by some of the unpacking software (namely `dat2fits`), I analyzed some data directly in the .dat format to

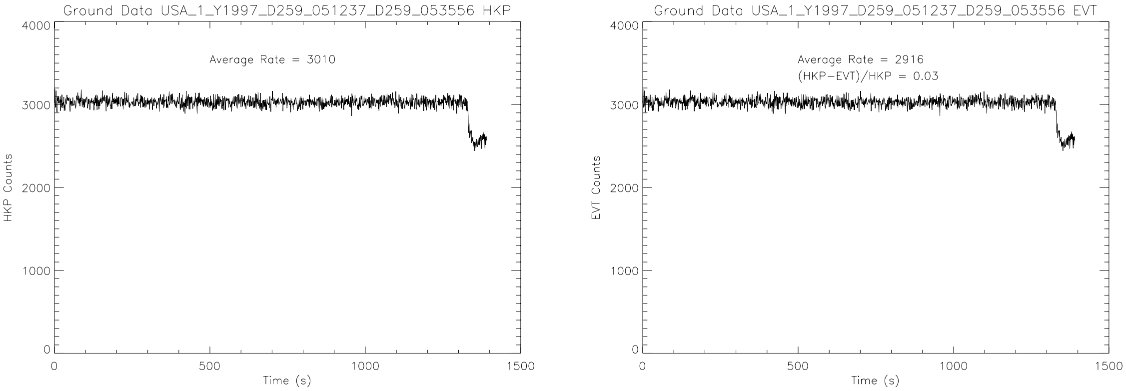

Figure C.9: Ground data (Iron calibration source) observation: Y1997_D259_051237_D259_053556. **Left** – HKP light curve. **Right** – EVT light curve.

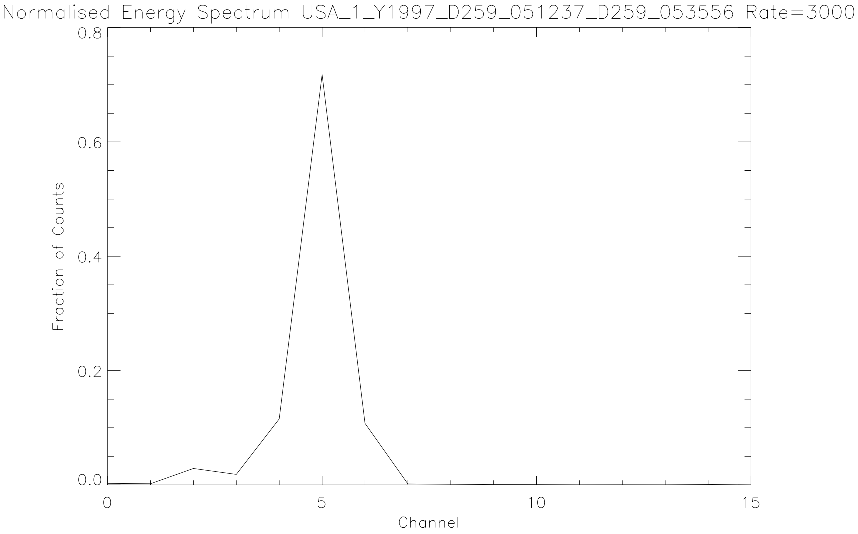

Figure C.10: Energy Spectrum (Mode 1) Y1997_D259_051237_D259_053556 make sure that the problem did not arise in the conversion from dat format to fits format. As can be seen from Figure C.11, the problem shows up exactly the same in the .dat files as in the .fits files. The top and middle panels of Figure C.11 show this discrepancy for a specific Crab observation. The bottom light curve in the top panel of Figure C.11 was obtained by using the program `parsedat` to output the number of science data (EVT) photons in each frame. The light curve in the middle panel was obtained by using `picktelem`[3] to output the corresponding housekeeping values. Figure C.12 shows that we obtain the same results by looking at a completely different source, such as Cas A.

How do the predicted hardness ratios compare with the observed ones?

I compared the hardness ratios of the Crab, Cas A, and Vela X-1. All three energy spectra are modeled as power laws of indices 2.1, 2.4, and 0.13 respectively. I estimated the hardness ratios (HR) by taking the number of counts in Channels 6 through 15 divided by the counts in Channels 0 through 5. Taking into account USA's efficiency as a function of energy and integrating each spectrum, I obtained a HR of 0.10 for the Crab, 0.07 for Cas A, and 0.89 for Vela X-1. To obtain the measured HR I looked at three files shown in Figure C.6[4]. I took the first 60 s of each observation to obtain a spectrum of the background which I then subtracted. I worked only with the science events. The following table summarizes my results. Note that the low background counts (35 and 67 respectively) are much larger in the HKP files (92 $\mathrm{cts\,s^{-1}}$ and 174 $\mathrm{cts\,s^{-1}}$ respectively). I checked another Crab observation[5], which I label Crab(2) to compare how the level of the background affects the results. As can be seen from the table, the background increases considerably (from 35 to 92), but the HR stays unchanged (up to 2 significant figures).

---

[3] picktelem is a program written by Ganwise Fewtrell at NRL to visualize USA data

[4] observations Y1999_D314_012744_D314_01361, Y2000_D057_162857_D057_163620, and Y1999_D299_054636_D299_055408

[5] observation USA_2_Y1999_D316_131516_D316_132119

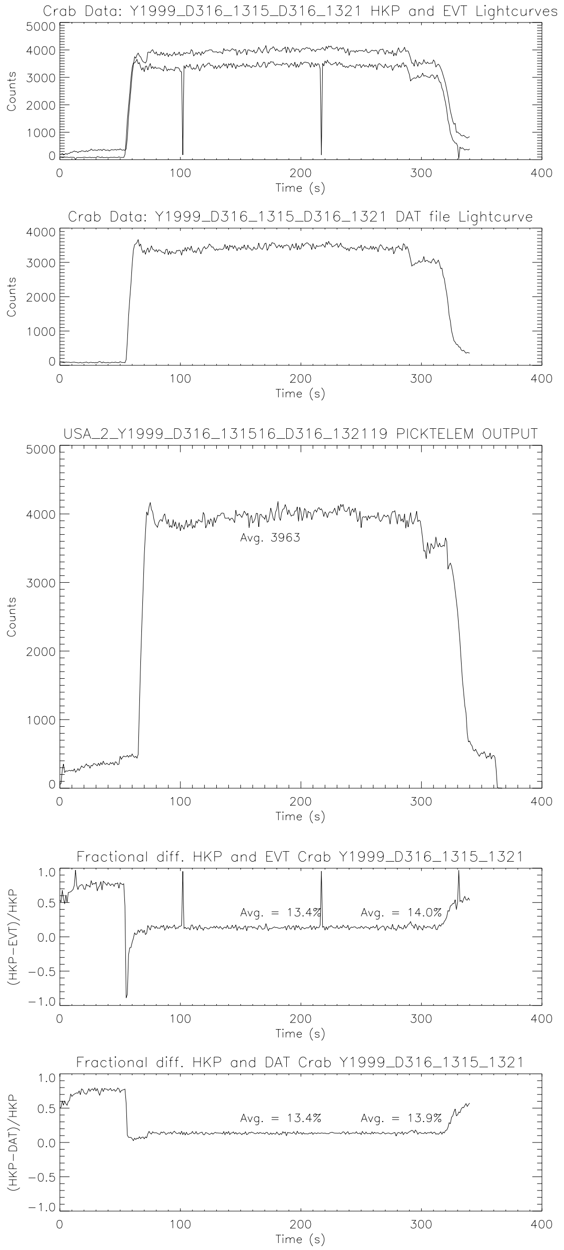

Figure C.11: Comparison of DAT files with FITS files: Crab (Y1999_D314_012744_D314_01361) HKP, EVT, DAT light curves. **Top two panels** – HKP, EVT, and DAT light curves. **Middle panel** – Picktelem light curve **Bottom two panels** – Fractional loss of events.

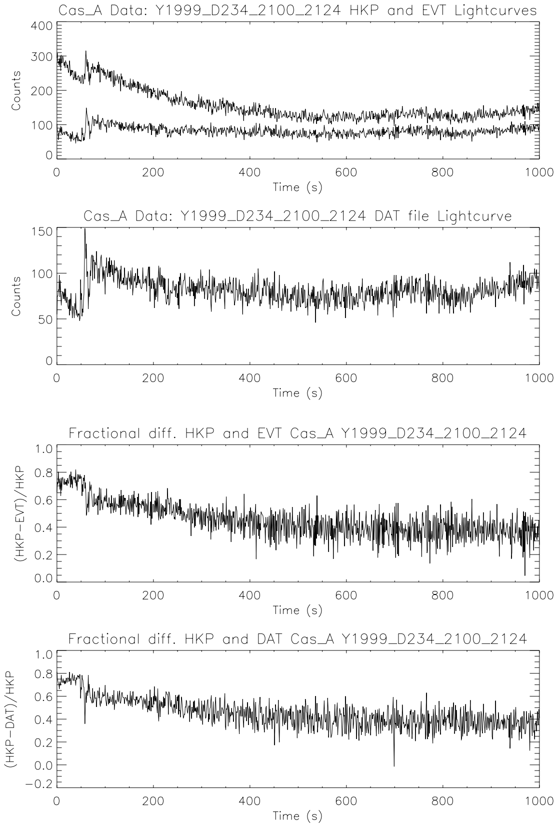

Cas_A Data: Y1999_D234_2100_2124 HKP and EVT Lightcurves

Cas_A Data: Y1999_D234_2100_2124 DAT file Lightcurve

Fractional diff. HKP and EVT Cas_A Y1999_D234_2100_2124

Fractional diff. HKP and DAT Cas_A Y1999_D234_2100_2124

Figure C.12: Comparison of DAT files with FITS files: Cas A Y1999_D234_2100_D234_2124 HKP, EVT, DAT light curves **Top two panels** – HKP, EVT, and DAT light curves. **Bottom two panels** – Fractional loss of events.

	Crab	Crab (2)	Cas A	Vela X-1
Power Law index	2.1	2.1	2.4	0.13
Predicted HR	0.10	0.10	0.07	0.89
Background Rate	35	92	67	157
On-source Rate	3747	3442	278	390
Source Rate	3712	3350	211	233
Ch 6-15/ Ch 0-5 HR	0.111	0.106	0.01	1.20
Ch 6-14/ Ch 1-5 HR	0.111	0.105	0.02	1.05

For the Crab, the observed HR is roughly what was predicted. For Cas A, however, I obtain a HR of 0.02 (neglecting channels 0 and 15), which is significantly less than predicted. This would indicate a deficit of high energy photons, suggesting the source is softer than it should be.

C.1.2 Explanation of the Effect

In the previous section, I attempted to constrain the problem of the disparity in the observed rates of the HKP files and the EVT files. The most salient feature of this observed disparity was that it seemed to be relatively much more pronounced when pointing off-source than when pointing on-source. Apparently, a larger fraction of photons is being lost from the background than photons coming from the source. The problem was also shown to worsen for dim sources (such as Cas A) than for bright ones (such as the Crab). Paradoxically, however, the problem seemed to get worse with increasing rate. These two somewhat contradictory observations can be explained if the disparity is treated not as one problem, but rather a combination of two different effects.

The first (and largest) effect can be explained as soft electrons creeping into the HKP data (but not the EVT data). This "excess" would be roughly a constant number of counts, depending on the background environment. This effect is independent of the rate of the source we are observing and will therefore represent a much larger fraction of a low rate (such as Cas A or background observations) than of a high rate observation, such as the Crab.

The second (and much smaller) effect can be explained if we can show that the HKP data somehow has a shorter dead-time than the EVT data. This effect is source-dependent, and manifests itself in the form of “missing” events in the science data. These are “real” photons that are being reported by the HKP and not by the EVT data (unlike the previous case, where no real photons are actually being lost). However, this represents a very small fraction which only becomes significant at very high rates. Moreover, it is not a surprise that we are missing these events (given that the USA dead-time is what was anticipated); rather, it is a surprise that these events are showing up in the HKP data.

To illustrate how this conclusion has been reached, I will show raster scans of several sources, showing how the problem varies as USA moves onto the source and then sweeps intermittently on and off the source.

Cas A

In Figure C.13 (left panel) we see a raster scan of Cas A, which has a relatively low count rate. The top curve shows the light curve produced from HKP data and the lower curve is obtained from the EVT data. We also see (right panel Figure C.13) that if we subtract the EVT count rate from the HKP count rate there is barely a sign of the raster across the source. Throughout most of the observation, in fact, the difference between the HKP and EVT data is almost constant. The increase towards the end of the observation is directly correlated with an increase in the coincidence veto events (background). Given that the count rate off-source is so much lower than the count rate on-source, this constant number (HKP-EVT) represents a much larger fraction of events in the former than in the latter. More importantly, however, this indicates that this disparity we are seeing most likely does not consist of photons coming from Cas A.

The Crab

I next looked at raster scans of the Crab, a source which has a rate more than ten times larger than Cas A. This gives us an idea of how the disparity between the HKP

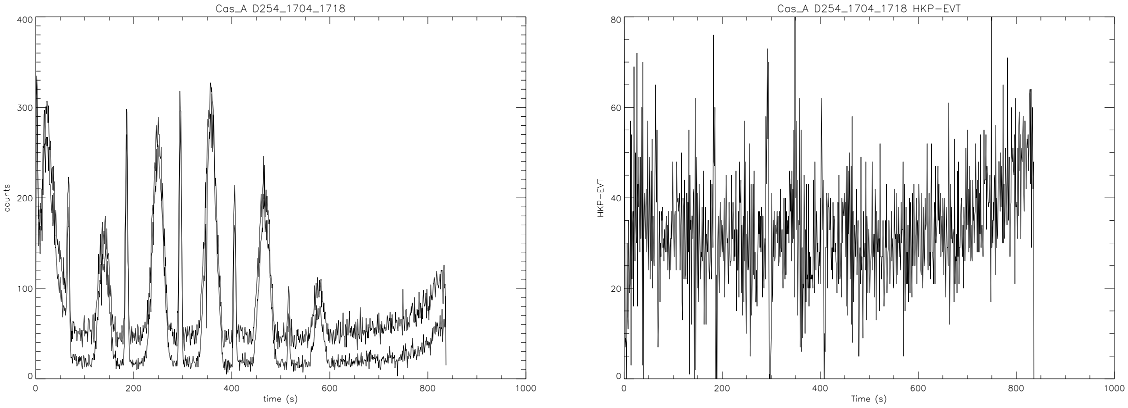

Figure C.13: Cas A: Y1999_D254_1704_D254_1718. **Left** – Raster Scan (HKP=top EVT=bottom) **Right** – HKP - EVT

and EVT rates behave as the source rate increases considerably.

Figure C.14 shows both the HKP and EVT light curves superimposed. The middle and right panels of Figure C.14 show the difference between the two light curves. Unlike the case of Cas A, here we do see a sign of the raster across the source. Two points are worth noting. First, there is a "ground-level" difference between the two light curves of around 30–40 counts. It should be noted that this value is of the same order as the difference we saw for Cas A. The second point to notice is that the HKP-EVT difference increases as USA sweeps onto the source and then decreases as we sweep off. This difference is clearly correlated with the rate of the Crab in the different sweeps. In fact, in the final sweep, when the count rate is around 300 counts, this difference is imperceptible. The large spikes that are prominent in the graph result from the fact that the HKP data is taken only once every second and therefore there can be a short lag between when the HKP second begins and when the EVT second begins.

Cyg X-3 and Cyg X-2

Next I looked at Cyg X-3 and Cyg X-2: two different sources, both quite variable, with rates of around 250 and 500 counts per second respectively. Figure C.15 shows the

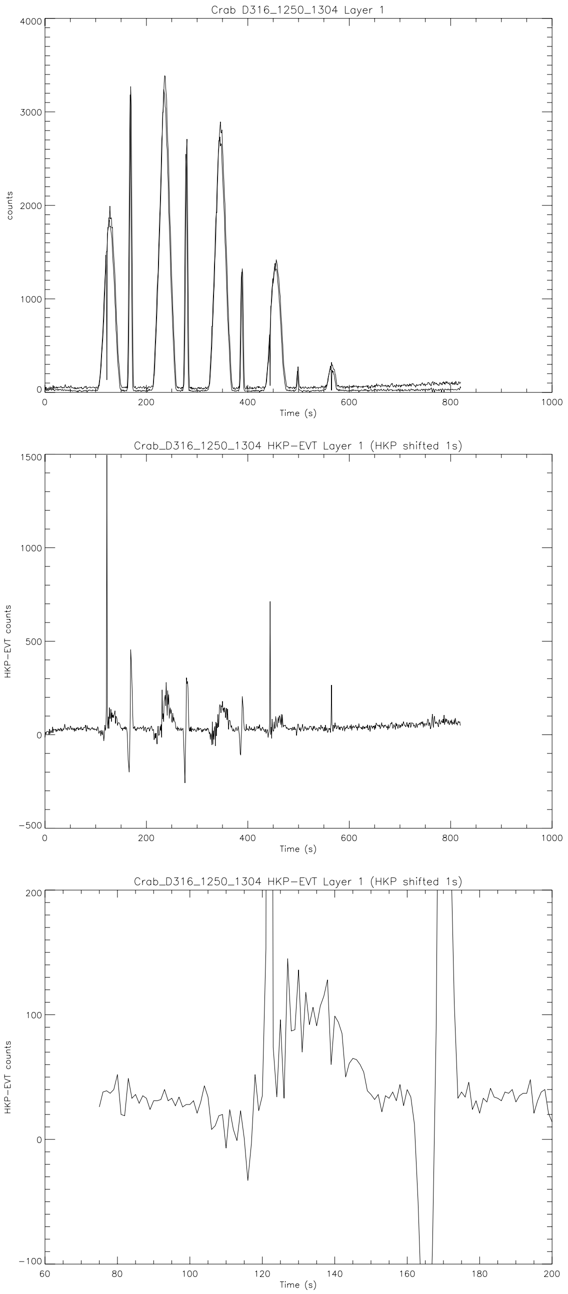

Figure C.14: Crab: Y1999_D316_1250_D316_1304. **Top** – Raster Scan (HKP=top EVT=bottom) **Middle** – HKP - EVT **Bottom** – HKP - EVT (close-up) familiar light curves (HKP and EVT) for Cyg X-3 with the middle and right panels showing the difference between the two. I have overplotted (in dots) the (EVT) light curve to show where in the plot we should be expecting signs of the source. As with Cas A, there is no sign of the source. The right panel of Figure C.15 shows the same as the middle panel at a larger scale.

Figure C.16 contains four subfigures (which I'll refer to as panels 1-4 starting from the top-left and going clockwise). The top right panel shows the two (HKP and EVT light curves). The bottom left shows the difference between the two. There is no sign of the raster scan, but there is a clear feature (bump). The bottom right panel shows how this feature is perfectly correlated with the total coincidence veto. To show both plots on the same scale, I have taken the HKP-EVT difference from the bottom left panel and multiplied it by 15 and added 500. The curve which appears to jump in steps is the lower resolution total coincidence veto rate, which is only read once every 16 seconds. This seems to be fairly strong proof that these events that are being registered by the HKP data are actually background electrons. Panel 1 shows that this "bump" corresponds to the edge of the SAA which, as can be seen on the background maps, has an "eye-shape" sticking out as far West as -135 degrees.

A (superficial) explanation of the USA electronics

In Figure C.17 I have sketched a simplified version of the USA electronics which will, nevertheless, serve to illustrate where I believe the problem of the HKP/EVT disparity arises. I have arrived at this picture mainly through looking at the original circuit diagrams with G. Godfrey at SLAC.

There are five wires which carry analog signals from the proportional chamber to the electronics board. Four of the wires are woven into an array providing two layers of nine 2.8 cm square cells, each containing one anode wire running the length of the counter. The fifth wire runs around the perimeter of the array as part of the cosmic vetoing system. The five analog signals go through their own preamplifier and discriminator (represented in Figure C.17 by five separate boxes labeled 1A and 1B (from layer 1), 2A and 2B (from layer 2) and P (from the perimeter). The threshold of

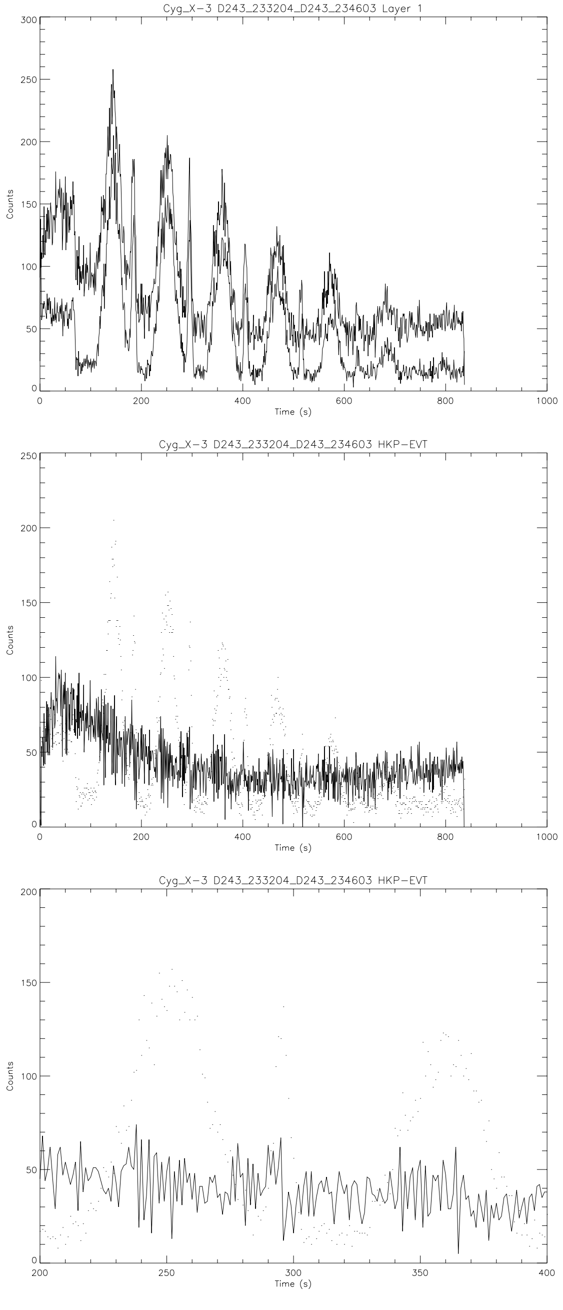

Figure C.15: Cyg X-3 Y1999_D243_2332_D243_2346. **Top** – Raster Scan (HKP=top EVT=bottom) **Middle** – HKP - EVT **Bottom** – HKP - EVT (close-up)

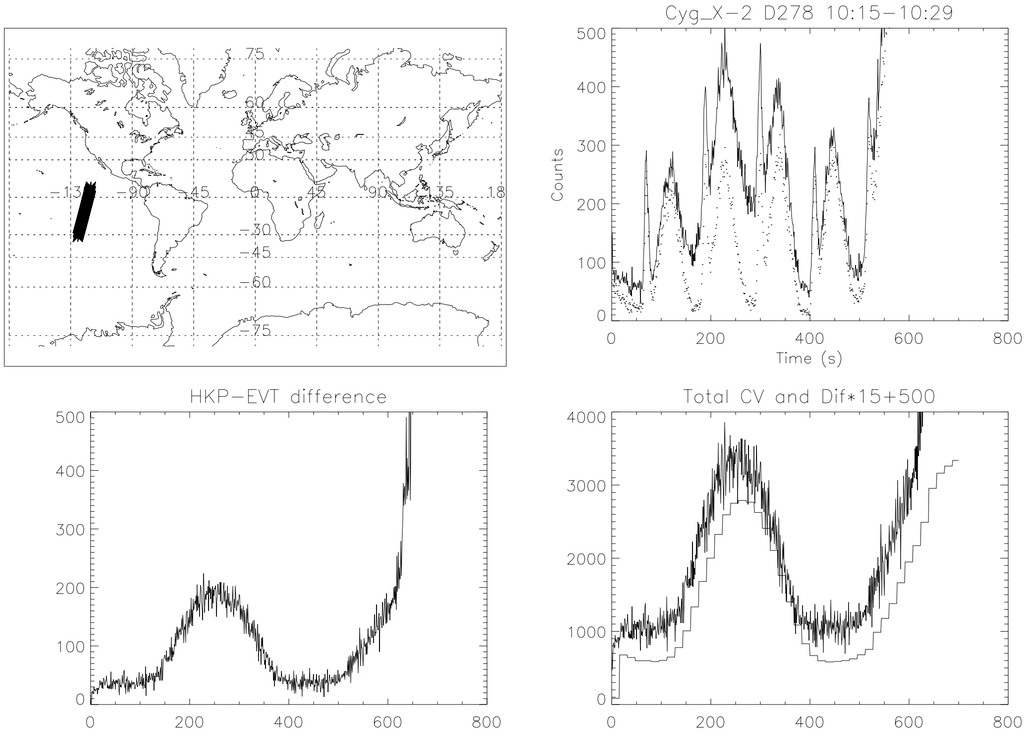

Figure C.16: Cyg X-2 Y1999_D278_1015_D278_1029: raster scan

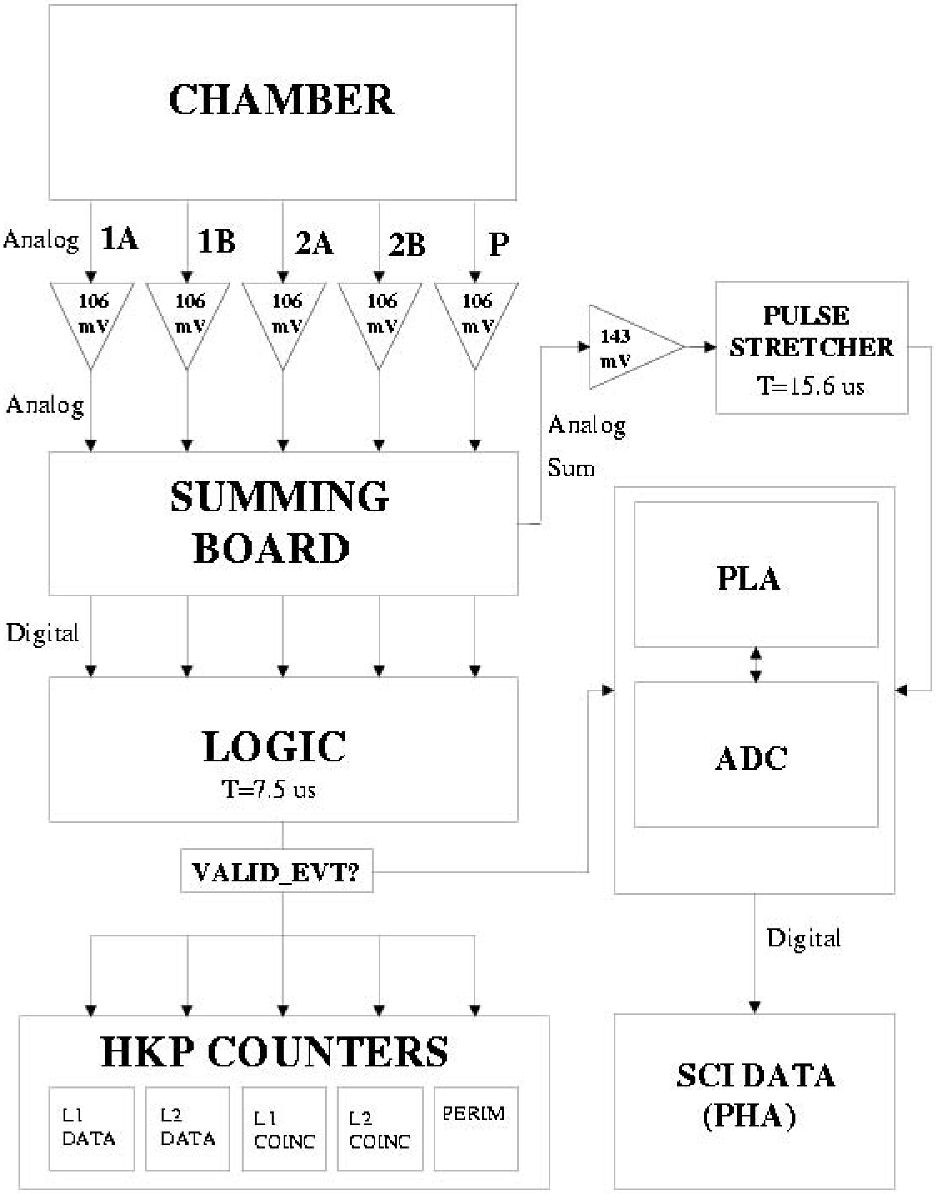

Figure C.17: USA detector electronics.

these first discriminators is 0.106 V. The five analog signals then go into the summing board. At this point, there is an important fork in the road. The summing board outputs 5 digital signals corresponding to the 5 analog ones that went in, as well as the analog sum of these signals. The 5 digital signals go through a series of logic operations which serve to sort out whether we have a valid event or whether the event should be vetoed. The amount of time it takes the logic to process an event is 7.5 clock cycles (7.5 μs). The result of this logic is fed directly to the HKP counters which are incremented accordingly. Meanwhile, the analog sum of the five signals (1A, 1B, 2A, 2B, and P) goes its own way, through the pulse stretcher, which stretches the signal to a nominal length of 15.6 μs. This pulse stretcher has its own discriminator threshold, which happens to be 0.143 V (not 0.106 V). The pulse stretcher gives the ADC enough time to process each event. The Programmable Logic Array (PLA) performs the logic operations which, among other things, decides whether we have a valid event or not. The ADC finally outputs the science data (PHA channel).

Conclusion

The two different discriminator thresholds (0.106 V vss 0.143 V) mean that there is a window (between 0.106V and 0.143 V) where photons or particles will come in, produce a signal which will register in one part of the circuit but not in the other. In the previous section I estimated the number of photons that would fall between this particular range of energies (which I estimated to lie between .24 Kev and .31 Kev) for several source energy spectra (including the background) and arrived at the conclusion that these would amount to less than 1 count per second. However, the number of (soft) electrons in this window can be several orders of magnitude larger. As we have seen from raster scans of the Crab, not all the difference between the HKP and EVT data can be attributed to background electrons. Some of this difference must indeed be attributed to photons coming from the source which are somehow “lost” by the science data. The fraction of photons being lost, as we have seen, is quite small. In fact, for sources like Cas A, Cyg X-2, or Cyg X-3 it is negligible. These differences can be attributed to the different dead-times experienced by the

HKP counters relative to that experienced by the science data. The signals which end up incrementing the HKP counters only go through the summing board and some digital veto logic, which introduces a dead-time of approximately 7.5μs. These signals never go through the pulse stretcher. On the other hand, the signal which ends up incrementing the science data counters first needs to go through the pulse strecher (which introduces a dead-time of around 15.6μs) in order to give the ADC enough time to perform its calculations and obtain (assuming the valid_evt flag is active) a PHA value for the incident photon. The following table summarises how different incident rates result in different observed rates for the two different dead-times mentioned. As can be seen, for a rate of around 500 (similar to Cas A), this difference amounts to only 2 cts s^{-1}. However, for a rate of 4000 cts s^{-1} (i.e. the Crab), the difference is of the order of 100 cts s^{-1}.

	Incident Rate	τ=7.5 μs	τ=15.6 μs	Difference
	250	249.5	249.0	0.5
	500	498.1	496.1	2
	750	745.8	741.3	4.5
	1000	992.5	984.6	8
	1500	1483	1466	18
	2000	1970	1939	31
	2500	2454	2406	48
	3000	2934	2866	68
	4000	3883	3765	120

C.2 The 400 Hz Energy Dependent Instrumental Effect (EDIE)

C.2.1 Description of the Problem

While working on the power spectrum of Cyg X-1, I first became aware of a strange feature (wiggle) around ∼400 Hz. This effect was only noticed on power spectra where only certain energy channels had been selected. When the entire energy range was selected, the effect was not seen. After the initial excitement about a possible scientific discovery in Cyg X-1, it was soon determined that this feature was present in many other sources and was therefore likely to be an instrumental effect. The main reason this effect had not been noticed before (on the ground, for example) was two-fold. Firstly, this is an effect that is observed only in 'asymmetric' count spectra, so it would not have been observed in the ground calibration data (which produces a symmetric spectrum) analyzed by Gayane Shabad. Secondly, no one had, up till then, performed power spectra on individual energy channels, which is how the problem manifests itself more prominently. This problem has come to be known as the Energy-Dependent Instrumental Effect (EDIE). Many people worked on developing an understanding of this problem, including Berrie Giebels, Gary Godfrey, Kaice Reilly, Gayane Shabad, Daniel Engovatov, and myself.

The working hypothesis (which originated with Gary Godfrey) is that EDIE is caused by a bouncing baseline in the USA electronics as a result of pile-up. When two (or more) photons arrive too close to each other, the baseline does not have time to re-set to zero and therefore the subsequent photons 'ride' on the tail of the previous photon and have incorrect energies assigned to them. If a source count spectrum is symmetric, this effect would not be noticed since for a given channel i, there would be as many photons originally from channel i being incorrectly placed in channel i+1 as photons from channel i-1 incorrectly being placed in channel i. In other words, channel i would not see an excess of photons. A count rate spectrum with a positive slope, however, would see more photons leaving channel i to go into channel i+1 than photons from channel i-1 being placed (incorrectly) into channel i. The result is a 'dip' in the power spectrum at around 400 Hz. For more details on this problem, see Reilly (2003) and Shabad (2000).

C.2.2 Correction Technique

Shabad (2000) developed a way of correcting for the problem for the specific case of XTEJ 1859, the BHC for which she detected high-frequency variability. While that technique proved to be acceptable, it is desirable to develop a correcting technique which would be independent of source. This is the aim of the technique which I will describe in this section.

Figure C.18 shows what one would expect Gary Godfrey's model for the origin of EDIE (described in section C.2.1). The plots show the relative (fractional) contribution of an individual channel to the overall spectrum of Cyg X-1, for photons arriving at different time intervals. They are constructed by selecting photons which arrive within a certain time of another photon and constructing a power spectrum. The left panel shows the relative importance of Channel 1 photons, whereas the panel on the right is the same plot constructed for Channel 3. If there were no EDIE, these plots would show a straight line. Note that the 'sign' of the effect (an initial 'deficit' in the left plot and a 'surplus' in the right plot) agrees with what the model would predict, reflecting the fact that in Channel 1, Cyg X-1 has a count spectrum slope with positive slope whereas in Channel 3 the slope negative.

To verify that the 'size' of the effect is also directly related to the slope of the count spectrum, as our model predicts, I look at the count spectra of several different sources (and at several different channels). This was done by analyzing data from the following sources: Crab, GX 349+2, X 1630, Cyg X-1, and GRS 1915. Not only was the same effect observed in all these sources, but we also observed the correlation we expected, that is, as the spectrum gets steeper, the effect of EDIE becomes more significant (more photons are switching over to neighboring PHA channels).

Lastly, having firmly established that our working interpretation of the effect is valid, we would like to use this to devise a method to correct our power spectra. To do this, we would like to explore the parameter space both in the Count Spectrum

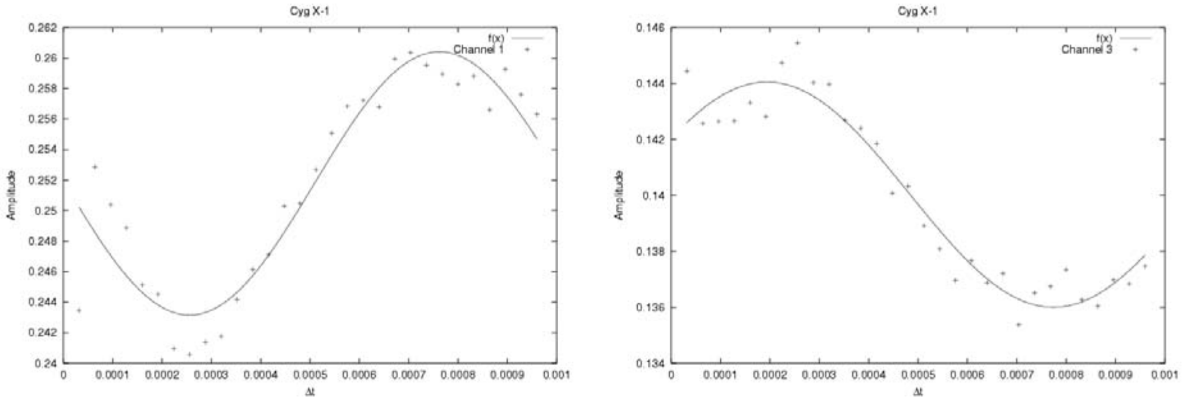

Figure C.18: EDIE in the time domain. **Left** – Channel 1 (positive slope) **Right** – Channel 3 (negative slope)

Domain and the Frequency Power Spectra domain. The goal is to use a source like the Crab, which is very constant and has a very high rate and to perform individual power spectra for different channels and rates. Each of these power spectra would give us an 'EDIE' curve with slightly different parameters, ultimately yielding a linear correlation plot which could then be used to 'predict' what EDIE would look like for any other source. The fitting function used for EDIE is the following:

$$F(x) = ax(x-b)(x-c)e^{-dx} \tag{C.1}$$

All that would be required to correct a power spectrum of a source would be to determine the count spectrum slope and the rate, and our correlation would give us the functional parameters of EDIE, allowing for its subtraction. Figure C.20 shows an example of a power spectrum of the Crab data (channel 2) at a particular rate (in this case 3400-3600 $\mathrm{cts\,s^{-1}}$).

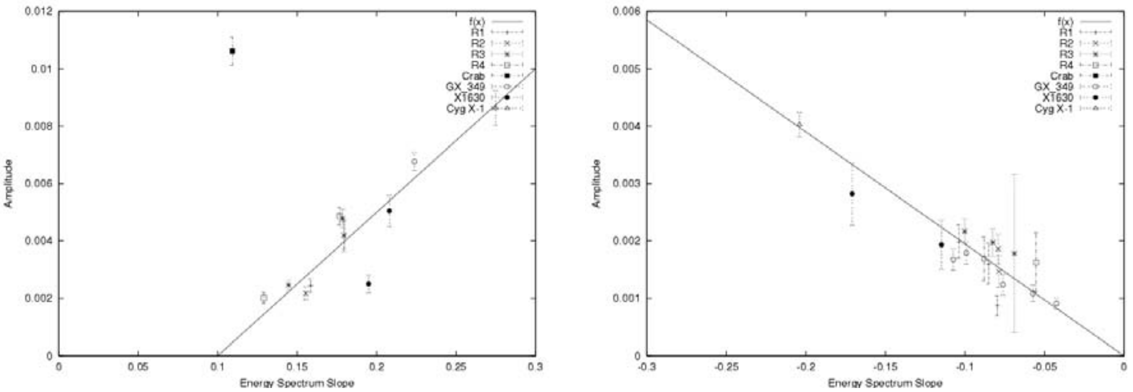

Figure C.19: EDIE correlation with spectral slope. **Left** – Positive slopes **Right** – Negative slopes

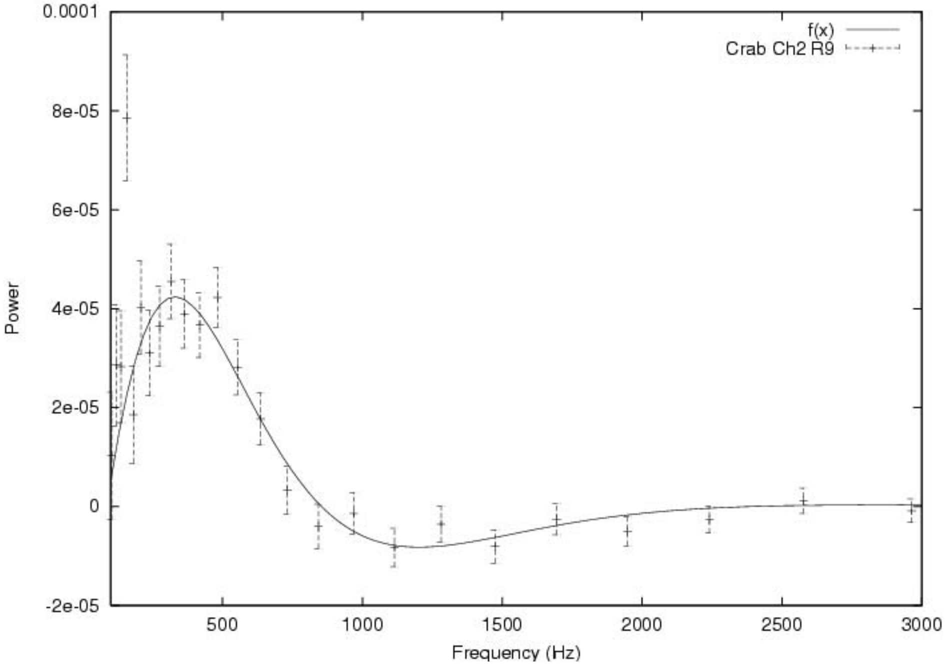

Figure C.20: EDIE in the frequency domain

Appendix D

Summary of USA Observations

Blame it on the black star
Blame it on the falling sky
Blame it on the satellite that beams me home.
Radiohead, “Black star” (1995)

D.1 USA Catalog

Summary of USA observations

NAME	CLASS	COMPACT OBJECT	EXPOSURE (ks)
Mkn 421	AGN	AGN	306.1
3C273	AGN	AGN	120.4
1es1959+650	AGN	AGN	59.0
Mkn 501	AGN	AGN	58.5
1es2344+514	AGN	AGN	26.8
NGC 1275	AGN	AGN	14.5
H1426+427	AGN	AGN	13.8
BL Lac	AGN	AGN	13.0
PKS2005-489	AGN	AGN	12.1

Summary of USA observations (continued)

2EG1224+2155	AGN	AGN	10.1
1es1741+196	AGN	AGN	9.8
MK 501	AGN	AGN	6.0
1Zw187	AGN	AGN	5.9
PG 1448+273	AGN	AGN	1.5
		TOTAL	**657.5**
Cyg X-1	HMXB	BH	728.6
XTE J1118+480	LMXB	BH	332.8
GRS 1915+105	HMXB	BH	292.0
XTE J1859+226	LMXB	BH	135.6
Cyg X-3	BHC	BH	116.4
XTE J1550-564	LMXB	BH	94.3
X1630-472	LMXB	BH	90.9
SAXJ1819-25	LMXB	BH	21.0
GRS 1758-258	LMXB	BH	16.0
X1957+115	LMXB	BH	6.2
GX 339-4	BHC	BH	2.9
		TOTAL	**1836.7**
X0142+614	AXP	NS	247.7
E 2259+586 SNR	AXP	NS	205.1
1E 1048.1-5937	AXP	NS	119.5
1E 1841-045	AXP	NS	80.5
1RXSJ170849.0-400910	AXP	NS	63.0
RX J0720.4-3125	AXP	NS	52.1
		TOTAL	**767.9**
Crab Pulsar	PSR	NS	603.5
PSR 1509-58	PSR	NS	203.8
PSR B0540-69	PSR	NS	93.2
SAX J0635+0533	PSR	NS	57.0
PSR 1821-24	PSR	NS	52.6

Summary of USA observations (continued)

PSR 1937+21	PSR	NS	10.1
SAX J1452-59 mon	PSR	NS	9.8
		TOTAL	**1030.0**
Cyg X-2	LMXB	NS	357.3
Cir X-1	LMXB	NS?	234.5
EXO 0748-676	LMXB	NS	231.5
X1820-30 (NGC 6624)	LMXB	NS	226.3
4U 0614+09	LMXB	NS	225.3
GX 349+2 (Sco X-2)	LMXB	NS	222.6
Rapid Burster (X1730-333)	LMXB	NS	184.0
Aql X-1	LMXB	NS	152.4
GX 354-0	LMXB	NS	150.4
X1636-536	LMXB	NS	139.1
Sco X-1	LMXB	NS	117.0
X1254-690	LMXB	NS	93.9
GX 340+0	LMXB	NS	78.4
X1735-444	LMXB	NS	68.2
GX 5-1	LMXB	NS	64.1
GX 17+2	LMXB	NS	59.4
Ser X-1	LMXB	NS	53.0
GX 3+1	LMXB	NS	46.2
X1624-490 (Big Dipper)	LMXB	NS	31.3
EXO 1745-248	LMXB	NS	30.4
X1659-298 (X1658-298)	LMXB	NS	28.2
GX 9+9	LMXB	NS	24.7
KS1731-260	LMXB	NS	22.4
X1608-522	LMXB	NS	22.2
GX 13+1 mon	LMXB	NS	20.6
GX 9+1 mon	LMXB	NS	12.2
GX 331-1	LMXB	NS	11.5
SAX J1712.6-3739	LMXB	NS	2.5

Summary of USA observations (continued)

1H 1556-605	LMXB	NS	0.4
		TOTAL	**2910.0**
SMC X-1	XPSR	NS	314.2
Cen X-3	XPSR	NS	211.0
LMC X-4	XPSR	NS	170.2
X0115+634	XPSR	NS	128.1
X1145-616	XPSR	NS	105.9
Her X-1	XPSR	NS	95.6
Vela X-1	XPSR	NS	86.0
GX 1+4	XPSR	NS	65.2
X1627-673	XPSR	NS	46.7
X1942+274	XPSR	NS	35.4
X1657-415	XPSR	NS	23.6
GX 301-2	XPSR	NS	11.2
1SAX J1452.8-5949	XPSR	NS	8.1
MX 0836-429	XPSR	NS	0.8
		TOTAL	**1302.0**

Summary of USA observations (continued)

X1700-377	HMXB	NS/BH	32.1
Cas A	SNR	SNR	209.2
EX Hya	CV	WD	41.2
AM Her	CV	WD	30.1
BL Hyi	CV	WD	19.1
AN UMa	CV	WD	7.7
TV Col	CV	WD	6.3
V834 Cen	CV	WD	6.2
V2301 Oph	CV	WD	4.5
BG CMi	CV	WD	4.3
EP Dra	CV	WD	3.9
GK Per	CV	WD	2.4
VV Pup	CV	WD	2.4
		TOTAL	**128.1**
Bckgnd *	BKG		189.1
Earth	BKG		4.2
Unknown (Pointing Cal)	CAL		88.4
		TOTAL	**281.7**
		GRAND TOTAL	**9155.2**

Table D.1: Accounting of the observations made during the lifetime of the USA experiment. The first column gives the source name, the second tells the source class, the third tells the type of compact object and the fourth gives the approximated actual exposure time. The different acronyms are active galactic nuclei (AGN), high-mass X-ray binary (HMXB), low-mass X-ray binary (LMXB), black hole candidate (BHC), anomalous X-ray pulsar (AXP), rotation powered pulsar (PSR), accretion powered pulsar (XPSR), cataclysmic variable (CV), background (BKG), calibration (CAL), white dwarf (WD), neutron star (NS), supernova remnant (SNR) and black hole (BH).

D.2 USA Observations of Cir X-1

USA data

Year	DOY	Date Start	Time Start	Time End	Type	Phase	Notes
2000	123	2 May	06:15:46	06:24:34	AN	0.76	
2000	123	2 May	17:43:08	17:48:51	SP	0.79	
2000	125	4 May	10:27:08	10:34:00	SP	0.89	
2000	126	5 May	03:40:54	03:50:55	AN	0.94	
2000	126	5 May	08:46:28	08:55:46	AN	0.95	
2000	126	5 May	13:29:56	13:36:22	SP	0.96	
2000	126	5 May	15:09:59	15:16:42	SP	0.96	
2000	126	5 May	16:50:10	16:57:19	SP	0.97	
2000	127	6 May	01:39:36	01:51:57	AN	0.99	
2000	127	6 May	03:22:55	03:33:34	AN	0.00	
2000	127	6 May	14:52:51	14:59:34	SP	0.02	
2000	127	6 May	16:32:45	16:39:54	SP	0.03	
2000	127	6 May	18:15:04	18:20:30	SP	0.03	
2000	128	7 May	12:56:33	13:01:31	SP	0.08	
2000	128	7 May	16:15:37	16:22:46	SP	0.09	
2000	128	7 May	17:57:39	18:03:22	SP	0.09	
2000	130	9 May	12:21:20	12:28:03	SP	0.20	
2000	131	10 May	03:55:13	04:05:54	AN	0.24	
2000	131	10 May	05:37:49	05:47:31	AN	0.24	
2000	131	10 May	07:02:17	07:11:13	SP	0.25	
2000	131	10 May	07:19:52	07:29:08	AN	0.25	
2000	131	10 May	10:42:23	10:52:23	AN	0.26	
2000	131	10 May	18:47:48	18:52:14	SP	0.28	
2000	132	11 May	05:20:25	05:30:12	AN	0.30	
2000	132	11 May	06:44:53	06:53:49	SP	0.31	
2000	132	11 May	07:02:27	07:11:49	AN	0.31	
2000	132	11 May	10:24:58	10:35:03	AN	0.32	
2000	132	11 May	11:47:13	11:53:56	SP	0.32	

USA data (Continued)

2000	132	11 May	13:27:15	13:33:33	SP	0.32
2000	134	13 May	14:32:54	14:39:37	SP	0.45
2000	135	14 May	02:44:50	02:56:36	AN	0.48
2000	135	14 May	04:27:36	04:38:13	AN	0.48
2000	135	14 May	14:15:55	14:22:21	SP	0.51
2000	135	14 May	15:55:23	16:02:49	SP	0.51
2000	135	14 May	17:37:25	17:43:25	SP	0.51
2000	136	15 May	04:10:11	04:20:55	AN	0.54
2000	136	15 May	05:52:22	06:02:32	AN	0.55
2000	136	15 May	10:59:56	11:07:24	AN	0.56
2000	136	15 May	12:18:45	12:25:11	SP	0.56
2000	136	15 May	13:58:47	14:05:13	SP	0.57
2000	136	15 May	15:38:07	15:45:33	SP	0.57
2000	138	17 May	08:22:54	08:31:16	SP	0.67
2000	138	17 May	10:22:06	10:32:46	AN	0.68
2000	138	17 May	15:04:00	15:10:52	SP	0.69
2000	139	18 May	06:42:10	06:52:13	AN	0.73
2000	139	18 May	08:23:47	08:33:50	AN	0.73
2000	139	18 May	09:47:19	09:54:19	SP	0.74
2000	139	18 May	10:04:41	10:15:27	AN	0.74
2000	139	18 May	18:09:23	18:15:06	SP	0.76
2000	140	19 May	12:50:08	12:56:34	SP	0.81
2000	141	20 May	12:33:00	12:39:43	SP	0.86
2000	141	20 May	14:13:03	14:19:29	SP	0.87
2000	141	20 May	15:52:30	15:59:56	SP	0.87
2000	141	20 May	17:34:33	17:40:33	SP	0.88
2000	142	21 May	00:40:56	00:55:26	AN	0.90
2000	143	22 May	03:49:43	04:01:20	AN	0.96
2000	146	25 May	11:07:35	11:14:01	SP	0.16
2000	148	27 May	10:53:23	11:02:57	AN	0.28
2000	149	28 May	08:52:21	09:04:02	AN	0.34

USA data (Continued)

2000	149	28 May	10:33:41	10:45:39	AN	0.34
2000	150	29 May	09:59:52	10:05:35	SP	0.40
2000	150	29 May	10:16:13	10:28:20	AN	0.40
2000	150	29 May	13:19:39	13:25:05	SP	0.41
2000	150	29 May	14:58:42	15:05:25	SP	0.41
2000	150	29 May	16:39:36	16:46:02	SP	0.42
2000	150	29 May	18:22:29	18:26:21	SP	0.42
2000	154	2 June	18:54:32	18:57:58	SP	0.67
2000	155	3 June	02:00:38	02:15:23	AN	0.68
2000	155	3 June	03:43:49	03:57:00	AN	0.69
2000	155	3 June	05:26:08	05:38:37	AN	0.69
2000	156	4 June	18:19:32	18:23:24	SP	0.79
2000	159	7 June	04:15:51	04:29:29	AN	0.93
2000	160	8 June	00:35:15	00:43:28	AN	0.98
2000	160	8 June	02:15:06	02:30:35	AN	0.99
2000	160	8 June	03:58:17	04:12:12	AN	0.99
2000	163	11 June	03:05:26	03:20:21	AN	0.17
2000	166	14 June	02:12:07	02:28:28	AN	0.35
2000	167	15 June	01:54:24	02:11:11	AN	0.41
2000	169	17 June	23:22:30	23:31:00	AN	0.58
2000	170	18 June	04:27:20	04:42:34	AN	0.60
2000	170	18 June	06:09:30	06:24:11	AN	0.60
2000	170	18 June	07:52:03	08:03:19	AN	0.61
2000	172	20 June	00:25:48	00:44:45	AN	0.71
2000	172	20 June	02:09:07	02:26:22	AN	0.71
2000	172	20 June	07:16:40	07:31:14	AN	0.73
2000	172	20 June	08:57:51	09:12:52	AN	0.73
2000	175	23 June	09:47:10	10:02:38	AN	0.91
2000	176	24 June	04:24:19	04:40:29	AN	0.96
2000	176	24 June	06:06:30	06:22:07	AN	0.96
2000	176	24 June	07:48:33	08:03:44	AN	0.97

USA data (Continued)

2000	177	25 June	02:26:29	02:36:57	AN	0.02
2000	177	25 June	04:09:57	04:18:09	AN	0.02
2000	177	25 June	07:31:07	07:46:27	AN	0.03
2000	177	25 June	09:12:50	09:25:32	AN	0.03
2000	179	27 June	03:32:15	03:45:56	AN	0.14
2000	180	28 June	03:13:50	03:29:04	AN	0.20
2000	181	29 June	02:56:23	03:14:04	AN	0.26
2000	182	30 June	02:40:33	02:52:44	AN	0.32
2000	188	6 July	06:00:27	06:18:01	AN	0.69
2000	188	6 July	07:42:29	07:59:38	AN	0.69
2000	189	7 July	02:21:34	02:31:26	AN	0.74
2000	192	10 July	18:33:53	18:39:53	AN	0.96
2000	194	12 July	17:59:51	18:05:20	AN	0.08
2000	199	17 July	18:13:58	18:20:27	AN	0.39
2000	201	19 July	17:40:04	17:45:50	AN	0.50
2000	202	20 July	17:22:38	17:28:41	AN	0.56
2000	204	22 July	15:06:34	15:12:31	AN	0.68
2000	209	27 July	06:23:42	06:32:21	SP	0.96
2000	209	27 July	08:04:19	08:12:41	SP	0.96
2000	209	27 July	11:29:06	11:32:45	SP	0.97
2000	210	28 July	07:47:09	07:55:31	SP	0.02
2000	211	29 July	19:46:16	19:56:29	AN	0.12
2000	212	30 July	04:06:03	04:28:03	AN	0.14
2000	212	30 July	05:51:08	06:04:46	AN	0.14
2000	212	30 July	07:13:25	07:20:54	SP	0.14
2000	212	30 July	08:53:05	09:01:31	SP	0.15
2000	212	30 July	10:34:42	10:41:25	SP	0.15
2000	212	30 July	10:56:06	11:11:30	AN	0.15
2000	212	30 July	12:45:07	12:51:09	AN	0.16
2000	212	30 July	17:50:49	17:57:01	AN	0.17
2000	212	30 July	21:08:26	21:21:39	AN	0.18

USA data (Continued)

2000	213	31 July	05:30:41	05:52:17	AN	0.20
2000	213	31 July	10:17:18	10:24:18	AN	0.21
2000	213	31 July	14:10:54	14:18:24	AN	0.22
2000	213	31 July	15:53:14	15:59:26	AN	0.23
2000	213	31 July	17:34:07	17:39:36	AN	0.23
2000	213	31 July	20:51:28	21:03:50	AN	0.24
2000	213	31 July	22:30:33	22:36:45	AN	0.24
2000	214	1 August	01:55:25	02:01:47	AN	0.25
2000	214	1 August	03:34:40	03:47:02	AN	0.26
2000	214	1 August	05:13:43	05:32:30	AN	0.26
2000	214	1 August	06:37:59	06:46:38	SP	0.26
2000	214	1 August	07:02:07	07:07:37	AN	0.26
2000	214	1 August	10:21:58	10:33:41	AN	0.27
2000	214	1 August	13:52:10	14:01:06	AN	0.28
2000	214	1 August	17:16:49	17:22:18	AN	0.29
2000	214	1 August	23:51:28	00:05:17	AN	0.31
2000	215	2 August	01:37:06	01:44:52	AN	0.31
2000	215	2 August	03:17:52	03:28:48	AN	0.32
2000	215	2 August	04:56:11	05:14:59	AN	0.32
2000	215	2 August	08:01:08	08:09:21	SP	0.33
2000	215	2 August	08:22:24	08:35:47	AN	0.33
2000	215	2 August	09:42:41	09:49:58	SP	0.33
2000	215	2 August	11:47:39	12:02:10	AN	0.34
2000	215	2 August	15:18:02	15:25:05	AN	0.35
2000	216	3 August	06:20:12	06:41:59	AN	0.38
2000	216	3 August	13:14:48	13:26:28	AN	0.40
2000	216	3 August	15:00:18	15:08:04	AN	0.41
2000	216	3 August	18:21:48	18:28:34	AN	0.41
2000	217	4 August	01:02:33	01:09:19	AN	0.43
2000	217	4 August	02:37:32	03:01:25	AN	0.43
2000	217	4 August	04:20:17	04:43:03	AN	0.44

USA data (Continued)

2000	217	4 August	07:26:39	07:34:52	SP	0.45
2000	217	4 August	10:49:40	10:55:22	SP	0.46
2000	217	4 August	11:11:13	11:26:53	AN	0.46
2000	217	4 August	14:43:07	14:50:36	AN	0.47
2000	217	4 August	16:25:01	16:30:47	AN	0.47
2000	217	4 August	18:04:54	18:10:57	AN	0.47
2000	226	13 August	15:29:31	15:36:17	AN	0.01
2000	226	13 August	17:10:34	17:16:03	AN	0.02
2000	237	24 August	10:26:20	10:41:56	AN	0.66
2000	237	24 August	15:40:53	15:47:22	AN	0.68
2000	238	25 August	15:23:08	15:30:11	AN	0.74
2000	238	25 August	17:04:28	17:10:14	AN	0.74
2000	239	26 August	15:05:24	15:12:53	AN	0.80
2000	239	26 August	16:47:18	16:52:47	AN	0.80
2000	239	26 August	20:05:55	20:16:08	AN	0.81
2000	239	26 August	23:26:21	23:31:50	AN	0.82
2000	240	27 August	14:48:14	14:55:43	AN	0.86
2000	240	27 August	16:30:07	16:35:36	AN	0.86

Table D.2: USA data

Bibliography

Argue, A. N., D. L. Jauncey, D. D. Morabito, and R. A. Preston (1984, July). The radio and optical identification of circinus x-1. MNRAS 209, 11–14.

Arnaud, K. and B. Dorman (2000). *XSPEC. An X-Ray Spectral Fitting Package. User's guide Version 11.* HEASARC, NASA/GSFC.

Arnaud, K. A. (1996). *XSPEC: The First Ten Years.* In ASP Conf. Ser. 101: Astronomical Data Analysis Software and Systems V, Volume 5, pp. 17–+.

Belloni, T., D. Psaltis, and M. van der Klis (2002, June). A Unified Description of the Timing Features of Accreting X-Ray Binaries. ApJ 572, 392–406.

Bracewell, R. N. (1986). *The Fourier Transform and Its Applications. 2nd Edition.* McGraw Hill.

Bradt, H. V., R. E. Rothschild, and J. H. Swank (1993, January). X-ray timing explorer mission. A&A Supplement Series 97, 355–360.

Brandt, W. N. and N. S. Schulz (2000, December). The Discovery of Broad P Cygni X-Ray Lines from Circinus X-1 with the Chandra High-Energy Transmission Grating Spectrometer. ApJL 544, L123–L127.

Brocksopp, C., P. J. Groot, and J. Wilms (2001, November). The optical long 'period' of LMC X-3. MNRAS 328, 139–146.

Case, G. L. and D. Bhattacharya (1998, May). Gamma Ray Emission from the Vicinity of the Supernova Remnant G312.4-0.4. Bulletin of the American Astronomical Society 30, 893–+.

Charles, P. A. and F. D. Seward (1995). *Exploring the X-ray Universe.* Cambridge, Great Britain: Cambridge University Press.

Clark, D. H., J. H. Parkinson, and J. L. Caswell (1975, April). Is Cir X-1 a runaway binary? Nature 254, 674–676.

Conner, J. P., W. D. Evans, and R. D. Belian (1969, September). The Recent Appearance of a New X-Ray Source in the Southern Sky. ApJL 157, L157+.

der Klis, M. V. (1988). Fourier Techniques in X-ray Timing. EXOSAT preprint 81.

der Klis, M. V. (2000). Millisecond Oscillations in X-ray Binaries. Annual Review of Astronomy and Astrophysics 38, 717–760.

Fabian, A. C. and X. Barcons (1992). The origin of the x-ray background. Annual Review of Astronomy and Astrophysics 30, 429–456.

Fender, R., R. Spencer, T. Tzioumis, K. Wu, M. van der Klis, J. van Paradijs, and H. Johnston (1998, October). An asymmetric arcsecond radio jet from circinus x-1. ApJL 506, L121–L125.

Frank, J., A. King, and D. Raine (2002). *Accretion Power in Astrophysics. 3rd Edition.* Cambridge University Press.

Friedman, H., E. T. Byram, and T. A. Chubb (1967, April). Distribution and Variability of Cosmic X-Ray Sources. Science 156, 374–378.

Giacconi, R., H. Gursky, F. Paolini, and B. Rossi (1962). Physical Review Letters 9, 439–43.

Gierliński, M. and C. Done (2002, April). A comment on the colour-colour diagrams of low-mass X-ray binaries. MNRAS 331, L47–L50.

Gies, D. R. and C. T. Bolton (1986, May). The optical spectrum of HDE 226868 = Cygnus X-1. II - Spectrophotometry and mass estimates. ApJ 304, 371–393.

Glass, I. S. (1978, May). Variations of CIR X-1 in the infrared. MNRAS 183, 335–340.

Goss, W. M. and U. Mebold (1977, November). The distance of cir x-1. MNRAS 181, 255–258.

Hasinger, G. and M. van der Klis (1989, November). Two patterns of correlated X-ray timing and spectral behaviour in low-mass X-ray binaries. A&A 225, 79–96.

Herrero, A., R. P. Kudritzki, R. Gabler, J. M. Vilchez, and A. Gabler (1995, May). Fundamental parameters of galactic luminous OB stars. II. A spectroscopic analysis of HDE 226868 and the mass of Cygnus X-1. A&A 297, 556–+.

Holt, S. S. (1976, June). Temporal X-ray astronomy with a pinhole camera. Astrophysics and Space Science 42, 123–141.

Horne, K., R. A. Wade, and P. Szkody (1986, April). A dynamical model for the dwarf nova AH Herculis. MNRAS 219, 791–808.

Iaria, R., L. Burderi, T. Di Salvo, A. La Barbera, and N. R. Robba (2001, January). A Hard Tail in the X-Ray Broadband Spectrum of Circinus X-1 at the Periastron: A Peculiar Z Source. ApJ 547, 412–419.

Iaria, R., T. Di Salvo, L. Burderi, and N. R. Robba (2001, November). Spectral Evolution of Circinus X-1 along Its Orbit. ApJ 561, 321–328.

Johnston, H. M., R. Fender, and K. Wu (1999, September). High-resolution optical and infrared spectroscopic observations of CIR X-1. MNRAS 308, 415–423.

Johnston, H. M., K. Wu, R. Fender, and J. G. Cullen (2001, December). Secular and orbital variability of Cir X-1 observed in optical spectra. MNRAS 328, 1193–1199.

Jones, C., R. Giacconi, W. Forman, and H. Tananbaum (1974, July). Observations of circinus x-1 from uhuru. ApJL 191, L71–+.

Kaluzienski, L. J., S. S. Holt, E. A. Boldt, and P. J. Serlemitsos (1976, September). Evidence for a 16.6 day period from circinus x-1. ApJL 208, L71–L75.

Kanji, G. K. (1999). *100 Statistical Tests. 2nd Edition.* Sage publications.

Knoll, G. F. (2000). *Radiation Detection and Measurement. Third Edition.* John Wiley & Sons.

Kowalski, M. P., R. G. Cruddace, W. A. Snyder, G. G. Fritz, M. P. Ulmer, and E. E. Fenimore (1993). Spartan 1 x-ray observations of the perseus cluster. iii - the distribution of iron in the intracluster gas. ApJ 412, 489.

Kuulkers, E., M. van der Klis, T. Oosterbroek, K. Asai, T. Dotani, J. van Paradijs, and W. H. G. Lewin (1994, September). Spectral and correlated timing behaviour of GX 5-1. A&A 289, 795–821.

Lamb, F. K., N. Shibazaki, M. A. Alpar, and J. Shaham (1985, October). Quasi-periodic oscillations in bright galactic-bulge X-ray sources. Nature 317, 681–687.

Leahy, D. A., W. Darbro, R. F. Elsner, M. C. Weisskopf, S. Kahn, P. G. Sutherland, and J. E. Grindlay (1983, March). On searches for pulsed emission with application to four globular cluster X-ray sources - NGC 1851, 6441, 6624, and 6712. ApJ 266, 160–170.

Lederer, C. M., J. M. Hollander, and I. Perlman (1967). *Table of Isotopes. Sixth Edition.* John Wiley & Sons.

Levine, A. M., H. Bradt, W. Cui, J. G. Jernigan, E. H. Morgan, R. Remillard, R. E. Shirey, and D. A. Smith (1996, September). First Results from the All-Sky Monitor on the Rossi X-Ray Timing Explorer. ApJL 469, L33+.

Lewin, W. H. G., J. van Paradijs, and E. P. J. van Den Heuvel (1995). *X-Ray Binaries. 2nd Edition.* Cambridge University Press.

Makishima, K., Y. Maejima, K. Mitsuda, H. V. Bradt, R. A. Remillard, I. R. Tuohy, R. Hoshi, and M. Nakagawa (1986, September). Simultaneous X-ray and optical observations of GX 339-4 in an X-ray high state. ApJ 308, 635–643.

Margon, B., M. Lampton, S. Bowyer, and R. Cruddace (1971, October). A Pulsing X-Ray Source in Circinus. ApJL 169, L23–+.

Mauche, C. W. (2002, November). Correlation of the Quasi-Periodic Oscillation Frequencies of White Dwarf, Neutron Star, and Black Hole Binaries. ApJ 580, 423–428.

Middleditch, J. (1976, December). *The measurement of the masses of the neutron star, HER X-1, and its binary companion, HZ Her, as derived rom the study of 1.24-second optical pulsations from the reversible reaction HZ HER equals HER X-1 binary system and the X-ray-to-optical reprocessing reflection and transmission mechanisms.* Ph.D. Thesis, University of California, Berkeley.

Mignani, R. P., A. De Luca, P. A. Caraveo, and I. F. Mirabel (2002, May). HST observations rule out the association between Cir X-1 and SNR G321.9-0.3. A&A 386, 487–491.

Miller, M. C., F. K. Lamb, and D. Psaltis (1998, December). Sonic-Point Model of Kilohertz Quasi-periodic Brightness Oscillations in Low-Mass X-Ray Binaries. ApJ 508, 791–830.

Mirabel, I. F. (2001). Microquasars: Open Questions and Future Perspectives. Astrophysics and Space Science Supplement 276, 319–327.

Mitsuda, K., H. Inoue, N. Nakamura, and Y. Tanaka (1989). Luminosity-related changes of the energy spectrum of X1608-522. Astronomical Society of Japan, Publications 41, 97–111.

Moneti, A. (1992, July). Optical and infrared observations of Circinus X-1. A&A 260, L7–L10.

Muno, M. P., R. A. Remillard, and D. Chakrabarty (2002, March). How Do Z and Atoll X-Ray Binaries Differ? ApJL 568, L35–L39.

Murdin, P., D. L. Jauncey, I. Lerche, G. D. Nicolson, L. J. Kaluzienski, S. S. Holt, and R. F. Haynes (1980, July). Binary model of Circinus X-1. I - Eccentricity from combined X-ray and radio observations. A&A 87, 292–298.

Nicolson, G. D. (1980, January). Circinus X-1. IAUCIRC 3449, 2–+.

Noergaard-Nielsen, H. U., C. Budtz-Joergensen, N. J. Westergaard, and H. W. Schnopper (1994, May). Excalibur - absolute calibration of the x-ray spectrum of the crab nebula. A&A 285, 705–709.

Oosterbroek, T., M. van der Klis, E. Kuulkers, J. van Paradijs, and W. H. G. Lewin (1995, May). Circinus X-1 revisited: Fast-timing properties in relation to spectral state. A&A 297, 141–158.

Orosz, J. A. (2002, September). Inventory of Black Hole Binaries. ArXiv Astrophysics e-prints, 9041–+.

Ortega-Rodríguez, M., A. S. Silbergleit, and R. V. Wagoner (2002, March). Relativistic Diskoseismology. III. Low-Frequency Fundamental p-Modes. ApJ 567, 1043–1056.

Paul, B., S. Kitamoto, and F. Makino (2000, January). Changes in the Long-Term Intensity Variations in Cygnus X-2 and LMC X-3. ApJ 528, 410–417.

Perez, C. A., A. S. Silbergleit, R. V. Wagoner, and D. E. Lehr (1997, February). Relativistic Diskoseismology. I. Analytical Results for “Gravity Modes”. ApJ 476, 589–+.

Press, W. H., S. A. Teukolsky, W. T. Vetterling, and B. P. Flannery (1992). *Numerical Recipes in C. 2nd Edition.* Cambridge University Press.

Pringle, J. E. and M. J. Rees (1972, October). Accretion Disc Models for Compact X-Ray Sources. A&A 21, 1+.

Ray, P. S., K. S. Wood, G. Fritz, P. Hertz, M. Kowalski, W. N. Johnson, M. N. Lovellette, M. T. Wolff, D. Yentis, R. M. Bandyopadhyay, E. D. Bloom, B. Giebels, G. Godfrey,

K. Reilly, P. Saz Parkinson, G. Shabad, P. Michelson, M. Roberts, D. A. Leahy, L. Cominsky, J. Scargle, J. Beall, D. Chakrabarty, and Y. Kim (2000). The usa x-ray timing experiment. In G. Malaguti, G. Palumbo, and N. White (Eds.), X-ray Astronomy 1999 – Stellar Endpoints, AGN, and the Diffuse Background, Singapore. Gordon & Breach. (astro-ph/9911236).

Reilly, K. T. (2003). *X-ray Timing and Spectral Observations of Galactic Black Hole Candidate XTE J1550-564 During Outburst.* PhD Thesis, Stanford University. SLAC Report No. 610.

Rhoades, C. E. and R. Ruffini (1971, January). Hagedorn Equation of State in Neutron Stars. ApJL 163, L83+.

Sauli, F. (1977). *Principles of Operation of Multiwire Proportional and Drift Chambers.* CERN.

Scargle, J. D. (1982, December). Studies in astronomical time series analysis. II - Statistical aspects of spectral analysis of unevenly spaced data. ApJ 263, 835–853.

Scargle, J. D., T. Steiman-Cameron, K. Young, D. L. Donoho, J. P. Crutchfield, and J. Imamura (1993, July). The quasi-periodic oscillations and very low frequency noise of Scorpius X-1 as transient chaos - A dripping handrail? ApJL 411, L91–L94.

Schmitt, J. H. M. M., S. L. Snowden, B. Aschenbach, G. Hasinger, E. Pfeffermann, P. Predehl, and J. Trumper (1991, February). A soft X-ray image of the moon. Nature 349, 583–587.

Shabad, G. (2000). *Detection of High-Frequency X-ray Variability in a Black Hole Transient with USA*. PhD Thesis, Stanford University. SLAC Report No. 562.

Shakura, N. I. and R. A. Sunyaev (1973). Black Holes in Binary Systems: Observational Appearances. In IAU Symp. 55: X- and Gamma-Ray Astronomy, Volume 55, pp. 155+.

Shirey, R. E. (1998, June). *Mass Transfer and Accretion in the Eccentric Neutron-Star Binary Circinus X-1.* Ph.D. Thesis, Massachusetts Institute of Technology.

Shirey, R. E., H. V. Bradt, and A. M. Levine (1999, May). The Complete “Z” Track of Circinus X-1. ApJ 517, 472–487.

Shirey, R. E., H. V. Bradt, A. M. Levine, and E. H. Morgan (1998, October). Quasi-periodic Oscillations Associated with Spectral Branches in Rossi X-Ray Timing Explorer Observations of Circinus X-1. ApJ 506, 374–383.

Sibgatullin, N. R. and R. A. Sunyaev (2000a, November). Energy Release During Disk Accretion onto a Rapidly Rotating Neutron Star. Astronomy Letters 26, 699–724.

Sibgatullin, N. R. and R. A. Sunyaev (2000b, December). Energy Release on the Surface of a Rapidly Rotating Neutron Star during Disk Accretion: A Thermodynamic Approach. Astronomy Letters 26, 772–778.

Silbergleit, A. S., R. V. Wagoner, and M. Ortega-Rodríguez (2001, February). Relativistic Diskoseismology. II. Analytical Results for C-modes. ApJ 548, 335–347.

Smale, A. P. and J. C. Lochner (1992, August). Long-term variability in low-mass X-ray binaries - A study using data from VELA 5B. ApJ 395, 582–591.

Smith, D. M., W. A. Heindl, and J. H. Swank (2002, October). Orbital and Superorbital Periods of 1E 1740.7-2942 and GRS 1758-258. ApJL 578, L129–L132.

Steiman-Cameron, T. Y., K. Young, J. D. Scargle, J. P. Crutchfield, J. N. Imamura, M. T. Wolff, and K. S. Wood (1994, November). Dripping handrails and the quasi-periodic oscillations of the AM Herculis objects. ApJ 435, 775–783.

Stella, L. and M. Vietri (1998, January). Lense-Thirring Precession and Quasi-periodic Oscillations in Low-Mass X-Ray Binaries. ApJL 492, L59+.

Stella, L. and M. Vietri (1999, January). kHz Quasiperiodic Oscillations in Low-Mass X-Ray Binaries as Probes of General Relativity in the Strong-Field Regime. Physical Review Letters 82, 17–20.

Stellingwerf, R. F. (1978, September). Period determination using phase dispersion minimization. ApJ 224, 953–960.

Stewart, R. T., J. L. Caswell, R. F. Haynes, and G. J. Nelson (1993, April). Circinus X-1 - A runaway binary with curved radio jets. MNRAS 261, 593–598.

Stewart, R. T., G. J. Nelson, W. Penninx, S. Kitamoto, S. Miyamoto, and G. D. Nicolson (1991, November). On the puzzling nature of the X-ray binary Circinus X-1. MNRAS 253, 212–216.

Sunyaev, R. and M. Revnivtsev (2000, June). Fourier power spectra at high frequencies: a way to distinguish a neutron star from a black hole. A&A 358, 617–623.

Tauris, T. M., R. P. Fender, E. P. J. van den Heuvel, H. M. Johnston, and K. Wu (1999, December). Circinus X-1: survivor of a highly asymmetric supernova. MNRAS 310, 1165–1169.

Tennant, A. F. (1987, June). High-frequency oscillations from CIR X-1. MNRAS 226, 971–978.

Tennant, A. F. (1988, February). Observations of 1.4-Hz quasi-periodic oscillations in CIR X-1. MNRAS 230, 403–414.

Tennant, A. F. (1991). *The QDP/PLT user's guide. Technical Memorandum 4301.* NASA.

Tennant, A. F., A. C. Fabian, and R. A. Shafer (1986a, July). Observation of type I X-ray bursts from CIR X-1. MNRAS 221, 27P–31P.

Tennant, A. F., A. C. Fabian, and R. A. Shafer (1986b, April). The discovery of X-ray bursts from CIR X-1. MNRAS 219, 871–881.

Thorsett, S. E. and D. Chakrabarty (1999, February). Neutron Star Mass Measurements. I. Radio Pulsars. ApJ 512, 288–299.

Titarchuk, L. (1994, October). Generalized Comptonization models and application to the recent high-energy observations. ApJ 434, 570–586.

Toor, A. (1977, July). Millisecond X-ray bursts from Circinus X-1. ApJL 215, L57–L60.

Toor, A. and F. D. Seward (1974, October). The crab nebula as a calibration source for x-ray astronomy. AJ 79, 995–999.

Tournear, D., E. Raffauf, E. D. Bloom, W. Focke, B. Giebels, G. Godfrey, P. M. S. Parkinson, K. T. Reilly, K. S. Wood, P. S. Ray, M. T. Wolff, R. M. Bandyopadhyay, M. N. Lovellette, and J. Scargle (2003, March). X-ray Bursts in Neutron Star and Black Hole Binaries from USA and RXTE Data: Detections and Upper Limits. ArXiv Astrophysics e-prints.

Truemper, J., W. H. G. Lewin, and W. Brinkmann (1986, December). The Evolution of Galactic X-Ray Binaries. Sky & Telescope 72, 595–+.

Tsunemi, H., S. Kitamoto, M. Manabe, S. Miyamoto, K. Yamashita, and M. Nakagawa (1989). All Sky Monitor on board the GINGA satellite and its performance. Astronomical Society of Japan, Publications 41, 391–403.

van der Klis, M. (1989). *Fourier Techniques in X-ray Timing. NATO Advanced Study Institute.* eds. H. Ogleman, & E. P. J. van den Heuvel, Kluwer Academic Publishers, p. 27-69.

Vigele (1973). *Atomic Data Tables, vol. 5.* John Wiley & Sons, p. 51.

Weaver, H. J. (1983). *Applications of Discrete and Continuous Fourier Analysis.* John Wiley & Sons.

Wen, H. C. (1997). *10 Microsecond Time Resolution Studies of Cygnus X-1.* PhD Thesis, Stanford University. SLAC Report No. 514.

Whelan, J. A. J., S. K. Mayo, D. T. Wickramasinghe, P. G. Murdin, B. A. Peterson, T. G. Hawarden, A. J. Longmore, R. F. Haynes, W. M. Goss, L. W. Simons, J. L. Caswell, A. G. Little, and W. B. McAdam (1977, November). The optical and radio counterpart of Circinus X-1 /3U 1516-56/. MNRAS 181, 259–271.

Wijnands, R. and M. van der Klis (1999, April). The Broadband Power Spectra of X-Ray Binaries. ApJ 514, 939–944.

Wijnands, R. A. D., E. Kuulkers, and A. P. Smale (1996, December). Detection of a approximately 78 day Period in the RXTE, VELA 5B, and Ariel 5 All-Sky Monitor Data of Cygnus X-2. ApJL 473, L45+.

Willingale, R., B. Aschenbach, R. G. Griffiths, S. Sembay, R. S. Warwick, W. Becker, A. F. Abbey, and J.-M. Bonnet-Bidaud (2001, January). New light on the X-ray spectrum of the Crab Nebula. A&A 365, L212–L217.

Wood, K. S., J. F. Meekins, D. J. Yentis, H. W. Smathers, D. P. McNutt, R. D. Bleach, H. Friedman, E. T. Byram, T. A. Chubb, and M. Meidav (1984, December). The HEAO A-1 X-ray source catalog. ApJ Supp. Ser. 56, 507–649.

Wood, K. S., L. Titarchuk, P. S. Ray, M. T. Wolff, M. N. Lovellette, and R. M. Bandyopadhyay (2001, December). Disk Diffusion Propagation Model for the Outburst of XTE J1118+480. ApJ 563, 246–254.

Young, K. and J. D. Scargle (1996, September). The Dripping Handrail Model: Transient Chaos in Accretion Systems. ApJ 468, 617–+.

Figure D.1: "Piled Higher and Deeper" by Jorge Cham www.phdcomics.com